Observations of ocean-ice shelf interaction at the Totten Glacier

By

Alessandro Silvano,

B.Sc., M.Sc. (University of Turin)

Submitted in fulfilment of the requirements for the Degree of

Doctor of Philosophy

A joint program between the Commonwealth Science and Industry Research Organisation and the Institute for Marine and Antarctic Studies

University of Tasmania

January, 2019

Abstract

The Antarctic Ice Sheet is the largest reservoir of glacial ice on Earth, containing the ice equivalent to 60 m of global sea level rise. Multiple observations have shown that the Antarctic Ice Sheet is losing mass at an accelerating rate, with the majority of the loss occurring in West Antarctica. This mass loss is triggered by ocean-driven melting of the ice shelves that form where the continental ice extends over the ocean. In contrast to the West Antarctic Ice Sheet, the much larger East Antarctic Ice Sheet has long been considered to be stable. However, recent studies suggest that a large part of the East Antarctic Ice Sheet is grounded well below sea level and therefore exposed to ocean heat flux. Moreover, recent satellite observations have revealed that the Totten Glacier, the largest discharger of ice in East Antarctica, has been losing mass for the past 25 years, suggesting that ocean-driven ice loss may also occur in East Antarctica.

In this thesis, the first oceanographic measurements collected near the Totten Glacier on the Sabrina Coast are used to investigate why the glacier is losing mass. Warm Modified Circumpolar Deep Water (MCDW) originating from the Southern Ocean is observed entering the cavity beneath the Totten Ice Shelf near the seafloor through a deep trough. The heat transport is sufficient to drive basal melt at a rate larger than 10 m $year^{-1}$, the highest rate among the major ice shelves in East Antarctica. These observations suggest that ocean heat flux drives mass loss of the Totten Glacier, as seen in West Antarctica.

Additional oceanographic observations show that MCDW is not only found in front of the Totten Glacier, but it fills the bottom layer on most of the continental shelf of the Sabrina Coast. Dense and cold waters typical of the East Antarctic coast are absent, despite the presence of a polynya where strong surface heat loss and salt flux by sea ice formation occur every winter. A simple ocean model driven by observed forcing reveals that freshwater released by ice-shelf basal melt inhibits the formation of dense waters on the Sabrina Coast, inducing a positive feedback of warming and increased ice-shelf melting. Finally, year-round observations of ocean properties collected by ice-capable profiling floats show that MCDW intrusions onto the shelf are persistent. Intrusions are warmer and thicker in autumn and early winter. A realistic ocean model shows that interaction between currents on the continental slope and a depression at the shelf break facilitates the MCDW intrusions onto the shelf. The seasonality of these currents explains the warmer and thicker intrusions in autumn and early winter.

This thesis provides the first direct evidence that the East Antarctic Ice Sheet is vulnerable to oceanic melting. Considering that the East Antarctic Ice Sheet contains a volume of ice grounded below sea level that is equivalent to 19 m of global sea level rise, the potential for ocean-driven melting to destabilize this large portion of the Antarctic Ice Sheet needs to be accounted for in assessments of future sea level rise.

Declaration of originality

This thesis contains no material which has been accepted for a degree or diploma by the University or any other institution, except by way of background information and duly acknowledged in the thesis, and to the best of my knowledge and belief no material previously published or written by another person except where due acknowledgement is made in the text of the thesis, nor does the thesis contain any material that infringes copyright.

Alessandro Silvano January 2019

Statement of authority of access

The publishers of the papers comprising Chapters 2, 3, 4 and 5 hold the copyright for that content. Access to the material should be sought from the respective journals. The remaining non-published content of the thesis may be made available for loan and limited copying in accordance with the Copyright Act 1968.

Alessandro Silvano January 2019

Acknowledgements

My first thanks go to my supervisory team: Steve Rintoul, Guy Williams and Beatriz Peña-Molino. It was a very disparate team that, somehow, worked. Steve provided me with real mentoring, which is (extremely) rare nowadays. Steve's genuine passion for science has been inspiring during these years. Guy helped me with all the bureaucratic issues that a PhD involves, provided answers to many of my scientific doubts, enabled me to create connections with scientists from all over the World and, more importantly, became a friend. Finally, Bea helped me with an infinite number of technical issues to process data and provided me with a knowledge on ocean dynamics that I would have never got otherwise. She helped me during stressful times, especially when I had to make difficult decisions. The team went beyond what I could ever expect. It became a family which, for Italians at least, represents the most you can get. Science needs to be inclusive: this is what I learnt from and with them.

A special thank goes to my family that has always supported me during the PhD (and before), despite over 15000 km distance. I thank my old friends Fede and Matteo for sharing everything over the years. There are so many friends I met here in Tasmania and during the V2 "expedition" to Antarctica that I can't mention everybody. If I have to mention one person, I would like to thank Cristina for the unexpected friendship during the second part of the PhD, which was the most challenging for me. Finally, I thank Hakima. Your criticism, love and support (the order is not random) have been the key.

This work was funded by the Australian Government Research Training Program Scholarship, former Australian Postgraduate Award (APA) and International Postgraduate Research Scholarship (IPRS). Additional funds came from the Institute for Marine and Antarctic Studies (IMAS) of the University of Tasmania and the Commonwealth Scientific and Industrial Research Organisation (CSIRO) through the PhD program Quantitative Marine Science (QMS).

Statement of co-author contributions

The following people contributed to the publication/preparation of work undertaken as part of this thesis:

- *Alessandro Silvano*. Institute for Marine and Antarctic Studies, University of Tasmania; Commonwealth Scientific and Industrial Research Organisation, Oceans and Atmosphere; Antarctic Climate and Ecosystems Cooperative Research Centre, University of Tasmania. **Candidate**
- *Guy D. Williams*. Institute for Marine and Antarctic Studies, University of Tasmania; Antarctic Climate and Ecosystems Cooperative Research Centre, University of Tasmania. **Supervisor**
- *Stephen R. Rintoul*. Commonwealth Scientific and Industrial Research Organisation, Oceans and Atmosphere; Antarctic Climate and Ecosystems Cooperative Research Centre, University of Tasmania. **Supervisor**
- *Beatriz Peña-Molino*. Commonwealth Scientific and Industrial Research Organisation, Oceans and Atmosphere; Antarctic Climate and Ecosystems Cooperative Research Centre, University of Tasmania
- *Esmee Van Wijk*. Commonwealth Scientific and Industrial Research Organisation, Oceans and Atmosphere; Antarctic Climate and Ecosystems Cooperative Research Centre, University of Tasmania
- *Mark Rosenberg*. Antarctic Climate and Ecosystems Cooperative Research Centre, University of Tasmania
- *William R. Hobbs*. Antarctic Climate and Ecosystems Cooperative Research Centre, University of Tasmania
- *Jamin S. Greenbaum*. Institute for Geophysics, University of Texas at Austin
- *Donald D. Blankenship*. Institute for Geophysics, University of Texas at Austin
- *Takeshi Tamura*. National Institute of Polar Research; Antarctic Climate and Ecosystems Cooperative Research Centre
- *Shigeru Aoki*. Institute of Low Temperature Science, Hokkaido University
- *Kazuya Kusahara*. Japan Agency for Marine-Earth Science and Technology (JAMSTEC); Antarctic Climate and Ecosystems Cooperative Research Centre, University of Tasmania.
- *David E. Gwyther*. Institute for Marine and Antarctic Studies, University of Tasmania.

1. Paper 1/Chapter 2: Rintoul, S. R., **A. Silvano**, B. Peña-Molino, E. van Wijk, M. A. Rosenberg, J. S. Greenbaum, and D. D. Blankenship (2016), Ocean heat drives rapid basal melt of Totten Ice Shelf, *Sci. Adv.*, *2*, e1601610, doi:10.1126/sciadv.1601610.

   S. R. Rintoul (40%), **A. Silvano** (30%), B. Peña-Molino (10%), E. van Wijk, (5%), M. Rosenberg (5%), J. S. Greenbaum (5%), D. D. Blankenship (5%).
   S.R.R. designed the experiment and secured funding for the research. S.R.R. and A.S. led the analysis and wrote the first draft of the manuscript. B.P.-M. analyzed the velocity profile data. E.v.W. and M.R. led the fieldwork and contributed to data analysis and interpretation. J.S.G. and D.D.B. conducted and analyzed the airborne geophysical surveys. All authors contributed to the analysis, discussion of results, and the writing of the manuscript.

2. Paper 2/Chapter 3: **Silvano**, **A**., S. R. Rintoul, B. Peña-Molino, and G. D. Williams (2017), Distribution of water masses and meltwater on the continental shelf near the Totten and Moscow University ice shelves, *J. Geophys. Res. Oceans*, *122*, doi:10.1002/2016JC012115.

   A. Silvano (80%), S. R. Rintoul (10%), B. Peña-Molino (5%), G. D. Williams (5%)
   A. S. conducted the analysis of the data and wrote the manuscript. S.R.R., B.P.-M. and G.D.W. contributed to interpretation of the results, provided input in writing the manuscript and supervised the work.

3. Paper 3/Chapter 4: **Silvano**, **A**., S. R. Rintoul, and L. Herraiz-Borreguero (2016), Ocean-ice shelf interaction in East Antarctica, *Oceanography*, *29*(4), 130–143, doi:10.5670/oceanog.2016.105.

   A. Silvano (70%), S. R. Rintoul (20%), L. Herraiz Borreguero (10%)
   A.S. led the synthesis of ice-ocean interaction in East Antarctica. A.S. wrote abstract, introduction, review of ice-ocean interaction at the Totten Glacier, discussion and conclusions. S.R.R. wrote the review of ice-ocean interaction at the Mertz Glacier and

L.H.B. wrote the review of ice-ocean interaction at the Amery Ice Shelf. S.R.R. and L.H.B. provided useful input to the writing of the entire manuscript.

4. Paper 4/Chapter 5: **Silvano**, **A**., S. R. Rintoul, B. Peña-Molino, W. R. Hobbs, E. van Wijk, S. Aoki, T. Tamura, and G. D. Williams (2018), Freshening by glacial meltwater enhances melting of ice shelves and reduces formation of Antarctic Bottom Water, *Sci. Adv.*, *4*, eaap9467, doi:10.1126/sciadv.aap9467.

   A. Silvano (60%), S. R. Rintoul (10%), B. Peña-Molino (5%), W. R. Hobbs (5%), E. van Wijk, (5%), S. Aoki (5%), T. Tamura (5%), G. D. Williams (5%).
   A.S. and S.R.R. conceived the study. A.S. led the analysis of the data and the interpretation of the model output. A.S. set up the mixed-layer model with useful input from B.P.M. S.R.R., B.P.-M., and E.v.W. led the fieldwork on the Sabrina Coast. S.R.R., B.P.-M., W.R.H., and G.D.W. contributed to the interpretation of the data and model output. E.v.W. processed the profiling float data. S.A. processed the oxygen-isotope data. T.T. processed the satellite sea ice production data. A.S. wrote the paper with input from all authors.

5. Chapter 6: **Silvano**, **A**., S. R. Rintoul, K. Kusahara, B. Peña-Molino, E. van Wijk, D. E. Gwyther, and G. D. Williams (in review), Warm water access to the continental shelf near the Totten Glacier. *J. Geophys. Res. Oceans*.

   A. Silvano (65%), S. R. Rintoul (5%), K. Kusahara (10%), B. Peña-Molino (5%), E. van Wijk, (5%), D. E. Gwyther (5%), G. D. Williams (5%).
   A. S. conducted the analysis of the observational and modelling data and wrote the chapter. K. K. run the numerical simulations. S.R.R., B.P.-M. and G.D.W contributed to the interpretation of the results, provided input in writing the chapter and supervised the work. E.v.W. processed the profiling float data. D.E.G. provided insights on the physical processes described in this chapter and contributed to the interpretation of the results.

We the undersigned agree with the above stated "proportion of work undertaken" for each of the above published (or submitted) peer-reviewed manuscripts contributing to this thesis:

_____

Dr Guy Williams 18 January 2019
Primary Supervisor
Institute for Marine and Antarctic Studies
Antarctic Climate and Ecosystems Cooperative Research Centre
University of Tasmania

_____

Dr Delphine Lannuzel 18 January 2019
Head, Oceans and Cryosphere Program
Institute for Marine and Antarctic Studies
University of Tasmania

Table of contents

List of tables

List of figures

Chapter 1
Introduction

East Antarctica is one of the least explored regions of our planet. Due to its great distance from inhabited areas, large portions of its coast and most of its interior have never been visited and therefore it has been somewhat 'out of sight' for the scientific community over the past decades. Another reason for the lack of scientific interest was due to previous consensus that the large ice sheet found in East Antarctica was stable and therefore not important to sea level rise in the next centuries. The major threats were considered to be the ice sheets in Greenland and West Antarctica, where ice loss was first detected more than 20 years ago. However, more recent studies have shown that areas of the East Antarctic Ice Sheet are also losing mass, with the most rapid loss observed at the Totten Glacier on the Sabrina Coast. The Totten Glacier alone holds ice equivalent to 4 meters of global sea level rise. It is therefore urgent to understand why the Totten Glacier is losing mass and what its contribution to future sea level rise will be. The main hypothesis put forward to explain the present mass loss is that warm ocean waters from the Southern Ocean are able to reach the marine extension of the Totten Glacier and melt it from below. However, until very recently, direct evidence to prove this hypothesis has been missing.

In December 2014 the Australian icebreaker *Aurora Australis* managed for the first time to reach the front of the Totten Glacier. Heavy sea-ice had blocked previous attempts to reach the glacier, but this time a change in winds opened a window of open water just in front of the glacier. During that window of 48 hours, the first oceanographic observations were collected at the front of the glacier. During the remaining weeks of that expedition, several other oceanographic measurements were collected on the continental shelf around the Totten Glacier. The analysis and interpretation of these measurements represent the core of this thesis. This chapter provides an overview of the global role of the Southern Ocean, the Antarctic Ice Sheet and their interaction. A detailed description of the region of the Totten Glacier is also included.

1.1. Antarctic Ice Sheet and sea level rise

The Antarctic Ice Sheet stores about 90% of the glacial ice on Earth (Meier, 1983). If all this ice was to melt, the global mean sea level would rise by ~ 58 m (Fretwell et al., 2013). During the past two decades the Antarctic Ice Sheet has been losing mass at an increasing rate (Rignot et al., 2011a;

Shepherd et al., 2018), contributing to sea level by 0.27 ± 0.11 mm year^{-1}, which is ~10% of the total rise (Church et al., 2013). Ocean thermal expansion has been the dominant contributor to sea level rise in the past century (Church et al., 2013). However, compared to projected contributions due to thermal expansion (0.10 – 0.33 m) by the end of the 21st century (Church et al., 2013), the amount of ice stored in the Antarctic Ice Sheet is vast. Melting of only a small fraction of the Antarctic Ice Sheet would dramatically affect the global sea level, with large consequences for human society. The biggest impact would be in coastal regions, where the cost for infrastructure adaptations to an increase of a few tens of centimeters in sea level can reach billions of dollars (Hinkel et al., 2014). Together with the Greenland Ice Sheet, mass loss from the Antarctic Ice Sheet is expected to make the largest contribution to global sea level in centuries to come (Dutton et al., 2015). The Antarctic Ice Sheet response to continued warming of the climate remains the largest single source of uncertainty in projections of long-term sea level rise (Church et al., 2013) with some models indicating a contribution of one meter by 2100 (DeConto and Pollard, 2016).

The enormous mass of ice stored in the Antarctic Ice Sheet has accumulated through snowfall in its interior over millions of years. The ice sheet flows from the interior toward the ocean through a number of fast-flowing glaciers. These outlet glaciers generally end in floating extensions, called ice shelves. Ice shelves are critical for the ice-sheet stability because they restrain ("buttress") the ice flux. A significant thinning or disappearance of the ice shelves would limit the effect of such buttressing, increasing the discharge of the ice sheet into the ocean. This mechanism is thought to have played a dominant role in the recent mass loss of the Antarctic Ice Sheet (e.g. Pritchard et al., 2012).

1.1.1. West Antarctic Ice Sheet

In past decades most of the mass loss of the Antarctic Ice Sheet has occurred in West Antarctica (Rignot et al., 2011a; Velicogna et al., 2014). Figure 1.1A shows satellite-derived mass loss of the Antarctic Ice Sheet between 2002 and 2016. It is apparent how West Antarctica is showing the highest loss, especially in the Amundsen and Bellingshausen sectors. Here the ice loss has been associated with the thinning of ice shelves and marine-terminating glaciers (Pritchard et al., 2012; Wouters et al., 2015; Cook et al., 2016). The West Antarctic Ice Sheet is particularly vulnerable because it is mostly grounded below sea level (Figure 1.1B) and therefore susceptible to melting by the ocean. Furthermore, several studies show how marine-based glacial basins are unstable if the boundary between the floating ice shelf and the grounded ice (grounding line) is located on a retrograde bed, namely where the bedrock slopes downwards inland (Weertman, 1974; Schoof,

2007). If the grounding line retreats over bedrock with a retrograde slope, the ice flux toward the ocean would increase, generating a positive feedback that is hard to reverse (Joughin and Alley, 2011). This process is called 'Marine Ice Sheet Instability' and may already be underway in Pine Island, Thwaites, Smith, and Kohler glaciers in the Amundsen Sea (Favier et al., 2014; Joughin et al., 2014; Rignot et al., 2014).

1.1.2. East Antarctic Ice Sheet and Totten Glacier

The West Antarctic Ice Sheet as a whole can potentially affect the sea level by about 4.5 m (Fretwell et al., 2013). In comparison, the Greenland Ice Sheet can contribute ~ 6-7 m (Cuffey and Marshall, 2000). However, the total contribution of these ice sheets is not even a quarter of the potential contribution stored in the East Antarctic Ice sheet. About 90% of grounded Antarctic ice is held by the East Antarctic Ice sheet, representing 53 m of sea level change equivalent (Fretwell et al. 2013). The East Antarctic Ice sheet has long been thought to be in balance (e.g. Rignot, 2002). However, recent studies suggest increased ice flux in parts of this large ice sheet (e.g. Rignot et al., 2008), including the Totten Glacier on the Sabrina Coast (see Figure 1.1 for location).

The Totten Glacier is the largest discharger of ice in East Antarctica (Rignot, 2006) and the primary outlet of the Aurora Subglacial Basin (Figure 1.1B). The Aurora Subglacial Basin is marine based and hence susceptible to ocean erosion and Marine Ice Sheet Instability (Sun et al., 2016). The Totten Glacier is important because it drains an ice volume equivalent to 3.9 m of global sea level rise (Li et al., 2015), an amount comparable to the entire West Antarctic Ice Sheet. Satellite records indicate that the Totten Glacier has the highest thinning rate in East Antarctica (Pritchard et al. 2009; Flament and Rémy 2012; Helm et al., 2014) and it has been continuously losing mass during the last 25 years (Li et al., 2016). Its floating end, the Totten Ice Shelf (TIS), shows periods of strong thinning and acceleration (Paolo et al., 2015; Greene et al., 2017), concurrent with the accelerated mass loss of grounded ice (Li et al., 2016). This evidence suggests that changes in the TIS drive the variability of mass loss in this sector of the East Antarctic Ice sheet, the same process happening in West Antarctica.

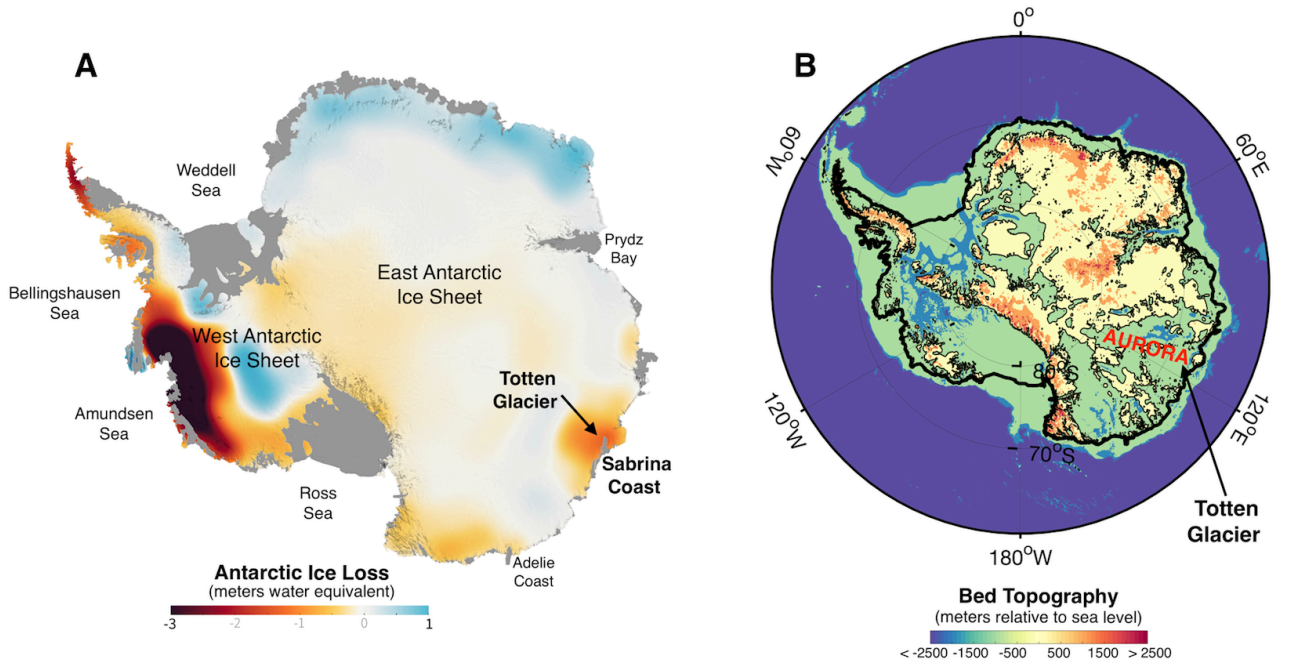

Figure 1.1. The Antarctic Ice Sheet. (A) Map of changes in Antarctic Ice Sheet mass (in meters of equivalent-water-height) between 2002 and 2016 based on observations from NASA's twin NASA/German Aerospace Center's twin Gravity Recovery and Climate Experiment (GRACE, credit NASA's Goddard Space Flight Center). In grey are the ice shelves. (B) Bed topography with coastline (thick black line) and 0-m bathymetric contour (light black line) overlaid (Fretwell et al., 2013). The locations of the Aurora Subglacial Basin and the Totten Glacier are highlighted.

Consistent with recent evidence of dynamic behaviour of multiple sectors of the Antarctic Ice Sheet, paleoclimate proxies and modelling studies conclude that both West and East Antarctic ice sheets advanced and retreated several times during the past (Naish et al., 2009; Pollard and DeConto, 2009; Williams et al., 2010a; Young et al., 2011; Cook et al., 2013; Patterson et al., 2014). This dynamic behaviour also occurred at the Totten Glacier, whose retreat during past warm climates contributed up to 2 meters to global sea level (Aitken et al., 2016). Modelling studies suggest that retreat of the Totten Glacier can be triggered by a collapse of the TIS (Golledge et al., 2015; DeConto and Pollard, 2016). In these models, ocean heat transport strongly contributes to the collapse of Antarctic ice shelves (including the TIS) under future warming scenarios. The interaction between the TIS and the surrounding ocean is therefore critical for the stability of this sector of the East Antarctic Ice Sheet and future sea level rise.

1.2. Ocean-ice shelf interaction

If we aim to estimate the Antarctic Ice Sheet contribution to sea level over the next decades and centuries, we have to understand the mechanisms and rates at which ice shelves lose their mass. At present, surface melting of ice shelves is relatively small due to the low Antarctic temperature, except for a few areas in the Antarctic Peninsula (Fyke et al., 2010; Picard and Fily, 2006). Two main mechanisms are therefore responsible for the current mass loss of Antarctic ice shelves: iceberg calving at the front and basal melt at the interface with the ocean. Historically, iceberg calving has been considered the dominant process, relegating the contribution of basal melt to about 25% of the total loss (e.g. Jacobs et al., 1992). However, thanks to the improvements of satellite image records, recent studies have revisited this hypothesis (Depooter et al., 2013; Rignot et al., 2013; Liu et al., 2015). These studies show that for many ice shelves the basal melt is well above 50% of the total mass loss, including the TIS and ice shelves in the Amundsen and Bellingshausen seas.

1.2.1. Variety of ocean-ice shelf interaction in Antarctica

Rapid ice-shelf basal melt in the Amundsen and Bellingshausen seas has been associated with intrusions of warm water onto the continental shelf (Jenkins et al., 2016). This water originates from the warm (1-2°C) and salty (34.6-34.7) Circumpolar Deep Water (CDW) found in the Southern Ocean. Close to the Antarctic margin, CDW is modified by mixing with cold Antarctic waters and is usually referred to as Modified Circumpolar Deep Water (MCDW). MCDW accesses the continental shelf of the Amundsen and Bellingshausen seas through deep troughs at the shelf break scoured during past ice ages (Jacobs et al., 2012; Jenkins and Jacobs, 2008). Once on the shelf, MCDW fills the bottom layer, overlaid by fresher and cooler surface water (also called Winter Water). MCDW flows near the seafloor along the deep troughs that connect the shelf break with the ice shelves, ultimately reaching deep areas beneath the ice shelves near the grounding lines where MCDW drives rapid basal melt (Jenkins et al., 2016). The grounding lines are typically located between 1000 and 3000 m below the sea level (Rignot and Jacobs, 2002) and here the ocean thermal forcing is further intensified because of the depression of the freezing temperature with depth (~ 0.75°C every 1000 m; Foldvik and Kvinge, 1974).

However, excluding a few regions such as the Amundsen and Bellingshausen seas, rates of ice-shelf basal melt are low in Antarctica (Figure 1.2A). This happens because most of the continental shelf around Antarctica is characterized by cold waters formed in coastal polynyas. Polynyas form when strong and cold katabatic winds flow down the continent, removing sea ice from the coast and

making the ocean surface ice-free. Heat is lost by the open ocean and new sea ice is formed. The newly-formed sea ice is again removed by winds and the process persists throughout the winter. Coastal polynyas are thus regions of enhanced sea-ice formation. Coastal regions to the west of ice barriers (grounded iceberg, fast ice or ice shelf) are especially suitable for the formation of polynyas. These barriers prevent sea ice from reaching the polynya from the east, advected by the westward Antarctic Coastal Current. During sea-ice formation some salt is rejected back into the ocean, a process called brine rejection. Cooling and salt input by brine rejection increase the density of the ocean surface (surface buoyancy loss) in polynyas (Morales Maqueda et al., 2004). Strong surface buoyancy loss in some active polynyas is sufficient to overturn the entire water column to produce cold (~ surface freezing point) and saline Dense Shelf Water (DSW, also referred to as High Salinity Shelf Water). During deep convection, the water column is homogenised and ocean heat, including that stored in the MCDW, is vented to the atmoshere. Examples of strong polynyas are found in the Ross Sea (Orsi et al., 2009), Weddell Sea (Nicholls et al., 2009), Adélie Coast (Rintoul et al., 1998), and Cape Darnley/Prydz Bay region (Ohshima et al., 2013; Williams et al., 2016). DSW formed in these regions is exported to the continental slope, where it mixes with ambient water to form Antarctic Bottom Water (AABW), a key component of the global overturning circulation and abyssal ventilation (Orsi et al., 1999; Johnson, 2008).

In summary, two main regimes can be observed in Antarctic ice-shelf cavitites. In “warm-cavity ice shelves”, as those found in the Amundsen and Bellinghsausen seas, warm MCDW drives rapid basal melt near the grounding line. A fresh mixture of MCDW and glacial meltwater upwells and exits the cavity near the surface, sustaining an overturning circulation within the cavity (Figure 1.2B). In cold-cavity ice shelves, cold DSW spreads along the seafloor from the ice front to the grounding line (Figure 1.2C). Due to the pressure dependence of the freezing point, DSW is still warmer than the local freezing point and therefore can melt the base of the ice shelf. A buoyant mixture of DSW and fresh glacial meltwater rises along the underside of the ice shelf. Where the temperature of the mixture of glacial meltwater and DSW is less than the surface freezing point (i.e. “supercooled”), this water mass is referred to as Ice Shelf Water (ISW). Formation of ISW is typical of cold-cavity ice shelves. As the ISW rises, it can reach a level where it is cooler than the in situ freezing point. This allows the formation of frazil ice crystals that may attach to the base of the ice shelf, forming what is called marine ice.

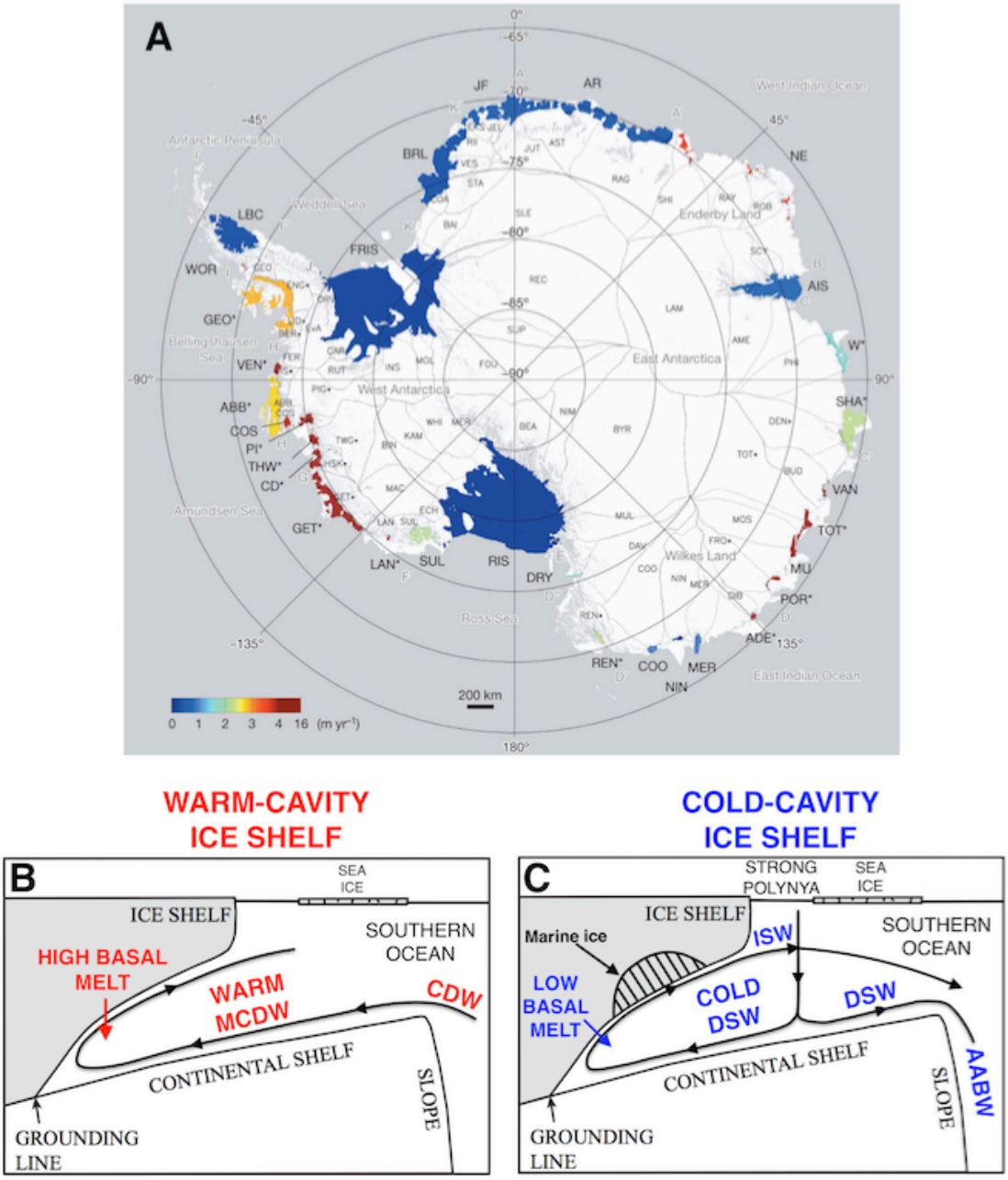

Figure 1.2. Ocean-ice shelf interaction. Map (A) of basal melt rates (m year^{-1}) of Antarctic ice shelves (from Depoorter et al., 2013 where TOT=Totten Ice Shelf and MU=Moscow University Ice Shelf). In warm-cavity ice shelves (B) Modified Circumpolar Deep Water (MCDW) drives rapid basal melt, as in the Amundsen and Bellingshausen seas. In cold-cavity ice shelves (C) Dense Shelf Water (DSW) formed in nearby polynyas drives low rates of basal melt, as for example in the Ross and Weddell seas. The outflow from the cavity is a mixture of glacial meltwater and MCDW (A) or DSW (B). The outflowing mixture can be below the local freezing point, sustaining the formation of marine ice at the base of the ice shelf. When the water produced by ocean-ice shelf interaction is below the surface freezing point, it is referred to as Ice Shelf Water (ISW) and is typical of cold-cavity ice shelves.

1.2.2. Ocean-ice shelf interaction at the Totten Glacier

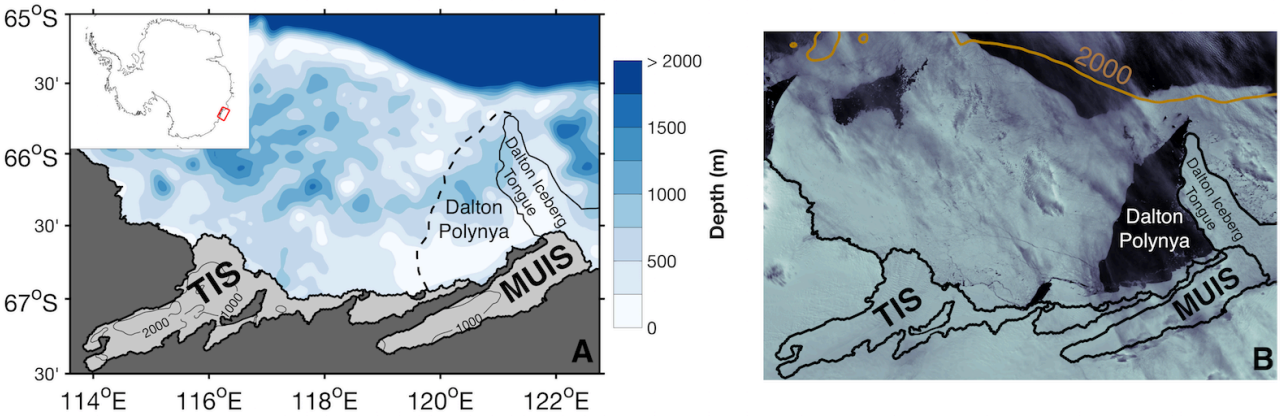

Figure 1.3. Sabrina Coast. (A) Map of the Sabrina Coast with overlaid bathymetry and coastline (Fretwell et al., 2013; Greenbaum et al., 2015). The red square in the inset shows the location of the Sabrina Coast in Antarctica. (B) MODIS (Scambos et al., 1996) satellite image (22 January 2015) with coastline overlaid. The brown line is the 2000 m isobath showing the approximate location of the continental slope. Highlighted are the Totten Ice Shelf (TIS), the Moscow University Ice Shelf (MUIS) and the Dalton Polynya formed to the west of the Dalton Iceberg Tongue.

The Sabrina Coast is characterized by the presence of two large ice shelves, the Totten and Moscow University Ice Shelf (TIS and MUIS), and by the formation of the Dalton Polynya to the west of the Dalton Iceberg Tongue, a combination of grounded icebergs and fast ice (Figures 1.3A and 1.3B). The only in-situ oceanographic measurements on the continental shelf of the Sabrina Coast were collected in 1996 and 2007 near the shelf break (Bindoff et al., 2000; Williams et al., 2011). These observations show the presence of relatively warm (0°C–0.5°C) MCDW in the bottom layer and no DSW. In terms of basal melt, satellite-derived estimates indicate that TIS basal melt rate is larger than 10 m yr^{-1}, the highest rate among the major ice shelves in East Antarctica and only exceeded by some ice shelves in the Amundsen Sea (Figure 1.2A; Depoorter et al., 2013; Rignot et al., 2013; Liu et al., 2015). The MUIS also shows a high rate of basal melt (> 4 m $year^{-1}$), much larger than rates typical of cold-cavity ice shelves (< 0.5 m $year^{-1}$). Furthermore, recent airborne-derived bathymetry indicates the presence of deep channels at the front of the TIS and beneath it, suggesting possible access of deep and warm ocean waters to the cavity (Greenbaum et al., 2015). All these observational studies on the Sabrina Coast suggest that 1) warm MCDW can reach the ice-shelf cavities in the bottom layer to drive rapid basal melt at depth and 2) that DSW does not form.

Several modelling studies have investigated coastal processes in East Antarctica. Some have found that temporal variability of water mass properties on the shelf in response to polynya variability can affect basal melt of nearby ice shelves, as simulated for TIS (Khazendar et al., 2013; Gwyther et al., 2014). However, there is not a general agreement in the modelling community on whether or not DSW can be formed in the Dalton Polynya. Some models show formation of DSW (Kusahara et al.,

2010; Gwyther et al., 2014), while others do not (Khazendar et al., 2013; Petty et al., 2014). The difference between modelling results is possibly due to the fact that models do not well reproduce local processes, such as sea ice formation in coastal polynyas and freshwater input from melting of ice shelves. The balance between different freshwater sources is a key element for DSW formation. While input of glacial meltwater into the ocean is relatively small in many cold regions around Antarctica, the rapid basal melt of ice shelves on the Sabrina Coast can potentially reduce/prevent the formation of DSW. Thus the impact of ice-shelf melting on water mass transformation needs to be assessed in this region.

The oceanographic processes on the Sabrina Coast remain poorly understood, despite their global implications. In particular, the absence of in situ oceanographic observations on the inner continental shelf has prevented confirmation of whether MCDW drives rapid basal melt of TIS and MUIS and whether DSW forms in the Dalton Polynya. Previous studies provide different and sometimes contradictory conclusions on these points.

1.3. Aims and structure of the thesis

This thesis analyzes and interprets the most comprehensive oceanographic dataset collected on the the continental shelf of the Sabrina Coast to date. The dataset includes a combination of summer measurements collected during the *Aurora Australis* expedition and year-round measurements collected by moored instruments and ice-capable profiling floats. Off-shelf measurements collected by CTD-instrumented seals are included as well as satellite-derived estimates of sea ice formation. Some ocean models are used to investigate those processes that measurements alone cannot address. More specifically, models are employed to study winter convection and cross-shelf exchange. Year-round ocean observations near the surface are required to study these processes. However, the presence of drifting icebergs prevents the deployment of fixed instruments in the top 300 m of the water column, limiting our ability to measure the upper ocean near Antarctica.

Using data and models introduced above, the thesis aims to achieve the following major goals:

- Confirm/reject the hypothesis that warm MCDW can reach the TIS and MUIS cavity to drive rapid basal melt
- Identify pathways for MCDW from the shelf break to the ice-shelf cavities
- Assess whether DSW forms in the Dalton Polynya

- Assess the influence of ice-shelf meltwater on water mass transformation
- Investigate the processes that allow MCDW to access the continental shelf

The thesis has the following structure:

- Chapter 2 analyses observations at the TIS front to confirm whether ocean heat can cause rapid basal melt of the ice shelf.
- Chapter 3 extends the observations to the wider continental shelf of the Sabrina Coast to understand if MCDW can reach the MUIS and, more generally, to quantify the spatial distribution of the water masses.
- Chapter 4 provides a synthesis of what is known about ocean-ice shelf interaction in East Antarctica, including results from Chapter 2 and 3.
- Chapter 5 investigates the mechanisms that favour/prevent formation of DSW in the Dalton Polynya and in other polynyas around Antarctica, with a focus on the role of glacial meltwater released by ice-shelf basal melt
- Chapter 6 quantifies the seasonal variability of the MCDW intrusions onto the continental shelf and investigates the physical mechanisms that allow the intrusions.
- Chapter 7 provides a summary and conclusions of the thesis, with some suggestions for future investigations.

Chapter 2

Ocean heat drives rapid basal melt of Totten Ice Shelf

This chapter has been published:
Rintoul, S. R., A. Silvano, B. Peña-Molino, E. van Wijk, M. A. Rosenberg, J. S. Greenbaum, and D. D. Blankenship (2016), Ocean heat drives rapid basal melt of Totten Ice Shelf, *Sci. Adv.*, *2*, e1601610, doi:10.1126/sciadv.1601610.

2.1. Abstract

Mass loss from the West Antarctic ice shelves and glaciers has been linked to basal melt by ocean heat flux. The Totten Ice Shelf in East Antarctica, which buttresses a marine-based ice sheet with a volume equivalent to at least 3.5 m of global sea level rise, also experiences rapid basal melt, but the role of ocean forcing was not known because of a lack of observations near the ice shelf. Observations from the Totten calving front confirm that $(0.22 \pm 0.07) \times 10^6$ m^3 s^{-1} of warm water enters the cavity through a newly discovered deep channel. The ocean heat transport into the cavity is sufficient to support the large basal melt rates inferred from glaciological observations. Change in ocean heat flux is a plausible physical mechanism to explain past and projected changes in this sector of the East Antarctic Ice Sheet and its contribution to sea level.

2.2. Introduction

Ice shelves form where the Antarctic Ice Sheet reaches the ocean and begins to float. Back stress produced by the interaction of the floating ice shelf with side walls and topographic rises buttresses the grounded ice sheet and inhibits the flow of ice into the ocean (Dupont and Alley, 2005). The thinning or weakening of ice shelves reduces the back stress, increasing the discharge of grounded ice into the ocean and raising sea levels. The thinning of Antarctic ice shelves has been attributed to basal melt by ocean heat flux (Pritchard et al., 2012; Paolo et al., 2015), with the most rapid thinning, grounding line retreat, and acceleration of glacial flow observed in the Bellingshausen Sea and the Amundsen Sea (Paolo et al., 2015; Rignot et al., 2014). Much of the ice sheet in that sector of Antarctica rests on bedrock below sea level that deepens upstream, a potentially unstable configuration that may result in rapid glacial retreat and mass loss to the ocean (Weertman, 1974; Schoof, 2007). Models and observations suggest that increased ocean heat flux may have already initiated the unstable retreat of some West Antarctic glaciers (Rignot et al., 2014; Favier et al.,

2014; Joughin et al., 2014). Therefore, the future evolution of the Antarctic Ice Sheet is tightly linked to change in the surrounding ocean.

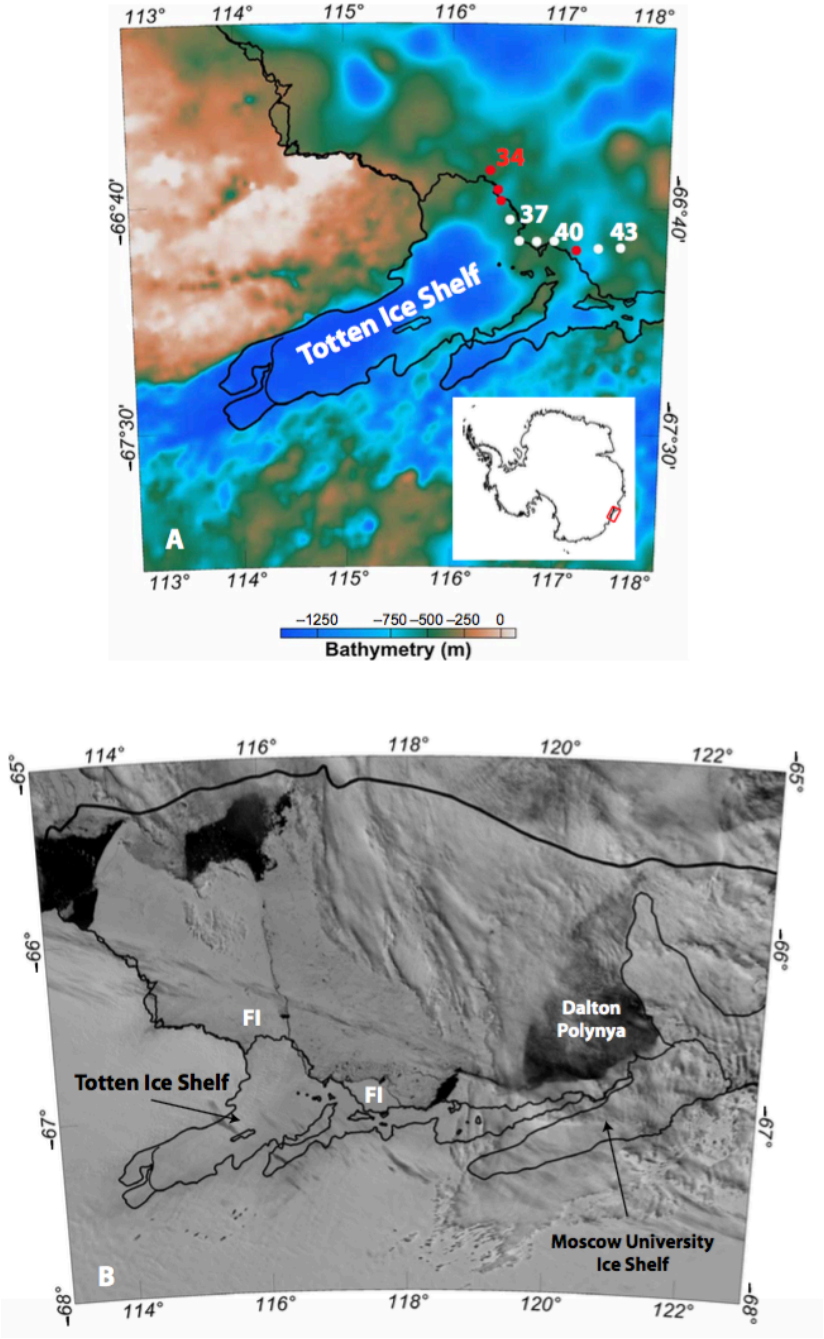

Figure 2.1. Bathymetry, ice shelf draft, sea ice conditions, and ocean station locations near the Totten Glacier. (A) Seafloor bathymetry and elevation of the ice-rock interface, in meters above sea level, from airborne geophysical data (Greenbaum et al., 2015). Dots indicate the locations of stations used in Figure 2.2; red dots indicate stations where MCDW was detected; the grounding line shown in black was derived from interpretation of satellite data (Rignot et al., 2011b) updated with airborne radar data to indicate ocean access to the eastern part of the ice shelf (Greenbaum et al., 2015). The coastline was derived from satellite radar imagery in 2004 (Bohlander and Scambos, 2007). (B) Sea ice conditions on 7 January 2015 from Moderate Resolution Imaging Spectroradiometer (Scambos et al., 2001). The outlines of the TIS, Moscow University Ice Shelf, and Antarctic continent are indicated by thin black lines. The continental shelf break is indicated by the heavy black line. Fast ice (FI) is present in front of the western and eastern limits of the TIS.

Warm ocean waters make their closest approach to the Antarctic continent in the Bellingshausen Sea/Amundsen Sea sector (Pritchard et al., 2012; Orsi et al., 1995), and the most rapid warming of continental shelf bottom waters has occurred there (Schmidtko et al., 2014), helping to explain the rapid mass loss from the West Antarctic Ice Sheet (WAIS). The WAIS has long been marine-based and susceptible to unstable retreat, whereas the East Antarctic Ice Sheet (EAIS) was assumed to be more stable as a result of its bedrock configuration and isolation from warm ocean waters. However, global sea level rise in excess of 10 m during past warm climate epochs requires a substantial contribution from East Antarctica (Naish et al., 2009; Miller et al., 2012). New observations have shown that large regions of the EAIS, including the Aurora Basin drained primarily by the Totten Glacier, are marine-based, with basal morphology (Young et al., 2011) and sediment erosion records (Aitken et al., 2016) that indicate repeated, large-scale advance and retreat of the ice sheet. The Totten Glacier drains more ice than any other glacier in the EAIS and contains a volume of marine-based ice above flotation equivalent to at least 3.5 m of global sea level rise (Greenbaum et al., 2015), comparable to that of the WAIS. The glacier occupies a deep fjord that connects to inland regions of retrograde bed slope, conducive to rapid retreat, although the bed is flat or rises upstream immediately inland of the grounding line (Li et al., 2015). Satellite altimetry and gravity measurements show that parts of the grounded portion of the EAIS have thinned in recent decades, with the most rapid changes observed at the Totten Glacier (Pritchard et al., 2009; Harig and Simons, 2015). Evidence for recent change in the Totten Ice Shelf (TIS) is mixed: Laser altimetry indicated thinning from 2003 to 2008 (Pritchard et al., 2012), radar altimetry showed large temporal variability with no significant net volume loss between 1994 and 2012 (Paolo et al., 2015), and a recent study found that the inferred mean basal melt rate for the period 2005–2011 was about one-third larger than the steady-state melt rate required to balance mass (Liu et al., 2015). Models suggest a substantial contribution to future sea level rise from both the Wilkes Subglacial Basin and the Aurora Subglacial Basin in East Antarctica if greenhouse gas emissions remain high (Golledge et al., 2015; DeConto and Pollard, 2016). The modeled retreat of the Totten Glacier is initiated by simulated or assumed increases in ocean temperature, but the processes transporting ocean heat to ice shelf cavities are not well represented in coarse-resolution climate models. To date, no oceanographic measurements from the Totten ice front have been available to test the hypothesis that warm ocean waters can reach the ice shelf cavity and drive basal melt.

2.3. Results

We collected oceanographic profiles and bathymetry data from the calving front of the TIS in January 2015 (Figure 2.1; Materials and methods). The heavy sea ice conditions that had prevented previous expeditions from reaching the ice front relaxed briefly during a period of southwest winds, allowing for access through a narrow and short-lived shore lead. Fast ice prevented access to the western 30 km of the ice front, where geophysical data (Greenbaum et al., 2015) indicate shallower seafloor depths (Figure 2.1A). Temperature, salinity, and oxygen were measured from the sea surface to within 8 m of the seafloor at 10 stations along the calving front and fast ice edge.

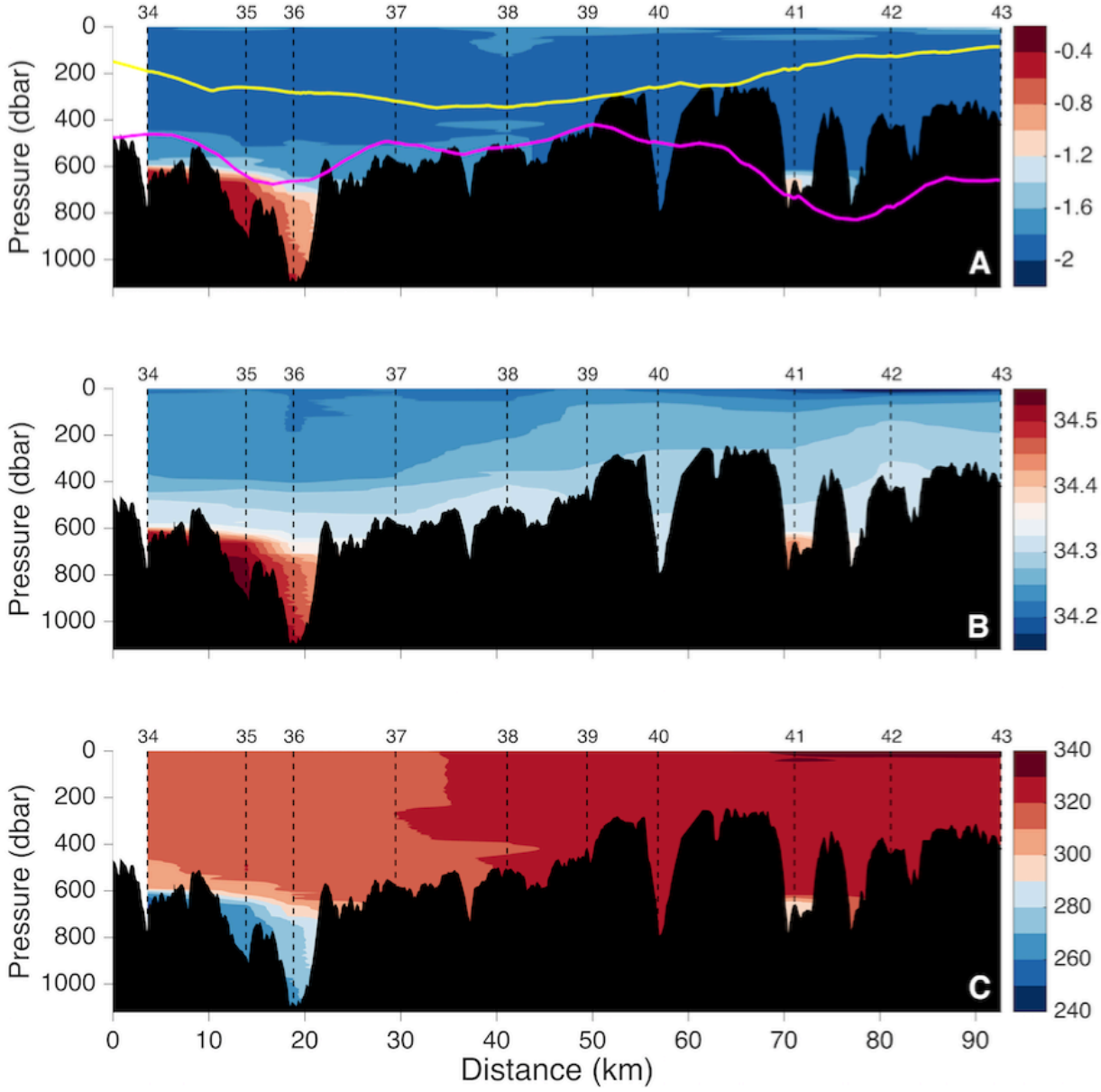

Figure 2.2. Ocean properties along the TIS calving front. (A) Section of potential temperature (°C, color) and observed seafloor bathymetry (black) running from west (left) to east (right) along the calving front. The yellow line indicates the BEDMAP2 bathymetry (Fretwell et al., 2013); the magenta line shows the seafloor depth inferred from airborne geophysical measurements (Greenbaum et al., 2015). (B) Salinity. (C) Oxygen (in μmol L^{-1}).

The shipboard bathymetry data reveal a deep trough in front of the western TIS cavity, with a maximum depth of 1097 m and a maximum width of 10 km at a depth of 600 m (Figure 2.2A). Below 600 m, the trough narrows to form two deep channels with widths of 2 to 4 km. These narrow channels are much deeper than the BEDMAP2 estimate of bottom depth at the ice front (< 350 m; Fretwell et al., 2013). Inversion of airborne geophysical data identified a trough in the same location as observed by the ship (Figure 2.1A) but with a shallower maximum depth (< 680 ± 190 m) as a result of smoothing by the inversion procedure (Greenbaum et al., 2015). The geophysical data indicate that the trough extends well south of the calving front and connects to the deep cavity beneath the TIS (Figure 2.1A).

Warm Modified Circumpolar Deep Water (MCDW) reaches the TIS cavity through these deep troughs (Figure 2.2A). The warmest water is found at the seafloor at stations 34 and 35 (potential temperature (θ) = –0.405°C), with slightly cooler water (θ = –0.569°C) in the deepest channel at station 36. A temperature maximum is also observed near the seafloor in a narrow channel further east (station 41), but the MCDW is much cooler there (maximum of –1.147°C) than that observed in the deep channel at stations 35 and 36. The channel at station 41 and that between stations 41 and 42 connects to the eastern trough identified by Greenbaum et al. (2015) (Figure 2.1A), representing the probable conduits for ocean heat to reach this eastward extension of the TIS.

The warm water in the deep trough is saline and low in oxygen, characteristic signatures of MCDW (Figures 2.2B and 2.2C). The Winter Water (WW) overlying the MCDW is cooler, fresher, and higher in oxygen. However, the salinity and oxygen of WW are lower (by > 0.03 and >10 μmol L^{-1}, respectively) in front of the western ice shelf than those observed further east, consistent with outflow from the ice shelf cavity of a mixture of low-oxygen MCDW and fresh glacial meltwater. Additional meltwater outflow may occur in the inaccessible area west of station 34.

The temperature of the MCDW near the seafloor in the deep trough exceeds the in situ freezing point by more than 2.2°C (the in situ freezing point decreases with increasing pressure; Figure 2.3A). If this warm water can access the grounding line at a depth of 2300 m (Greenbaum et al., 2015), the temperature would exceed the local freezing point at the grounding line by 3.2°C. Velocity measurements collected by a lowered acoustic Doppler current profiler (LADCP) confirm that the warm water at the bottom of stations 35 and 36 flows strongly (> 0.2 m s^{-1}) into the sub–ice shelf cavity (Figure 2.3B). The velocity profile is highly sheared, with weak flow in the cold water above the thermocline near 600 m depth and maximum inflow near the seafloor, where the warmest

water is found. The deep flow in the eastern trough (station 41) also flows into the cavity but is substantially weaker (Figure 2.3B).

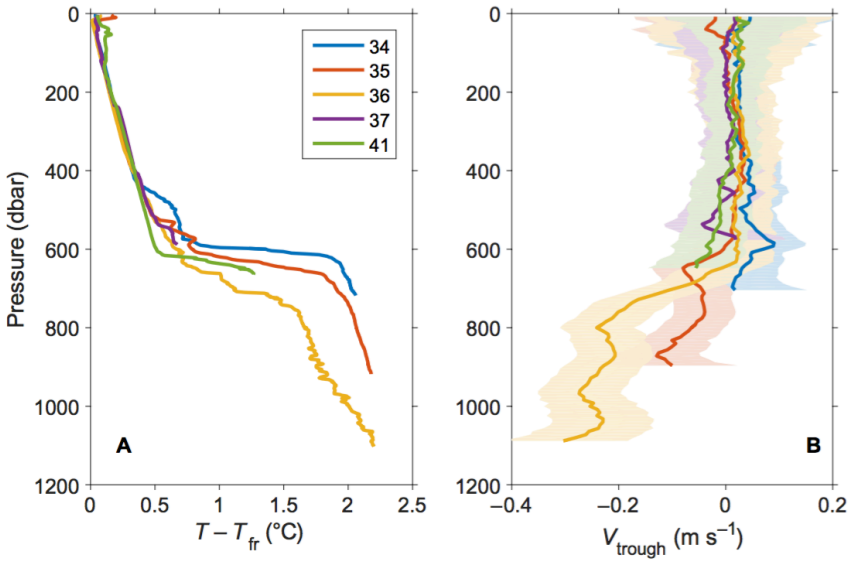

Figure 2.3. Temperature above freezing and along-trough velocity. (A) Temperature elevation above the in situ freezing point at stations 34 to 37 (western trough) and 41 (eastern trough). (B) Velocity from the LADCP rotated in the along-trough direction (35° east of north for the western trough (stations 34 to 37) and 0° for the eastern trough (station 41) (Greenbaum et al., 2015).

Integration of the along-trough velocity gives an inflow of 0.22 ± 0.07 Sv of warm ($\theta > -1.0$°C) water at stations 34 to 36 (Materials and methods). The LADCP provides a synoptic snapshot of the velocity field and may be aliased by tides or other motions; the error bar represents the uncertainty in the synoptic snapshot assuming a ± 0.05 m s^{-1} barotropic tide (Materials and methods). Although the representativeness of the LADCP-based transports cannot be assessed from direct observations, estimates of net basal melt inferred from glaciological measurements can be combined with temperature measured at the ice front to provide an independent estimate of the exchange rate (Materials and methods; Wilson and Straneo, 2015). Glaciological estimates of basal melt at the Totten range from 63.2 ± 4 gigatons Gt year^{-1} (Rignot et al., 2013) to 80 ± 5 Gt year^{-1} (Liu et al., 2015), the largest (Rignot et al., 2013; Depoorter et al., 2013) or the second largest (after the Amery (Liu et al., 2015)) basal melt rate for East Antarctic ice shelves with an area > 1000 km^2. On an area-averaged basis, the Totten melt rate (10.5 ± 0.7 m year^{-1} in the study of Rignot et al. (2013) and 9.89 ± 1.92 m year^{-1} in the work of Depoorter et al. (2013)) is higher than that of any other East Antarctic ice shelf larger than 1000 km^2. Using the temperature of the inflow and outflow layers observed at the ice front, an overturning exchange flow of 0.16 ± 0.03 Sv is required to provide sufficient heat to support the inferred basal melt rate (Materials and methods). The agreement within errors of the two independent transport estimates (0.22 ± 0.07 Sv from instantaneous

velocity measurements and 0.16 ± 0.03 Sv from the multiyear mean basal melt rate), despite the different time periods and assumptions made, demonstrates that the observed water properties and circulation are consistent with high basal melt rates inferred from satellite data. Although ocean heat transport to the cavity likely varies in response to local and remote forcing (Khazendar et al., 2013; Gwyther et al., 2014), the fact that the observed ocean heat flux is sufficient to support the multiyear mean basal melt rate derived from glaciological observations suggests that the conditions measured during the voyage were representative.

2.4. Conclusions

Therefore, several lines of evidence support the conclusion that rapid basal melt of the TIS (Liu et al., 2015; Rignot et al., 2013; Depoorter et al., 2013) is driven by the flux of warm MCDW into the cavity: the presence of warm water at the ice front, the existence of a deep trough providing access of this warm water to the cavity, direct measurements of mass and heat transport into the cavity, the signature of glacial meltwater in the outflow, and exchange rates inferred from the heat budget and satellite-derived basal melt rates. Observations of recent change in some East Antarctic glaciers and ice shelves (Li et al., 2015; Pritchard et al., 2009; Harig and Simons, 2015; Liu et al., 2015) and studies of past (Miller et al., 2012; Young et al., 2011; Aitken et al., 2016, Cook et al., 2013; Dutton et al., 2015) and future (Golledge et al., 2015; DeConto and Pollard, 2016) sea levels support the hypothesis of a dynamic EAIS. Our observations confirm the existence of a pathway allowing for communication of ocean anomalies to the TIS cavity, highlighting variation in ocean-driven basal melt as a plausible mechanism to explain past and projected changes in the TIS and the ice sheet it buttresses.

2.5. Materials and methods

2.5.1. Observations

Oceanographic profiles of temperature, salinity, and dissolved oxygen were collected using a Seabird 911 CTD with dual temperature and conductivity sensors and calibrated against bottle samples analyzed for salinity and oxygen. Velocity profiles were obtained with upward- and downward-looking LADCPs mounted on the CTD frame and an ADCP mounted in the hull of the ship. The LADCP data were processed using the inversion method of Visbeck (2002) and Thurnherr (2010). The LADCP velocity estimates were referenced using constraints from bottom-tracking, shipboard ADCP, and Global Positioning System position information. The inversion

provided formal error bars (shown in Figure 2.3); Thurnherr (2014) argued that these formal error bars were often overly conservative. The shipboard ADCP was processed using the CODAS software package developed at the University of Hawaii (http://currents.soest.hawaii.edu/docs/adcp_doc/index.html).

2.5.2. Calculation of synoptic volume and heat transports

The transport of warm MCDW into the cavity was calculated by multiplying the LADCP velocity, rotated into the along-trough direction (35° east of north; Greenbaum et al., 2015), by the width of the channel in each 8-m-deep velocity bin and summing over the layer warmer than −1.0°C. (The −1.0°C isotherm lays roughly in the middle of the thermocline separating MCDW from WW; because the thermocline was sharp (~1.0°C/60 m), the transport integral was not sensitive to the temperature threshold chosen.) The LADCP measurements were potentially aliased by tides and other motions that were not resolved by the snapshot obtained by a single voyage. The tidal model of Padman et al. (2002) suggested barotropic tidal velocities of less than ±0.015 m s^{-1} in this region, but tidal models are highly uncertain in this region of poorly known bathymetry. As a rough measure of uncertainty, we estimated the transport change resulting from a ±0.05 m s^{-1} barotropic tide and used this as an error bar on the volume transport. Heat transport into the cavity was estimated by multiplying the transport by the mean potential temperature in each 8-m-deep bin.

Multiyear fast ice prevented the ship from reaching the coast on the western end of the calving front. Airborne geophysical data indicated the seafloor shoals further west (Greenbaum et al., 2015), suggesting that we have resolved the major inflows of warm MCDW. However, we likely missed some of the shallow outflow of glacial meltwater on the western end of the section. Hence, rather than directly integrating the LADCP velocity to calculate the outflow, we assumed that mass was conserved and that the total outflow must equal the total inflow plus meltwater input. (Note that we did not assume that the outflow and inflow were in the same vertical plane.)

We estimated the heat transport out of the cavity by multiplying the total outflow by the mean potential temperature in the layer with salinity less than 34.3 at stations 34 to 37. The difference between the ocean heat transport into and out of the cavity was the heat flux used to melt the base of the ice shelf. The heat flux estimated in this way was sufficient to produce 2.8 ± 0.9 mSv of meltwater.

2.5.3. Exchange estimated from satellite-derived basal melt

The transport calculation was based on a synoptic survey and may not represent the long-term mean exchange of volume and heat. The observed temperatures of the inflow and outflow layers could be used to provide an estimate of the volume exchange with the cavity that is independent of the velocity measurements. Following the study of Wilson and Straneo (2015), we assumed a two-layer estuarine circulation in which warm water enters the cavity and drives basal melt, and a mixture of meltwater and MCDW leaves the cavity. Given a known basal melt rate and the temperature of the inflow and outflow, the heat budget can be used to estimate the exchange rate.

Several approaches have been used to estimate basal melt rates at the Totten Glacier. Flux gate calculations using satellite data indicated steady-state net basal melt rates of 63.2 ± 4 Gt $year^{-1}$ (Rignot et al., 2013) and 64 ± 12 Gt $year^{-1}$ (Depoorter et al., 2013), equivalent to area-average melt rates of 10.5 ± 0.7 and 9.89 ± 1.92 m $year^{-1}$, respectively. The calculations were based on a number of data sets spanning different time periods and, thus, were best thought of as a multiyear average rather than an estimate for a particular time interval. Liu et al. (2015) used a similar method, but did not assume a steady-state calving front as in the previous studies, and found a melt rate of 80 ± 5 Gt $year^{-1}$ during the period 2005–2011. Numerical models gave net basal melt rates similar to these values (for example, 7 to 15 m $year^{-1}$ (Khazendar et al., 2013) and 9.1 m $year^{-1}$ with an interannual range of 5.7 m $year^{-1}$ (Gwyther et al., 2014)). We used the values from the study of Depoorter et al. (2013) to estimate the exchange rate (Rignot et al. (2013) gave a similar value, with smaller error bars; using the melt rate of Liu et al. (2015) would give a larger exchange rate, closer to our synoptic estimate).

The exchange rate is given by $M = L_f M_{melt} / c_w (T_{in} - T_{out})$, where M is the exchange rate, L_f is the latent heat of fusion (334 kJ kg^{-1}), c_w is the specific heat capacity of seawater (3.985 kJ $kg^{-1} K^{-1}$), M_{melt} is the flux of meltwater, and T_{in} and T_{out} are the potential temperatures of the inflow and outflow, respectively. A basal melt rate of 64 ± 12 Gt $year^{-1}$ (Depoorter et al., 2013) corresponds to a meltwater flux M_{melt} of 2 ± 0.4 mSv. T_{in} is set to the transport-weighted temperature of the inflowing MCDW (–0.81°C). T_{out} is the mean temperature of the outflow layer at the calving front (–1.88°C). A meltwater flux of 2 ± 0.4 mSv requires an exchange rate M of 0.16 ± 0.03 Sv, assuming a two-layer flow with a temperature difference $T_{in} - T_{out} = 1.07$°C. A basal melt rate of 80 ± 5 Gt $year^{-1}$ (Liu et al., 2015) equates to a meltwater flux of 2.5 ± 0.4 mSv, requiring an exchange rate M of 0.20 ± 0.03 Sv.

Chapter 3

Distribution of water masses and meltwater on the continental shelf near the Totten and Moscow University ice shelves

This chapter has been published:
Silvano, A., S. R. Rintoul, B. Peña-Molino, and G. D. Williams (2017), Distribution of water masses and meltwater on the continental shelf near the Totten and Moscow University ice shelves, *J. Geophys. Res. Oceans*, *122*, doi:10.1002/2016JC012115.

3.1. Abstract

Warm waters flood the continental shelf of the Amundsen and Bellingshausen seas in West Antarctica, driving rapid basal melt of ice shelves. In contrast, waters on the continental shelf in East Antarctica are cooler and ice shelves experience relatively low rates of basal melt. An exception is provided by the Totten and Moscow University ice shelves on the Sabrina Coast, where satellite-derived basal melt rates are comparable to West Antarctica. Recent oceanographic observations have revealed that relatively warm (~-0.4°C) Modified Circumpolar Deep Water (MCDW) enters the cavity beneath the Totten Ice Shelf through a 1100 m deep trough, delivering sufficient heat to drive rapid basal melt. Here we use observations from a recent summer survey to show that MCDW is widespread on the continental shelf of the Sabrina Coast, forming a warm (up to 0.3°C) and saline (34.5–34.6) bottom layer overlaid by cold (~ freezing point) and fresh (salinity 34.3) Winter Water. Dense Shelf Water is not observed. A 1000 deep m trough allows water at -1.3°C to reach the Moscow University ice-shelf cavity to drive basal melt. Freshening by addition of glacial meltwater is widespread on the southern shelf at depths above 300–400 m, with maximum meltwater concentrations up to 4–5 ml L^{-1} observed in outflows from the ice-shelf cavities. Our observations indicate that the ocean properties on the Sabrina Coast more resemble those found on the continental shelf of the Amundsen and Bellingshausen seas than those typical of East Antarctica.

3.2. Introduction

The Antarctic Ice Sheet flows toward the coast through several outlet glaciers. Floating ice shelves form where an outlet glacier reaches the ocean. Back stresses generated by interaction of the flowing ice shelves with side-walls and topographic rises can restrain (‘‘buttress’’) the glacial flow

into the ocean (Dupont and Alley, 2005). A thinning or collapse of the buttressing ice shelves would reduce the restraint on the glacial flow, increasing the ice discharge into the ocean. Acceleration during the last few decades in the flow of some of the outlet glaciers has led to a dramatic increase in Antarctic ice loss, with most of the ice discharge occurring along the coast of the Amundsen and Bellingshausen seas in West Antarctica (Rignot et al., 2008; Harig and Simons, 2015; Wouters et al., 2015). Here the ice loss has been primarily attributed to thinning of the buttressing ice shelves as a result of rapid basal melt by ocean heat flux (Shepherd et al., 2004; Pritchard et al., 2012).

The ocean heat flux in West Antarctica is associated with intrusions of warm (> 0°C), salty (> 34.5), and slightly modified Circumpolar Deep Water (MCDW) onto the continental shelf. This warm water fills the bottom layer and is able to access the cavity beneath several ice shelves to drive rapid basal melt (Jenkins and Jacobs, 2008; Jacobs et al., 2011; Dutrieux et al., 2014; Jacobs et al., 2013). Winter convection does not extend to sufficient depth to destratify the water column and erode the MCDW in these regions, resulting in a shallow mixed layer overlying the warm MCDW (Petty et al., 2013).

In many other parts of Antarctica, active coastal polynyas drive strong convection in winter. Polynyas are regions of enhanced sea-ice formation, where water masses are transformed by local processes such as atmospheric cooling, wind stress, and brine rejection. In the strongest polynyas, the wintertime convection from sea-ice formation is sufficient to overturn the entire water column to produce cold (~ surface freezing point) and saline (> 34.5) Dense Shelf Water (DSW). Examples of strong polynyas are found in the Ross Sea (Jacobs et al., 1970), in the Weddell Sea (Gill, 1973), and in several areas in East Antarctica, such as the Adélie Coast (Rintoul, 1998), Vincennes Bay (Kitade et al., 2014), and Prydz Bay/Cape Darnley (Williams et al., 2016; Ohshima et al., 2013). DSW formed in these regions overflows the shelf break and cascades down the slope, mixing with ambient water to form Antarctic Bottom Water, thus contributing to the global overturning circulation (Johnson, 2008; Marshall and Speer, 2012).

Part of the DSW produced in these polynyas is able to access the cavities of nearby ice shelves. Since the seafloor usually gets deeper toward the grounding line of an ice shelf, DSW spreads along the seafloor to reach the deepest areas near the grounding line (Jacobs et al., 1992). The depression of the seawater freezing point with increasing pressure, 0.75°C every 1000 dbar (Foldvik and Kvinge, 1974), means that the DSW is warmer than the local freezing point and therefore able to

melt the base of the ice shelf.

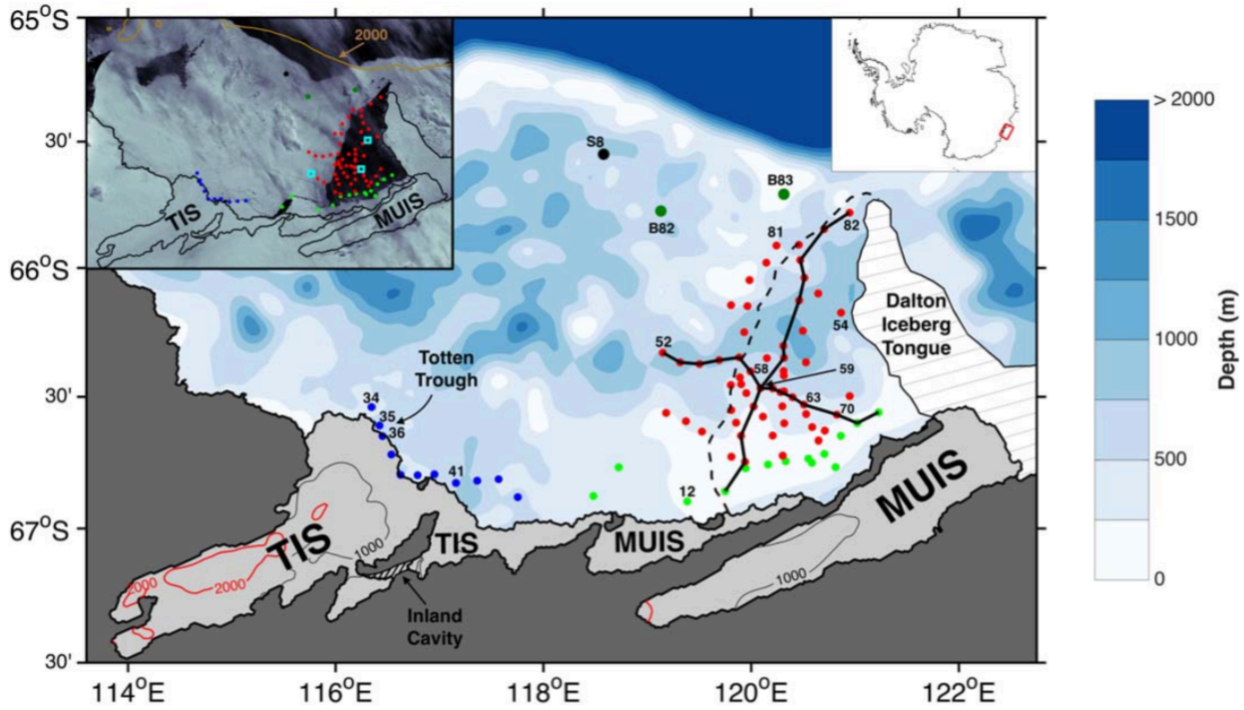

Figure 3.1. Map of the survey area. Overlaid is the bathymetry and the coastline (BEDMAP2, Fretwell et al., 2013). Bathymetry from geophysical data beneath the Totten Ice Shelf (TIS) is included (Greenbaum et al., 2015). Red, green, and blue dots indicate the stations collected in the Dalton Polynya (DP), in proximity to the Moscow University Ice Shelf (MUIS) and TIS calving fronts, respectively. The location of stations 82 and 83 from BROKE is shown in dark green (B82–B83), while station 8 from SIPEX is shown in black (S8). The inland cavity identified by Greenbaum et al. (2015) and the Totten Trough (located near stations 35 and 36) are highlighted. The dashed white area north of the MUIS is the Dalton Iceberg Tongue, a combination of grounded icebergs and fast ice. The black lines highlight the two transects shown in Figures 3.2 and 3.3. The dashed line indicates the approximate eastern boundary of the area covered by sea ice. Stations shown in Figures 3.5, 3.6, 3.8, 3.10, and 3.11 are labeled. In the inset on the upper-left corner is a MODIS (Scambos et al., 1996) image (22 January 2015) with coastline overlaid. Light blue squares are the location of the moorings, while the brown line is the 2000 m isobath which shows the approximate location of the continental slope.

East Antarctic ice shelves located in regions where cold DSW is formed (e.g., the Mertz Glacier Tongue on the Adélie Coast and the Amery Ice Shelf in Prydz Bay) experience low area-averaged rates of basal melt (typically less than 2 m year^{-1}) compared to the Amundsen and Bellingshausen seas where rates are usually higher than 4–5 m year^{-1}, reaching values up to 15–20 m year^{-1} at the floating ends of Pine Island and Thwaites glaciers (Rignot et al., 2013; Depoorter et al., 2013; Liu et al., 2015). However, an exception is provided by ice shelves located on the Sabrina Coast, namely the Totten and Moscow University ice shelves (TIS and MUIS, respectively, Figure 3.1), which show rates of basal melt (> 4 m year^{-1}) comparable with those observed in the Amundsen and Bellingshausen seas.

TIS and MUIS represent the floating ends of the Totten and Moscow University glaciers,

respectively. These glaciers drain a large sector of the marine-based Aurora Subglacial Basin and understanding their stability is important for determining the future contribution of this sector of the East Antarctic Ice Sheet to global sea level (Sun et al., 2016). The Totten Glacier alone drains a volume of ice above flotation equivalent to 3.5 m of sea level rise, an amount similar to the entire West Antarctic Ice Sheet (Greenbaum et al., 2015). Two recent studies show that the grounded part of the Totten Glacier has experienced sustained thinning (0.7 ± 0.1 m $year^{-1}$) and mass loss (7 ± 2 Gt $year^{-1}$) during the past two decades (Li et al., 2015, 2016). Satellite estimates suggest that the TIS has experienced periods of thinning and thickening, with no significant trend during the past 20 years (Paolo et al., 2015). Ocean modeling studies suggest that MCDW is able to access the TIS cavity to drive basal melt (Khazendar et al., 2013; Gwyther et al., 2014). The model results indicate that ocean heat flux to the cavity is regulated by the activity of the Dalton Polynya (DP) east of the TIS (Figure 3.1). When sea-ice production is higher than average, cold water formed in the polynya mixes with the MCDW that intrudes onto the continental shelf, reducing the temperature of water reaching the ice-shelf cavity. When sea-ice production is lower, MCDW reaches the TIS cavity in a less modified form and drives more basal melt, possibly triggering a thinning of the Totten Glacier.

Measurements collected on the outer continental shelf of the Sabrina Coast show the presence of warm MCDW near the seafloor in summer 1996 and late winter 2007, and no evidence of DSW (Bindoff et al., 2000; Williams et al., 2011). More recently, Rintoul et al. (2016) used observations from the TIS calving front to quantify exchange with the ice-shelf cavity. They found that warm MCDW entered the TIS cavity through a deep trough at the calving front, the Totten Trough, and carried sufficient heat to sustain an area-averaged basal melt rate > 10 m $year^{-1}$, in agreement with satellite observations (Rignot et al., 2013; Depoorter et al., 2013; Liu et al., 2015). The TIS basal melt rate is the highest observed on the Sabrina Coast and the largest among the East Antarctic ice shelves with an area bigger than 1000 km^2 (Silvano et al., 2016). Here we use an extended data set to show the spatial variability of the ocean properties on the continental shelf of the Sabrina Coast and to describe how ocean heat is transported to the MUIS and TIS. Our results from the Sabrina Coast are then compared with two other sites around Antarctica, Pine Island Bay in West Antarctica, and the Adélie Coast in East Antarctica.

3.3. Data

A survey was conducted on the shelf of the Sabrina Coast (115°E–125°E) on the R/V *Aurora Australis* (cruise AU1402) between 23 December 2014 and 6 January 2015 (Figure 3.1). We show

the results from the analysis of 81 CTD stations collected during this expedition (Figure 3.1). CTD data include continuous profiles of temperature (°C), salinity (PSS78), pressure (dbar), and dissolved oxygen (μmol L^{-1}). Data were vertically averaged in 2 dbar bins with calibration performed using bottle samples (Rosenberg and Rintoul, 2016). Uncertainties on the measurements of temperature, salinity, and pressure are ~0.001°C, 0.002 (PSS78), and 1 dbar, respectively. The relative uncertainty on the dissolved oxygen data is ~1%. Three moorings were deployed on the continental shelf between 300 m and the bottom (see the inset in Figure 3.1 for location) in February 2014 during the NBP1402 expedition on the US R/V *Nathaniel B. Palmer* and recovered in January 2015 during the AU1402 voyage. At each mooring, temperature and salinity data were collected at four equally spaced depths (Rosenberg and Rintoul, 2016). Individual time series shows decorrelation time scales exceeding 2 weeks (i.e., the duration of our survey on the Sabrina Coast), with an average value of about 30 days, confirming the synopticity of the survey.

We compare our measurements to data collected on two previous surveys on the continental shelf of the Sabrina Coast. Two CTD stations were occupied in austral summer 1996 during Baseline Research on Oceanography Krill and the Environment (BROKE; Bindoff et al., 2000) (Figure 3.1). Temperature from a single ice station in late winter 2007 during Sea Ice Physics and Ecosystem eXperiment (SIPEX) is also used (Williams et al., 2011) (Figure 3.1). We also compare our data to measurements of temperature, salinity, and dissolved oxygen from the Adélie Coast in East Antarctica and from Pine Island Bay in West Antarctica. Data from the Adélie Coast were collected during the AU1402 voyage after the survey of the Sabrina Coast, while measurements from Pine Island Bay were collected in austral summer 2009 (Jacobs et al., 2011).

3.4. Results

3.4.1. Water mass classification

A meridional section in the DP reveals four water masses present on the shelf (Figure 3.2). Relatively warm and salty MCDW is found near the seafloor. Neutral density is not well defined in regions where few data are available, as on the continental shelf of the Sabrina Coast; therefore, we use surfaces of potential density anomaly referenced to the surface, σ_θ, to define different layers. The σ_θ = 27.7 kg m^{-3} isopycnal is chosen to define the upper boundary of MCDW. The MCDW is the densest water mass found on the shelf during the survey; no DSW was observed.

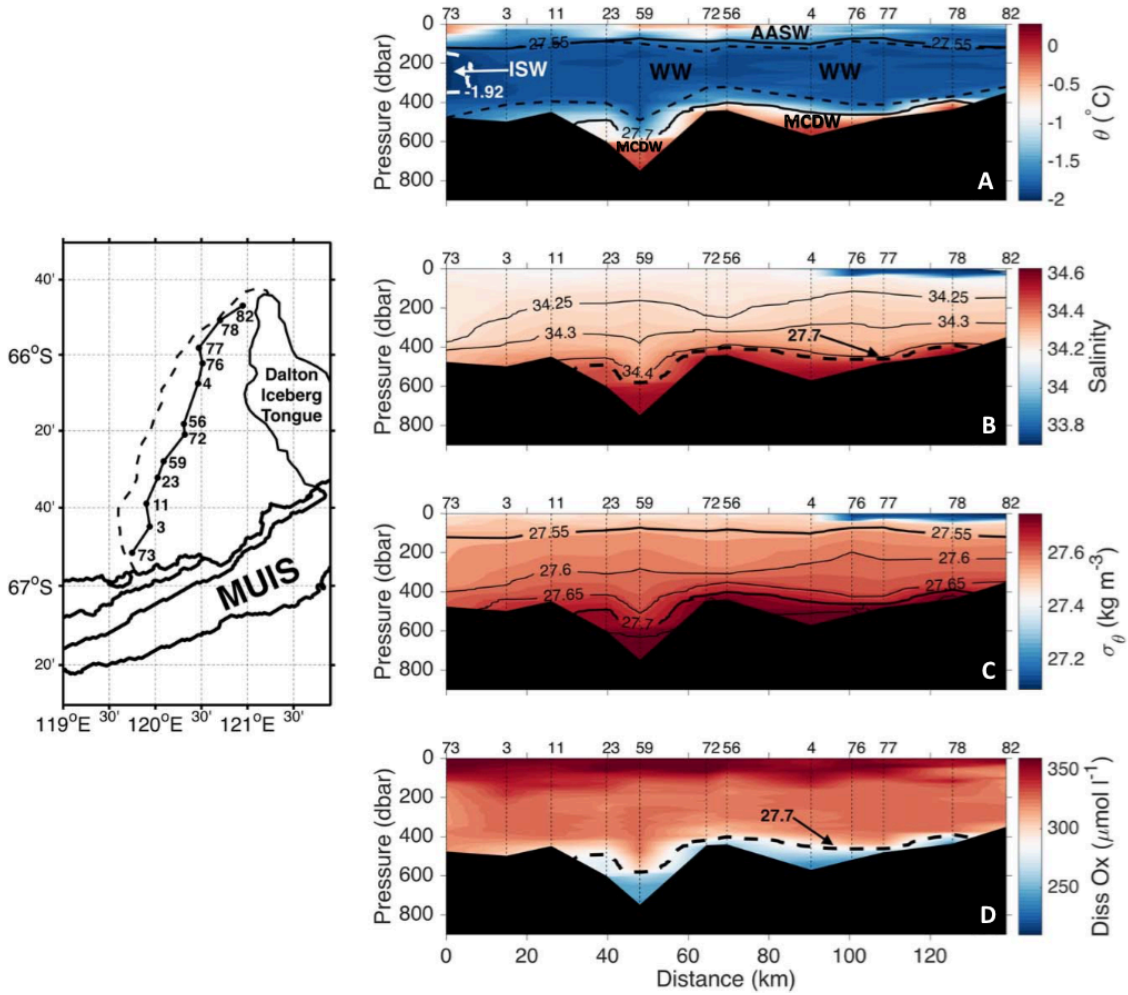

Figure 3.2. Meridional section through the Dalton Polynya. (A) Potential temperature θ, (B) salinity, (C) potential density σ_θ, and (D) dissolved oxygen section from the meridional transect shown in Figure 3.1 and highlighted in the inset map (the dashed black line is the approximate eastern boundary of the area covered by sea ice). CTD stations are indicated by the vertical dashed lines (numbered along the top of the plot). In plot (A) contours of σ_θ are included in black as well as the contour of θ = -1.92°C (Ice Shelf Water) in dashed white, while the black dashed lines indicate the top and the bottom of the Winter Water (WW) layer. The Modified Circumpolar Deep Water (MCDW) is found below the contour of σ_θ = 27.7 kg m^{-3} (dashed black line in the plots (B) and (D)) and the Antarctic Surface Water (AASW) above the contour of σ_θ = 27.55 kg m^{-3}.

Table 3.1: Classification of the water masses

Water Mass	σ_θ (kg m^{-3})	θ (°C)
AASW	$\sigma_\theta < 27.55$	
WW	$27.55 < \sigma_\theta < 27.7$	$-1.92 < \theta < -1.75$
ISW	$27.55 < \sigma_\theta < 27.7$	$\theta < -1.92$
MCDW	$\sigma_\theta > 27.7$	

A homogeneous layer of remnant Winter Water (WW), a product of wintertime convection, lies above the MCDW. The WW temperature is close to the surface freezing point (~ -1.8°C). A thin layer of warm Antarctic Surface Water (AASW) produced by summer heating overlies the WW. The σ_θ = 27.55 kg m^{-3} surface appears to be a reasonable boundary between WW and AASW (Figure 3.2A). However, in order to capture the water mass that is the product of winter convection, excluding water from the seasonal and main pycnocline, we restrict our definition of WW to subsurface water in the σ_θ range 27.55 to 27.7 kg m^{-3} and potential temperature range -1.92 to -1.75°C.

The final water mass found during the survey is Ice Shelf Water (ISW), which results from mixing between glacial meltwater from ice-shelf basal melt and ambient shelf water masses. ISW is distinguished from the other water masses by temperatures colder than the surface freezing point, reflecting basal melting at depth. We define ISW as water colder than -1.92°C, which corresponds roughly to the local subsurface freezing point at 50 dbar; it is unlikely that water colder than this value is the result of the interaction with the atmosphere during the winter (Orsi and Wiederwohl, 2009). ISW is found near the coast (see Figure 3.2A) in the same density range as the WW (27.55 kg $m^{-3} < \sigma_\theta <$ 27.7 kg m^{-3}). The classification of the relevant water masses found on the shelf of Sabrina Coast is summarized in Table 3.1.

3.4.2. Spatial distribution of water properties

We divide the domain into two regions in order to analyze the spatial variability of the water properties: the DP (red points in Figure 3.1) and the ice front, which includes the stations closest to the TIS and MUIS calving front (blue and green points in Figure 3.1, respectively). A recent airborne survey revealed the presence of an inland cavity (highlighted in Figure 3.1) that connects the main trunk of the TIS with the adjacent fringing ice shelf (Greenbaum et al., 2015). In order to include this cavity in the definition of the TIS, we extend the eastern boundary of this ice shelf to 118°E. We define the floating ice shelves between 118°E and 122.5°E as the MUIS. Furthemore, for simplicity, the DP group includes stations located in sea ice west of the actual polynya and the ice-front group includes stations collected along the narrow part of the coast where the ice front is not floating but grounded on bedrock (between the main trunk and the subsidiary part of the MUIS, according to BEDMAP2).

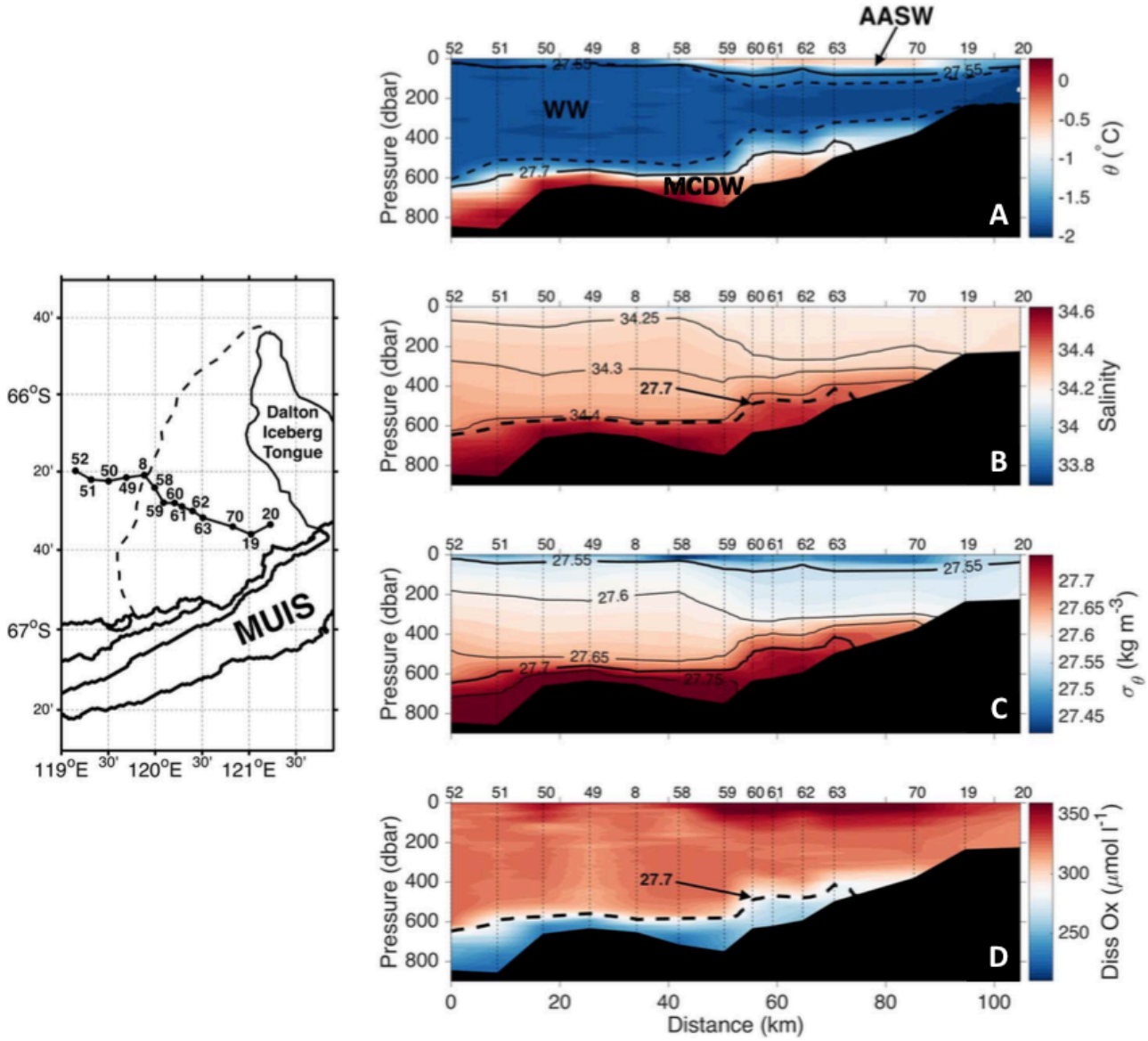

Figure 3.3. Zonal section through the Dalton Polynya. As in Figure 3.2 but for the zonal transect shown in Figure 3.1 and in the inset map.

3.4.2.1. Dalton Polynya

The MCDW is widespread at depth in the DP and its southward spreading is steered by bathymetry. The meridional transect through the DP indicates that MCDW is found below 400-500 m across most of the section (Figure 3.2). However, closer to the ice front, the deepest water gets colder as the bottom shoals. Near the MUIS, the seafloor rises to about 500 m and the bottom water temperature is almost at the surface freezing point. The distributions of salinity and dissolved oxygen are closely related to potential temperature. The warmest MCDW is also the most saline and lowest in oxygen, while the cooler bottom water near the coast is fresher and higher in oxygen. A similar pattern is found in the zonal direction (Figure 3.3). In the south-eastern sector of the polynya, MCDW is not found in the shallow waters (< 300 m) near the coast. Moving north-westward, the temperature at the bottom increases as the bottom deepens. At station 63, where the

seafloor is about 500 m deep, the MCDW signal reappears. In both transects, isopycnals follow the slope of the seafloor, implying that MCDW is steered by bathymetry.

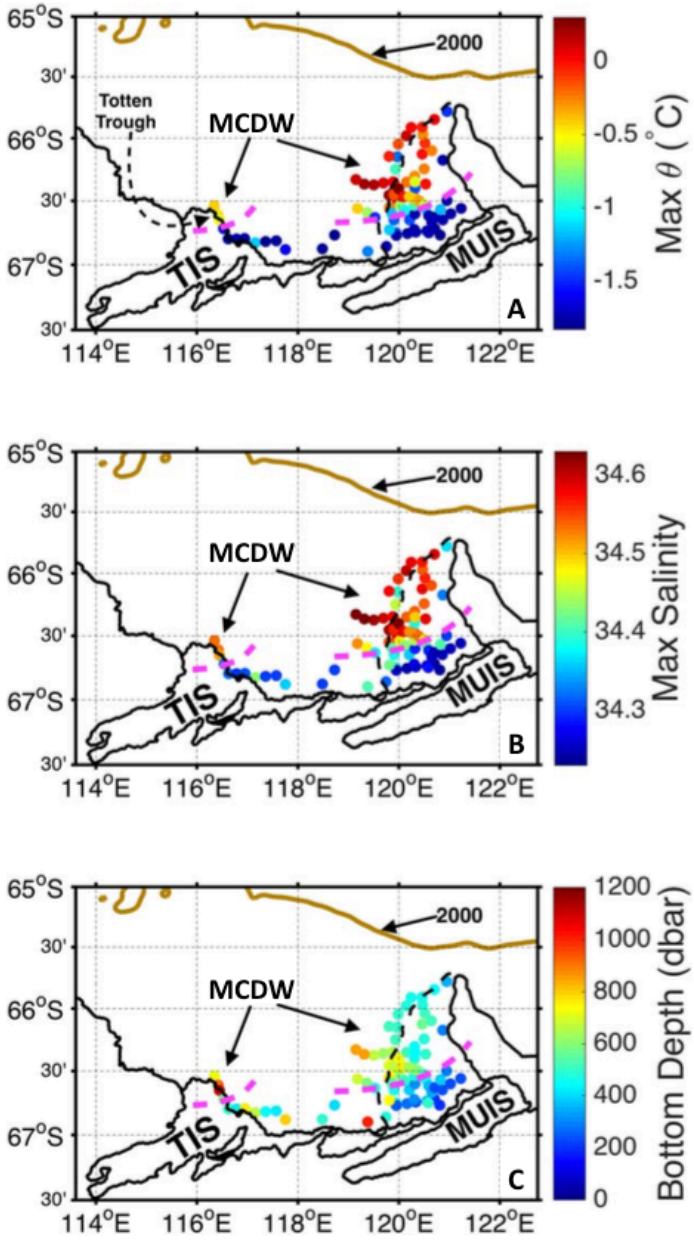

Figure 3.4. Maximum Property Values. (A) Maximum potential temperature θ and (B) salinity beneath the summer mixed layer. The brown line is the 2000 m isobath (showing the approximate location of the continental slope) and the black dashed line the approximate eastern boundary of the area covered by sea ice. The magenta dashed lines are the MCDW southern boundary. (C) Bottom depth (dbar).

To help visualize the spreading of MCDW on the shelf, we show the spatial distribution of the warmest and saltiest water found beneath the summer mixed layer (Figures 3.4A and 3.4B). The warmest (0.3°C), saltiest (34.63), and lowest oxygen (~ 230 μmol L^{-1}, Figure 3.3D) MCDW is located in the western part of the DP. In the north, the MCDW is slightly cooler and fresher. Approaching the coast in the DP, the bottom shoals (Figure 3.4C) and the deep water becomes cooler and fresher. The magenta dashed line indicates the southern boundary of the MCDW core.

As expected, this boundary corresponds roughly to where the bathymetry becomes shallower than 500 m. In the DP, south of this line, the bottom layer gets progressively cooler and fresher until any trace of MCDW vanishes and the WW extends to the bottom.

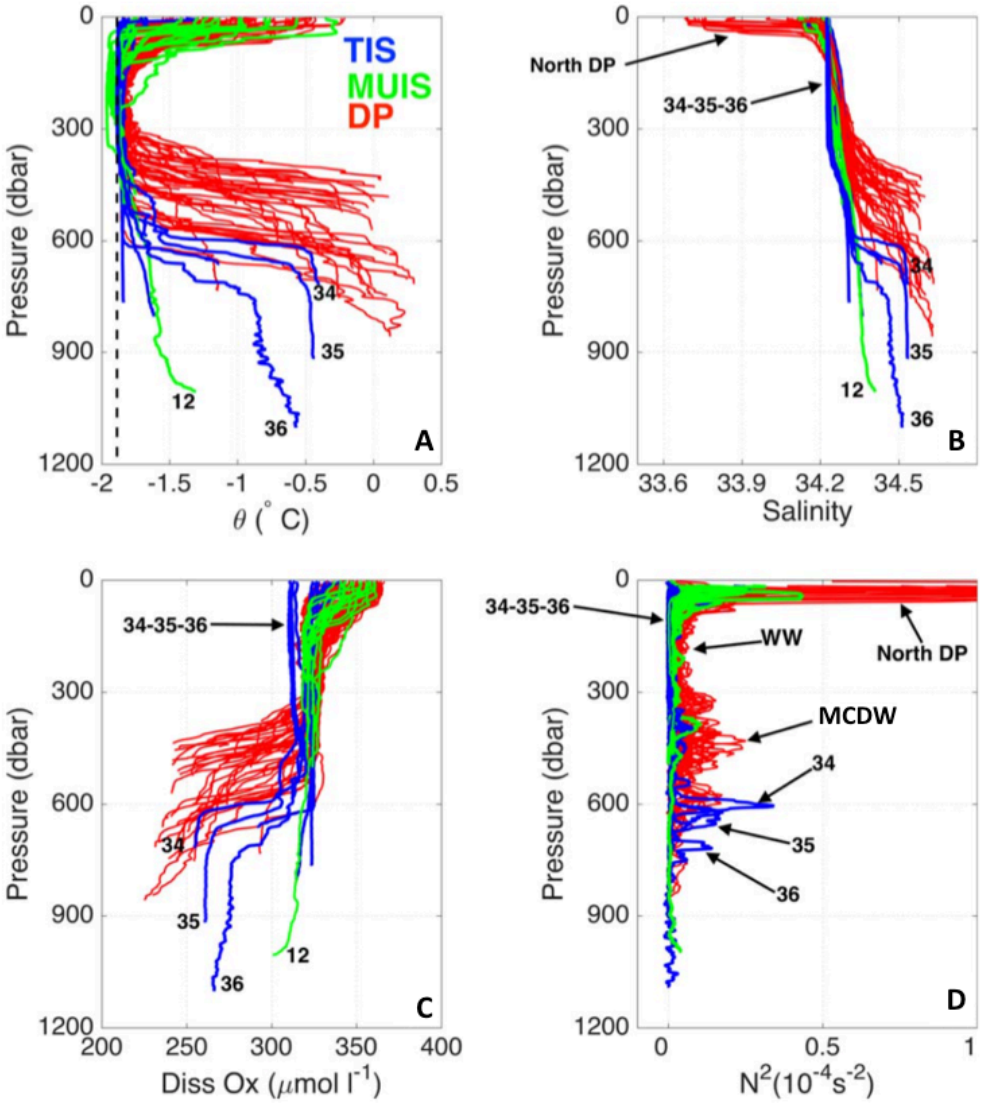

Figure 3.5. Vertical profiles. (A) Potential temperature θ, (B) salinity, (C) dissolved oxygen, and (D) N^2 (square of the Brunt-Väisälä frequency) profiles from DP (red), MUIS (green), and TIS (blue) calving fronts. The westernmost profiles (34, 35, and 36) are labeled, as well as station 12 where a deep trough is found at the MUIS calving front. Overlaid in black in Figure 3.5A is the surface freezing temperature profile for a salinity of 34.4, representative of the domain. N^2 has been smoothed with a vertical running mean over 20 dbar.

The MCDW layer in the polynya is characterized by strong vertical gradients: temperature and salinity increase with depth, while the oxygen content diminishes (Figures 3.5A-3.5C). The strong salinity gradient, and the consequent strong density gradient, indicates that MCDW is more stable than the overlying WW (Figure 3.5D). The pycnocline deepens from ~400 m in the shallower northern region to ~600 m in the deeper water in the west, resulting in a 100–200 m thick bottom layer in both regions (Figures 3.2 and 3.3) that shows small spatial variability of the water

properties (Figure 3.4).

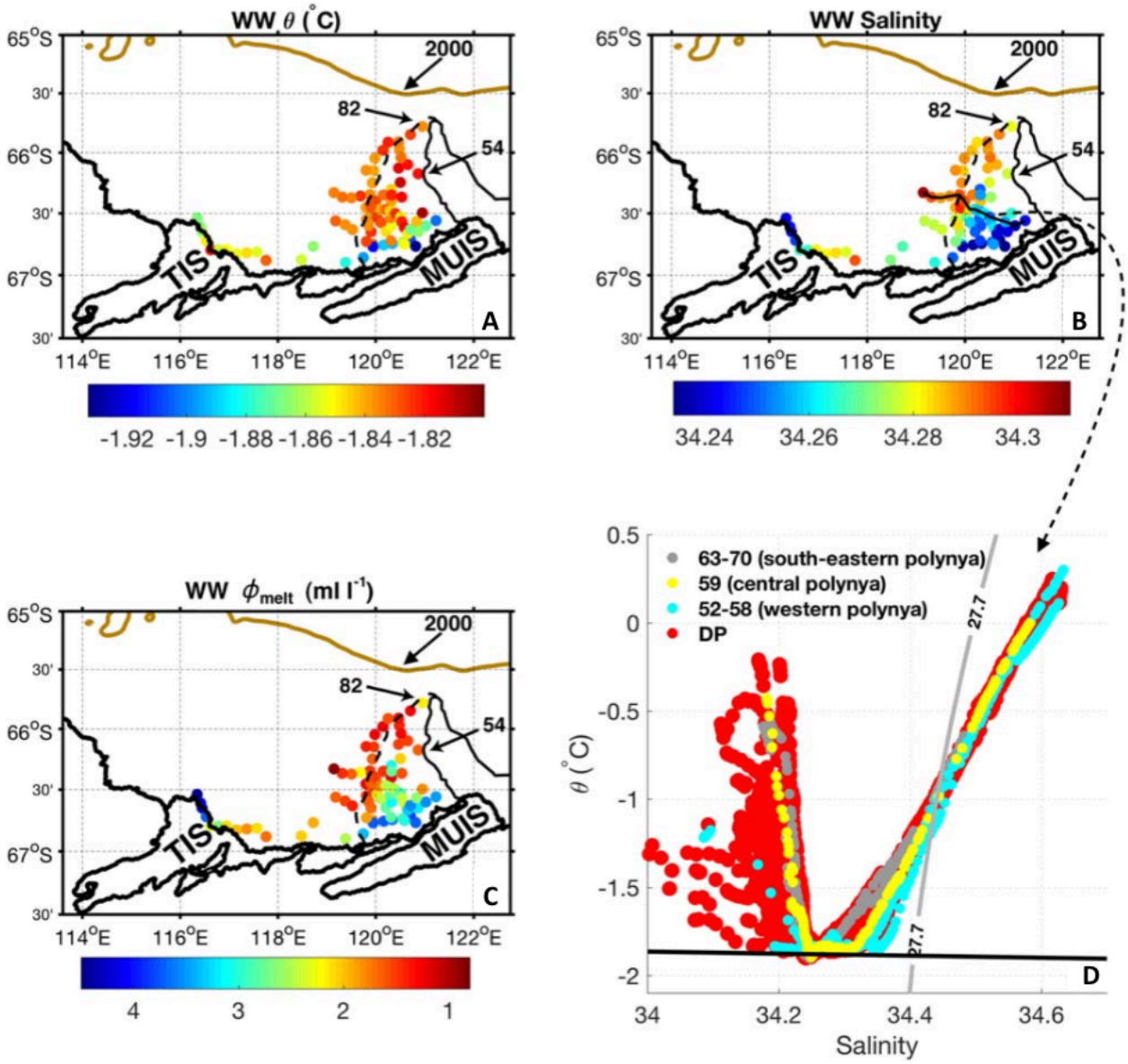

Figure 3.6. WW Properties. (A) Mean potential temperature θ, (B) salinity, (C) basal meltwater fraction ϕ_{melt} of Winter Water, WW. The brown line indicates the 2000 m isobath (showing the approximate location of the continental slope) and the black dashed line is the approximate eastern boundary of the area covered by sea ice. Note that the Ice Shelf Water is included in the WW properties. We calculate the vertical average above the lower limit of WW and below the upper limit of WW or the maximum depth where the ϕ_{melt} estimate is contaminated by surface processes, whichever is deeper. (D) Potential temperature θ versus salinity from DP. The red points indicate data from all the profiles collected in the DP, while gray points (stations 63 and 70) are indicative of the south-eastern DP, yellow points (station 59) of the central DP and the light blue points (stations 52 and 58) of the western DP. These stations are chosen along the zonal transect highlighted in Figure 3.6B and in Figure 3.3. For the exact location of these stations see Figure 3.1. The grey line is the contour of $\sigma_0 = 27.7$ kg m^{-3} (upper boundary of MCDW) and the black line is the surface freezing point.

Above the MCDW, the WW fills most of the water column, occupying a 300 to 500 m thick layer, depending on the bathymetry. The WW is cold (~ -1.8°C), relatively fresh (salinity ~ 34.3) and higher in oxygen (~ 330 μmol L^{-1}) than the underlying MCDW. In contrast to their vertical

homogeneity, the WW properties show a large horizontal variability. First, the WW temperature near the coast is ~ 0.1°C lower than in rest of the polynya (Figure 3.6A, note that we included both WW and ISW in order to capture the product of the interaction between ice and ocean on intermediate waters). Moreover, the WW salinity substantially decreases approaching the coast with values up to 0.05-0.06 lower than in the western/northern polynya (Figure 3.6B). This gradual freshening is reflected in the downward tilting of isohalines and isopycnals toward the coast (clearly seen along the 34.25 isohaline, see Figures 3.2B and 3.3B). Few measurements have been collected near the Dalton Iceberg Tongue (stations 54 and 82, see Figure 3.1 for location). Here the WW has similar temperatures but slightly lower salinity values (~ 0.01-0.02) compared to further west (Figures 3.6A and 3.6B).

The shift to cooler and fresher values near the coast is not restricted to the WW layer, but also observed in the underlying pycnocline. This behavior is clearly seen by following the properties of the pycnocline on a θ-S diagram. In the zonal line shown in Figure 3.3, there is a shift of the pycnocline (MCDW-WW mixing line) toward the bottom left (cooler and fresher) corner of the diagram approaching the coast (Figure 3.6D). Our results therefore show that most of the water column (WW layer and the underlying pycnocline, to a depth of 300–400 m) is affected by cooling and freshening near the coast.

Finally, the upper part of the water column is occupied by the AASW. The AASW varies strongly across the region reflecting the absence or presence of sea ice and whether or not sea-ice melt has occurred. The polynya was completely ice free in November and during the first weeks of December 2014 (Scambos et al., 1996), just before the survey, allowing warming of surface waters in early summer. In the polynya, a ~50 m thick layer of relatively warm (up to ~ -0.2°C) AASW overlies the WW. Outside the polynya, sea ice was present prior to and during the survey. Here AASW is essentially absent and the WW layer extends to the surface. In the northern polynya we observe a fresh (salinity < 34) surface layer due to sea-ice melting that occurred in the last days of the survey (Figures 3.2B and 3.5B). This surface layer is highly stratified ($N^2 \sim 10^{-4}$ s^{-2}, Figure 3.5D) due to the strong input of freshwater at the surface. Because of the strong stratification, the observed freshwater input due to melting of sea ice does not affect the underlying WW. In fact the WW properties (e.g., salinity) are similar, here, to the western polynya, where sea-ice melting did not occur (Figures 3.6A and 3.6B).

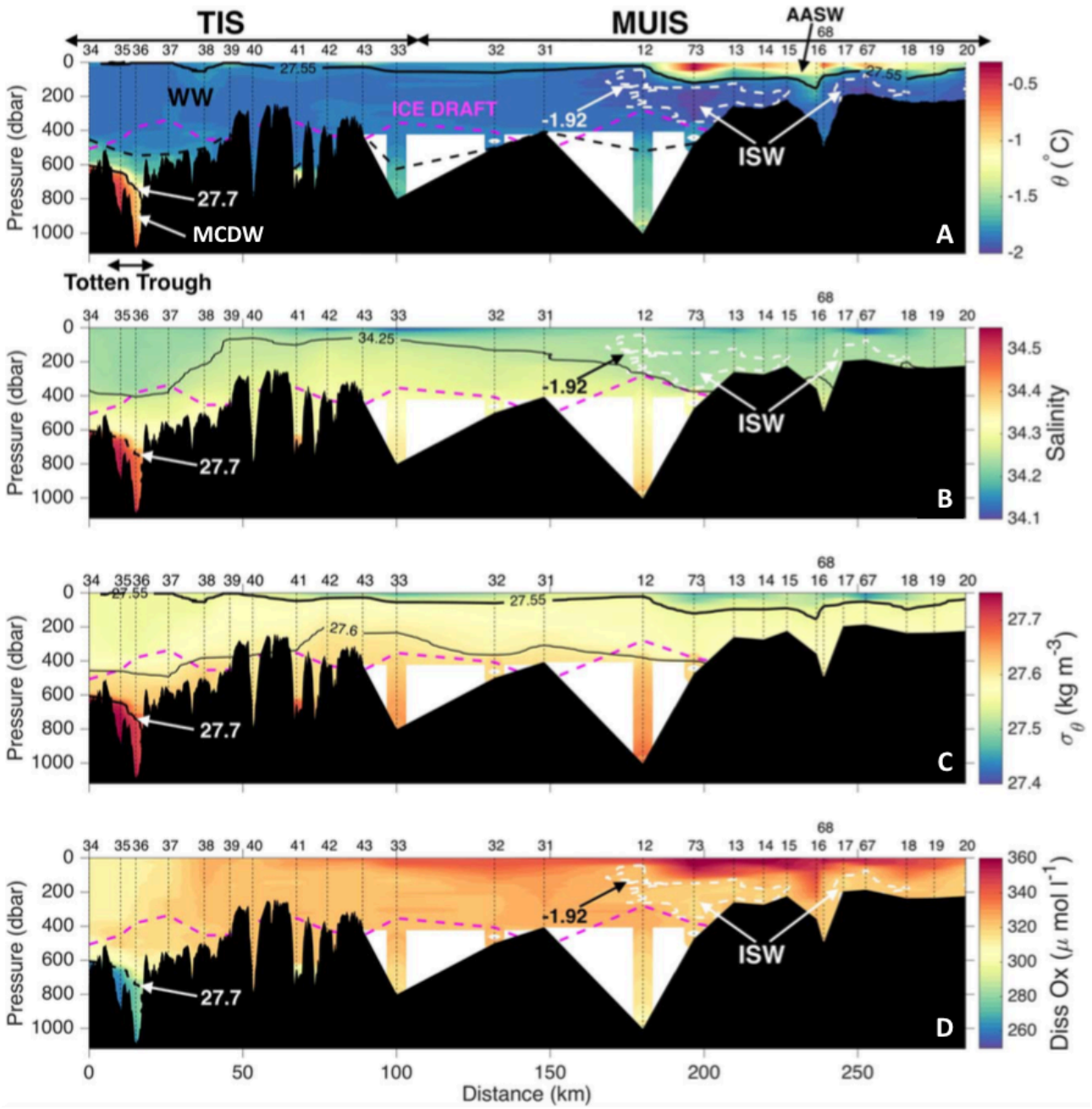

Figure 3.7. Ice-front section. As Figure 3.2 but for the calving front of TIS and MUIS (blue and green dots in Figure 3.1, respectively). Note that the upper limit of the WW layer roughly overlaps the potential density contour of 27.55 kg m^{-3} and therefore is not labeled. From stations 34 to 43, we use the bathymetry data collected during the voyage. East of station 43, the coverage does not provide high resolution bathymetry on a straight line between the stations and therefore only the depth at each station is used. Along the MUIS calving front, where the distances between stations are large, we do not interpolate below the deepest common depth at each station pair. The magenta dashed line indicates the approximate draft of the ice shelf near the calving front. From station 34 to station 42, the draft is interpolated from airborne measurements (Greenbaum et al., 2015), while from stations 43 to 15, the draft is obtained from BEDMAP2 estimate of ice thickness (Fretwell et al., 2013). East of station of 15 the ice front is grounded, according to BEDMAP2.

3.4.2.2. Ice front

The ice-front section indicates that relatively warm (~ -0.4°C), salty (~ 34.53) and oxygen-poor (~ 260 μmol L^{-1}) MCDW reaches the western sector of the TIS calving front (Figure 3.7). Here the deep water is colder and fresher than the MCDW found in the DP, but still 2-2.2°C above the in situ freezing temperature. Direct velocity measurements from a Lowered Acoustic Doppler Current Profiler (LADCP) confirm that the warm water is flowing strongly into the cavity through the Totten Trough at stations 35 and 36 (Rintoul et al., 2016). Because the warm water at depth is flowing into the cavity, the interleaving observed below ~800 m at station 36 (Figures 3.5A-3.5C) is a surprise. The interleaving signal (e.g., temperature variations of of 0.05-0.1°C over tens of meters) is large relative to the error in the measurement. The interleaving at depth might indicate mixing with a small amount of glacial meltwater that detrains from the ice-shelf base at depth. With the exception of the weak interleaving, the MCDW at the western TIS front forms a relatively homogeneous deep layer (Figure 3.5), in contrast to the well-stratified MCDW found in the DP. The homogeneity and relatively cool temperature of the MCDW at the ice front likely reflects the presence of a sill that restricts access of water warmer than - 0.4°C to the TIS cavity.

Above the MCDW layer, the θ-S diagram shows that the pycnocline (MCDW-WW mixing line) observed at stations 34, 35, and 36 in the western sector of the TIS front departs from the trend observed in the polynya (Figure 3.8A). This shift toward fresher (and cooler) values is a signal of addition of freshwater. Other measurements from the TIS calving front (station 41) overlap the DP trend, confirming that this shift is not due to different ambient water properties on the Sabrina Coast continental shelf, but rather the addition of freshwater along the western ice front. The O_2-S diagram confirms the strong departure of the MCDW-WW mixing line from the ambient trend (Figure 3.8B).

The WW at the western TIS front is fresh (~34.25), low in oxygen (~ 300 μmol L^{-1}), and very weakly stratified compared to the WW found elsewhere on the shelf (Figures 3.5B-3.5D), including further east along the calving front (Figure 3.7). The low oxygen and salinity are responsible for the bump observed in the O_2-S plot (Figure 3.8B) and reflects an outflow driven by upwelling of a mixture of glacial meltwater and MCDW from the cavity. Further east along the TIS calving front there are no indications of any substantial fresh outflows. At the eastern TIS calving front, the deep water that can reach the inland cavity hypothesized by Greenbaum et al. (2015) is cooler than -1.1°C (stations 41, 42, 43, and 33, Figure 3.7A), significantly colder than in the Totten Trough.

In contrast to the TIS, the WW reaches the bottom along most of the MUIS calving front. Only one deep (~1000 m) trough at station 12 shows relatively warm (~ -1.3°C) and oxygen-poor (~ 300 μmol L^{-1}) deep water (Figures 3.7A and 3.7D). Near this trough the WW is replaced by ISW (θ < -1.92°C) at depths shallower than the ice draft, between 100 and 400 m below the sea surface (Figure 3.7A). The ISW is fresher (~ 34.25) and lower in oxygen (~ 320 μmol L^{-1}) than the surrounding WW (salinity ~ 34.3 and oxygen ~ 330 μmol L^{-1}, Figures 3.7B and 3.7D). The ISW properties are also clear in the θ-S and O_2-S diagram by the bumps below the surface freezing point and below the WW-MCDW mixing line trend, respectively (Figure 3.8). To summarize, we observe at the MUIS ice front relatively warm water at depth that can access the cavity through a deep trough, coincident with low oxygen ISW at depths shallower than the ice draft. These findings indicate that the ISW results from basal melt driven by deep intrusions of relatively warm and low oxygen water into the MUIS cavity, similar to the TIS. Low oxygen ISW is found not only in front of the ice shelf, but along most of the coast where the ice is grounded, up to 75 km east of the deep trough located at station 12 (Figure 3.7).

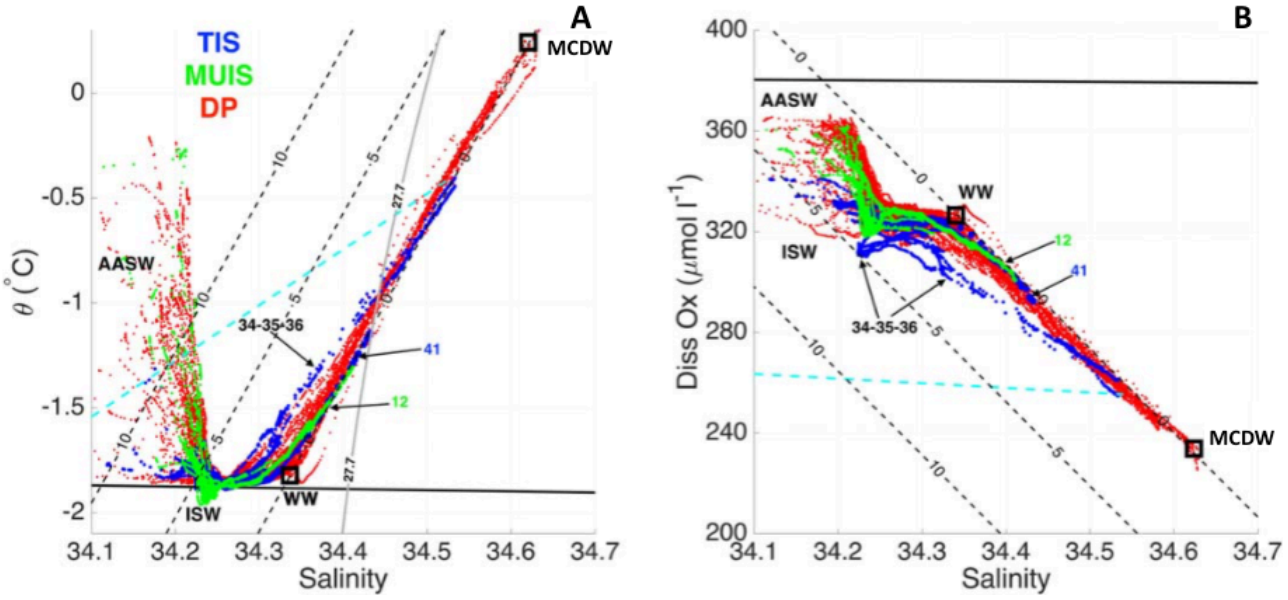

Figure 3.8. θ-S/O_2-S diagram. (A) Potential temperature θ versus salinity and (B) dissolved oxygen versus salinity from DP (red), MUIS (green), and TIS calving fronts (blue). The cyan dashed line is the mixing line (in the θ-S plot also known as Gade Line) between the warmest MCDW found in front of TIS and pure glacial meltwater, while the black dashed lines indicate contours of basal meltwater fraction (ml L^{-1}). The square boxes refer to the ambient properties used to calculate the basal meltwater fraction. The black line is the surface freezing point in Figure 3.8A and the surface of saturation for water at the surface freezing point in Figure 3.8B. The westernmost profiles (34, 35, and 36) are labeled. The grey line in plot (A) represents the surface of σ_0 = 27.7 kg m^{-3} (upper boundary of MCDW). AASW, Antarctic Surface Water; ISW, Ice Shelf Water; MCDW, Modified Circumpolar Deep Water; and WW, Winter Water.

3.4.3. Distribution of glacial meltwater

In this section we quantify the glacial meltwater concentration in the water column throughout the survey area. Glacial meltwater is produced by ice-shelf/iceberg basal melting and surface runoff. The contribution from surface runoff is negligible since summer air temperature in the interior of the East Antarctic Ice Sheet and on the Sabrina Coast is well below freezing and therefore surface melting can be ignored (Fyke et al., 2010; Picard and Fily, 2006). For simplicity, we refer to glacial meltwater produced by basal melt of ice shelves and icebergs as basal meltwater. We use the method of Jenkins (1999) to estimate the basal meltwater fraction ϕ_{melt} from potential temperature, salinity and dissolved oxygen. This method has been successfully applied both at the calving front of several ice shelves (e.g., Jenkins and Jacobs, 2008; Jacobs et al., 2011) and on the continental shelf further offshore (e.g., Randall-Goodwin et al., 2015). Estimates of ϕ_{melt} using this technique have been found to be consistent with studies using other tracers like neon and helium (Jenkins and Jacobs, 2008; Kim et al., 2016).

The method of Jenkins (1999) can be used to estimate the meltwater concentration relative to the ambient water. In the simple case where basal meltwater is added to a single ambient water mass, we can write a conservation equation for a conservative tracer χ:

$$\chi_{obs} = (1 - \phi_{melt})\chi_{wm} + \phi_{melt}\chi_{melt} \quad (3.1)$$

where χ_{obs} is the measured tracer property, and χ_{wm} and χ_{melt} are the tracer properties of the ambient water mass and basal meltwater, respectively. From equation (3.1), it follows that ϕ_{melt} can be estimated as:

$$\phi_{melt} = \frac{\chi_{obs} - \chi_{wm}}{\chi_{melt} - \chi_{wm}} \quad (3.2)$$

If the ambient water is a mixture of two water masses ("wm1" and "wm2"), we can write conservation equations for two conservative tracers χ^1 and χ^2:

$$\begin{cases} \chi^1_{obs} = (1 - \phi_{melt} - \phi_{wm2})\chi^1_{wm1} + \phi_{melt}\chi^1_{melt} + \phi_{wm2}\chi^1_{wm2} \\ \chi^2_{obs} = (1 - \phi_{melt} - \phi_{wm2})\chi^2_{wm1} + \phi_{melt}\chi^2_{melt} + \phi_{wm2}\chi^2_{wm2} \end{cases} \quad (3.3)$$

where ϕ_{wm2} represents the concentration of the water mass "wm2". On the Sabrina Coast continental shelf, we can use observations of two conservative tracers to solve the system of equations (3.3)

beneath the summer mixed layer, where the ambient water is a mixture of MCDW ("wm1") and WW ("wm2"). After some simple algebra, we obtain that the basal meltwater fraction is given by:

$$\phi_{melt} = \frac{(\chi^2_{obs} - \chi^2_{MCDW}) - \alpha(\chi^1_{obs} - \chi^1_{MCDW})}{(\chi^2_{melt} - \chi^2_{MCDW}) - \alpha(\chi^1_{melt} - \chi^1_{MCDW})} \quad (3.4)$$

where $\alpha = \frac{(\chi^2_{WW} - \chi^2_{mCDW})}{(\chi^1_{WW} - \chi^1_{mCDW})}$. This derivation of equation (3.4) differs from that of Jenkins (1999), but gives the same result.

Using potential temperature, salinity and dissolved oxygen as conservative properties below the surface layer, three different estimates of ϕ_{melt} can be obtained based on three possible pairs of these tracers (θ-S, θ-O_2 and O_2-S). The values corresponding to the warmest, saltiest, lowest oxygen water found on the shelf (θ = 0.3°C, S = 34.63 and O_2 = 230 μmol L^{-1}) are taken as representative of the MCDW core. The WW end member (θ = -1.8°C, S = 34.34 and O_2 = 327 μmol L^{-1}) is defined by the saltiest WW found in the domain (Randall-Goodwin et al., 2015).

The temperature of pure glacial meltwater θ_{melt} can be extrapolated from the so-called Gade Line which describes the mixing line in θ-S space between pure glacial meltwater and the oceanic water source (Gade, 1979; Jenkins and Jacobs, 2008):

$$\theta_{melt} = \theta_f - \frac{L}{c_w} - \frac{c_i}{c_w}(\theta_f - T_i) \quad (3.5)$$

where θ_f is the freezing point temperature at the ice-shelf base and depends on salinity and pressure; L is the latent heat of ice fusion (3.35×10^5 J kg^{-1}); c_W and c_i are the specific heat capacity of seawater and ice (4000 and 2010 J $kg^{-1}C^{-1}$, respectively) and, T_i is the mean ice temperature of ice shelves and icebergs. No measurements are available on the Sabrina Coast to estimate the latter quantity. We assume T_i to be -15°C in agreement with the ice temperature measured at the Amery Ice Shelf in East Antarctica (Herraiz-Borreguero et al., 2013). The oceanic source can be any water parcel found along the MCDW-WW mixing line. Considering a typical ice draft in TIS of 500 m (from BEDMAP2; Fretwell et al., 2013) and a salinity of 34.4 representative of the domain, we find that θ_{melt} is about - 92°C, comparable to estimated values in Amundsen ice shelves (e.g., Hellmer et al., 1998; Jenkins and Jacobs, 2008). Note that ϕ_{melt} is not very sensitive to the estimated θ_{melt} and hence to the values of the freezing point temperature or ice temperature selected.

The oxygen content of pure glacial meltwater is estimated from the empirical relation obtained by Martinerie et al. (1992) between oxygen concentration of the ice (and therefore of pure glacial meltwater) and the elevation where the ice is formed. According to this empirical law and considering that the elevation of the catchment that feeds the TIS and MUIS is around 2000–3000 m (Fretwell et al., 2013), we obtain a value around 900 μmol L^{-1} for the dissolved oxygen content of pure glacial meltwater (note that ϕ_{melt} is not particularly sensitive to this value). The mixing line between the warmest, saltiest, and lowest oxygen MCDW found in front of TIS and pure glacial meltwater in θ-S (Gade Line) and O_2-S space is shown in Figure 3.8 by the cyan line. The shift of the pycnocline at the western TIS front toward the Gade Line supports the hypothesis that basal melt supplies a source of freshwater.

Following Jenkins and Jacobs (2008), we regard O_2-S as the most reliable pair to calculate ϕ_{melt}. When the difference between the basal meltwater fraction calculated with the other two property pairs (θ-S and θ-O_2) is larger than 3.5 ml L^{-1}, we disregard the calculation because it is likely affected by interaction with the atmosphere. Beneath this level, the uncertainty in the estimated ϕ_{melt} is mainly due to the deviation from linear mixing between WW and MCDW (Jenkins and Jacobs, 2008). In order to provide a quantitative estimate of this uncertainty, we calculate the difference between ϕ_{melt} estimated as described above and ϕ_{melt} calculated considering the freshest form of WW found on the shelf (S = 34.27). We perform this calculation for every set of in situ θ, S and O_2. In other words, we investigate the impact of a shifted mixing line on the calculation of ϕ_{melt}. Although this shift is not observed, it provides an upper bound on the uncertainty, as it represents the maximum plausible departure from the observed mixing line. Neglecting negative values of ϕ_{melt}, which are not physical and arise from shifting the mixing line, the average difference between the two calculations is smaller than 2 ml L^{-1}. We then treat 2 ml L^{-1} as the upper bound on the uncertainty of ϕ_{melt}.

The basal meltwater fraction agrees well with the observed water properties (Figure 3.9). Where there are inflows of deep and warm water, as in the Totten Trough and in the MUIS trough at station 12, the basal meltwater content is small. Where there are fresh outflows, ϕ_{melt} increases. The highest basal meltwater content is found in the outflow along the western TIS calving front with values up to 5 ml L^{-1}. The ISW also has a strong meltwater signature, as expected, with maximum values of ϕ_{melt} up to 4 ml L^{-1}. The meltwater content of the outflow is higher at the TIS calving front than at the MUIS front. This result is consistent with the observation that warmer MCDW reaches

the TIS cavity, driving higher rates of basal melt.

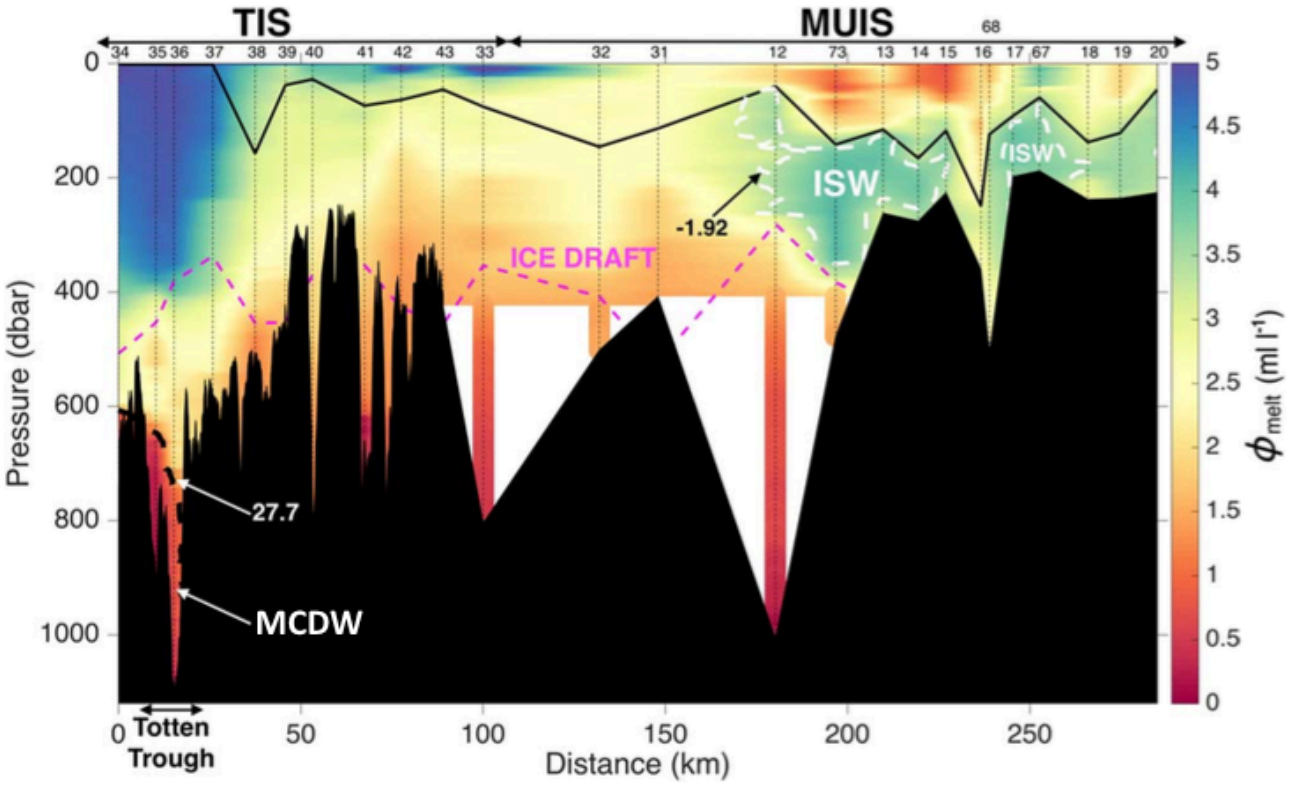

Figure 3.9. Basal Meltwater Fraction. Vertical section of the basal meltwater fraction ϕ_{melt} (ml L^{-1}) in front of TIS and MUIS. The surface of σ_θ = 27.7 kg m^{-3} (upper boundary of MCDW) is indicated by the dashed black line, while the magenta dashed line represents the ice draft, as in Figure 3.7. The black line is the maximum depth where surface contamination is likely to affect the calculation of ϕ_{melt}. θ = -1.92°C contours (Ice Shelf Water) are in dashed white.

The influence of the basal meltwater input is not limited to the TIS and MUIS calving front. As noted above, the WW salinity decreases near the coast in the polynya (Figure 3.6B). The basal meltwater concentration shows a similar distribution, with values of 1-1.5 ml L^{-1} in the western/northern polynya increasing to values in excess of 3 ml L^{-1} in the southern polynya (Figure 3.6C). The similarity between the two patterns suggests the low salinity of WW in the southern polynya reflects dilution by basal meltwater. Near the Dalton Iceberg Tongue, at stations 54 and 82, the meltwater fraction in WW is about 1.5–2 ml L^{-1} (Figure 3.6C), a relatively small concentration considering the estimated uncertainty on ϕ_{melt} of 2 ml L^{-1}. The low meltwater concentration near the Dalton Iceberg Tongue is in agreement with the small decrease in salinity there compared to that observed in the southern polynya. This implies that the input of basal meltwater from Dalton Iceberg Tongue is relatively small.

3.5. Discussion

Our observations show that relatively warm MCDW is widespread below 500 m on the continental shelf of the Sabrina Coast. Fresh WW overlies the saline MCDW. No DSW was observed on the continental shelf, suggesting that winter convection was too weak to erode the stratification and produce water dense enough to mix with the MCDW. The distribution of MCDW properties can be explained largely in terms of bathymetry. The warmest MCDW is found in the deep area on the western side of the polynya (it is possible that even warmer waters might be found further west). Southward shoaling of the bottom prevents the MCDW from reaching the coast in the polynya; relatively warm water can reach the TIS and MUIS cavities only through localized troughs. The warmest MCDW observed on the shelf is ~0.7°C warmer than the warmest water reaching the TIS and ~1.6°C warmer than the water reaching the MUIS. A sill or other bathymetric barrier in an area not covered by our survey presumably prevents the warmest water found on the shelf from reaching the TIS and MUIS cavities. With the exception of airborne surveys that cover the TIS cavity and surroundings, the only available bathymetric information on the shelf is derived from satellite altimetry measurements (e.g., Smith and Sandwell, 1997), which do not resolve small-scale features such as sills or narrow troughs. Our results highlight the need for high resolution bathymetric surveys to identify the controls on delivery of ocean heat to the ice shelves and for use in model simulations of warm water intrusions into the ice-shelf cavities.

Deep water observed at the ice front is cooler than the MCDW observed in the polynya but still about 1°C (at the MUIS) and 2°C (at the TIS) above the local freezing point and therefore sufficiently warm to produce substantial basal melt at depth. Rintoul et al. (2016) showed that the ocean heat flux into the TIS cavity was sufficient to account for the rapid basal melt inferred by satellites. Using our extended data set we conclude that the high rate of basal melt inferred at the MUIS is also likely driven by deep intrusions of cooler, but still relatively warm, water.

Input of basal meltwater causes the observed shoreward freshening in the southern DP of the water column above the MCDW. Four lines of evidence support this statement. (1) The distributions of WW salinity and WW basal meltwater fraction co-vary in the polynya, with substantial freshening and increase in meltwater concentration near the coast. (2) Shoreward shift of the MCDW-WW mixing line toward cooler and fresher values (i.e., toward the MCDW-meltwater mixing line or Gade Line) indicates that the signal of meltwater is detected to 300–400 m depth. (3) Freshening by melting of sea ice is expected to be more intense in the northern side of the polynya than near the coast. (4) The precipitation rate integrated over the southern half of the Dalton Polynya estimated

using ERA-Interim (European Centre for Medium-Range Weather Forecasts Interim Re-Analysis) precipitation data (Dee et al., 2011) is more than an order of magnitude smaller than freshwater fluxes from basal melt of the nearby MUIS (both the main trunk and the subsidiary part; Liu et al., 2015). The resolution of the ERA-Interim data does not allow to detect any spatial variability within the polynya. Indeed precipitation could be enhanced near the coast, but given the small magnitude of the integrated precipitation rate, such contribution is likely to be negligible. Freshening by input of glacial meltwater has been also reported in the Amundsen and Bellingshausen seas, where the meltwater signature is widespread on the continental shelf above the MCDW layer (Wåhlin et al., 2010; Kim et al., 2016; Randall-Goodwin et al., 2015; Zhang et al., 2016).

The widespread influence of basal meltwater on water properties in the southern polynya suggests there may be multiple sources. In particular, high meltwater concentrations are observed well to the east of the outflow from the MUIS cavity near the deep trough at station 12, whereas we would expect meltwater to be advected westward by the coastal current. One possible source is basal melt from the main trunk of the MUIS that exits the cavity at the calving front east of 121.5°E and is then advected west by the coastal current. Additional channels or cavities may also connect the main MUIS trunk to the DP, providing a pathway for meltwater. Another possible source is submarine melting of icebergs in the Dalton Iceberg Tongue. However, three observations suggest the contribution from the Dalton Iceberg Tongue is less important than that of the MUIS. (1) The weak freshening of WW observed near the iceberg tongue suggests the meltwater input is small. (2) The draft of the grounded icebergs is too shallow (< 500 m) to reach the warm MCDW layer and the thermal forcing driving melt is weak. (3) The low oxygen content of ISW found in the south-eastern polynya indicates the melting is driven primarily by MCDW, which does not reach the Dalton Iceberg Tongue (see Figure 3.4A). Therefore, we speculate that basal melt under the main trunk of the MUIS represents the major source of the basal meltwater found in the DP. If correct, this implies that MCDW is able to access the cavity beneath the main trunk of the MUIS, as also suggested by modeling studies (Khazendar et al., 2013; Gwyther et al., 2014).

A comparison with data collected during BROKE and SIPEX reveals that the stratification observed in the polynya in 2015 was similar to that found on the outer shelf in 1996 and 2007 (Figure 3.10): in each year, relatively warm and saline MCDW was present near the seafloor, overlaid by cold and fresh WW. (The depth of the pycnocline varies between stations, likely reflecting differences in bottom depth and temporal variability.) Most importantly, none of the profiles collected on the continental shelf shows evidence of DSW. The large salinity (hence density) contrast between fresh

WW and saline MCDW stabilizes the water column. This stable stratification persists through winter: the SIPEX profile from later winter 2007 shows a salinity contrast of ~ 0.3 between WW and MCDW (Williams et al., 2011), similar to summer profiles in 1996 and 2015. Sea-ice production in the DP is low relative to other active Antarctic polynyas (Tamura et al., 2016; Williams et al., 2011) and winter buoyancy loss is apparently insufficient to overcome the stable stratification. Meltwater input contributes to the freshening of the WW, as discussed above, and likely inhibits DSW formation (Williams et al., 2016). These observations indicate that DSW is not produced in the DP, counter to suggestions from some modeling studies (e.g., Gwyther et al., 2014).

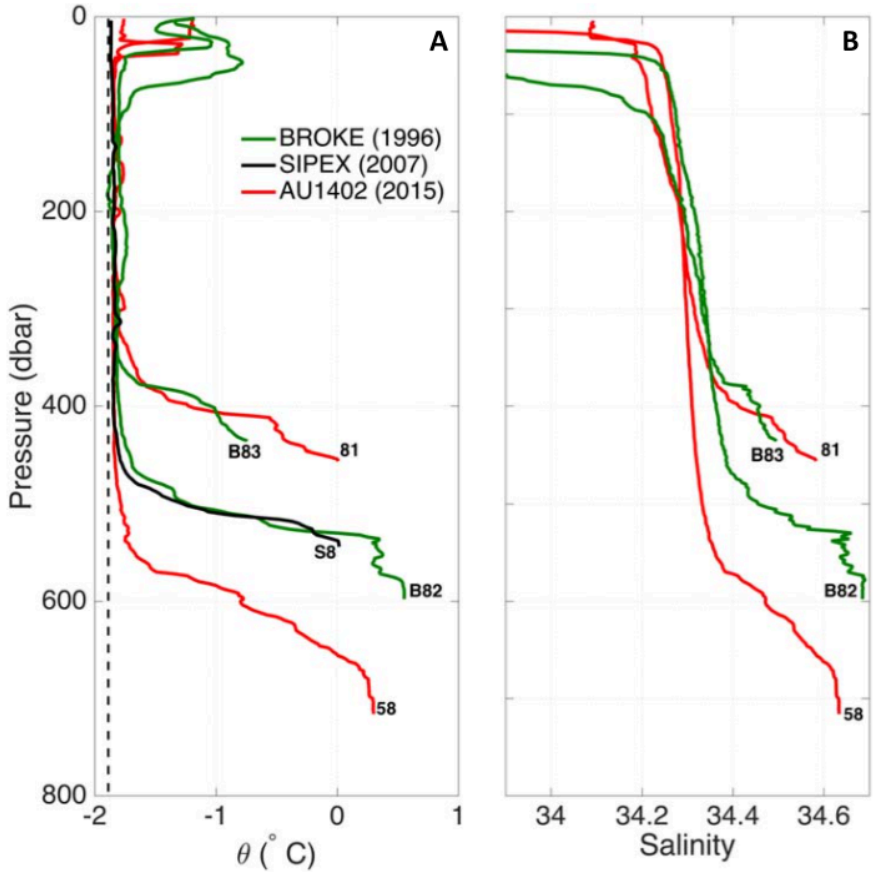

Figure 3.10. SIPEX-BROKE-AU1402. Vertical profiles of (A) potential temperature θ and (B) salinity from BROKE in 1996 (dark green, stations B82 and B83) and SIPEX in 2007 (black, station S8). For comparison two profiles from the AU1402 expedition in 2015, one from the northern DP (station 81) and one from the western DP (station 58) are overlaid in red. In Figure 3.10A overlaid in dashed black is the surface freezing temperature for a salinity of 34.4, representative of the domain. The location of the stations is labeled in Figure 3.1. Salinity data from SIPEX presented a large offset (> 0.1) and therefore are not included here.

To place our results in a broader context, we compare the ocean properties observed near the Totten Glacier with the Mertz Glacier on the Adélie Coast in East Antarctica and with Pine Island Glacier in Pine Island Bay, West Antarctica (Figure 3.11). The MCDW is found on the continental shelf in each location, but with different properties. The warmest MCDW is observed in Pine Island Bay

(3–4°C above the in situ freezing point). On the Sabrina Coast the MCDW is colder, but still 2–2.5°C above the local freezing point, while on the Adélie Coast the MCDW is less than 1.3°C above the local freezing point. The ocean stratification is qualitatively similar on the Sabrina Coast (see station 52) and in Pine Island Bay (see station 13): beneath the summer mixed layer, cold and fresh WW overlies warm, salty MCDW. In contrast, on the Adélie Coast, the densest water is cold and oxygen-rich DSW formed during winter (Shadwick et al., 2013). Above the DSW is the MCDW, a thin layer of cold WW, and the summer mixed layer (see station 131). Intrusions of MCDW are less dense than the DSW on the Adélie Coast, and as a result, the temperature maximum associated with MCDW is found at intermediate depth. In Figure 3.12, we show a schematic of the different stratification found on the Sabrina Coast, in Pine Island Bay, and on the Adélie Coast.

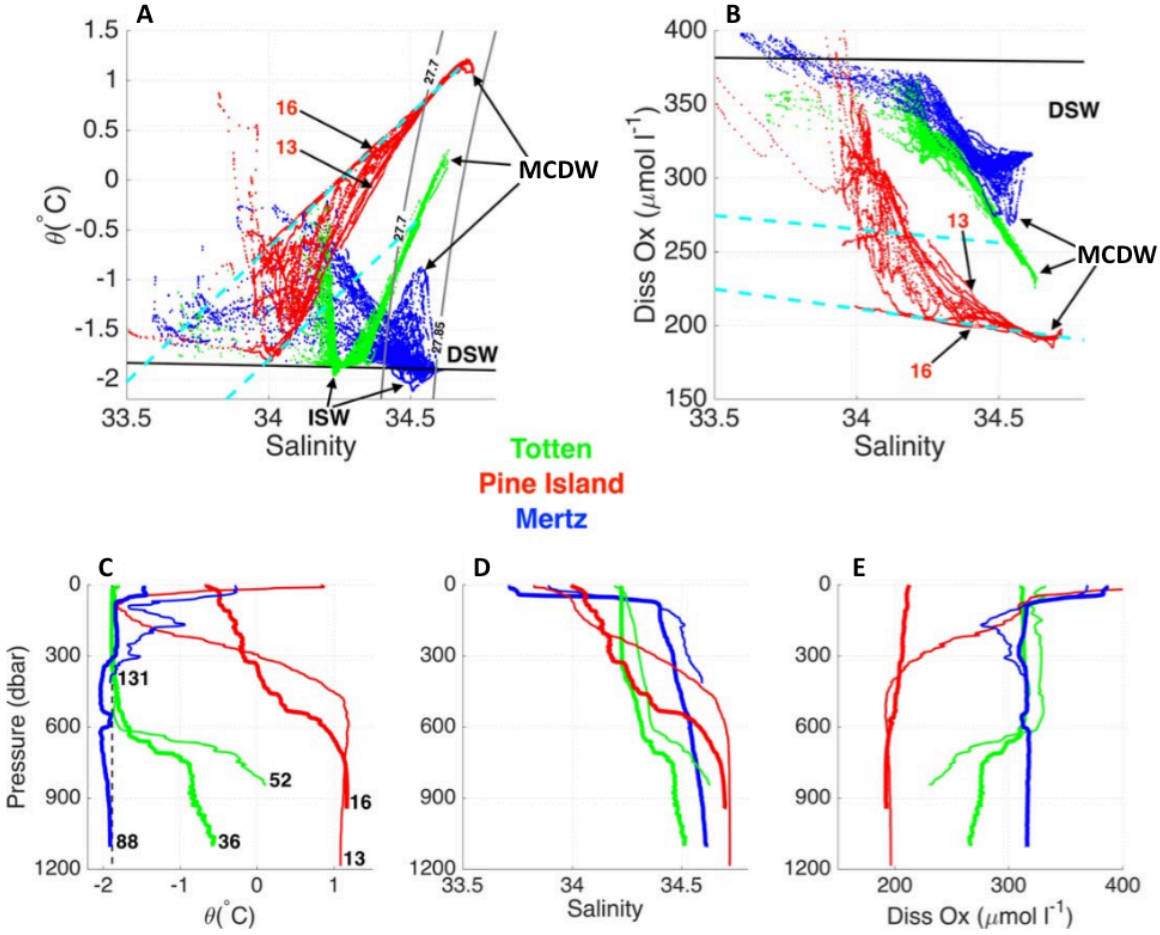

Figure 3.11. Comparisons between Totten, Mertz, and Pine Island glaciers. (A) Potential temperature θ versus salinity from the shelf in front of Totten (green), Mertz (blue), and Pine Island (red) glaciers. The grey lines represent the surface of σ_θ = 27.7 kg m^{-3} (upper boundary of MCDW) and σ_θ = 27.85 kg m^{-3} (upper boundary of DSW). The black line is the surface freezing point. The cyan dashed lines are the mixing line between the warmest MCDW found in front of Totten/Pine Island Glacier and pure glacial meltwater. (B) As Figure 3.11A for dissolved oxygen versus salinity. The black line indicates the surface of saturation for water at the surface freezing point. Vertical profiles of (C) θ, (D) salinity, (E) dissolved oxygen showing two profiles for each region. The thin lines are profiles representative of the shelf conditions (station 52/13/131 for Totten/Pine Island/Mertz). The thick lines are profiles representative of the ice-front conditions (station 36/16/88 for Totten/Pine Island/Mertz). The vertical dashed line in plot (C) indicates the surface freezing line for a salinity of 34.3, an intermediate value between the salinity observed at these three locations.

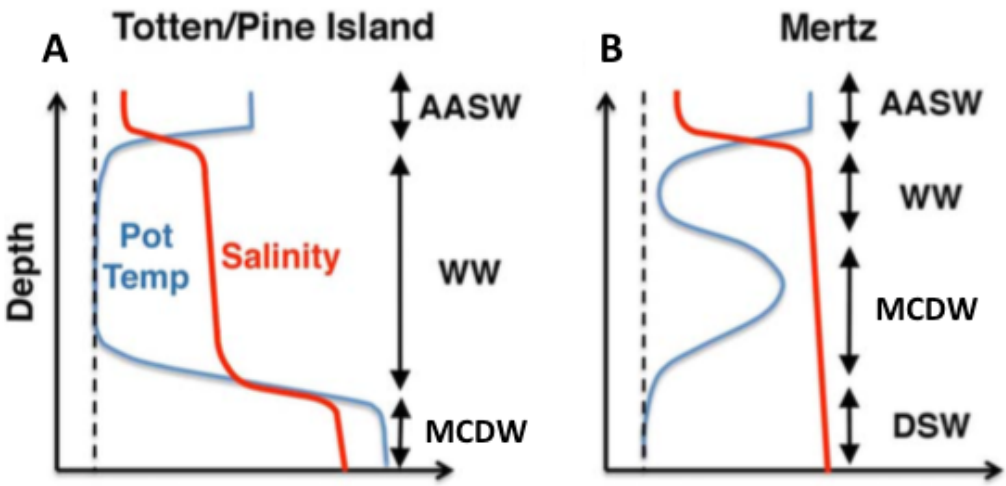

Figure 3.12. Schematic of the ocean summertime stratification in potential temperature and salinity in front of (A) Totten/Pine Island Glacier and (B) Mertz Glacier. AASW, Antarctic Surface Water; WW, Winter Water; MCDW, Modified Circumpolar Deep Water; DSW, Dense Shelf Water.

The difference in stratification found in front of Totten/Pine Island and Mertz glaciers has a large influence on ocean-ice shelf interaction. Near the Mertz Glacier, relatively warm MCDW is found at depths shallower than 300 m and so has limited access to the cavity beneath the Mertz Glacier Tongue. Cold DSW fills the cavity and drives basal melt at depth. The cold and high oxygen ISW at the calving front (e.g., station 88) confirms that high oxygen DSW is the main source of melting under the Mertz Glacier Tongue. The outflow from the Totten and Pine Island cavities is lower in oxygen because the melting source is low oxygen MCDW. A critical difference between the regions is the salinity of the WW: WW is much fresher in Pine Island Bay and on the Sabrina Coast (~34.0 and 34.3, respectively) than on the Adélie Coast (~34.5–34.6). Weak winter salinification results in fresh WW and inhibits convection in West Antarctica and near the Totten Glacier, allowing deep intrusions of warm water into the ice-shelf cavities to drive rapid basal melt. In contrast, strong heat loss and deep convection "protects" most of the East Antarctic outlet glaciers, like Mertz, by limiting the transport of ocean heat to the base of the ice shelves.

The continental shelves on the Sabrina Coast and in West Antarctica share several characteristics: widespread warm MCDW in the bottom layer, weak polynya activity, fresh WW, absence of DSW, high basal melt rates, and widespread glacial meltwater. There are also some important differences. The MCDW is warmer, saltier, and lower in oxygen in Pine Island Bay than on the Sabrina Coast continental shelf. WW is fresher near Pine Island Glacier. The concentration of meltwater in the outflow from the TIS cavity is ~30% of that observed at Pine Island Glacier (Jacobs et al., 2011). Near Pine Island Glacier, some profiles fall on the MCDW-glacial meltwater mixing line in θ-S and O_2-S space (see station 16 in Figure 3.11). This is not observed at the Totten calving front, possibly

because the outflow has already mixed with WW or because the major outflow from the cavity occurs further west, where fast ice prevented access during the cruise.

A broad trough in front of Pine Island Glacier allows MCDW to reach the cavity along the full width of the calving front, in contrast to the TIS and MUIS, where MCDW inflow is limited to narrow channels. However, bathymetry inside the cavity likely regulates the flux of warm water to the grounding line of Pine Island Glacier (Dutrieux et al., 2014). Shoaling or deepening of the interface between warm MCDW and cold WW is likely to alter the ocean heat transport to the TIS and MUIS cavity and therefore basal melt, as shown by Dutrieux et al. (2014) at Pine Island Glacier. Several processes can influence the depth of the pycnocline on the continental shelf. Variability of MCDW intrusions onto the shelf can modify the thickness of the bottom layer and the depth of the overlying pycnocline (Thoma et al., 2008). Local changes in winds associated with upwelling/downwelling variability or increased/decreased freshwater fluxes from ice-shelf basal melt can also cause substantial changes in the pycnocline depth (Padman et al., 2012). Finally, variability in winter convection and thus in the mixed layer thickness can alter the depth at which the pycnocline starts (St-Laurent et al., 2015).

Polynya variability and resulting changes in winter convection may alter heat delivery to the ice-shelf cavities, especially for the nearby MUIS where our observations show that the warm water reaching the cavity comes from the upper pycnocline rather than the MCDW. Deepening of the upper pycnocline in the polynya could prevent relatively warm water from reaching the base of the MUIS. The models of Khazendar et al. (2013) and Gwyther et al. (2014) suggest that a mixture of MCDW and cold water formed in the polynya drives basal melt of the TIS. In years when the polynya is more active this mixture is cooler and the TIS basal melt is substantially reduced. Since the pathways by which warm water reaches the TIS cavity are unknown, our observations cannot assess the validity of the modeling output. However, the bathymetry used in these models does not capture the complex network of channels present near the TIS front. Our results indicate that if these topographic features are not resolved it is not possible to properly simulate the ice-ocean interactions at the TIS, suggesting that the modeled sensitivity of TIS basal melt rate to polynya activity might not be realistic.

Variability of most of the processes just described is influenced by local processes (e.g., coastal winds and polynya activity), suggesting that small-scale regional variability can drive changes in basal melt of the ice shelves on the Sabrina Coast. However, variability of MCDW intrusions onto

the shelf may be driven by large-scale climate variability. Spence et al. (2014) show that the projected poleward shift of the southern hemisphere westerly winds at the end of the 21st century under sustained anthropogenic CO_2 emissions would cause a shoaling of the pycnocline depth on the continental slope, producing a thicker and warmer layer of MCDW on the continental shelf of the Sabrina Coast. Both local and remote processes therefore might affect the future ocean heat flux to the TIS and MUIS. Further surveys on the Sabrina Coast as well as ocean models with realistic bathymetry will be required to quantify the interannual variability of ocean heat flux to the cavities and to assess the processes that drive temporal variability of pycnocline depth and cross-shelf exchange.

3.6. Conclusions

Oceanographic data collected in the austral summer of 2015 provide the most comprehensive hydrographic survey of the Sabrina Coast continental shelf to date. In most of the region covered by our survey, we find warm MCDW in the bottom layer below fresh Winter Water. Glacial meltwater is widespread on the southern shelf at depths shallower than 300–400 m. These features are atypical for East Antarctica but resemble those observed in the Amundsen and Bellingshausen seas, where rapid basal melt and thinning of ice shelves in recent decades have been linked to inflow of MCDW to the ice-shelf cavities.

Relatively warm water drives high rates of ice-shelf basal melt on the Sabrina Coast, but access to the cavities is restricted to narrow troughs; bathymetric obstacles in uncharted areas presumably prevent the warmest water found on the shelf from accessing the ice-shelf cavities. Topographic features therefore strongly influence the ocean heat flux to ice shelves on the Sabrina Coast. Variations in pycnocline depth and cross-shelf exchange driven by changes in local and remote forcing may alter the temperature of the water reaching the ice-shelf cavities. Models suggest that under continued high emissions of greenhouse gases, ocean-initiated collapse of the Totten Ice Shelf leads to rapid ice loss from the Aurora Subglacial Basin, contributing several meters of global sea level rise in coming centuries (Golledge et al., 2015; DeConto and Pollard, 2016). Our observations show that there is a substantial reservoir of heat on the continental shelf near the Totten Glacier, but the processes that control ocean heat transport to the ice-shelf cavity are not known. It is therefore critical to improve our understanding of the mechanisms regulating oceanic variability on the Sabrina Coast in order to predict the future contribution of the East Antarctic Ice Sheet to sea level rise.

Chapter 4

Ocean-ice shelf interaction in East Antarctica

This chapter has been published:
Silvano, A., S. R. Rintoul, and L. Herraiz-Borreguero (2016), Ocean-ice shelf interaction in East Antarctica, *Oceanography*, *29*(4):130–143, doi:10.5670/oceanog.2016.105.

4.1. Abstract

Assessments of the Antarctic contribution to future sea level rise have generally focused on ice loss in West Antarctica. This focus was motivated by glaciological and oceanographic observations that showed ocean warming was driving loss of ice mass from the West Antarctic Ice Sheet (WAIS). Paleoclimate studies confirmed that ice discharge from West Antarctica contributed several meters to sea level during past warm periods. On the other hand, the much larger East Antarctic Ice Sheet (EAIS) was generally considered to be relatively stable because of being largely grounded above sea level and therefore protected from ocean heat flux. However, recent studies suggest that a large part of the EAIS is grounded well below sea level and that the EAIS also retreated and contributed several meters to sea level rise during past warm periods. We use ocean observations from three ice shelf systems to illustrate the variety of ocean-ice shelf interactions taking place in East Antarctica and to discuss the potential vulnerability of East Antarctic ice shelves to ocean heat flux. The Amery and the Mertz are "cold cavity" ice shelves that exhibit relatively low area-averaged basal melt rates, although substantial melting and refreezing occurs beneath the large and deep Amery Ice Shelf. In contrast, new oceanographic measurements near the Totten Ice Shelf show that warm water enters the sub-ice-shelf cavity and drives rapid basal melting, as is seen in West Antarctica. The Totten Glacier is of particular interest because it holds a marine-based ice volume equivalent to at least 3.5 m of global sea level rise, an amount comparable to the entire marine-based WAIS, and recent glaciological measurements show the grounded portion of the Totten Glacier is thinning and the grounding line is retreating. Multiple lines of evidence support the hypothesis that parts of the EAIS are more dynamic than once thought. Given that the EAIS contains a volume of marine-based ice equivalent to 19 m of global sea level rise, the potential for ocean-driven melt to destabilize the marine-based ice sheet needs to be accounted for in assessments of future sea level rise.

4.2. Background

Global mean sea level rose by 0.19 ± 0.02 m between 1901 and 2010 in response to global warming (Church et al., 2013). Ocean thermal expansion and ice loss from glaciers have been the dominant contributors to sea level rise over the past century (Church et al., 2013). The amount of ice stored in ice sheets, equivalent to ~7 m of global sea level rise for Greenland (Dowdeswell, 2006) and ~58 m for Antarctica (Fretwell et al., 2013), is vast compared to projected sea level contributions from glaciers (0.04–0.23 m) and thermal expansion (0.10–0.33 m) by the end of the twenty-first century (Church et al., 2013). Melt of even a small fraction of the water stored in the ice sheets would therefore have a substantial impact on future sea level rise, with widespread consequences for society, particularly in coastal regions. Satellite measurements show that the Greenland and Antarctic Ice Sheets have made positive and growing contributions to sea level rise in the last two decades (Rignot et al., 2011a), and the ice sheets are expected to make the largest contribution in centuries to come (Rignot et al., 2011a; Dutton et al., 2015). The response of the ice sheets to continued warming of the climate remains the largest single source of uncertainty in projections of long-term sea level rise.

Ice sheet stability depends on the balance between gains (from snowfall) and losses (from iceberg calving and melting). The presence of floating ice shelves around the margin of Antarctica contributes to the stability of the Antarctic Ice Sheet. Ice shelves form where ice streams flow off the continent into the ocean and start to float. Back stresses generated when a flowing ice shelf interacts with the seafloor or side walls restrains the drainage of glacial ice into the ocean and thus "buttresses" the ice sheet (Dupont and Alley, 2005). Thinning or collapse of an ice shelf reduces the buttressing effect and increases the discharge of ice into the ocean. Ice shelves thin when the inflow of ice from the continent is insufficient to balance the loss of ice to melt and iceberg calving. Melting from above by a warm atmosphere and melting from below by a warm ocean can both contribute to thinning of ice shelves. For most of Antarctica, air temperatures remain below freezing year-round at present (Picard and Fily, 2006), so basal melting by the ocean makes the dominant contribution. This means the future of Antarctic ice shelves, and the grounded ice sheets buttressed by the ice shelves, is strongly tied to the surrounding ocean. Ice shelves whose grounding lines (the boundaries between the floating ice and the grounded ice) are located well below sea level are potentially more sensitive to ocean forcing. Because the freezing temperature is lowered by pressure, the thermal forcing available for melting is higher for deeper grounding lines for a given water temperature. Moreover, ice sheets grounded on bedrock that slopes upward toward the sea are particularly vulnerable (Weertman, 1974; Schoof, 2007). In this geometry, a retreat of the

grounding line increases the thickness at the ice front and therefore the ice discharge, producing a self-sustaining retreat that is hard to reverse (Joughin and Alley, 2011). This process is called marine ice sheet instability. Several studies suggest that marine ice sheet instability is already underway in West Antarctica (Favier et al., 2014; Joughin et al., 2014; Rignot et al., 2014). If this is the case, a threshold has been crossed that implies a commitment to meters of sea level rise from West Antarctica alone in centuries to come.

Observations from recent decades support the hypothesis that the ocean controls the stability of the Antarctic Ice Sheet. Antarctica as a whole is losing mass, with the largest losses in the Amundsen and Bellingshausen Sea sectors in West Antarctica (Rignot et al., 2008; Harig and Simons, 2015; Wouters et al., 2015). Here, the ice loss has been attributed to thinning of the buttressing ice shelves as a result of increased basal melting by ocean heat flux (Shepherd et al., 2004; Pritchard et al., 2012). Oceanographic evidence confirms that the most rapid mass loss, grounded ice thinning, and grounding line retreat have occurred where relatively warm ocean waters reach sub-ice shelf cavities, driving rapid basal melting (e.g., Jenkins and Jacobs, 2008; Jacobs et al., 2011). The rate of ice loss and thinning of floating ice shelves has increased over the past two decades (Rignot et al., 2011a; Paolo et al., 2015). Consistent with recent observations of dynamic behavior in response to ocean forcing, studies of past climate suggest the West Antarctic Ice Sheet has waxed and waned many times in the past (Scherer, 1991; Naish et al., 2009; Pollard and DeConto, 2009).

East Antarctica, on the other hand, has long been thought to be more stable. Most of the East Antarctic Ice Sheet (EAIS) was understood to be grounded on bedrock well above sea level, and the marine-based parts of the EAIS were believed to be isolated from warm Southern Ocean waters. But recent studies have overturned these assumptions. For example, inferences of past sea level from proxy data and models conclude that the EAIS retreated and made substantial contributions to sea level during past warm periods in Earth's history, suggesting the EAIS is more dynamic than previously thought (Williams et al., 2010a; Young et al., 2011; Cook et al., 2013; Patterson et al., 2014; Pollard et al., 2015; Aitken et al., 2016). New measurements from airborne sensors show that large sectors of the EAIS rest on bedrock well below sea level (Figure 4.1A; Ferraccioli et al., 2009; Young et al., 2011; Roberts et al., 2011; Jamieson et al., 2016). In fact, the marine-based EAIS holds a volume of ice equivalent to 19 m of global sea level rise, five times larger than the marine-based ice sheet in West Antarctica (Fretwell et al., 2013). While early studies indicated no significant ice loss in East Antarctica (e.g., Rignot, 2002), more recent glaciological observations show that some regions of the EAIS have lost mass in the last two decades. In particular, some

aspects of recent change observed at the Totten Glacier are similar to those seen in West Antarctica, including thinning of the grounded ice (e.g., Pritchard et al., 2009; Flament and Remy, 2012; Harig and Simons, 2015; Li et al., 2015) and retreat of the grounding line (Li et al., 2015). While the rates of change at Totten Glacier are not as large as those seen at Pine Island Glacier and other glaciers in West Antarctica, these observations come as a surprise, given that little warm water was thought to reach the continental shelf in this region, which lies well south of the core of the Antarctic Circumpolar Current (ACC). Until recently, no oceanographic data from the Totten ice front were available to test the hypothesis that ocean-ice shelf interaction could explain the dynamic behavior of this sector of East Antarctica.

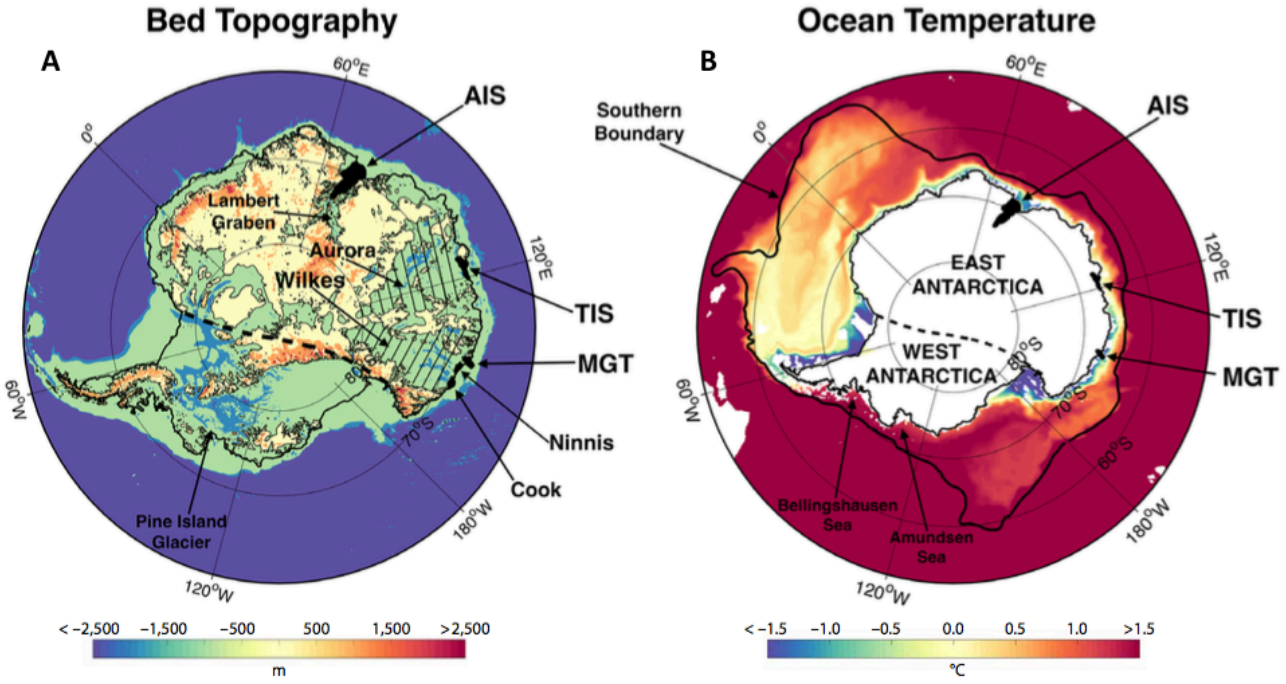

Figure 4.1. Map of Antarctica. (A) Bed topography with coastline (thick black line) and 0-m bathymetric contour (light black line) overlaid (Fretwell et al., 2013). Highlighted are the Amery Ice Shelf (AIS), Totten Ice Shelf (TIS), Mertz Glacier Tongue (MGT), and Ninnis and Cook ice shelves. In the Aurora and Wilkes basins of East Antarctica (dashed areas) and in West Antarctica, the Antarctic Ice Sheet sits on bedrock as much as 2–3 km below sea level. (B) Ocean temperature at 438 m depth, close to the core of the Circumpolar Deep Water in the Antarctic Circumpolar Current, based on the six-year (2005–2010) mean from the Southern Ocean State Estimate (Mazloff et al., 2010). The heavy black line marks the southern boundary of the Antarctic Circumpolar Current (Orsi et al., 1995).

Given the large volume of marine-based ice in East Antarctica, it is critical to develop a better understanding of the potential vulnerability of the EAIS to changes in the ocean. New modeling studies of the response of the Antarctic Ice Sheet to continued high emissions of greenhouse gases underscore the urgency of this task, showing that mass loss from Antarctica may be larger and more rapid than previously thought, with a large contribution from the EAIS (Golledge et al., 2015;

DeConto and Pollard, 2016).

In this review, we summarize what is known about ocean-ice shelf interaction in East Antarctica. The region has received much less attention than West Antarctica, but recent studies have started to fill these gaps and provide new insights into the role of the ocean in driving changes in ice shelves. We focus on the three largest and deepest marine-based sectors of the EAIS: Lambert Graben drained by the Amery Ice Shelf, Aurora Basin mostly drained by the Totten Glacier, and Wilkes Basin near the Mertz Glacier (Figure 4.1A).

4.3. Ocean-ice shelf interaction

Ice shelves form the interface between the Antarctic Ice Sheet and the surrounding Southern Ocean. Interaction between these two systems affects both the ice and the ocean. The ocean supplies heat to ice shelves, driving basal melting and influencing ice sheet dynamics, while freshwater input from ice shelf melting modifies ocean properties. The rate of ice shelf basal melting is determined by the ocean heat transport entering the ice shelf cavities and by the dependence on pressure of the seawater freezing temperature, which decreases ~0.75°C for every 1000 m increase in depth (Foldvik and Kvinge, 1974). The heat transport depends on the temperature of the water (heat content) and on how fast ocean heat is transported to the base of the ice shelf. Thus, the rate of melting at the ice base depends on how fast heat and salt can be transported across the boundary layer to the ice-ocean interface. This, in turn, depends on other factors that are difficult to measure in the ice shelf cavity, such as ice shelf basal roughness, ocean circulation and tides, and turbulence (which, in its turn, depends on heat and salt gradients across the boundary layer). Direct measurements of the ocean beneath an ice shelf can only be made by drilling boreholes through the thick ice shelf or by sending underwater autonomous vehicles into the cavity. While such measurements have been made at a few ice shelves, we still have very few observations of the ocean circulation and heat transport beneath ice shelves. However, a strong correlation has been found between basal melting (inferred by satellite measurements) and ocean temperature measured at the front of the ice shelf (Rignot and Jacobs, 2002). For this reason, ocean temperature provides a good proxy for ice shelf basal melting. The highest basal melt rates occur near deep grounding lines due to the pressure dependence of the seawater freezing temperature. An increase of melt in this region will reduce the ice thickness and increase the gradient of ice thickness change near the grounding line, resulting in a reduction of buttressing to ice discharge and a rise in global sea level (Rignot and Jacobs, 2002). The deepest grounding lines in the world are located in East Antarctica,

up to 2100 m and 2400 m deep for the Totten and Amery ice shelves, respectively (Fretwell et al., 2013).

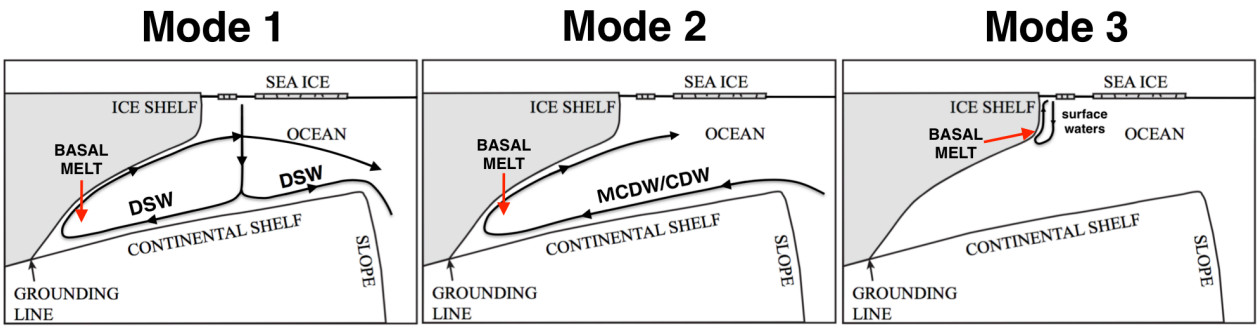

Figure 4.2. Three modes of ice-shelf basal melting (from Jacobs et al., 1992). Mode 1 is driven by cold Dense Shelf Water (DSW), Mode 2 by warm (Modified) Circumpolar Deep Water (MCDW/CDW), and Mode 3 by surface waters. The outflow from the cavity is a mixture of glacial meltwater with DSW (Mode 1) or MCDW (Mode 2); the mixture is called Ice Shelf Water (ISW) when its temperature is below the surface freezing point.

How does the ocean melt an ice shelf? The schematic in Figure 4.2 illustrates three modes of basal melting. Mode 1 is typical of so-called "cold cavity" ice shelves. In winter, waters on the continental shelf are cooled to the surface freezing point. As the ocean freezes to form sea ice, salty brine is left behind in the water column. The decrease in temperature and increase in salinity both act to increase the density of the surface shelf water. The density may increase to the point where surface waters will sink to the seafloor, forming Dense Shelf Water (DSW; also called High Salinity Shelf Water). DSW is generally formed in coastal polynyas, where the combination of strong katabatic winds and a physical barrier that blocks inflow of sea ice (e.g., an ice tongue or grounded icebergs) acts to create an area of low ice concentration and hence strong air-sea interaction. Polynyas are characterized by elevated sea ice production because sea ice is continuously produced and advected away by the wind. The continental shelf often gets deeper toward the grounding line of an ice shelf, allowing DSW to spread along the seafloor to the grounding line (Figure 4.2). Due to the pressure dependence of the freezing point, the DSW is warmer than the local freezing point and therefore melts the underside of the ice shelf. A buoyant mixture of DSW and fresh meltwater upwells and flows out of the cavity along the ice shelf base, sustaining an overturning circulation within the sub-ice-shelf cavity (Mode 1 in Figure 4.2). Where the temperature of the mixture of meltwater and DSW is less than the surface freezing point (i.e., "supercooled"), this water mass is called Ice Shelf Water (ISW). The formation of ISW by ocean-ice shelf interaction is generally a feature of cold cavity ice shelves. As the mixture of DSW and meltwater rises, it may reach a level where it is cooler than the in situ freezing point. This can result in formation of frazil ice crystals that may accrete to the base of the ice shelf, forming what is called

marine ice. Marine ice layers stabilize the ice shelf, protecting it from fracturing and melting (Khazendar et al., 2009; Kulessa et al., 2014). Recently, marine ice has been identified as an important source of iron (Herraiz-Borreguero et al., 2016b), a limiting nutrient essential for phytoplankton growth. Icebergs with a visible marine ice layer are often known as jade icebergs due to their green color.

Mode 2 circulation dominates in "warm cavity" ice shelves (Figure 4.2). At these ice shelves, relatively warm Circumpolar Deep Water (CDW) spreads from offshore across the continental shelf to the sub-ice-shelf cavities. Where CDW mixes with surrounding waters and cools as it crosses the continental shelf, the resulting water mass is called Modified CDW, or MCDW. CDW, which is the most voluminous and warmest mid-depth water mass found in the Southern Ocean (Worthington, 1981), is transported eastward around the continent in the ACC. The southern limit or "boundary" of this current (see Figure 4.1B) is located close to the West Antarctic coast in the Amundsen and Bellingshausen seas (Orsi et al., 1995). In this sector, the southern edge of the ACC reaches the shelf break and allows warm (up to 1°C–1.5°C) and relatively salty (34.5–34.7) CDW to reach the continental shelf (Figure 4.1B). DSW is not formed in the Amundsen and Bellingshausen seas, so the CDW fills the bottom layer and can reach the deepest regions of the ice shelf cavities and drive rapid basal melting. The most prominent example of a "warm cavity" ice shelf is Pine Island Glacier in West Antarctica, where inflow of CDW reaches the grounding line with temperatures in excess of 3°C above the local freezing point (Jenkins et al., 2010). In the Weddell and Ross Sea sectors, large clockwise gyres of relatively cold water isolate the continental margin from the warm waters of the ACC (Figure 4.1B), and the ice shelf cavities there are filled with DSW. East Antarctica was long thought to be similarly isolated from warm offshore waters because the axis of the ACC was far to the north. However, the southern boundary of the ACC approaches the East Antarctic coast between 60°E and 140°E (Figure 4.1B), providing a reservoir of ocean heat near the continental shelf break. Due to a lack of observations, it was not known whether warm offshore waters crossed the continental shelf and reached the ice shelf cavities in these locations. As discussed in the next section, recent measurements show that in some locations, relatively warm water does cross the shelf break to drive rapid basal melting, demonstrating that East Antarctica is more vulnerable to changes in ocean heat fluxes than previously thought.

Atmospheric heating during summer months leads to warming of the surface waters. Mode 3 is related to the transport of warm surface waters to the calving fronts of ice shelves by tides, eddies, Ekman transport, and ocean currents (Figure 4.2). There is usually less melt at an ice front than near

the grounding line due to the suppression of the freezing point with depth. However, in some cases where the grounding line is relatively shallow, basal melt rates driven by warm surface waters can rival those observed at the grounding line. Examples where Mode 3 plays a primary role are the Ronne-Filchner and Fimbul ice shelves in the Weddell Sea (Makinson and Nicholls, 1999; Joughin and Padman, 2003; Hattermann et al., 2012) and the Ross and McMurdo ice shelves in the Ross Sea (Arzeno et al., 2014; Stern et al., 2013).

4.4. Ocean-ice shelf interaction in East Antarctica

The ice shelves most susceptible to basal melting, and therefore the systems with the greatest potential to contribute to sea level rise, are those with deep grounding lines. Here, we focus on the three outlet glaciers and related ice shelves at the margins of the large marine-based sectors of the EAIS (Figure 4.1A). The Totten Glacier drains more ice from East Antarctica than any other glacier and forms the Totten Ice Shelf (TIS) where it reaches the sea. The Amery Ice Shelf (AIS) is fed by several glaciers, including Lambert Glacier, the largest glacier in the world, which drains about 16% of the area of East Antarctica (Allison, 1979). The Mertz Glacier is near Wilkes Basin, the largest marine-based drainage system in East Antarctica, and forms the Mertz Glacier Tongue (MGT) where it starts to float. Ice shelf systems all have different geographic and oceanographic settings; the three examples below illustrate the variety of ocean-ice shelf interactions in East Antarctica.

4.4.1. Totten Ice Shelf

The Totten Glacier on the Sabrina Coast is the major outlet of the Aurora Basin and drains a marine-based ice volume equivalent to 3.5 m of global sea level rise (Greenbaum et al., 2015). Strong retreat and mass loss of the Totten Glacier made substantial contributions to global sea level change during past warm periods in Earth's history such as the Pliocene, when global temperatures were comparable to those predicted for the end of this century and atmospheric CO_2 concentrations were similar to those of the present (Williams et al., 2010a; Pollard et al., 2015; Aitken et al., 2016). Future climate projections under continued high anthropogenic greenhouse emissions indicate mass loss from the Aurora Basin will contribute several meters to sea level rise in the coming centuries (Golledge et al., 2015; DeConto and Pollard, 2016). Recent glaciological observations reveal that during the last two decades, the Totten Glacier has been retreating, thinning, and losing mass (Li et al., 2015, 2016). The basal melt rate at the Totten Ice Shelf is 10–18 m yr^{-1} , the highest among the major ice shelves in East Antarctica and only exceeded by Pine Island and neighboring ice shelves

in the Amundsen–Bellingshausen seas (Depoorter et al., 2013; Rignot et al., 2013; Liu et al., 2015). However, no oceanographic measurements had been made near the front of TIS so it was not known whether ocean-ice shelf interaction was responsible for the recent changes in the glacier and ice shelf. Temperature profiles collected in 1996 and 2007 revealed the presence of relatively warm (0°C–0.5°C) MCDW near the seafloor on the outer continental shelf (Bindoff et al., 2000; Williams et al., 2011), but until recently, heavy sea ice had prohibited access to the calving front to confirm that warm water reached the ice shelf cavity.

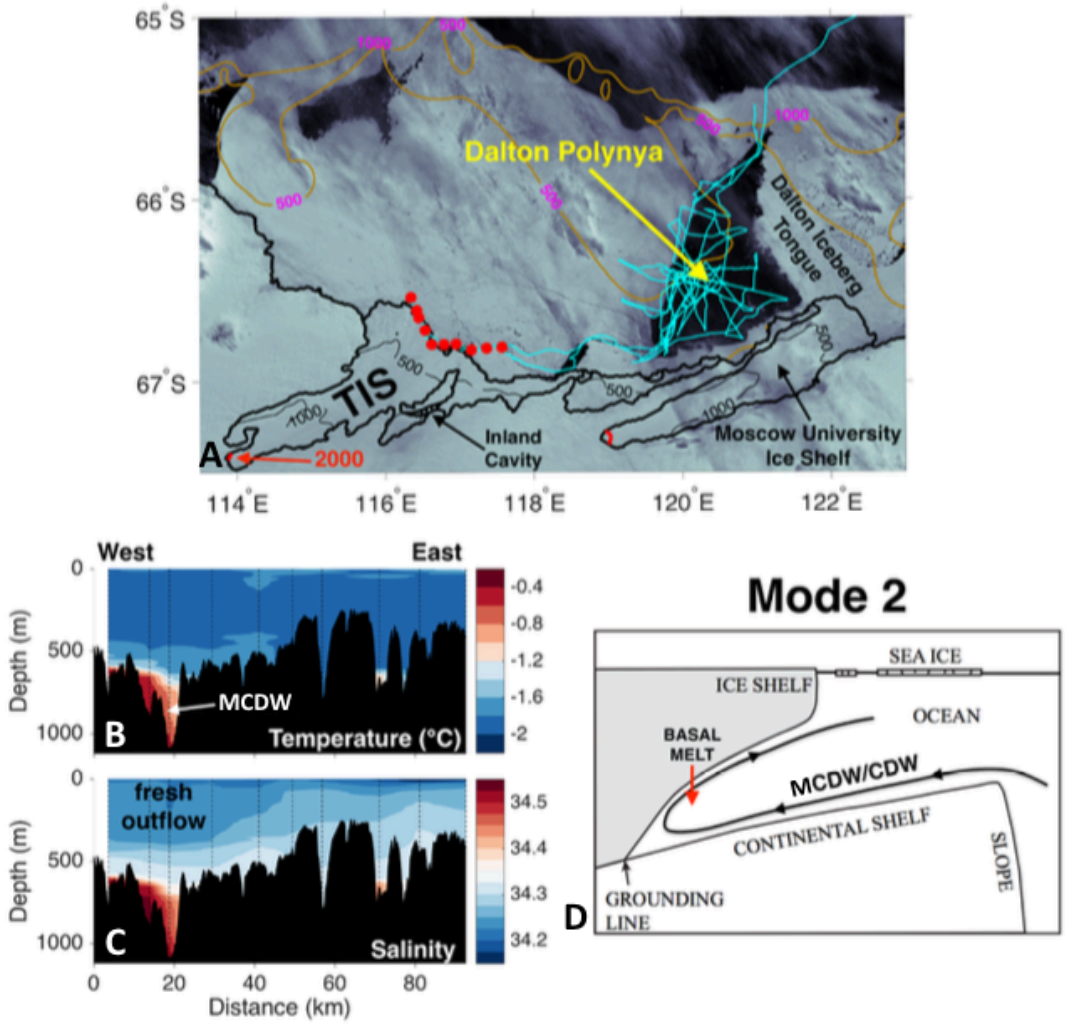

Figure 4.3. Totten Ice Shelf. (A) Satellite image of the Totten Ice Shelf (TIS) and surroundings on January 22, 2015 (Scambos et al., 1996). The bathymetry (Arndt et al., 2013) and the coastline (Fretwell et al., 2013) are shown by brown and black lines, respectively. The red dots mark the locations of the stations undertaken at the Totten calving front in summer 2015. The small dashed area indicates an inland cavity that connects the main trunk of TIS with the adjacent fringing ice shelf (Greenbaum et al., 2015). East of TIS is the Moscow University Ice Shelf where no data are available at the calving front. A series of grounded icebergs and fast ice (Dalton Iceberg Tongue) blocks inflow of sea ice from the east driven by westward coastal currents and allows the formation of the Dalton Polynya, east of TIS. (B) Vertical section of in situ temperature (°C) measurements along the calving front in 2015 (locations of stations shown by red dots in Figure 4.3A). (C) As in (B) for salinity. (D) Schematic showing that basal melting of TIS is dominated by Mode 2, where warm Modified Circumpolar Deep Water (MCDW) enters the sub-ice-shelf cavity to drive relatively rapid melt.

The Totten Ice Shelf calving front was finally reached in January 2015 by R/V *Aurora Australis*. Offshore winds opened a narrow and short-lived coastal lead that allowed the ship to occupy a section along the calving front of the glacier (Figure 4.3A). Measurements of water depth, temperature, salinity, and velocity were collected. A narrow 1100 m deep trough was found at the ice front, almost twice as deep as suggested by earlier measurements (Fretwell et al., 2013; Greenbaum et al., 2015). A thick layer of relatively warm MCDW (–0.4°C) was present at the bottom of the trough (Figure 4.3B; Rintoul et al., 2016; Silvano et al., 2017). If the warmest water observed at the calving front were to reach the grounding line at 2100 m depth, it would be more than 3°C above the local freezing point, approaching that observed near Pine Island Glacier (Jenkins et al., 2010).

Velocity measurements confirm that the warm water was flowing strongly into the cavity at the time of the section (Rintoul et al., 2016). The ocean heat flux into the cavity was consistent with that required to support the large multiyear mean basal melt rates inferred from independent glaciological data (Depoorter et al., 2013; Rignot et al., 2013; Liu et al., 2015), supporting the hypothesis that ocean heat flux drives rapid basal melting of the Totten Glacier and suggesting the snapshot obtained during the voyage was broadly representative. Water properties observed at the ice shelf calving front provide further evidence of active basal melting. Fresher water in the upper 500 m on the western side of the calving front (Figure 4.3C) reflects the outflow of a buoyant mixture of MCDW and glacial meltwater. Using the approach of Jenkins (1999), Silvano et al. (2017) recently used oxygen and salinity data to show that the water flowing out of the cavity contains up to 5 ml L^{-1} of glacial meltwater, about one-third of that observed at the front of Pine Island Glacier.

Oceanographic observations show the Totten Glacier is a "warm cavity" ice shelf, similar to the rapidly melting ice shelves in the Bellingshausen and Amundsen seas in West Antarctica (Figure 4.3D). No DSW has been observed on the Totten continental shelf in summer or winter (Williams et al., 2011), consistent with observations of weak sea ice formation in Dalton Polynya east of the TIS (see Figure 4.3A; Tamura et al., 2016). As a consequence, warm MCDW, the densest water on the shelf, has access to the ice shelf cavity, as found in the Amundsen and Bellingshausen seas, although waters in the bottom layer are about 1°C cooler near Totten Glacier compared, for example, to Pine Island Glacier. The water properties confirm substantial meltwater in the outflow from the Totten cavity. As large basal melt rates have been observed since at least the early 2000s (Rignot and Jacobs, 2002; Depoorter et al., 2013; Liu et al., 2015; Rignot et al., 2013), it is likely

that MCDW has been entering the cavity for at least this time period.

4.4.2. Mertz Glacier Tongue

The Wilkes Basin contains a volume of marine-based ice equivalent to 3–4 m of global sea level rise (Mengel and Levermann, 2014). Like the Totten Glacier in the Aurora Basin, the Wilkes Basin ice sheet has retreated and contributed to sea level rise during past warm periods (Williams et al., 2010a; Cook et al., 2013; Patterson et al., 2014). Also like the Totten, models suggest that continued high emissions of greenhouse gases could drive mass loss from the Wilkes Basin, resulting in several meters of sea level rise in coming centuries (Mengel and Levermann, 2014; Golledge et al., 2015; DeConto and Pollard, 2016). The two main ice streams draining the Wilkes Basin, Cook and Ninnis glaciers (see Figure 4.1A for the location of the Cook and Ninnis ice shelves), appear to be largely in balance at the present time based on satellite measurements of gravity and surface elevation (e.g., Velicogna and Wahr, 2013). The potential for the ocean to destabilize the ice sheet in this sector remains poorly understood. Both Cook and Ninnis glaciers are almost inaccessible due to heavy sea ice conditions, and no measurements have been made near the calving fronts of these glaciers. The Wilkes Land Expedition on USCGC *Polar Star* in 1985 showed that water as warm as −1.2°C crossed the shelf break between 150°E and 155°E, but the warm intrusions did not extend more than halfway across the continental shelf (Foster, 1995). Measurements made by the Russian R/V *Ob* in the 1950s about 120 km north of the Ninnis ice front showed no evidence of warm MCDW (Gordon and Tchernia, 1972).

The Mertz Glacier lies about 100 km west of the Ninnis Glacier. While the Mertz Glacier does not drain the main Wilkes Basin, it is well studied in comparison to Ninnis and Cook glaciers, and its proximity makes it a useful analogue for the oceanographic conditions typical of the area's coast. Prior to a major calving event in 2010, the Mertz Glacier Tongue extended about 120 km northward from the coast (Figure 4.4A, cyan line) and blocked the general east-to-west movement of sea ice along the continental shelf. The combination of strong katabatic winds and restricted inflow of sea ice resulted in formation of a strong and active polynya to the west of the MGT as well as others in coastal embayments further west. Over the period 1992–2013, the Mertz Polynya was the fourth most active Antarctic polynya in terms of sea ice production (Tamura et al., 2016). Formation and export of large volumes of sea ice results in the production of DSW, which flows down the slope and mixes with surrounding waters to form the local variety of Antarctic Bottom Water (Gordon and Tchernia, 1972; Rintoul, 1998). Calving of the glacier tongue has reduced the polynya's sea ice production and hence the density of shelf water and bottom water formed in the region (Shadwick

et al., 2013; Nihashi and Ohshima, 2015).

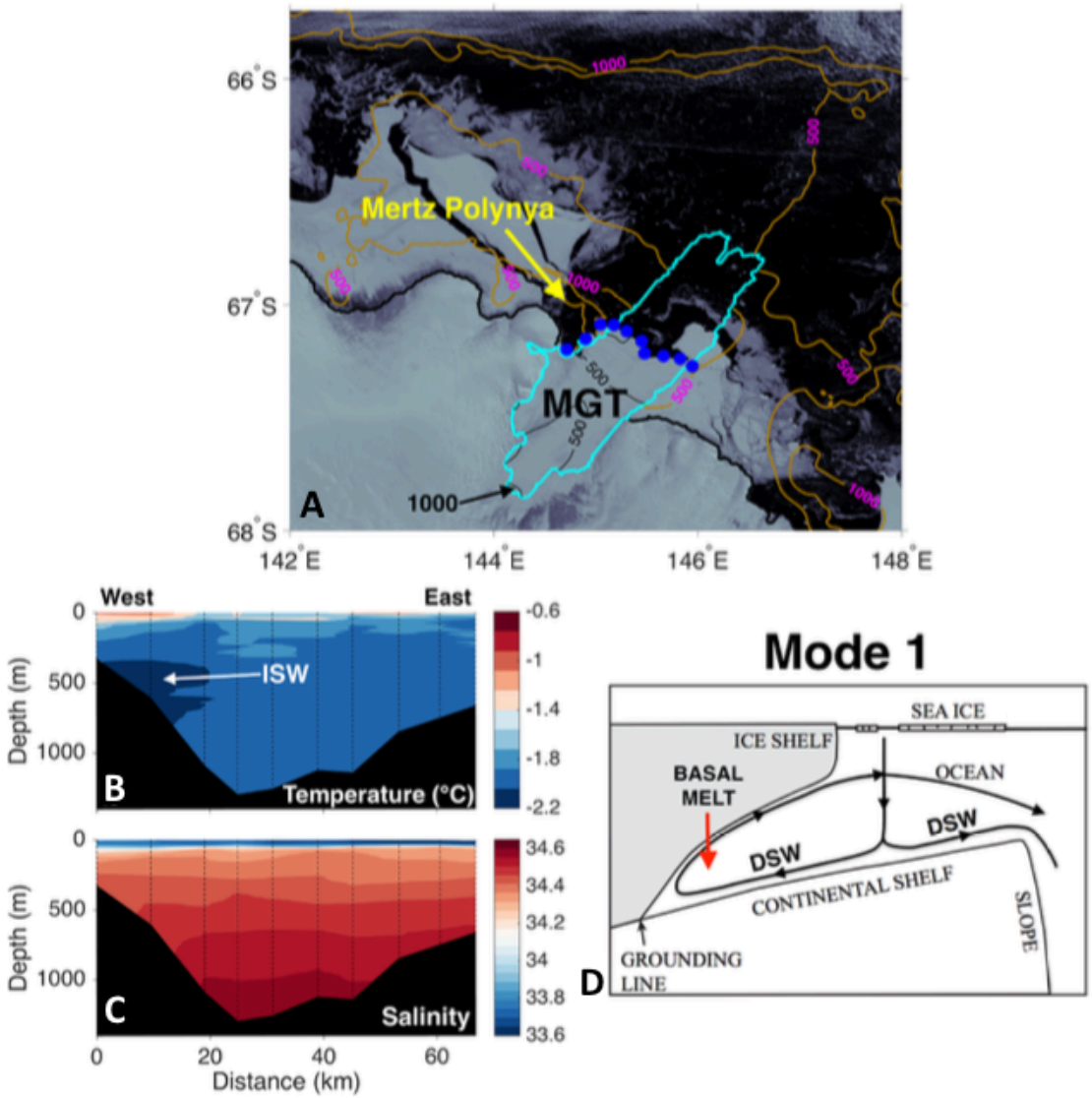

Figure 4.4. Mertz Glacier Tongue (MGT). (A) Satellite image of the MGT and surroundings on December 2, 2014 (Scambos et al., 1996). The bathymetry (Arndt et al., 2013) and coastline (Fretwell et al., 2013) are shown by brown and black lines, respectively. The blue dots represent the locations of stations undertaken along the calving front in summer 2015, and the cyan line indicates the ice shelf boundary prior to a major calving event in 2010. (B) Vertical section of in situ temperature (°C) recorded at the calving front in 2015 (blue dots in Figure 4.4A). ISW = Ice Shelf Water. (C) As in (B) for salinity. (D) Schematic showing that basal melting of the MGT is dominated by Mode 1, where cold Dense Shelf Water (DSW) formed in the Mertz Polynya flows into the sub-ice-shelf cavity and drives melt at the grounding line.

Active formation of DSW in the Mertz Polynya has a significant impact on ocean-ice shelf interaction, as well as on bottom water formation. Figure 4.4B shows temperature along the MGT front in January 2015 (i.e., post-calving). The Mertz is primarily a cold cavity ice shelf, like those found at other locations around the Antarctic margin where polynyas produce large volumes of DSW. The DSW, with relatively high salinity and temperature close to the surface freezing point, enters the cavity and flows downslope to the grounding line (Figure 4.4C). At the 1200 m deep grounding line of the Mertz Glacier, water at the surface freezing point is about 0.9°C warmer than

the local freezing point and drives basal melting. The mixture of inflowing DSW and glacial meltwater forms Ice Shelf Water (ISW), with the coldest and strongest outflow of ISW found on the western side of the ice front (Figure 4.4B). While the presence of ISW with temperatures cooler than −2°C confirms that glacial melting occurs at depth and the meltwater exits the cavity, the relatively weak thermal forcing is consistent with low estimates of basal melting (1–2 m yr^{-1}) inferred from glaciological measurements (Depoorter et al., 2013; Rignot et al., 2013; Liu et al., 2015). No warm MCDW was observed at the ice front during the 2015 voyage (Figure 4.4B). However, MCDW has been observed over the continental shelf in this region, with highly modified CDW extending as far south as the offshore end of the MGT prior to calving (Rintoul, 1998; Williams et al., 2010b; Lacarra et al., 2011; Snow et al., 2016). The MCDW reaching the continental shelf is lighter than the DSW and is found at mid-depth there, in contrast to the Totten continental shelf where MCDW is the densest and deepest water mass present. In this way, the Mertz Polynya conditions the ocean stratification and the interaction of the ocean with the ice shelf, as also seen in modeling studies (Cougnon et al., 2013). Calving of the MGT has reduced sea ice formation and DSW formation in Mertz Polynya, and may therefore have altered basal melt rates, but no studies have yet been published quantifying the impact of the calving event on ocean-ice shelf interaction.

4.4.3. Amery Ice Shelf

The Lambert Glacier system is the major outlet of the MacRobertson Land sector, draining 16% of the area of East Antarctica (Fricker et al., 2000). It contains an ice volume equivalent to 4–6 m of sea level. Lambert Glacier and several tributary glaciers supply the Amery Ice Shelf, the third largest embayed ice shelf in Antarctica, with an area of 62000 km^2. The deepest part of the southern grounding line is at 2500 m (Fricker et al., 2001). Craven et al. (2009) estimated that about 80% of the continental ice entering the AIS is lost to basal melting (~43.2 Gt yr^{-1}). A layer of marine ice up to 190 m thick on the northwestern side of the AIS base constitutes as much as 9% of the ice shelf volume (Fricker et al., 2001) and is thought to stabilize the AIS (Khazendar et al., 2009; Kulessa et al., 2014). Like the Totten Glacier and the glaciers draining the Wilkes Basin, evidence from paleoclimate studies (Passchier, 2011) and simulations of the future response of the ice sheet (Golledge et al., 2015; DeConto and Pollard, 2016) suggest the Amery Ice Shelf is also dynamic.

The Amery Ice Shelf-Ocean Research (AMISOR) project measured ocean properties beneath the ice shelf continuously from 2001 to 2012. Outside the ice shelf cavity, a few oceanographic expeditions were conducted in the 1980s and in 2001 and 2002. However, not until the appearance

of “seal oceanographers” in 2010 was it possible to draw a picture of the spatial and seasonal variability of Prydz Bay water masses (Herraiz-Borreguero et al., 2015, 2016a; Williams et al., 2016).

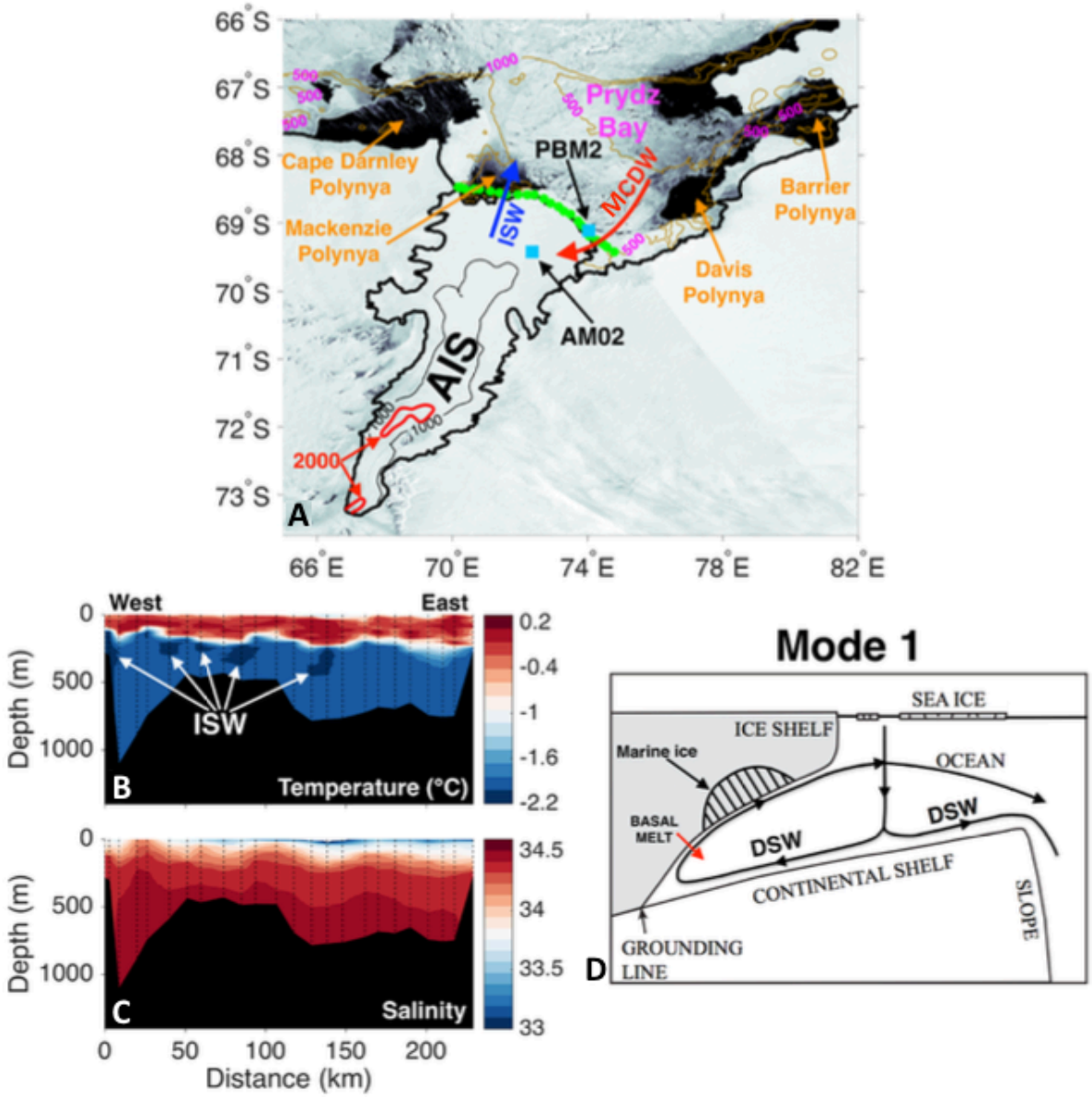

Figure 4.5. Amery Ice Shelf. (A) Satellite image (NASA Worldview data, NASA EOSDIS, https://earthdata.nasa.gov/labs/worldview) of the Amery Ice Shelf (AIS) and surroundings on October 30, 2014, when the Cape Darnley, Mackenzie, Davis, and Barrier polynyas were clearly visible. Red and blue arrows depict the inflow of MCDW in winter in the east and the outflow of ISW in the west. The bathymetry (Arndt et al., 2013) and coastline (Fretwell et al., 2013) are shown in brown and black lines, respectively. The light blue squares show the location of one borehole site, AM01, and one Australian mooring, PBM2, deployed 2001–2002. The green dots represent the locations of stations undertaken along the calving front in summer 2001. (B) Vertical section of in situ temperature (°C) recorded at the calving front in 2001 (green dots in Figure 4.5A). (C) As (B) for salinity. (D) Schematic showing that Mode 1 dominates basal melting at the AIS, driven by cold DSW formed in the Mackenzie, Davis, and Barrier polynyas.

Both DSW and MCDW drive basal melting beneath the AIS (Herraiz-Borreguero et al., 2015). Cold and salty DSW occupies the deepest part of the water column in the bay and near the AIS front (Figures 4.5B and 4.5C). This DSW is created during active sea ice formation at three polynyas—Barrier, Davis, and Mackenzie (Williams et al., 2016; Figure 4.5A)—and enters the AIS cavity (Herraiz-Borreguero et al., 2013, 2016a). When DSW reaches the deep grounding line where it is ~2°C above the in situ freezing point, it drives rapid basal melting (up to 25 m yr^{-1} near the grounding line; Wen et al., 2010). The total basal melt of the AIS is 33.5 ± 24.4 Gt yr^{-1} (area-averaged basal melt rate of 0.6 ± 0.4 m yr^{-1}). ISW formed by mixing of glacial meltwater with DSW rises along the base of the ice shelf and freezes to form frazil ice crystals that accrete to the ice shelf base to form the thick layer of marine ice found on the western side of the cavity (Fricker et al., 2001), with most the marine ice formed in winter (Herraiz-Borreguero et al., 2013). The lower part of the marine ice layer is hydrologically connected to the ocean below (Craven et al., 2009), and so potentially subject to rapid melting. The circulation in the AIS cavity is dominated by this Mode 1 circulation, with inflow of DSW and outflow of ISW (Figure 4.5D).

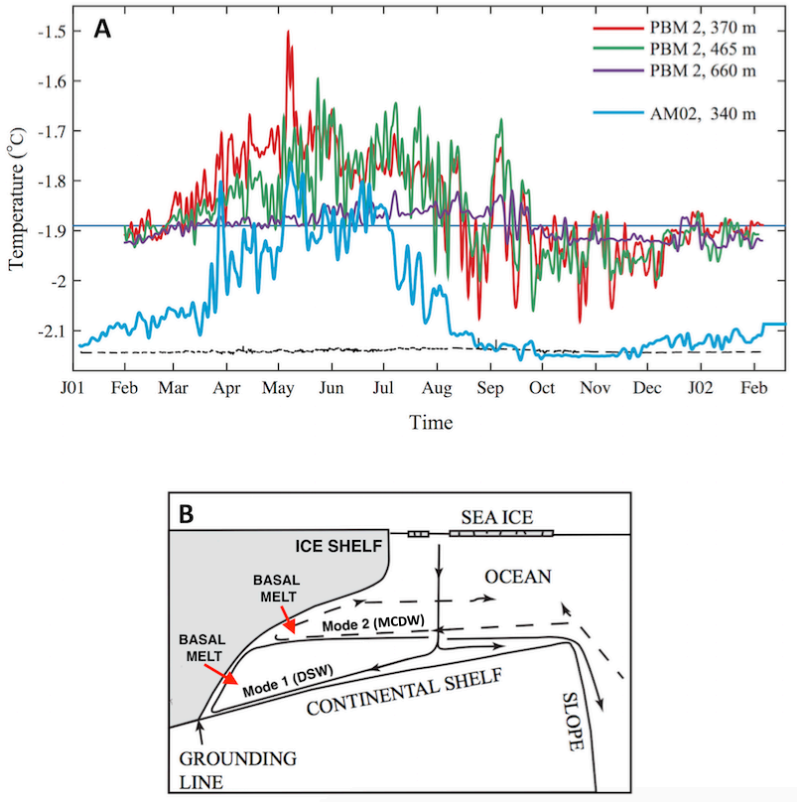

Figure 4.6. Temporal variability at the Amery Ice Shelf. (A) In situ temperature (°C) between January 2001 and February 2002 at the eastern calving front of the Amery Ice Shelf (PBM2) and in the eastern sub-ice-shelf cavity (AM02). See Figure 4.5A for the locations of PBM2 and AM02. The 40 h Butterworth filtered time series are shown. From April to August, relatively warm MCDW (green and red lines) reaches the eastern Amery Ice Shelf to drive basal melting at mid-depths. Cold DSW is found year-round in the bottom layer (purple line) and drives basal melting near the grounding line. (B) Schematic showing that Mode 1 (cold DSW) dominates basal melting at the Amery Ice Shelf near the grounding line, while Mode 2 contributes to basal melting at mid-depths when relatively warm MCDW enters the eastern cavity in winter.

However, inflow of MCDW on the eastern side of the AIS cavity drives basal melting during austral winter (Herraiz-Borreguero et al., 2015). CDW upwells into Prydz Bay where it cools very rapidly and deepens on its way to the AIS (Herraiz-Borreguero et al., 2015). MCDW occupies the eastern flank of Prydz Bay during summer (Herraiz- Borreguero et al., 2015; Williams et al., 2016) and is not observed at the ice-shelf front until April (Figure 4.6A; Herraiz-Borreguero et al., 2015, 2016a). Very cold MCDW (−1.7°C) is observed at borehole AM02 (~80 km from the ice shelf front) in mid-winter (Figure 4.6A), causing up to 2 ± 0.5 m yr^{-1} (23.9 ± 6.5 Gt yr^{-1}) of basal melting in a limited area of the northeastern flank of the ice shelf base (Herraiz-Borreguero et al., 2015). The interaction of the MCDW with the AIS also results in the formation of a distinct variety of ISW. This "warm" circulation is characteristic of Mode 2 and occurs in conjunction with Mode 1 circulation (Figure 4.6B).

Interaction of the ocean with the Amery Ice Shelf likely influences formation of Antarctic Bottom Water (AABW). Recent studies show how ISW controls the formation rate and thermohaline properties of DSW in Prydz Bay (Herraiz-Borreguero et al., 2016a; Williams et al., 2016). Prydz Bay DSW has, in turn, been linked to the formation and interannual variability of AABW formed at Cape Darnley, a persistent polynya immediately west of Prydz Bay (Figure 4.5A; Couldrey et al., 2013; Ohshima et al., 2013; Williams et al., 2016).

4.5. Varieties of ocean-ice shelf interaction in East Antarctica

The three ice shelves discussed above illustrate the different mechanisms driving basal melting in East Antarctica. The basal melt rate is strongly influenced by the water properties and stratification near the front of the ice shelf, which in turn are influenced by a number of processes, including sea ice formation and melt, coastal circulation, winds, intrusions of offshore waters, and freshwater input from ice shelf basal melt. The water properties and the stratification where water flows into the cavities of the Amery, Totten, and Mertz ice shelves are shown in Figure 4.7; a profile from the Pine Island Glacier calving front is included to provide a comparison to West Antarctica. Amery and Mertz ice shelves are similar in many ways. Both are primarily cold cavity ice shelves dominated by Mode 1 circulation. Active polynyas produce large volumes of DSW, which enters their cavities to drive basal melting. The mixture of cold DSW with glacial meltwater at depth produces ISW. More importantly for ocean-ice shelf interaction, the presence of DSW restricts intrusions of warmer and lighter MCDW to mid-depth and prevents the warm water from reaching the grounding lines of Amery and Mertz ice shelves. The inflow of MCDW sets up a secondary

Mode 2 circulation during winter, and it makes a relatively small contribution to basal melting of the Amery Ice Shelf when compared to Totten and Pine Island glaciers. There are also some clear differences between the Amery and the Mertz. The grounding line of Amery Ice Shelf is much deeper than that of Mertz, resulting in stronger thermal forcing and melt at the grounding line. Marine ice is widespread on the northwestern underside of the large Amery Ice Shelf. The Mertz Polynya is more active than the polynyas adjacent to the Amery (Tamura et al., 2016), and ISW is less widespread at the Mertz. As a result, the Mertz region produces saltier (Figure 4.7B) and denser shelf water that contributes directly to AABW formation, while the fresher and lighter DSW from the Amery region contributes to AABW formation at Cape Darnley Polynya.

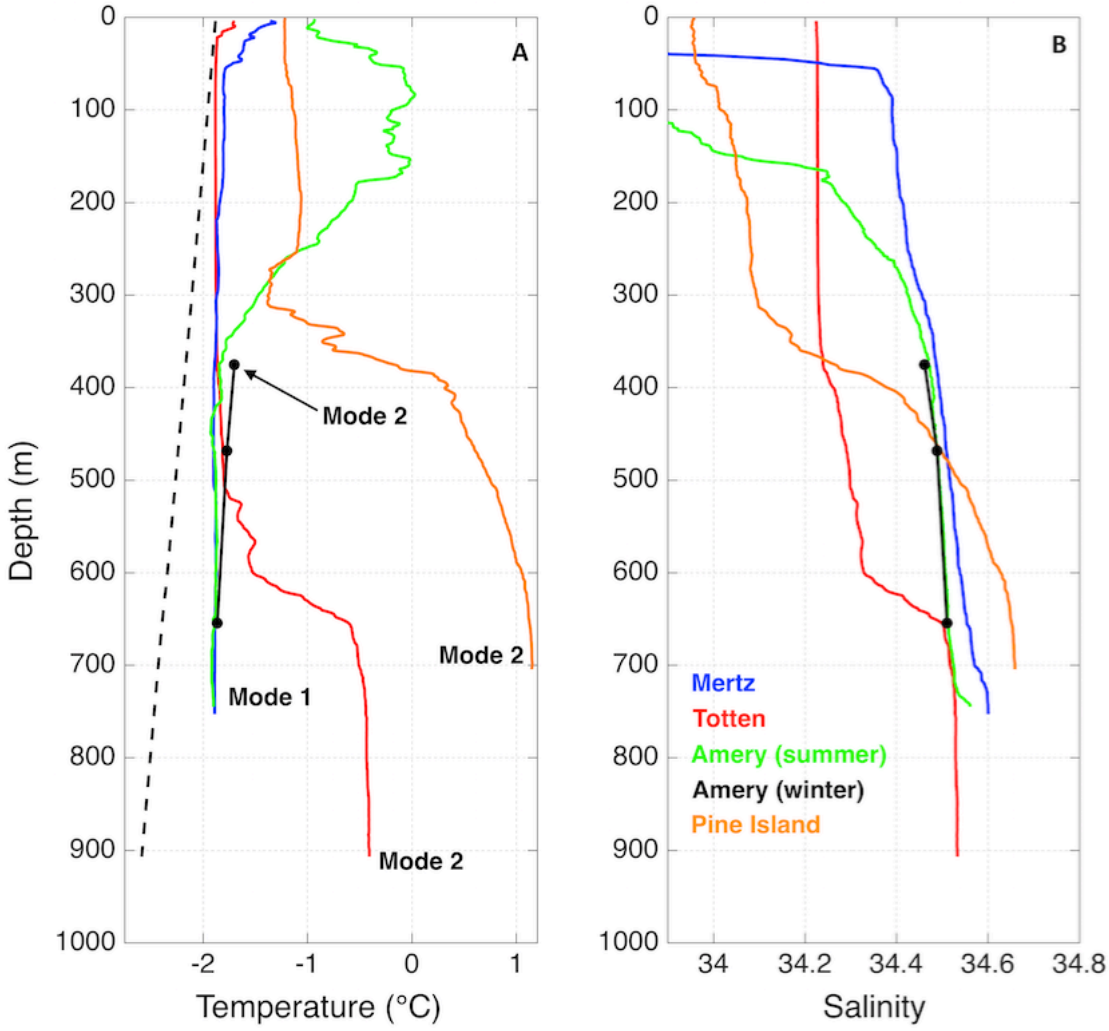

Figure 4.7. Water properties of the strongest inflow to ice-shelf cavities in East and West Antarctica. (A) In situ temperature (°C) versus depth (m) of individual profiles from Figures 4.3, 4.4, and 4.5 representative of summer ocean stratification near the calving fronts of Totten Glacier (red), Mertz Glacier (blue), and Amery Ice Shelf (green). Mean winter temperature in 2001 measured by a mooring at the Amery ice front (PBM2; see Figure 4.5A) is shown by the black line (instruments at 370, 465, and 660 m depths). For comparison, a summer profile collected in 2009 near Pine Island Glacier is included in orange (Jacobs et al., 2011). The black dotted line is the local freezing temperature, which decreases with depth. (B) As in (A) for salinity.

The water properties and stratification at the Totten Glacier are very different from those observed at the Amery and Mertz (Figure 4.7). The relatively weak Dalton Polynya does not produce enough brine to convert the fresh surface waters on the Totten continental shelf into DSW. In the absence of DSW, MCDW occupies the deepest part of the water column and has access to the Totten Ice Shelf cavity. The warm cavity Totten Ice Shelf therefore experiences high basal melt rates driven by the inflow of MCDW (i.e., Mode 2). The outflow from the Totten cavity is relatively warm and low in oxygen compared to the outflow from Amery and Mertz, reflecting the mixture of glacial meltwater with warm MCDW rather than cold DSW (Silvano et al., 2017). These characteristics are similar to, but not as extreme as, those observed at the front of Pine Island Glacier, where warm ocean waters reach the grounding line and drive rapid melt (Jenkins et al., 2010).

Comparison of the four ice shelves illustrates the strong influence of stratification on ocean-ice shelf interaction. The stratification, in turn, is strongly influenced by polynya dynamics. Where active polynyas produce DSW, access of warm water to the ice shelf cavity is restricted and area-averaged basal melt rates are low. Where DSW is not formed, because sea ice production is low and/or stratification is strong, MCDW that crosses the continental shelf can access the ice shelf cavity and area-averaged basal melt rates are high. Ocean temperatures are, of course, not the only factors affecting basal melt rates. For a given ocean temperature, melting will be more rapid at deeper grounding lines due to the pressure dependence of the freezing point. The melt rate also depends on a number of other factors, including cavity geometry and the surface characteristics of the underside of the ice shelf. Ocean heat flux to ice shelf cavities, and hence basal melting, can also vary in time in response to atmospheric variability (Dutrieux et al., 2014) and changes in the shape of the ice shelf cavity (Jacobs et al., 2011). Though most oceanographic observations have been made in summer, the winter data that are available from Amery Ice Shelf show that seasonal evolution of water properties and circulation can influence ocean-ice shelf interaction and basal melt rates (Herraiz-Borreguero et al., 2015), highlighting the need for year-round observations near ice-shelf calving fronts.

The similarities and differences among ice shelves can also be illustrated by comparing total and area-averaged basal melt rates inferred from glaciological measurements (Table 4.1). The warm cavity ice shelves in West Antarctica have high basal melt rates, both in total and on an area-averaged basis. (These ice shelves also show the largest acceleration in the rate of volume loss; Paolo et al., 2015). The cold cavity ice shelves in East Antarctica (e.g., Amery and Mertz) have relatively low area-averaged melt rates. Totten, in contrast, has the largest area-averaged basal melt

rate of all East Antarctic ice shelves (for ice shelves larger than 1000 km^2). The nearby Moscow University Ice Shelf also has a relatively large area-averaged basal melt rate compared to other East Antarctic ice shelves. Amery and Shackleton have relatively low rates of melt on an area-averaged basis, but lose substantial mass to basal melting. The Shackleton Ice Shelf system is important because it drains Denman Glacier, and deep connections between Denman Glacier and Aurora Basin make this glacier potentially susceptible to marine ice sheet instability (Roberts et al., 2011). However, lack of oceanographic data prevents an assessment of the susceptibility of this part of the EAIS to ocean-driven ice loss.

Table 4.1: Basal melt rates at selected West and East Antarctic ice shelves. Total basal melt (Gt yr^{-1}) and area-averaged basal melt (m yr^{-1}) are shown for each ice shelf. Data from Rignot et al. (2013).

West Antarctica			**East Antarctica**		
	Total basal melt (Gt yr^{-1})	Area-averaged basal melt (m yr^{-1})		Total basal melt (Gt yr^{-1})	Area-averaged basal melt (m yr^{-1})
Pine Island	101.2±8	16.2±1	**Amery**	35.5±23	0.6±0.4
Thwaites	97.5±7	17.7±1	**West**	27.2±10	1.7±0.7
Crosson	38.5±4	11.9±1	**Shackleton**	72.6±15	2.8±0.6
Dotson	45.2±4	7.8±0.6	**Totten**	63.2±4	10.5±0.7
Getz	144.9±14	4.3±0.4	**Moscow Univ.**	27.4±4	4.7±0.8
			Mertz	7.9±3	1.4±0.6

4.6. Conclusions

Growing evidence from studies of past sea level, oceanographic and glaciological observations, and simulations of ice sheet responses to high emissions of greenhouse gases suggest the East Antarctic Ice Sheet is more dynamic than once thought. In West Antarctica, there is evidence that ocean-driven basal melting is the primary control on mass loss from the floating ice shelves and the grounded ice sheets they buttress (Pritchard et al., 2012). The lack of oceanographic observations in East Antarctica has prevented an assessment of the extent to which ocean heat flux influences the East Antarctic ice shelves. New measurements show that warm water enters the Totten Ice Shelf cavity (Rintoul et al., 2016) and drives rapid basal melting (Depoorter et al., 2013; Rignot et al., 2013; Liu et al., 2015). In this sense, the Totten system behaves in a similar way to the rapidly melting West Antarctic ice shelves that have received much more attention. Simulations of future change in the Antarctic Ice Sheet show that all three of the East Antarctic marine-based ice sheets discussed here lose mass and contribute to sea level rise on time scales of a few centuries (Golledge

et al., 2015; DeConto and Pollard, 2016). Estimates of future sea level rise need to take the potential contribution from a dynamic EAIS into account.

Further work is needed to improve our understanding of the vulnerability of the East Antarctic Ice Sheet. We show here that warm water approaches the margin of Antarctica along much of the East Antarctic coastline, but that delivery of ocean heat to ice shelf cavities varies strongly from region to region, even for ice shelves that are relatively close together. This highlights the need for future work to more fully understand the physical processes regulating the transport of heat from the open ocean to an ice shelf cavity, and how these processes vary from region to region. In particular, very few oceanographic measurements have been made near Ninnis and Cook glaciers, the primary ice streams draining the large marine-based Wilkes Basin ice sheet, or near the Denman Glacier, which drains a portion of the Aurora Basin and supplies the Shackleton Ice Shelf. How ocean heat flux to ice-shelf cavities varies in time is even less well understood. Very few time-series measurements have been made near East Antarctic ice shelves (the mooring and borehole work at the Amery Ice Shelf is a notable exception). Glaciological measurements indicate the grounded portion of Totten Glacier has thinned (Harig and Simons, 2015) and retreated (Li et al., 2015) in recent decades and that the ice shelf volume is either decreasing (Liu et al., 2015) or highly variable in time, with no significant trend (Paolo et al., 2015). No oceanographic data exist to test the hypothesis that changes in ocean heat transport have driven the recent changes observed in the floating and grounded portions of the Totten Glacier. Observing systems capable of tracking variations in ocean temperature and circulation over time near Antarctic ice shelves are urgently needed to improve our understanding of the susceptibility of the ice sheet to ocean change.

Chapter 5

Freshening by glacial meltwater enhances melting of ice shelves and reduces formation of Antarctic Bottom Water

This chapter has been published:
Silvano, A., S. R. Rintoul, B. Peña-Molino, W. R. Hobbs, E. van Wijk, S. Aoki, T. Tamura, and G. D. Williams (2018), Freshening by glacial meltwater enhances melting of ice shelves and reduces formation of Antarctic Bottom Water, *Sci. Adv.*, *4*, eaap9467, doi:10.1126/sciadv.aap9467.

5.1. Abstract

Strong heat loss and brine release during sea ice formation in coastal polynyas act to cool and salinify waters on the Antarctic continental shelf. Polynya activity thus both limits the ocean heat flux to the Antarctic Ice Sheet and promotes formation of Dense Shelf Water (DSW), the precursor to Antarctic Bottom Water. However, despite the presence of strong polynyas, DSW is not formed on the Sabrina Coast in East Antarctica and in the Amundsen Sea in West Antarctica. Using a simple ocean model driven by observed forcing, we show that freshwater input from basal melt of ice shelves partially offsets the salt flux by sea ice formation in polynyas found in both regions, preventing full-depth convection and formation of DSW. In the absence of deep convection, warm water that reaches the continental shelf in the bottom layer does not lose much heat to the atmosphere and is thus available to drive the rapid basal melt observed at the Totten Ice Shelf on the Sabrina Coast and at the Dotson and Getz ice shelves in the Amundsen Sea. Our results suggest that increased glacial meltwater input in a warming climate will both reduce Antarctic Bottom Water formation and trigger increased mass loss from the Antarctic Ice Sheet, with consequences for the global overturning circulation and sea level rise.

5.2. Introduction

The Antarctic Ice Sheet is losing mass at an increasing rate (Rignot et al., 2011a; Velicogna et al., 2014), with the largest loss observed in glaciers that flow into the Amundsen Sea in West Antarctica (Sutterley et al., 2014). In East Antarctica, ice loss has been reported on the Sabrina Coast (Velicogna et al., 2014; Li et al., 2016), where the Totten Glacier is thinning and its grounding line is retreating (Li et al., 2015). On both the Amundsen Sea and Sabrina Coast

continental shelves, warm (> 0°C) and saline (salinity > 34.7 g kg^{-1}) Modified Circumpolar Deep Water (MCDW) spreads poleward in the bottom layer in deep troughs (Jacobs et al., 2012; Silvano et al., 2017; Nitsche et al., 2017). Where MCDW reaches ice shelf cavities, it drives rapid basal melt, as observed at the Totten and Moscow University ice shelves on the Sabrina Coast (Silvano et al., 2017; Rintoul et al., 2016) and Pine Island, Thwaites, Dotson, and Getz ice shelves in the Amundsen Sea (Jacobs et al., 2011; Biddle et al., 2017; Miles et al., 2016; Jacobs et al., 2013). Rapid basal melt of these ice shelves is believed to be a major driver of the mass loss of the glaciers that they buttress (Li et al., 2016; Khazendar et al., 2013; Pritchard et al., 2012; Khazendar et al., 2016).

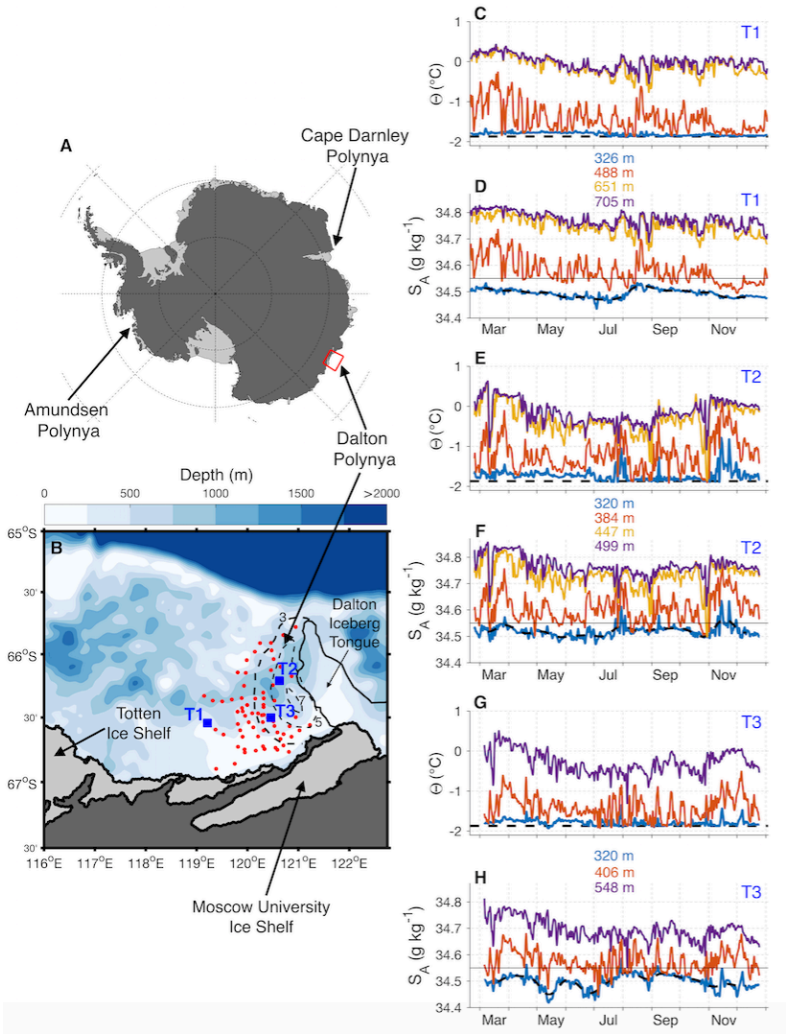

Figure 5.1. Water properties on the Sabrina Coast. Map (B) of the Sabrina Coast (red rectangle in (A)) with bathymetry and coastline overlaid (Fretwell et al., 2013). Oceanographic stations where conductivity-temperature-depth (CTD) and oxygen isotope measurements have been collected are shown in red, whereas moorings T1, T2, and T3 are shown in blue. Black dashed lines are contours of the 2014 annual sea ice production (in meters) in the Dalton Polynya (Tamura et al., 2016). Time series of conservative temperature Θ and absolute salinity S_A, low-pass filtered using a fourth-order 40-hour Butterworth filter, are shown for T1 (C and D), T2 (E and F), and T3 (G and H) with indicated depths. A 30-day low-pass filter is shown in black dashed lines for salinity time series at the shallowest instrument of each mooring, whereas the thin black lines represent S_A = 34.55 g kg^{-1} (that is, upper salinity limit for WW). The black dashed lines in (C), (E), and (G) are the surface freezing temperatures for a salinity of 34.4 g kg^{-1}.

Most of the continental shelf around Antarctica is characterized by cold waters formed in coastal polynyas and, consequently, by low rates of ice shelf basal melt. Coastal polynyas are regions of enhanced sea ice formation, where water masses are modified by atmospheric cooling, wind stress, and salt flux associated with brine rejection. Strong buoyancy loss in the most active polynyas is sufficient to overturn the entire water column to produce cold (approximately at the surface freezing point) and saline (> 34.6 g kg^{-1}) Dense Shelf Water (DSW; also referred to as High Salinity Shelf Water). Examples of strong polynyas are found in the Ross Sea (Orsi and Wiederwohl, 2009), Weddell Sea (Nicholls et al., 2009), Adélie Coast (Rintoul, 1998), and Cape Darnley/Prydz Bay region (Ohshima et al., 2013; Williams et al., 2016). DSW formed in these regions is exported to the continental slope, where it mixes with ambient water to form Antarctic Bottom Water, a key component of the global overturning circulation and abyssal ventilation (Orsi et al., 1999; Johnson, 2008).

However, not all polynyas produce DSW. The Dalton Polynya on the Sabrina Coast and the Amundsen Polynya in the Amundsen Sea (see location in Figure 5.1A) are among the most active of Antarctic polynyas in terms of the volume of sea ice formed each year (~50 and 120 km^3, respectively; Tamura et al., 2016). However, the convection driven by winter buoyancy loss does not reach the bottom, and no DSW is formed. The water column remains stratified year-round, with relatively fresh (< 34.55 g kg^{-1}) Winter Water (WW) overlying the saltier MCDW (Silvano et al., 2017; Randall-Goodwin et al., 2015). The absence of full-depth convection and DSW formation allows warm MCDW to spread across the continental shelf to the ice shelf cavities, where it drives the rapid basal melt observed on the Sabrina Coast and Amundsen Sea. Given that ice shelves in these regions buttress a volume of marine-based ice equivalent to more than 4 m of global sea level rise (Greenbaum et al., 2015; Mouginot et al., 2014), it is essential to understand the processes that regulate their basal melt.

Earlier studies have shown that local and remote atmospheric forcing can drive variability in basal melt of ice shelves on the Sabrina Coast and in the Amundsen Sea by influencing the MCDW properties and depth of the WW-MCDW interface on the continental shelf (Khazendar et al., 2013; Dutrieux et al., 2014; St-Laurent et al., 2015; Gwyther et al., 2014; Greene et al., 2017). However, it is not yet understood why active polynyas in these regions do not form DSW. Here, we use observations and a simple model to investigate the links between sea ice formation in coastal polynyas, DSW formation, and basal melt of ice shelves. We find that increased stratification induced by input of glacial meltwater inhibits formation of DSW and allows warm MCDW to reach

ice shelf cavities where it drives basal melt.

5.3. Results

5.3.1. Seasonal changes in continental shelf waters on the Sabrina Coast

Three moorings deployed on the continental shelf measured the evolution of water mass properties and stratification on the Sabrina Coast from February to December 2014 (see Figure 5.1 and Materials and methods). Two moorings (T2 and T3) were located in the Dalton Polynya, and a third mooring (T1) was located to the west of the polynya, closer to the Totten Ice Shelf. The water column remains stratified year-round at all three locations, and no DSW is present. MCDW is found in the bottom layer throughout the year at each mooring location, with absolute salinity ranging between ~34.65 and ~34.8 g kg^{-1} and conservative temperature ranging between ~–0.5° and ~0.5°C (Figures 5.1C-5.1H). Because MCDW does not interact with the atmosphere, temporal variability in this water mass is associated with offshore variability and cross-shelf exchange (Greene et al., 2017).

Cold (approximately at the surface freezing point), fresh (~34.5 g kg^{-1}) WW overlies the MCDW layer. At T1, the shallowest instrument at 326-m depth remains in the WW layer and provides a record of the seasonal evolution of WW properties. The salinity of the WW increases in July and August, reflecting the salinification and deepening of the winter mixed layer driven by brine released during sea ice formation. More surprising, however, is the steady freshening of the WW layer between February and July and between August and December. An increase in WW salinity in winter and freshening in other seasons is also discernible at the shallowest instruments at moorings T2 and T3. However, at these locations, the shallowest instrument does not remain regularly in the WW layer, and vertical displacements of the sharp WW-MCDW interface, presumably driven by winds, result in substantial variability at the two shallowest instruments.

It is not immediately clear why the deep WW layer freshens throughout most of the year. In Lützow-Holm Bay in East Antarctica, WW freshening in autumn has been explained by Ekman convergence of surface waters, causing accumulation and downwelling of fresh sea ice melt in summer (Ohshima et al., 1996). However, WW freshening on the Sabrina Coast occurs also in other seasons, including in September and October when sea ice is forming, and is observed below 300-m depth, too deep to be affected by Ekman downwelling of surface waters (Ohshima et al., 1996). A hypothesis we now test is that glacial meltwater exiting nearby ice shelf cavities can explain the

depth, timing, and magnitude of the freshening signal.

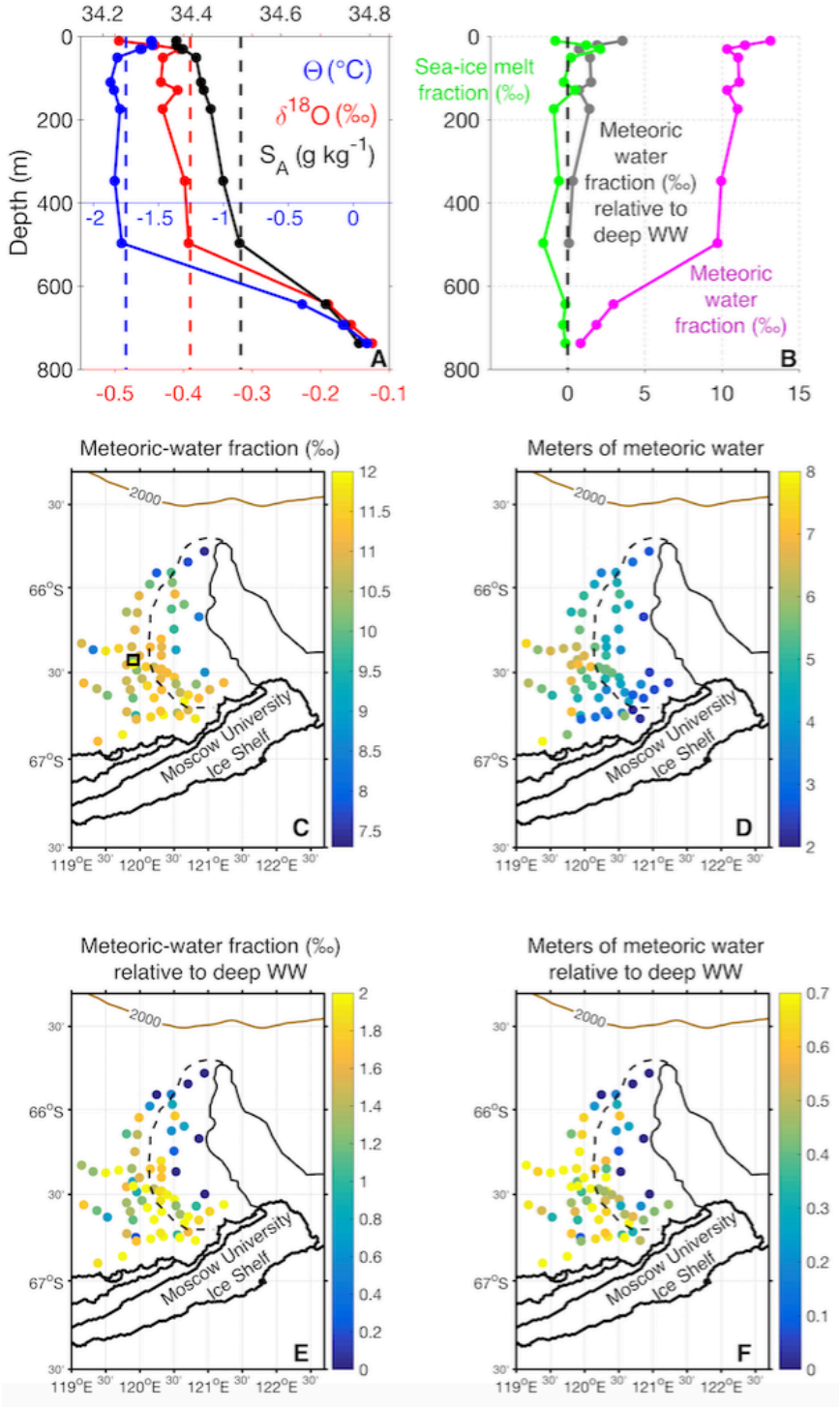

Figure 5.2. Freshwater input on the Sabrina Coast. (A) Vertical profiles of conservative temperature Θ, oxygen isotope $\delta^{18}O$, and absolute salinity S_A from station 21 (black square in (C)). The vertical black (red) dashed line represents S_A ($\delta^{18}O$) used to estimate the meteoric water fraction relative to deep WW (see Materials and methods). The dashed blue line is Θ = –1.75°C, the upper temperature limit for WW. (B) Vertical profiles at station 21 of the fractions of meteoric water (magenta), sea ice melt (green), and meteoric water relative to deep WW (gray) (see Material and methods). (C) Vertically-averaged meteoric water fraction above the MCDW layer. The black dashed line delimits the Dalton Polynya, defined as the area where the annual sea ice production is larger than 3 m. (D) Meters of meteoric water. (E) Same as (C) but relative to deep WW. (F) Meters of meteoric water accumulated above the MCDW layer since the commencement of mixed-layer retreat.

5.3.2. WW freshened by glacial meltwater on the Sabrina Coast

We use summer observations of oxygen isotope and salinity to quantify the sources of freshwater to shelf waters on the Sabrina Coast (see Materials and methods). We assume that saline MCDW, high in the oxygen isotope $\delta^{18}O$ (Figure 5.2A), represents pure ocean water, whereas fresh WW and surface layers, low in $\delta^{18}O$, are a mixture of MCDW, sea ice melting/freezing, and meteoric water. Meteoric water is supplied by direct precipitation into the ocean or from snow accumulated on the Antarctic Ice Sheet, which enters the ocean as glacial meltwater. Under these assumptions, we can use $\delta^{18}O$ and salinity data to estimate the fraction of meteoric water and sea ice melt in the water column (Meredith et al., 2008), where negative fractions of sea ice melt indicate freezing.

Example vertical profiles show that the meteoric water fraction is ~0‰ in the MCDW layer and increases upward to values between 10 and 13‰ in the WW and surface layers (Figure 5.2B). The sea ice melt fraction is zero in the MCDW layer, negative in the WW layer because of sea ice growth during the previous winter, and positive near the surface because of summer sea ice melt. Figure 5.2C shows the meteoric water fraction averaged between the base of the WW layer and the surface. Relatively high concentrations of meteoric water (~10‰) are observed in the domain, with higher values (~12‰) near the coast and lower values in the northern polynya (~8 to 9‰). By vertically integrating the fractions, we find that typically 4 to 5 m of meteoric water accumulate in the water column, with higher values west of the polynya and lower values near the coast (Figure 5.2D). The lower inventory near the coast reflects the shallower bathymetry and thinner WW layer there (about 250 to 300 m thick; Silvano et al., 2017).

We now estimate the rate of meteoric water input to determine whether it is sufficient to explain the freshening seen in the mooring observations. The same method is applied, except that as pure ocean water, we use a water type representative of the mixed layer at the end of winter (see Materials and methods). We can thus quantify the meteoric water accumulated above the MCDW layer between the commencement of the mixed-layer retreat (that is, restratification) and the time of the summer survey (Meredith et al., 2013). For this analysis, we use WW found below 400-m depth as pure ocean water (see Figure 5.2A for the properties of this “deep” WW). This water preserves the properties of the winter mixed layer without being largely affected by glacial meltwater released by nearby ice shelves since the end of winter convection, which accumulates in the top 300 to 400 m of the water column (Silvano et al., 2017).

The vertical profile shown in gray in Figure 5.2B highlights the addition of meteoric water to the

water column above 400-m depth since the commencement of mixed-layer retreat. The spatial pattern of meteoric water fraction relative to deep WW (Figure 5.2E) is similar to that of total meteoric water (Figure 5.2C), indicating stronger input in the southern polynya, close to the Moscow University Ice Shelf. This is expected because fractions calculated relative to deep WW represent a subset of the total values (Meredith et al., 2013). The inventories and concentrations relative to deep WW (Figures 5.2E and 5.2F) are smaller than the total values (Figures 5.2C and 5.2D), the latter reflecting accumulation of meteoric water over time scales longer than a few months.

Considering all stations, the linear average of the meteoric water accumulated since the end of winter convection is 0.5 m, with a standard error of 0.04 m. Mooring observations show that the mixed layer starts to shoal around September, about 3 months before the summer survey. The rate of meteoric water input into the water column during these 3 months is then estimated to be ~0.17 m $month^{-1}$. Assuming that the WW freshening rate (~0.01 g kg^{-1} $month^{-1}$) detected by the mooring observations after September is representative of the domain of the summer survey and vertically homogeneous between 400-m depth and the surface, a rate of ~0.12 m of freshwater input per month is obtained, in good order-of-magnitude agreement with our estimate of the rate of meteoric water input. In addition, the rate of decrease in WW salinity between March and July is similar to that observed after September, further confirming that the observed WW freshening is caused by sustained input of meteoric water at depths shallower than 300 to 400 m. Processes such as eddy-induced restratification (Marshall and Schott, 1999) can also contribute to the freshening, but the consistency between the observed salinities and the estimated meteoric water input indicates that meteoric water is the primary source of the observed freshening.

The tracers used here to quantify the meteoric water content cannot differentiate between the contributions from glacial meltwater and precipitation into the ocean. The 2014 average rate of precipitation minus evaporation in the domain of our survey from ERA-Interim reanalysis (Dee et al., 2011) is ~0.03 m $month^{-1}$. Although the rate at which precipitation is mixed into the ocean is uncertain, the precipitation rate is less than 20% of the rate estimated for the meteoric water input, suggesting that glacial meltwater is the dominant source of meteoric water. A previous study of Silvano et al. (2017) shows that most of the glacial meltwater found in the area of our survey comes from basal melt of the Moscow University Ice Shelf, which, after exiting the ice shelf cavity, is advected westward by the coastal current toward the Dalton Polynya. The authors found higher concentrations of glacial meltwater in the southern polynya, in agreement with our results of higher

meteoric water fractions in the same area. We conclude that glacial meltwater released by the Moscow University Ice Shelf explains the WW freshening revealed by mooring observations.

5.3.3. Influence of glacial meltwater input on stratification of shelf waters

We now seek to understand how meteoric water input influences the mixed-layer evolution during winter in the Dalton Polynya. We use a bulk mixed-layer model (see Materials and methods) to investigate the processes involved in producing wintertime water masses and stratification. The model is run from March (beginning of the winter season) to September, after which the mixed layer shoaled at all mooring locations. Initial conditions are based on in situ observations collected by a profiling float around the time of the mooring deployment (see Materials and methods and Figure 5.5). The model is forced by salt flux at the ocean surface based on satellite-derived sea ice production (see Materials and methods and Figure 5.5B; Tamura et al., 2016). The input rate of meteoric water is set to 0.15 m month^{-1}, an intermediate value between the freshening rate inferred from mooring observations and that calculated from $\delta^{18}O$ and salinity data. The input of 0.15 m of freshwater per month is sufficient to compensate ~35% of the salt flux by sea ice production (see Materials and methods). In our model runs, we reduce the surface salt flux by 35% to simulate the freshening impact of the meteoric water injected into the ocean.

The experiment with meteoric water input included shows good agreement with mooring observations (Figures 5.3A and 5.3B). The water column is destratified to ~350-m depth by the end of September, and the mixed-layer salinity reaches ~34.5 g kg^{-1}, as observed. If the contribution from meteoric water is not taken into account, convection extends to the seafloor and the mixed-layer salinity (~34.6 g kg^{-1}) is higher than observed. The largest uncertainty in the model is associated with sea ice production, whereas other factors such as changes in initial conditions have less effect (see Materials and methods). Even considering the ±25% (Tamura et al., 2008) uncertainty in sea ice production, the experiment without the meteoric water contribution cannot reproduce the observations (see shaded red area in Figures 5.3A and 5.3B). Our results show that meteoric water, mostly in the form of glacial meltwater released by the Moscow University Ice Shelf, acts to reduce deepening and salinification of the mixed layer in the Dalton Polynya. Therefore, DSW is not formed, and warm MCDW intruding onto the shelf at the longitude of the Dalton Polynya and further west floods the bottom layer (Nitsche et al., 2017), ultimately delivering enough heat to the base of the Totten Ice Shelf to drive rates of basal melt that are among the highest in Antarctica (Silvano et al., 2016).

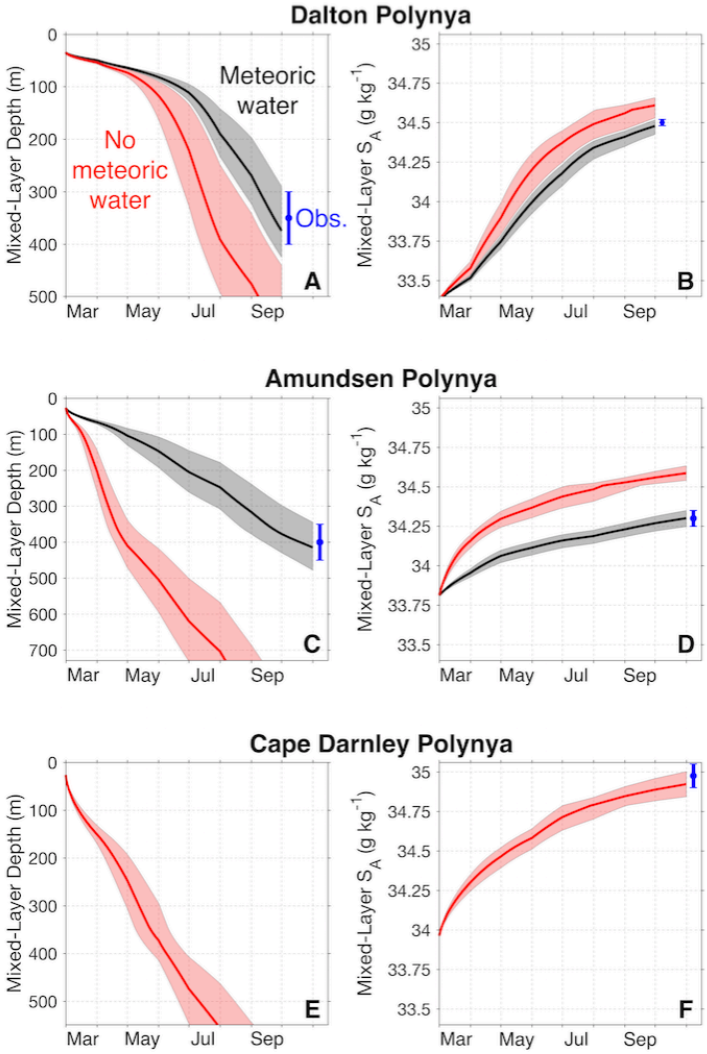

Figure 5.3. Mixed-layer evolution in Antarctic polynyas. Modeled temporal evolution of mixed-layer depth (A) and absolute salinity S_A (B) in the Dalton Polynya. In red, we show the case with no meteoric water included. In black, meteoric water is included by reducing the surface salt flux by 35%. Shaded areas represent uncertainty in the model output related to uncertainty in sea ice production (±25%; Tamura et al., 2008), whereas blue bars indicate the range of observed WW properties. (C and D) Same as (A) and (B) for the Amundsen Polynya. Surface salt flux is reduced by 75% in the black line case. Blue bars are based on WW variability in different years (Jacobs et al., 2012; Miles et al., 2016; Randall-Goodwin et al., 2015). (E and F) Same as (A) and (B) for the Cape Darnley Polynya but only showing the no–meteoric water case because it reproduces observations of DSW formation (Ohshima et al., 2013). Note that the y axis stops at the full depth of the ocean, different in (A), (C), and (E) (Figures 5.5-5.7).

The Amundsen Polynya is one of the most productive polynyas in Antarctica, forming more than twice as much sea ice as the Dalton Polynya (Tamura et al., 2016). We next examine whether input of glacial meltwater can also explain the lack of DSW formation in the Amundsen Sea. Initial conditions in the Amundsen Polynya are based on data collected in late summer 2007, and the model is integrated between March and October 2007, when strong sea ice production is observed (see Materials and methods and Figure 5.6). Multiyear observations from this area show that the WW salinity is of the order of 34.3 g kg^{-1} and that the maximum mixed layer depth is about 400 m (Jacobs et al., 2012; Miles et al., 2016; Randall-Goodwin et al., 2015). In the absence of freshwater

input, the mixed layer in the model reaches the bottom and is much saltier (~34.6 g kg^{-1}) than observed (Figures 5.3C and 5.3D). To reproduce observed values, the net surface salt flux needs to be reduced by ~75% (Figures 5.3C and 5.3D).

To compensate 75% of the salt flux provided by sea ice formation, about 0.4 m of freshwater must be added to the ocean each month. Freshwater input from melting of sea ice is small in this location (Randall-Goodwin et al., 2015). The 2007 precipitation minus evaporation rate in the region is ~0.06 m $month^{-1}$ in the ERA-Interim reanalysis. Melting of icebergs can also contribute to meteoric water input to the Amundsen Polynya, but recent modeling studies indicate that the iceberg contribution is smaller than that of precipitation (Merino et al., 2016; Rackow et al., 2017). Most of the meteoric water input must therefore come from glacial meltwater released by melting ice shelves. By integrating over the area of the Amundsen Polynya, we find that ~8.5 km^3 $month^{-1}$ of freshwater is required to offset 75% of the surface salt flux supplied by sea ice formation. The primary source of glacial meltwater to the Amundsen Polynya is likely basal melt of upstream ice shelves (for example, Crosson, Pine Island, and Thwaites). The combined basal mass loss of these ice shelves is about 20 km^3 $month^{-1}$ over the 2003–2008 period (Depoorter et al., 2013; Rignot et al., 2013). Most of the glacial meltwater released by these ice shelves is transported westward in the coastal current to the Amundsen Polynya in the top 300 to 400 m of the water column (Biddle et al., 2017). (Meltwater exits the cavity beneath the Dotson Ice Shelf south of the polynya (Figure 5.6), but the core of this outflow is located on the western edge of the polynya (Miles et al., 2016) and therefore likely has less impact on convection in the Amundsen Polynya.) Basal melt of upstream ice shelves therefore provides sufficient freshwater input to compensate a large fraction of the salt flux released during sea ice formation in the Amundsen Polynya. As a result, winter convection does not extend to the seafloor, no DSW is formed, and warm MCDW flowing through the Dotson Trough (Figure 5.6) can reach the Dotson (Miles et al., 2016) and Getz ice shelves (Jacobs et al., 2013) and drive rapid basal melt.

We have shown that DSW formation is inhibited in polynyas downstream of the outflow from "warm-cavity" ice shelves characterized by rapid rates of basal melt. In contrast, observations in the Ross Sea (Orsi and Wiederwohl, 2009), Weddell Sea (Nicholls et al., 2009), Adélie Coast (Bindoff et al., 2001), and Prydz Bay (Williams et al., 2016) show that, although glacial meltwater released by nearby cold-cavity ice shelves can reduce the DSW salinity, it is not sufficient to prevent the top-to-bottom convection necessary for DSW formation. Next, we apply the model to the Cape Darnley Polynya where similar rates of sea ice formation to the Amundsen Polynya (Tamura et al.,

2016) drive formation of DSW (Ohshima et al., 2013). We use data from a CTD-instrumented elephant seal collected in late summer 2011 as initial conditions and surface salt fluxes from March to October 2011 (see Materials and methods and Figure 5.7). The model run without meteoric water input produces a mixed layer that reaches the bottom with salinity values around 35 g kg^{-1} (Figures 5.3E and 5.3F), in good agreement with the properties of the DSW formed in 2011 (Ohshima et al., 2013). This result confirms that mixed-layer deepening is not greatly affected by glacial meltwater reaching the Cape Darnley Polynya. The primary source of glacial meltwater here is basal melt of the upstream Amery Ice Shelf (Herraiz-Borreguero et al., 2016b), where basal melt rates are relatively low, being mostly driven by cold DSW formed in Prydz Bay polynyas (Herraiz-Borreguero et al., 2016a).

5.4. Discussion

On the Sabrina Coast and in the Amundsen Sea, input of glacial meltwater is sufficient to partially compensate brine supplied during sea ice formation, reducing the depth and salinity of the winter mixed layer. This mechanism helps explain why polynyas in these regions do not produce DSW, despite strong buoyancy loss. In cold regions such as Prydz Bay (Williams et al., 2016), glacial meltwater can reduce the salinity of the DSW escaping the continental shelf, thus freshening the resulting Antarctic Bottom Water. However, in Prydz Bay, the low rates of ice shelf basal melt are insufficient to prevent the formation of cold DSW, and the water column is completely destratified during winter convection (Herraiz-Borreguero et al., 2016a). In contrast, on the Sabrina Coast and in the Amundsen Sea, the absence of deep convection and DSW formation allows warm MCDW to persist at depth throughout the year within the polynya and further downstream, where it can reach ice shelf cavities. In these regions, glacial meltwater thus both prevents DSW formation and supports rapid basal melt by inflow of warm MCDW to ice shelf cavities (Figure 5.4A).

The model used here is very simple, but the fact that the observed properties of the winter mixed layer can be reproduced in very different polynya systems suggests that the model captures key elements of the interplay between polynya activity, stratification, dense water formation, and ice shelf basal melt. Studies of these regions using more comprehensive models have produced different and sometimes conflicting results. For example, some regional models show formation of DSW in the Dalton Polynya (Gwyther et al., 2014; Kusahara et al., 2010), possibly because the impact of glacial meltwater from the Moscow University Ice Shelf is not well reproduced. Other models reproduce the observed stratification on the Sabrina Coast and in the Amundsen Sea, but the

modeled rates of sea ice formation in the polynyas tend to be underestimated (Petty et al., 2013; Petty et al., 2014) or the rates of ice shelf basal melt tend to be overestimated (Khazendar et al., 2013). A common feature found in many regional modeling studies is that interannual variability in waters formed in coastal polynyas affects the basal melt of nearby ice shelves (Khazendar et al., 2013; St-Laurent et al., 2015; Gwyther et al., 2014), confirming the primary role of coastal polynyas in regulating the delivery of ocean heat to the margin of the Antarctic Ice Sheet. However, regional models of coastal polynyas face a number of challenges, including the complex and time-evolving icescape (Nihashi and Ohshima, 2015), the poorly known bathymetry (Rintoul et al., 2016; Nitsche et al., 2007), the small spatial scale of ocean processes happening near ice shelves (Naveira Garabato et al., 2017) and at the shelf break (Stewart and Thompson, 2015), and uncertainties in air-sea forcing, including the impact of fine-scale atmospheric phenomena such as katabatic winds (Morales Maqueda et al., 2004). Climate models have also been used to study the impact of glacial meltwater input to the Southern Ocean (Hellmer, 2004; Fogwill et al., 2015). They show that glacial meltwater drives a freshening of shelf waters and Antarctic Bottom Water. However, processes happening in coastal polynyas and beneath the ice shelves cannot be accurately represented in these coarse resolution models. Our study highlights that the coupled interplay between coastal polynyas, water mass formation, and ocean-ice shelf interaction must be properly represented in models that aim to simulate the present and future behavior of the Antarctic Ice Sheet and Southern Ocean overturning circulation.

Currently, Antarctic shelf waters are mostly cold, and basal melt rates are low at many ice shelves, indicating that glacial meltwater input is insufficient to prevent DSW formation, as found at Cape Darnley Polynya (Figure 5.4B). In regions such as the Weddell Sea (Darelius et al., 2016), Ross Sea (Arzeno et al., 2014), and Prydz Bay (Herraiz-Borreguero et al., 2015), DSW floods the bottom layer, and MCDW can only access the ice shelf cavities sporadically at mid-depth, with limited impact on basal melt rates. A decrease of DSW formation in a warmer climate might lead to a reduced circulation in cold-cavity ice shelves and a slight decrease in basal melt (Nicholls, 1997). However, projections simulating the impact of sustained emissions of anthropogenic greenhouse gases show that melting of Antarctic ice shelves and glaciers will increase in the coming decades and centuries in response to warming of the ocean and atmosphere (DeConto and Pollard, 2016) and redirection of warm coastal currents (Hellmer et al., 2012). There is already evidence of freshening of bottom waters in the Weddell and Ross seas associated with recent increase of glacial mass loss in the upstream Antarctic Peninsula (Jullion et al., 2013) and Amundsen Sea (Jacobs and Giulivi, 2010), respectively. We show that present rates of glacial meltwater input are sufficient to

prevent DSW formation in some locations, despite strong air-sea forcing and buoyancy loss. This mechanism can help explain past and projected future behavior of the Antarctic Ice Sheet and Southern Ocean (Menviel et al., 2010; Golledge et al., 2014; Weber et al., 2014). Our results suggest that a further increase in the supply of glacial meltwater to Antarctic shelf waters may trigger a transition from a cold regime (characterized by full-depth convection, low rates of ice shelf basal melt, and active bottom water formation) to a warm regime (characterized by year-round stratification, high rates of ice shelf basal melt, and reduced bottom water formation). A slowdown of DSW formation in response to increased glacial meltwater input would have consequences for the deep overturning circulation and abyssal ventilation. At the same time, meltwater-induced changes in stratification would facilitate the spreading of warm waters across the continental shelf to ice shelf cavities, driving increased ice shelf basal melt, reduced buttressing of the Antarctic Ice Sheet, and additional rise in sea level.

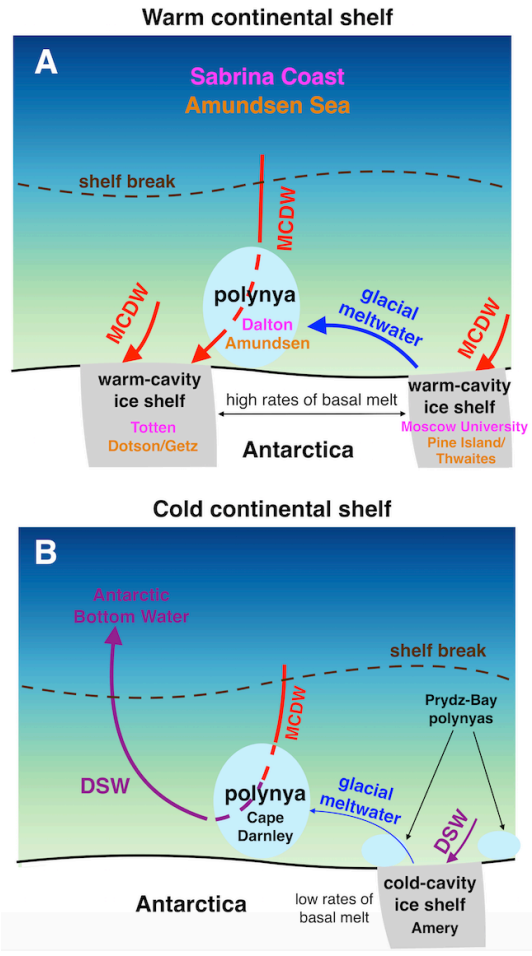

Figure 5.4. Impact of glacial meltwater on dense water formation and shelf stratification. On warm continental shelves, as those on the Sabrina Coast and in the Amundsen Sea (A), MCDW drives rapid ice shelf basal melt. The large volume of glacial meltwater prevents DSW formation in polynyas downstream of the meltwater outflow. MCDW remains in the bottom layer throughout the year in the polynya and further downstream, where it can access the ice shelf cavities. On cold continental shelves, the ice shelf cavities are filled by cold shelf waters, and basal melt rates are low. Glacial meltwater input is not sufficient to suppress winter convection in polynyas downstream of the meltwater outflow, as seen at Cape Darnley Polynya (B), allowing formation of DSW, the precursor to Antarctic Bottom Water.

5.5. Materials and methods

5.5.1. Oceanographic observations

An oceanographic survey was conducted on the continental shelf of the Sabrina Coast (115° to 125°E) onboard the *Aurora Australis* (cruise AU1402) between 24 December 2014 and 7 January 2015 (Silvano et al., 2017). Oceanographic profiles were collected using a Seabird 911plus CTD with dual temperature and conductivity sensors and calibrated against bottle samples. Here, we included the analysis of 68 CTD stations (see location in Figure 5.1B) collected during this expedition along with measurements of the ratio of stable oxygen isotopes in seawater ($\delta^{18}O$, the standardized ratio of $H^{18}O$ to $H^{16}O$). $\delta^{18}O$ data were extracted from water samples at various depths using a Finnigan DELTAplus mass spectrometer at the Institute of Low Temperature Science, Hokkaido University, Japan. Measurements for each sample were duplicated, and the precision of the replicates was estimated to be 0.02‰.

Three moorings (T1, T2, and T3) were deployed on the continental shelf of the Sabrina Coast (see location in Figure 5.1B) in February 2014 during the NBP1402 expedition on the US R/V *Nathaniel B. Palmer* and recovered in January 2015 during the AU1402 voyage. Measurements, including temperature, salinity, and pressure, were collected at four different depths between about 300 m and the bottom at each location. Salinity measurements at the second deepest instrument of mooring T3 showed some drift, and therefore data from this instrument were excluded from our analysis. For more details about records and specific instruments, the reader is referred to table 5.1.

In addition, we used salinity and temperature data acquired between the beginning of February and the first week of March 2015 by a profiling float deployed during the AU1402 voyage (see location of profiles in Figure 5.5A). We also included in our analysis shipboard measurements of surface salinity and temperature collected in the Dalton Polynya during the *Nathaniel B. Palmer* survey between the last week of February and the first week of March 2014 (see location in Figure 5.5A; Takahashi et al., 2009). Finally, CTD data from the Amundsen and Cape Darnley polynyas were used. Data from the Amundsen Polynya were collected on 27 February 2007 onboard the R/V *Nathaniel B. Palmer* (Figure 5.6; Jacobs et al., 2013). Data from Cape Darnley Polynya were acquired on 22 February 2011 by a CTD-instrumented elephant seal (seal deployment ft07, seal number 346, seal tag number Cy27, and platform number 00022332; Figure 5.7; Ohshima et al., 2013; Roquet et al., 2013, 2014). All temperature and salinity data in this study have been converted to absolute salinity S_A (in grams per kilogram, g kg^{-1}) and conservative temperature Θ (in degrees Celsius, °C) (McDougall and Barker, 2011).

5.5.2. Quantification of freshwater sources

S_A and $\delta^{18}O$ can be used as conservative tracers to estimate fractions (f) of meteoric water and sea ice melt in the water column (Meredith et al., 2008). The fraction of sea ice melt can be negative in the case of net sea ice growth. We assumed that the observed values ("obs") of S_A and $\delta^{18}O$ represent a mixture of sea ice melt ("sim"), meteoric water ("met"), and oceanic water (MCDW). The mass balance is then given by

$$\begin{cases} f^{sim} + f^{met} + f^{MCDW} = 1 \\ f^{sim} S_A^{sim} + f^{met} S_A^{met} + f^{MCDW} S_A^{MCDW} = S_A^{obs} \\ f^{sim} \delta^{18}O^{sim} + f^{met} \delta^{18}O^{met} + f^{MCDW} \delta^{18}O^{MCDW} = \delta^{18}O^{obs} \end{cases} \quad (5.1)$$

S_A and $\delta^{18}O$ values for MCDW were chosen to be 34.8 g kg^{-1} and –0.1‰, respectively, based on our observations on the Sabrina Coast. Values relative to sea ice (S_A^{sim} = 6.2 g kg^{-1} and $\delta^{18}O^{sim}$ = 1.2‰) were obtained from sea ice core measurements collected on the Sabrina Coast continental shelf in 2007 during Sea Ice Physics and Ecosystems eXperiment (SIPEX; Worby et al., 2011). Salinity of the meteoric water was set to zero. $\delta^{18}O^{met}$ is the most uncertain parameter because of the large difference in $\delta^{18}O$ values for precipitation in the region (~–20‰; Masson-Delmotte et al., 2008) and the value relative to the glacial ice that feeds the ice shelves on the Sabrina Coast (~–40‰; Masson-Delmotte et al., 2008). We chose an intermediate value for $\delta^{18}O^{met}$ equal to –30‰. Given the range in the $\delta^{18}O^{met}$ end-member, the uncertainty in the calculated meteoric water and sea ice melt fractions is less than 1%, diminishing when averages of numerous samples are calculated. Uncertainties associated with other end-members or errors in the measurements had a marginal impact on this calculation compared to the uncertainty in $\delta^{18}O^{met}$.

We followed the method described by Meredith et al. (2013) to estimate the meteoric water accumulated between the commencement of the mixed-layer retreat and the time of the AU1402 survey. A modified version of the balance shown in equation (5.1) was used, considering deep (below 300- to 400-m depth in the case of the Sabrina Coast) Winter Water (dWW) as the ambient water to calculate the fractions of meteoric water and sea ice melt above the MCDW layer

$$\begin{cases} f^{sim} + f^{met} + f^{dWW} = 1 \\ f^{sim} S_A^{sim} + f^{met} S_A^{met} + f^{dWW} S_A^{dWW} = S_A^{obs} \\ f^{sim} \delta^{18}O^{sim} + f^{met} \delta^{18}O^{met} + f^{dWW} \delta^{18}O^{dWW} = \delta^{18}O^{obs} \end{cases} \quad (5.2)$$

S_A and $\delta^{18}O$ of deep WW were set to 34.51 g kg^{-1} and –0.39‰, respectively, based on observations of WW below 400-m depth (Figure 5.2A). By vertically integrating f^{met}, we obtained the meters of meteoric water accumulated above the MCDW layer since the commencement of the mixed-layer retreat.

5.5.3. Mixed-layer model

We used a bulk model to simulate the mixed layer during winter months, based on the works of Kraus and Turner (1967) and Niiler and Kraus (1977). More recent studies (Petty et al., 2013, 2014) have used the same model to assess the role of atmospheric forcing on ocean stratification around Antarctica. In the latter studies, the authors couple the ocean model with a sea ice model forced by atmospheric reanalysis data. They succeed in reproducing the bulk ocean stratification on the Antarctic continental shelf, confirming the validity of the model for this region. However, the estimated rates of sea ice growth are much lower than those based on satellite observations in some coastal polynyas, including the Amundsen and Dalton polynyas. This might be due to the absence in their model of fast ice and glacier tongues, which allow the formation of polynyas in their lee, as it occurs in the regions considered in this study (Nihashi and Ohshima, 2015).

The model assumes a balance in the mixed layer between sources and sinks of turbulent kinetic energy. We further assumed that wind stirring acts to keep the mixed layer "well-mixed," without influencing the energy budget (Martinson, 1990). The main sources/sinks of energy to the mixed layer are those associated with entrainment of deep water and surface buoyancy fluxes. The power required to entrain deep water into the mixed layer was obtained as

$$P_E = w(d_{mix}\Delta b + c_m^2) \qquad (5.3)$$

where w is the mixed-layer entrainment rate (in meters per second, m s^{-1}), d_{mix} is the mixed-layer depth (in meters, m), and c_m is a parameter describing the unsteadiness in the budget of turbulent kinetic energy and equals 0.03 m s^{-1} (Kim, 1976). Δb is the difference in the buoyancy across the mixed-layer base, here expressed as

$$\Delta b = g\alpha(T_{mix} - T_b) - g\beta(S_{mix} - S_b) \qquad (5.4)$$

where T_{mix} (T_b) and S_{mix} (S_b) are the temperature and salinity, respectively, in (directly below) the mixed layer, g is the gravitational acceleration (9.81m s^{-2}), α is the thermal expansion coefficient (4

x 10^{-5} K^{-1}), and β is the saline contraction coefficient (8 x 10^{-4} kg g^{-1}).

We assumed that salt flux dominates the surface buoyancy flux. This is based on the fact that the mixed-layer temperature during winter is approximately constant at the surface freezing point (Martinson, 1990), and therefore, the influence of surface heat loss (used to form sea ice) on the buoyancy budget is minimal. The power input per unit density (in cubic meters per cubic second, m^3 s^{-3}) to the mixed layer from buoyancy flux was calculated as

$$P_S = c_1 d_{mix} g \beta F_S \qquad (5.5)$$

where c_1 is a coefficient describing the frictional energy dissipation of convective mixing and equals 0.83 when the mixed layer is deepening (Tang, 1991), and F_S is the salt flux (in grams per kilogram meters per second, g kg^{-1} m s^{-1}) into the mixed layer. For reasons mentioned above, F_S was estimated using satellite-derived sea ice production from ERA-Interim data (Tamura et al., 2016), whose uncertainty is ~25% (Tamura et al., 2008). Estimates of sea ice production in Antarctic polynyas using this technique have been found to be consistent within 20 to 25% of estimates derived from in situ oceanographic observations (Tamura et al., 2016). Following Cavalieri and Martin (1994), the flux of salt F_S' in units of kilograms per square meter per second (kg m^{-2} s^{-1}) is given by $F_S' = 0.69 \times 10^{-3} \rho_i V S_O$, where V is the rate of sea ice growth (in meters per second, m s^{-1}), ρ_i is the density of sea ice (920 kg m^{-3}), and S_O is the salinity at the ocean surface assumed to be 34 g kg^{-1}. This formula indicates that 69% of salt is rejected back into the ocean during sea ice growth and implies a sea ice salinity of ~10.5 g kg^{-1}. This value represents the early stages of sea ice growth in coastal polynyas (Martin and Kauffman, 1981), as compared to the lower salinity (6.2 g kg^{-1}) used to calculate sea ice melt in equation (5.1), representative of older sea ice. The flux F_S into the mixed layer was then computed as $F_S = \frac{1}{\rho_w}(1000 - S_{mix})F_S'$, where ρ_w is the density of seawater (1027 kg m^{-3}) and 1000 g kg^{-1} is the salinity of pure salt (Petty et al., 2014). Monthly mean salt fluxes averaged over the polynya were used as forcing to the model. The polynya was defined as the area where the annual sea ice production is higher than 3 m.

From the above relationship between salt flux and rate of sea ice growth, we found that sea ice has to grow by ~1.7 m to bring the salinity of the meteoric water that accumulates in the Dalton Polynya between March and September (1.05 m) from zero to WW values (~34.5 g kg^{-1}). The area-averaged cumulative sea ice production in the Dalton Polynya during the same period is 4.8 m, implying that ~35% of sea ice production is required to offset the injection of meteoric water into

the water column. We included in the model of the Dalton Polynya the effect of meteoric water input by reducing the satellite-derived surface salt flux by 35%, implicitly assuming that the input was entirely distributed over the modeled mixed layer.

Using equations (5.3) to (5.5), we obtained from energy and salt conservation that the temporal evolution of mixed-layer depth and salinity are given by

$$\begin{cases} \frac{d}{dt} d_{mix} = \frac{P_S}{(d_{mix}\Delta b + c_m^2)} \\ \frac{d}{dt} S_{mix} = \frac{F_S}{d_{mix}} + \frac{w}{d_{mix}} (S_b - S_{mix}) \end{cases} \quad (5.6)$$

where $w = \frac{d(d_{mix})}{dt}$. As discussed above, we assumed the mixed-layer temperature during months of sea ice formation to be constant at the surface freezing point (with reference salinities for the mixed layer of 34.4, 34.2, and 34.7 g kg^{-1} for the Dalton, Amundsen, and Cape Darnley polynyas, respectively). Variability of the freezing point with changes in S_{mix} did not influence the output of the model, as confirmed by Martinson (1990) by showing that the freezing point dependence on salinity affects the mixed-layer depth in the Southern Ocean by ~1%. (Note that we used a constant value of 34 g kg^{-1} for the salinity at the ocean surface when we estimated the surface salt flux F_S' (see above). Varying the ocean surface salinity by ± 0.7 g kg^{-1} in the estimate of the surface salt flux resulted in minimal changes of the modeling results (< 10 m and < 0.01 g kg^{-1} of d_{mix} and S_{mix}, respectively, at the end of the model runs).

Equation (5.6) was integrated using a finite-difference second-order Runge-Kutta scheme, with a time step of 15 min and a vertical resolution of the ocean profile of 0.5 m. The model is not sensitive to time and vertical resolutions because using a time step of 1 day or a vertical resolution of 2 m results in negligible changes of the output. During mixed-layer deepening, salinity and temperature values were set to S_{mix} and to the surface freezing point above d_{mix} and kept constant below. Initial conditions were based on in situ observations at the end of the summer before the simulated winter in the Amundsen and Cape Darnley polynyas (Figures 5.6 and 5.7). In the Dalton Polynya, CTD profiles at the end of the summer before the simulated winter (that is, 2014) are not available. For this polynya, we used data collected by a profiling float between February and early March 2015 (Figures 5.5C and 5.5D). We note that (i) the surface salinity in the float profiles is similar to that observed at the end of summer 2014 during the *Nathaniel B. Palmer* survey and that (ii) the properties of the WW and MCDW along with the depth of their interface in the float profiles

are similar to those observed by the moorings in early March 2014 (Figures 5.5C and 5.5D), implying that ocean conditions in 2014 and 2015 were similar. Furthermore, as shown below, the sensitivity of the model to small changes in properties of the initial ocean profiles is small compared to the uncertainty in estimates of sea ice production. This indicates that possible small changes of the initial conditions between 2014 and 2015 did not influence the output of the model.

Analysis of the wind curl over the Dalton Polynya using the ERA Interim reanalysis (Dee et al., 2011) indicates that vertical velocities associated with Ekman dynamics are more than one order of magnitude smaller than velocities associated with buoyancy forcing. This is consistent with the fact that convective processes dominate in terms of mixed-layer deepening near the coast in Antarctica (Petty et al., 2013, 2014). Therefore, we did not include Ekman vertical velocities in our model.

We ran several sensitivity tests in the Dalton Polynya varying one of the parameters in the initial conditions in each simulation. We varied the surface salinity between 33.15 and 33.3 g kg^{-1} (based on the range of values measured during the *Nathaniel B. Palmer* survey in 2014; see Figure 5.5D), the bottom salinity/temperature between 34.65 and 34.8 g kg^{-1}/–0.5° and +0.5°C (based on the variability observed at the mooring locations), and the salinity at the base of the seasonal pycnocline between 34.3 and 34.4 g kg^{-1} (to consider possible changes of the seasonal pycnocline between 2014 and 2015). We also varied the depth of the WW-MCDW interface between 300 and 400 m based on the variability observed at the mooring locations and the maximum depth of the profiles between 350 and 600 m to account for variability of the seafloor depth in the Dalton Polynya (Silvano et al., 2017). All of the above tests were run for both simulations including and excluding meteoric water input. In all cases, the change in mixed-layer depth is less than 30 m, and the change in salinity is less than 0.03 g kg^{-1} at the end of the model run. These changes are smaller than those associated with the uncertainty in the surface salt flux (see Figure 5.3A and 5.3B).

The model did not include diapycnal mixing because observations on the Antarctic continental shelf show that vertical fluxes in the pycnocline associated with diapycnal mixing are one (or more) order of magnitude smaller than winter surface fluxes (Smith and Klinck, 2002). Petty et al. (2013) include the effect of advection by restoring the ocean properties beneath the mixed layer to some reference values during spring and summer, when the mixed layer is retreating. Because we were not simulating the retreating period, we did not include any restoration of the ocean properties. We do note, however, that reducing the net surface salt flux due to input of meteoric water is a way of including the advection of freshwater. Our sensitivity tests in the Dalton Polynya indicate that

MCDW variability does not substantially affect the mixed-layer evolution, suggesting that MCDW advection is not of primary importance. This is consistent with the fact that the mixed layer never reaches the core of the MCDW layer in the Dalton (and Amundsen) Polynya. At Cape Darnley Polynya, our simulation is also in good agreement with the observations, suggesting that wintertime MCDW advection has a small impact on DSW formation there.

5.6. Supporting information

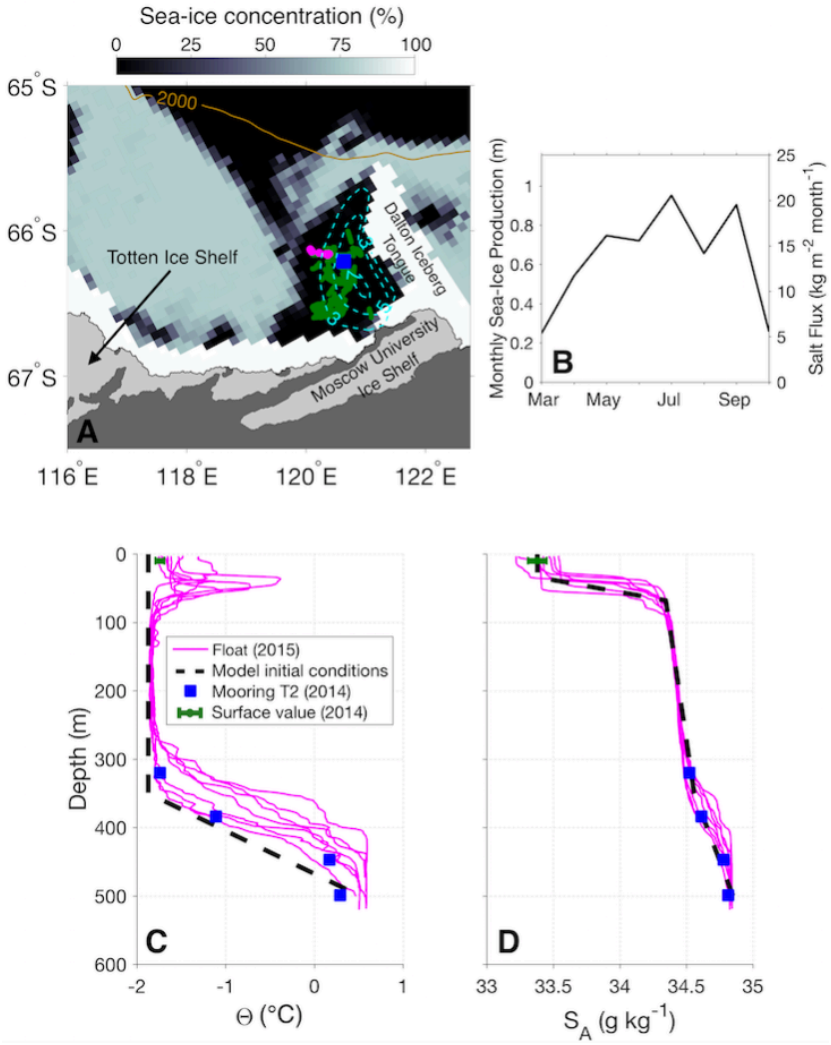

Figure 5.5. Dalton Polynya. (A) Map of sea-ice concentration on the Sabrina Coast on 25 February 2014 (Spreen et al., 2008). The cyan dashed lines are contours of the 2014 annual sea-ice production (m) (Tamura et al., 2016). The Dalton Polynya is characterized by low sea-ice concentration in summer and high sea-ice production in winter. (B) Monthly sea-ice production and associated salt flux in 2014 averaged over the area of the Dalton Polynya. (C) Magenta lines are vertical profiles of conservative temperature Θ measured between February and early March 2015 by the profiling float. Blue squares are from an average of data collected during the first two weeks of the deployment of mooring T2 (early March 2014). The green errorbar represents the mean (±1 standard deviation) of the surface temperature values measured during the *Nathaniel B. Palmer* survey in late summer 2014. The location of the float profiles (magenta), mooring T2 (blue) and surface temperature measurements (green) are shown in panel (A). The black dashed line is the profile used as initial condition for the mixed-layer model. (D) as (C) but for absolute salinity S_A.

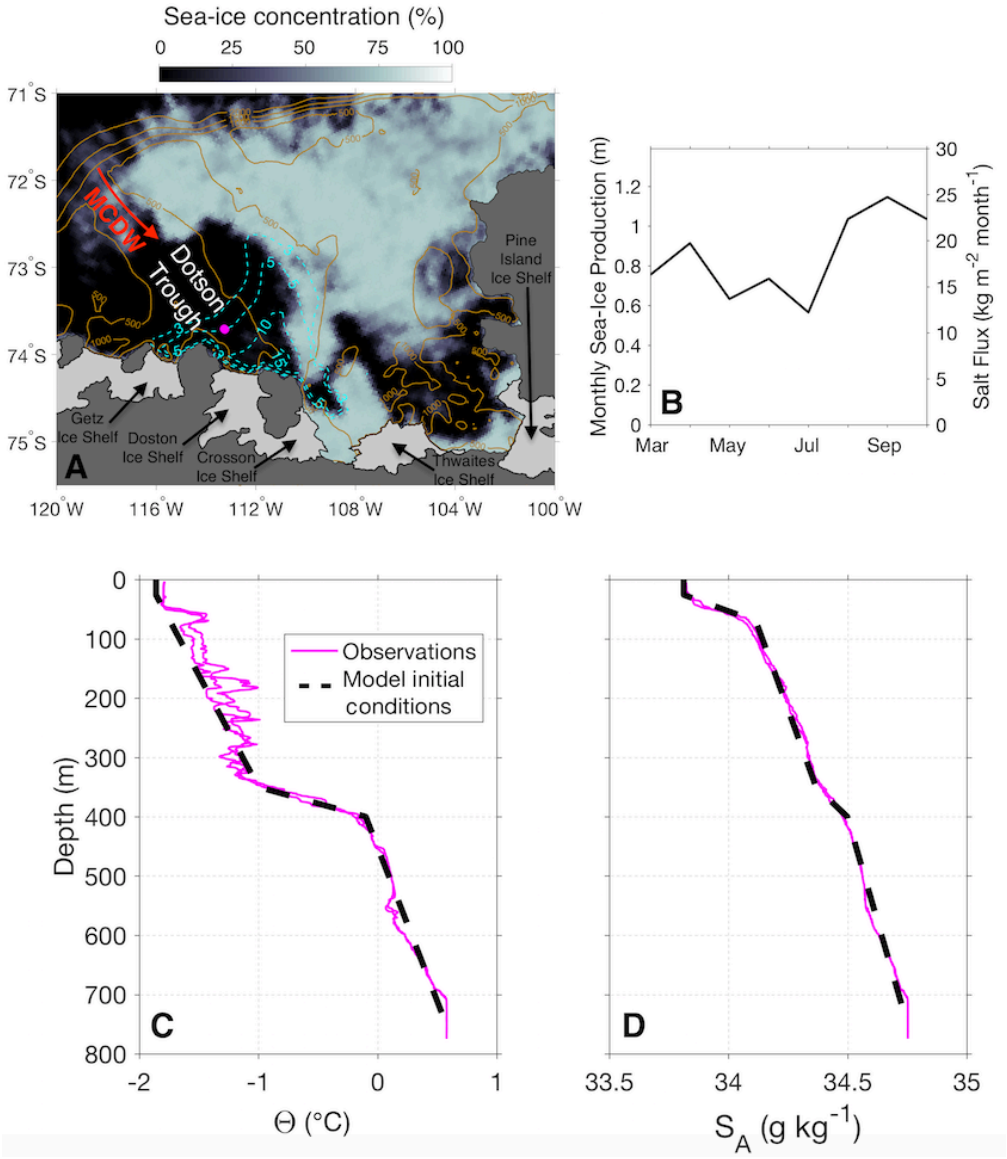

Figure 5.6. Amundsen Polynya. (A) Map of sea-ice concentration in the Amundsen Sea on 25 February 2007 (Spreen et al., 2008). The cyan dashed lines are contours of the 2007 annual sea-ice production (m) (Tamura et al., 2016). The Amundsen Polynya is characterized by low sea-ice concentration in summer and high sea-ice production in winter. Overlaid are the bathymetry and the coastline (Fretwell et al., 2013). (B) Monthly sea-ice production and associated salt flux in 2007 averaged over the area of the Amundsen Polynya. (C) Magenta lines are vertical profiles of conservative temperature Θ measured on 27 February 2007 in the Amundsen Polynya (see magenta dots in (A) for location). The black dashed line is the profile used as initial condition for the mixed-layer model. (D) as (C) but for absolute salinity S_A.

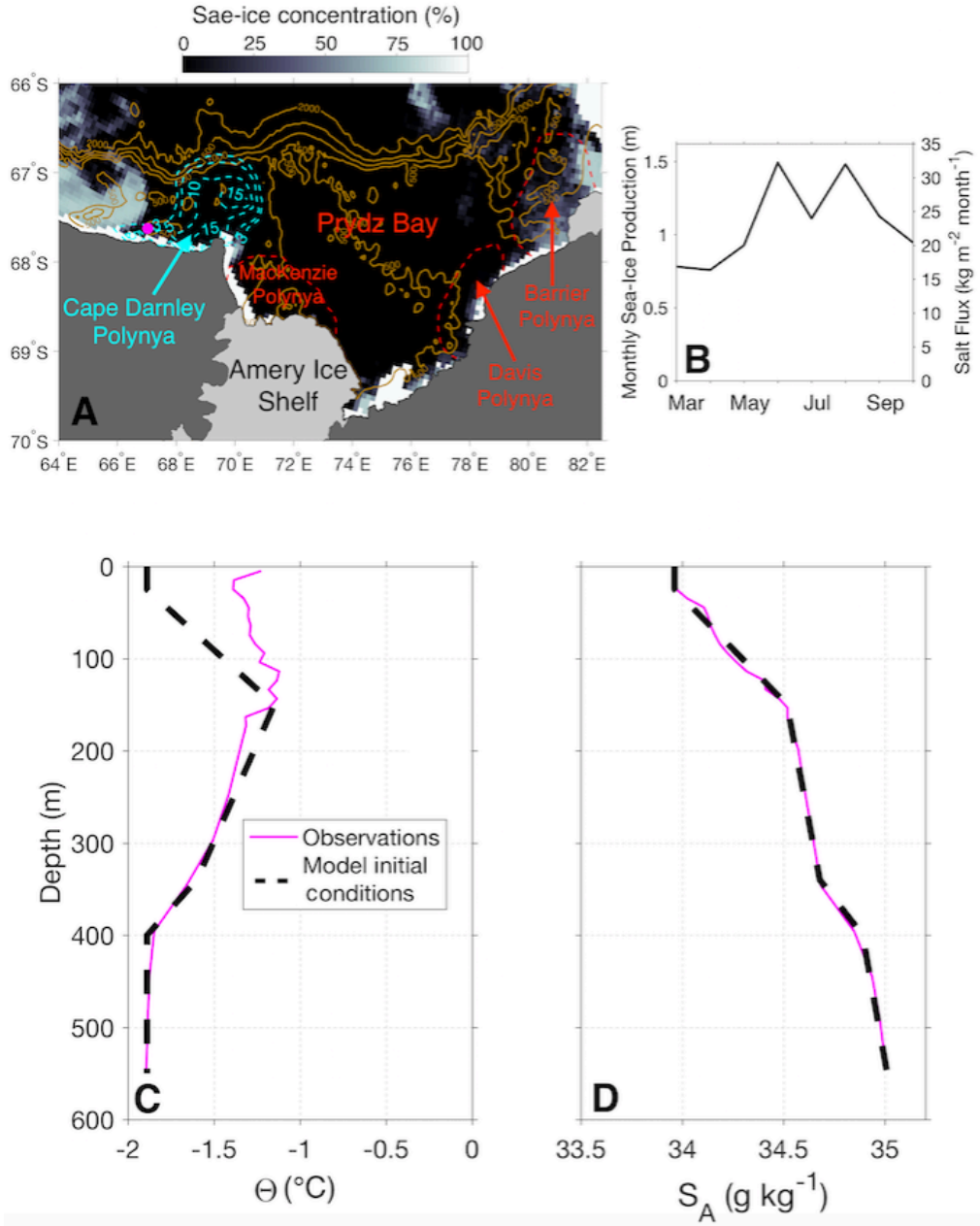

Figure 5.7. Cape Darnley Polynya. (A) Map of sea-ice concentration in the area of the Cape Darnley Polynya on 25 February 2011 (Spreen et al., 2008). The cyan dashed lines are contours of the 2011 annual sea-ice production (m) (Tamura et al., 2016). The Cape Darnley Polynya is characterized by low sea-ice concentration in summer and high sea-ice production in winter. In red are the boundaries (3-m contours of annual sea ice production) of the polynyas formed in Prydz Bay. Overlaid are the bathymetry and the coastline (Fretwell et al., 2013). (B) Monthly sea-ice production and associated salt flux in 2011 averaged over the area of the Cape Darnley Polynya. (C) Magenta line is a vertical profile of conservative temperature Θ measured on 22 February 2011 in the Cape Darnley Polynya (see magenta dot in (A) for location). The black dashed line is the profile used as initial condition for the mixed-layer model. For this we assume that the surface temperature is at the surface freezing point when sea ice starts to grow in March and we linearly interpolate between the surface layer and ~150 m, the base of the seasonal pycnocline. Stratification at high latitudes is dominated by salinity and therefore the choice of the temperature profile used to fill the near surface data does not influence the model results. (D) as (C) but for absolute salinity S_A.

Table 5.1. Moorings on the Sabrina Coast.

Mooring	**Latitude** (°S)	**Longitude** (°E)	**Deployment Period** (dd/mm/yy)	**Ocean Depth** (m)	**Instrument**	**Measurements**	**Recording Interval** (minutes)	**Instrument Depth** (m)
T1	66°32.558'	119°12.685'	18/02/2014 to 03/01/2015	708	SBE37 Microcat	Temperature Salinity Pressure	10	326
					SBE37 Microcat	Temperature Salinity Pressure	10	488
					SBE37ODO Microcat	Temperature Salinity Pressure	60	651
					SBE37 Microcat	Temperature Salinity	10	705
T2	66°12.628'	120°37.638'	22/02/2014 to 26/12/2014	501	SBE37 Microcat	Temperature Salinity Pressure	10	320
					SBE37 Microcat	Temperature Salinity Pressure	10	384
					SBE37 Microcat	Temperature Salinity Pressure	10	447
					SBE37 Microcat	Temperature Salinity	10	499
T3	66°30.082'	120°27.398'	05/03/2014 to 25/12/2014	550	SBE37 Microcat	Temperature Salinity Pressure	10	320
					SBE37 Microcat	Temperature Salinity Pressure	10	406
					SBE37 Microcat	Temperature Salinity	10	548

Chapter 6

Warm water access to the continental shelf near the Totten Glacier

This chapter has been submitted:

Silvano, A., S. R. Rintoul, K. Kusahara, B. Peña-Molino, E. van Wijk, D. E. Gwyther, and G. D. Williams (in review), Warm water access to the continental shelf near the Totten Glacier. *J. Geophys. Res. Oceans*.

6.1. Abstract

Warm Modified Circumpolar Deep Water (MCDW) from the Southern Ocean drives rapid basal melt of the Totten Ice Shelf on the Sabrina Coast (East Antarctica), affecting the mass balance of the grounded Totten Glacier. Recent observations show that MCDW accesses the continental shelf through a depression at the shelf break. Here we show hydrographic and bathymetric data collected for two consecutive years by ice-capable profiling floats in previously uncharted areas south of the shelf break. The depression is up to 900 m deep and provides a pathway for persistent inflow of warm (0°C to 1°C) MCDW to the inner shelf. In Austral autumn and early winter MCDW intrusions are up to 0.5°C warmer and are ~75 m thicker than in spring and summer. Using a combination of offshore observations and an ocean model, we propose that seasonality of the flow on the continental slope explains the seasonality of the intrusions. The MCDW layer on the upper slope is warmer and thicker to the east of the depression than to the west. In autumn and early winter a strong, top-to-bottom westward current (Antarctic Slope Current) transports the warmer and thicker MCDW layer along the slope and is diverted poleward at the eastern entrance of the depression. A bottom eastward current (Antarctic Slope Undercurrent) develops in other months, allowing cooler and thinner intrusions to enter the depression from the west. Our study illustrates how circulation on the Antarctic slope regulates the delivery of ocean heat to the continental shelf and ultimately to the ice shelves.

6.2. Introduction

Recent satellite observations have shown that the Antarctic Ice Sheet is losing mass at an accelerating rate (Velicogna et al., 2014), with the most rapid loss observed in the Amundsen and Bellingshausen sectors in West Antarctica (Harig and Simons, 2015; Shepherd et al., 2018). The

that form where outlet glaciers reach the ocean (Scambos et al., 2004; Pritchard et al., 2012). In case of thinning or collapse, the backstress that ice shelves exert on the grounded glaciers reduces or vanishes. This process accelerates the flow of the outlet glaciers into the ocean, triggering a net mass loss of the Antarctic Ice Sheet that contributes to sea level rise.

The primary forcing causing ice-shelf thinning is thought to be ocean heat flux (Pritchard et al., 2012; Christianson et al., 2016). The largest reservoir of ocean heat in the Southern Ocean is the Circumpolar Deep Water (Rintoul and Naveira Garabato, 2013), a warm (2-3°C) and salty (salinity ~ 34.7) water mass found below 2000 m depth north of 40°S. The Circumpolar Deep Water shoals south of 40°S due to wind-driven upwelling (Marshall and Speer, 2012; Greene et al., 2017). As it moves poleward, the Circumpolar Deep Water mixes with cold Antarctic waters, losing its core properties but maintaining a temperature over 0°C as it moves poleward (Orsi et al., 1995). It is then referred to as Modified Circumpolar Deep Water (MCDW). MCDW is observed on the Antarctic upper continental slope roughly between 400 and 1000 m depth (e.g. Bindoff et al., 2000; Walker et al., 2013), where it can access the continental shelf.

MCDW found on the upper slope is able to reach the continental shelf in many regions around Antarctica. The warmest intrusions are observed in West Antarctica, where MCDW on the continental shelf of the western Antarctic Peninsula (Moffat et al., 2009), Amundsen (Jacobs et al., 2012) and Bellingshasen seas (Jenkins and Jacobs, 2008) is above 0.5°C. Here MCDW accesses the continental shelf in the bottom layer, overlaid by a layer of fresh and cold Winter Water that is the product of winter mixing near the surface. Warm water is thus able to reach the ice-shelf cavities and drive rapid basal melt at depth.

Recently, warm (up to 0.3°C) MCDW has been observed in the bottom layer on the continental shelf of the Sabrina Coast in East Antarctica (see Figure 6.1 for location; Silvano et al., 2017). Here, relatively warm MCDW reaches the Totten and Moscow University ice shelves to drive rapid basal melt (Rintoul et al., 2016; Silvano et al., 2017). As in the Amundsen and Bellingshsausen seas, rapid basal melt of the Totten and Moscow University ice shelves is associated with mass loss and acceleration of the grounded portion of the Totten and Moscow University glaciers (Li et al., 2016; Mohajerani et al., 2018). These observations suggest that MCDW triggers mass loss of this sector of the East Antarctic Ice Sheet (Silvano et al., 2016), which holds the equivalent of 5 m of global sea level rise (Mohajerani et al., 2018).

While the importance of MCDW for melting of ice shelves is well documented, the physical mechanisms that allow MCDW to access the Antarctic continental shelf remain poorly understood (Gille et al., 2016; Rintoul, 2018). This is mostly due to the paucity of long-term observing systems capable of collecting data over multiple seasons and years. The few existing observations suggest that the main way for warm MCDW to access the continental shelf is through glacially scoured troughs in the seafloor (e.g. Jacobs et al., 2012). Many of these troughs connect the shelf break with the ice-shelf cavities, thus providing a direct pathway for MCDW to reach the ice shelves (Jenkins et al. 2016).

Interaction between currents on the upper continental slope and troughs at the shelf break promotes MCDW intrusions onto the continental shelf (e.g. Jenkins et al., 2016; Dinniman et al., 2018). Easterly winds drive a westward current along most of the Antarctic slope, the Antarctic Slope Current (e.g. Armitage et al., 2018). The Antarctic Slope Current transports MCDW and it is diverted poleward along isobaths when it encounters a trough, causing intrusions from the east of a trough (Klinck, 1996). Intrusions from the east of a trough are observed in the Ross Sea (Orsi and Wiederwohl, 2009; Kohut et al., 2013), Weddell Sea (Darelius et al., 2016), Bellingshausen Sea (Zhang et al., 2016) and on the Adélie Coast (Williams et al., 2008). The MCDW then follows a cyclonic circulation within the trough to reach the ice shelves (e.g. Zhang et al., 2016; Darelius et al., 2016).

Observations have revealed the presence of an eastward undercurrent (the Antarctic Slope Undercurrent) that forms beneath the westward Antarctic Slope Current in some locations (Heywood et al., 1998; Núñez-Riboni and Fahrbach, 2009; Chavanne et al., 2010; Walker et al., 2013). Where the undercurrent encounters a trough, its flow is diverted poleward (Klinck 1996; Allen and Durrieu de Madron, 2009) and a cyclonic circulation arises within the trough that steers the MCDW poleward (St-Laurent et al., 2013). In this case, MCDW intrusions originate to the west of a trough, as observed in the Amundsen Sea (Walker et al., 2013; Assmann et al., 2013).

The interaction between currents on the upper slope and troughs at the shelf break is not the only mechanism that can drive cross-shelf exchange. Other processes can also be important, including waves on the upper slope (St-Laurent et al., 2013), tidal fluctuations (Stewart et al., 2018), curvature of the isobaths (Dinniman et al., 2003) and eddy fluxes (Nøst et al., 2011; Stewart and Thompson, 2015). These processes can be especially important in those regions where topographic depressions are absent at the shelf break and a geostrophic flow along isobaths cannot support

MCDW access to the continental shelf.

In this study we focus on intrusions of MCDW onto the continental shelf of the Sabrina Coast. A recent survey has revealed the presence of a deep (> 500 m) depression at the shelf break that facilitates the intrusions of MCDW onto the continental shelf (Nitsche et al., 2017). Here we show new in-situ oceanographic and bathymetric observations collected in deep areas of the depression on the inner continental shelf. Measurements were collected for two consecutive years by a novel application of ice-capable profiling floats. Profiles from CTD-instrumented seals are used to characterize the properties of MCDW on the upper continental slope. Finally, simulations from a moderately high resolution model are used to investigate mechanisms of cross-shelf exchange.

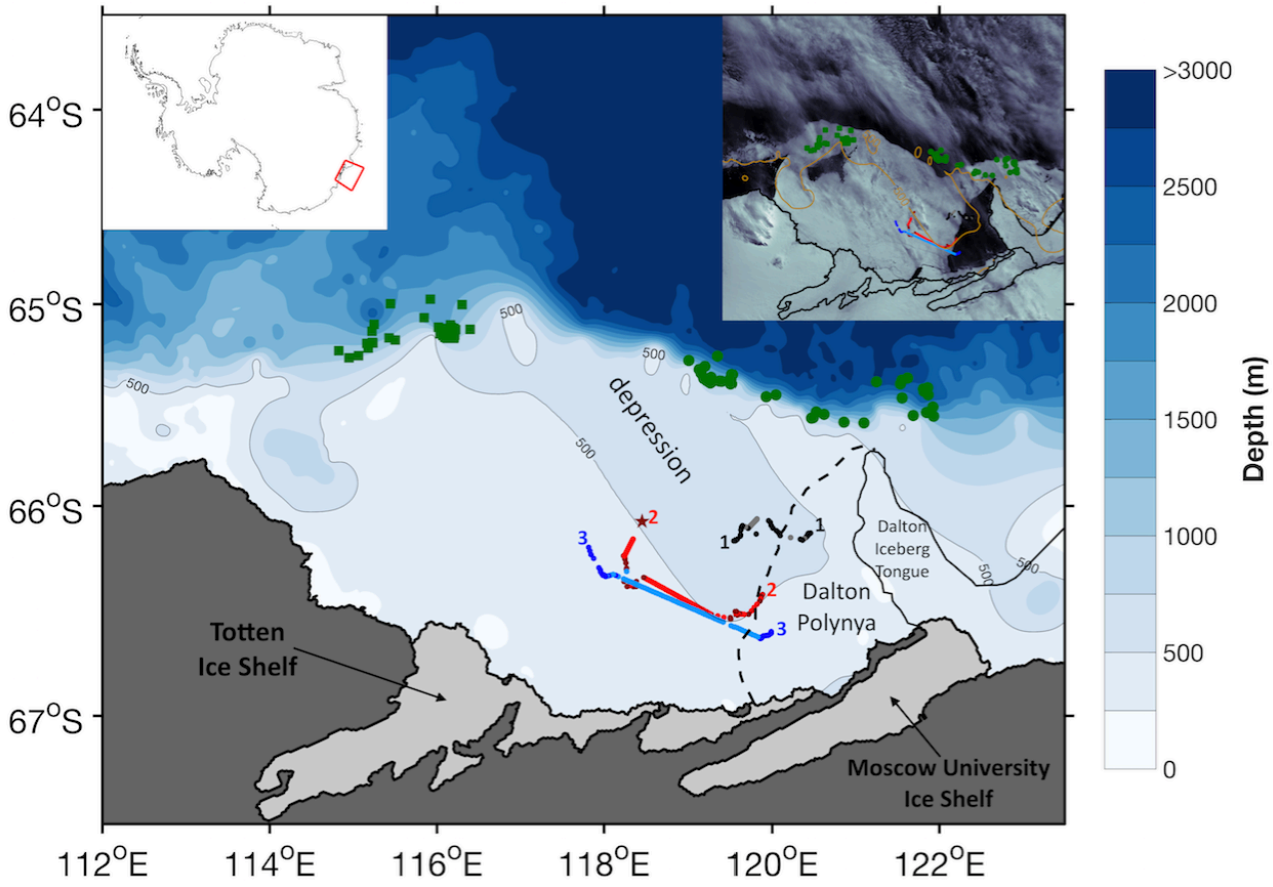

Figure 6.1. Sabrina Coast. Map of the survey area with overlaid bathymetry and coastline (IBCSO; Arndt et al., 2013). The contour of the 500-m isobath is included in black to highlight the depression. Black, red and blue dots indicate the location of profiles collected by float 1, float 2 and float 3, respectively. Lighter dots show interpolated locations when the floats were under sea ice, while darker dots show locations when the floats surfaced. Floats were deployed in the Dalton Polynya and then drifted to the west. The red star shows the location of the last time float 2 surfaced (November 2017). The Dalton Polynya forms in the lee of the Dalton Iceberg Tongue, a combination of grounded icebergs and fast ice located to the north of the Moscow University Ice Shelf. Green circles (square) show the location of data collected by CTD-instrumented seals on the upper slope to the east (west) of the depression. In the upper right inset is a MODIS (Scambos et al., 1996) image (22 January 2015) with coastline overlaid. The area of the survey is highlighted in red in the upper left inset.

6.3. Methods

6.3.1. Oceanographic measurements

6.3.1.1. On-shelf measurements

Three ice-capable profiling floats were deployed in the Dalton Polynya (Figure 6.1) between late December 2014 and early January 2015 on the R/V *Aurora Australis* voyage (cruise AU1402). Profiles of temperature, salinity and pressure were collected every five days. Data from the profiling floats after delayed-mode quality control is expected to be accurate to within ± 2.4 dbar for pressure, ± 0.01 psu for practical salinity, and ± 0.002 °C for temperature. The floats were designed to park on the bottom. In this way they reduced drift between consecutive casts and recorded the bottom pressure, providing information on the bathymetry of the depression. Geolocation of the profiling float was recorded for every surfacing events during data collection with a Global Positioning System fix. Positions have been linearly interpolated when the floats were under sea ice (lighter dots in Figure 6.1 show interpolated positions). Uncertainty in the linearly interpolated float positions may be of the order of 10's of kilometres from the actual location.

Float 1 was deployed in the northern part of the Dalton Polynya and collected data for about 13 months until late January 2016 before disappearing under sea ice. Float 2 was deployed further south and collected data until late November 2017 (see red star in Figure 6.1 for location of this last surface event), when it surfaced for the first and only time since May 2016 allowing to transmit data collected until late January 2017. Unfortunately, the float did not have enough time at the surface to transmit the data collected between February 2017 and November 2017. Float 2 transmitted a total of about two years of data. Float 3 was deployed near float 2 and collected data for about 15 months until late March 2016, before finishing under sea ice and never surfacing again.

In the study we focus on the seasonality of the MCDW detected by the floats. We refer to December, January and February as summer; March, April and May as autumn; June, July and August as winter; and September, October, November as spring.

6.3.1.2. Off-shelf measurements

We use measurements from the Marine Mammals Exploring the Oceans Pole to Pole (MEOP-CTD) database (Roquet et al., 2013, 2014; see http://www.meop.net) to characterize water properties over the continental slope. These data were collected between 2012 and 2015 by CTD-instrumented southern elephant seals (*Mirounga leonina*) on the upper slope of the Sabrina Coast (Figure 6.1). Data were collected during autumn and winter months (March to July). Measurements were

calibrated against historical data in nearby regions (Roquet et al., 2011). The calibrated data have estimated uncertainties of 0.02°C for temperature and 0.02 psu for practical salinity. We use data collected in a band between the 1000 m isobath and 20 km offshore of the 1000 m isobath in order to detect the MCDW that can potentially intrude onto the depression, without being strongly affected by outflowing water from the depression (e.g. Zhang et al., 2016).

6.3.2. Ocean model

In this study we use the monthly output of a coupled ocean/sea ice/ice shelf numerical model (Kusahara and Hasumi, 2013, 2014; Kusahara et al., 2017) to assess temporal and spatial variability of the ocean flow over the continental slope and shelf break. The model uses an orthogonal, curvilinear coordinate horizontally. Two singular points are placed at 110°E, 40°S and at 110°E, 77°S to increase the horizontal resolution around East Antarctica (~7 km on the Sabrina Coast). In the vertical the model uses a hybrid σ-/z-coordinate. The σ coordinate is applied to the uppermost levels between the free surface and 15 m below the mean surface level to avoid outcropping of surface layers, and the z coordinate is applied below. The vertical grid spacing in the z-coordinate region is 5 m (1 grid) just below the σ coordinate and 20 m (49 grids) in depth range from 20 to 1000 m. We use 20 grids at a spacing of 50 m between 1000 and 2000 m, and 20 grids at a spacing of 150 m between 2000 and 5000 m. The maximum ocean depth in the model is set to 5000 m to save computational resources. The model bathymetry is from the International Bathymetric Chart of the Southern Ocean (IBCSO; Arndt et al., 2013). Surface boundary conditions are calculated from the atmospheric surface data of ERA-Interim (Dee et al. 2011). The model has been spun up for 10 years using the 1979 forcing repeatedly, before performing a hindcast simulation for the period 1979-2016. For more details about the model setup, the reader is referred to Kusahara et al. (2017).

The numerical model adequately reproduces water masses, stratification and currents observed on the upper slope and shelf break on the Sabrina coast (see Supporting information, Figures 6.10-6.14). We note that there are almost no ship-based bathymetric data of the depression south of the shelf break. As a consequence, the numerical model cannot well reproduce water mass properties and circulation in the depression. The modelling results are used in this study to investigate processes on the upper slope and shelf break where the IBCSO bathymetry is more reliable (Nitsche et al., 2017).

6.4. Results

6.4.1. Observations

6.4.1.1. Bathymetry of the depression

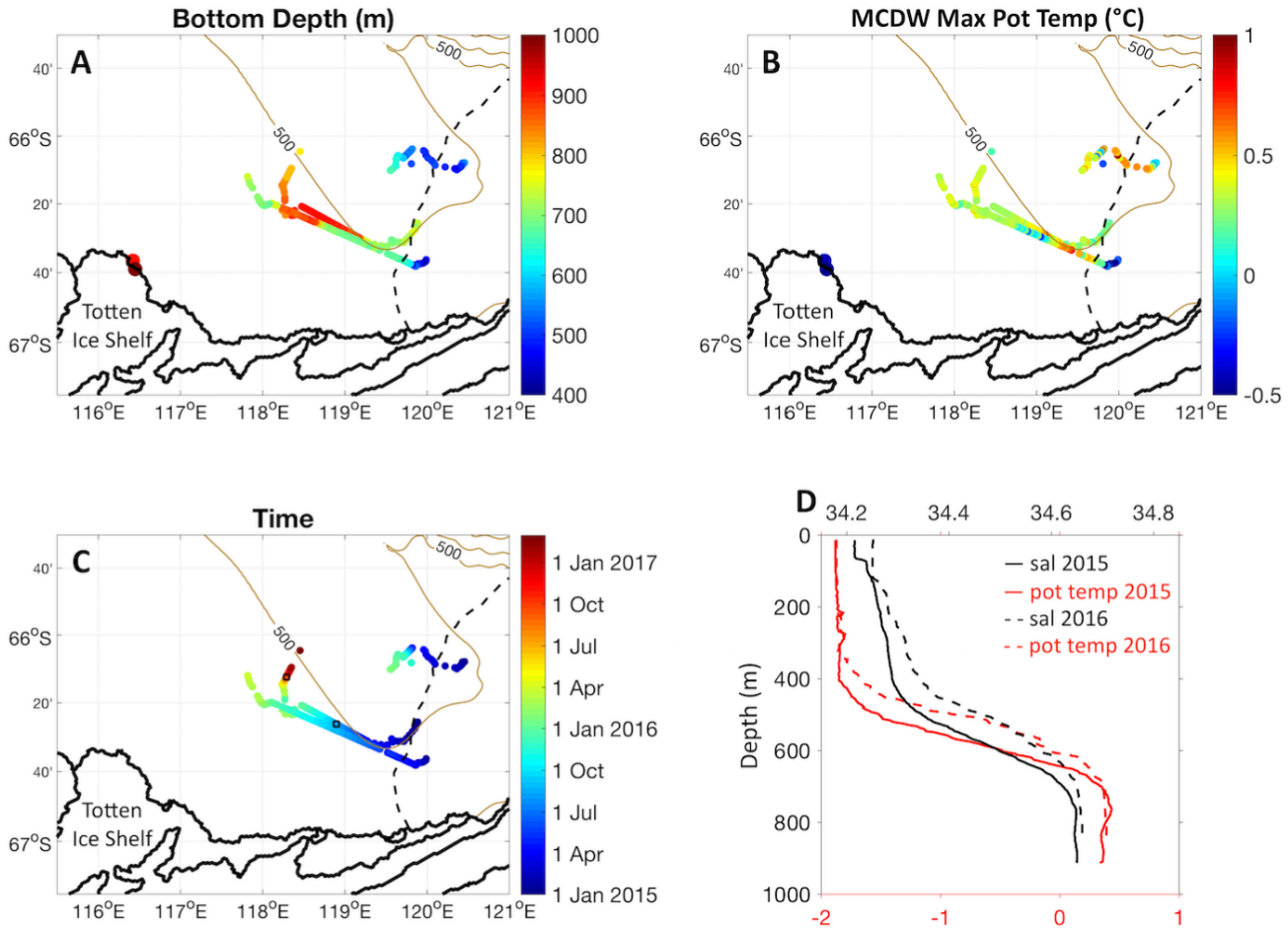

Figure 6.2. Float observations. (A) Bottom depth (m), (B) maximum MCDW potential temperature (°C) and (C) acquisition time for each profile collected by the floats. Overlaid in brown are bathymetric contours from IBCSO (Arndt et al., 2013). In (A) and (B) are included observations collected in December 2015 at the front of the Totten Ice Shelf where two deep troughs allow intrusions of MCDW into the ice cavity (Rintoul et al., 2016). (D) Representative vertical profiles of potential temperature (black) and salinity (red) collected in the depression in August 2015 (solid lines) and August 2016 (dashed lines). The interpolated location of these profiles is indicated by the black squares in (C).

The floats provide unique information about the bathymetry in deep areas of the depression on the inner continental shelf of the Sabrina Coast where no ship-based bathymetric data are available due to the persistent sea ice cover (Gulick et al., 2017; Fernandez et al., 2018; Silvano et al., 2017). Bathymetry is shallow in the polynya (< 500 m), but it gets deeper as the profiling floats moved westward into the depression (Figure 6.2A). The floats reached the eastern flank of the depression between March and May 2015 (see deepening of the seafloor in Figure 6.3B). Float 1 disappeared in January 2016 (Figure 6.2C) while still on the eastern flank of the depression at ~700 m depth (Figure 6.2A). Float 2 and 3 sampled deep areas (up to 900 m as detected by float 2) of the depression and then reached shallower areas to the west of the depression (Figure 6.2A) before

disappearing in January 2017 and March 2016, respectively (Figure 6.2C). The depression is up to 300 m deeper than the maximum depth provided by the IBCSO bathymetry (~600 m). In autumn, winter and spring sea ice covered the depression and locations of the profiles are interpolated (see straight lines in Figure 6.2). It is therefore not possible from our dataset to estimate the accurate shape and width of the depression.

6.4.1.2. Circulation in the depression

A picture of the ocean circulation in the depression is provided by the trajectories of float 2 and 3 (Figure 6.2). Both trajectories suggest a cyclonic circulation as seen in other depressions around Antarctica (e.g. Assmann et al., 2013; Zhang et al., 2016). Initially the floats moved south-westward along the eastern flank of the depression. Then, the drift of the floats when they were under sea ice was westward, presumably following the bathymetry along a southern edge of the depression. Finally, the two floats moved northward most likely along the western flank of the depression. It is not possible to quantify seasonal changes in the circulation because the floats spent most of their life under sea ice and therefore we cannot estimate the distance travelled during their drift.

6.4.1.3. MCDW intrusions

MCDW is observed throughout the two years of the observations (Figure 6.2B). The water column remains stratified year-round, with warm and salty MCDW overlaid by fresh and cold Winter Water (see typical winter profiles in Figure 6.2D). MCDW in the depression is typically warmer than 0°C, while it is cooler in the shallow waters (< 500 m) of the polynya. The MCDW temperature is higher in autumn and early winter (up to 0.9°C in March and June) compared to the rest of the year (< 0.4°C) (see Figure 6.3A). In autumn, one cooler (≤ 0.4°C) event is observed by all floats between late April and early May. Other than that, some isolated cold (< 0°C) events are observed at different times by different floats, especially by float 1. Moreover, float 1 shows strong temporal variability on time scales similar to the sampling rate (5 days, see black dashed line in Figure 6.3A). This "high frequency" variability is greatly reduced in the deeper measurements collected by float 2 and 3. This signal might come from topographic Rossby waves with a period of few days, as observed in the Dotson trough in the Amundsen Sea (Wåhlin et al., 2016). In this work we focus on the seasonality of the MCDW properties and higher frequency variability is not discussed (because the sampling rate is not adequate to study these types of oscillations).

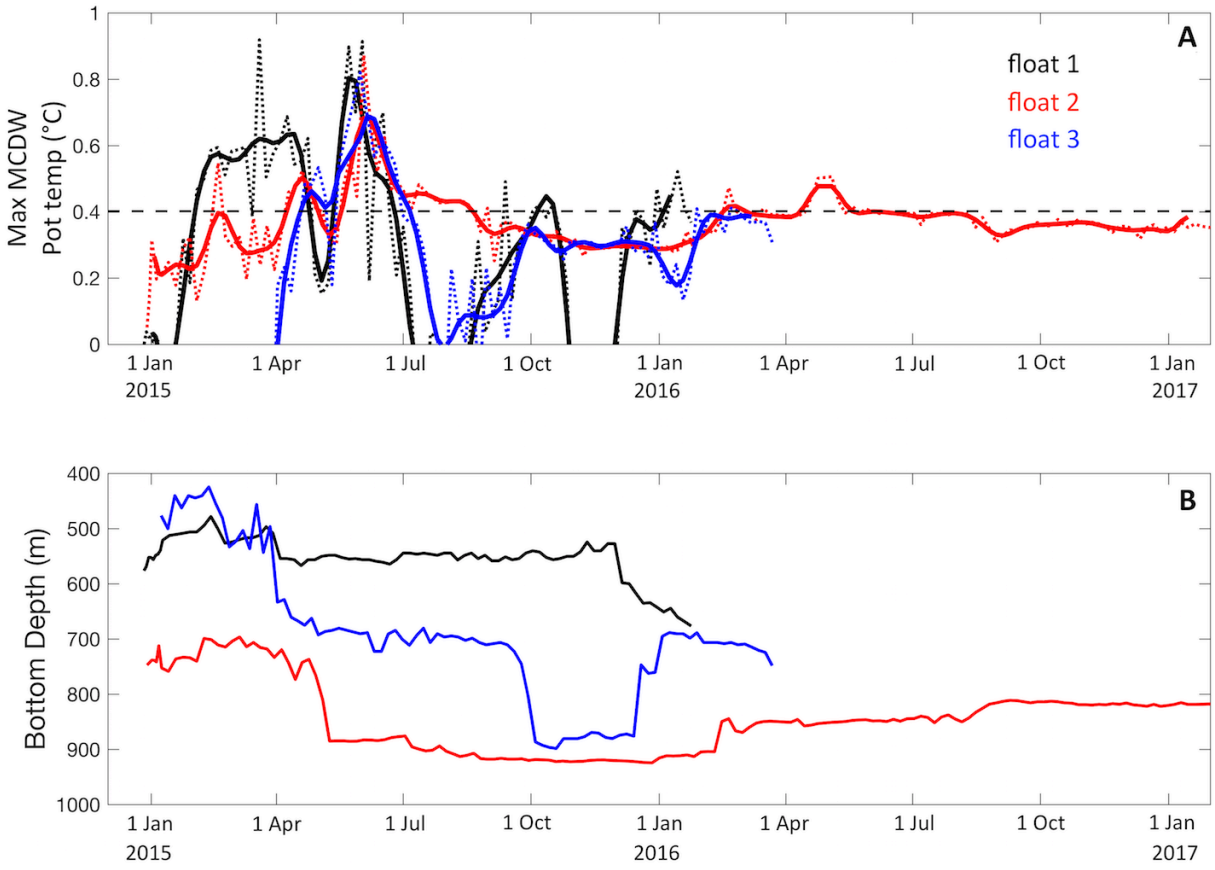

Figure 6.3. MCDW intrusions. Time series of (A) maximum MCDW potential temperature (°C) and (B) bottom depth measured by float 1 (black), float 2 (red) and float 3 (blue). In (A) the thick solid lines show data low-pass filtered with a 30-day fourth-order Butterworth Filter, while the dotted lines show the raw data. The dashed black lines in (A) shows the contour of 0.4°C, which approximately discriminates between "warmer" and "colder" intrusions.

We provide two lines of evidence that indicate that the observed seasonality is due to temporal variability of MCDW in the depression rather than spatial variability associated with drift of the floats. 1) A general pattern of higher MCDW temperature in autumn and early winter and lower temperatures during other times is observed by all floats despite different locations. 2) The seasonality is most apparent when the changes in seafloor depth during float drift is minimal, indicating that bathymetric gradients during the drift cannot explain the observed temporal variability at the seasonal time scale. Float 2 measured ocean properties in the deepest areas surveyed, providing thus the most reliable data to analyse the MCDW intrusions. The clearest signal of the seasonality is seen between May 2015 and February 2016 when float 2 remained at ~900 m. During this period, the warmest temperatures were recorded in June (> 0.6°C), while the coolest temperatures were observed in December and January (~ 0.3°C). The same seasonality was observed by float 2 in 2016, even though the signal is smoother possibly because of mixing near the bottom during the transit of MCDW around the depression to reach the western flank (Venables et al., 2017). Indeed, MCDW showed a maximum in temperature above the seafloor between May

2015 and February 2016 (see solid lines in Figure 6.2D for a representative profile during this period). This maximum disappeared in profiles further "downstream" (on the western flank of the depression) and the properties near the bottom were vertically homogeneous, indicating mixing (see dashed lines in Figure 6.2D for a representative profile during this period).

To better characterize the seasonality of the MCDW in the depression, we reconstruct the seasonal cycle of the thickness and mean potential temperature of the MCDW layer using data collected by float 2, which best captured the MCDW intrusions. The 0°C isotherm well represents the top of the MCDW layer and the time variability of its depth is chosen to characterize the seasonality of the MCDW thickness. We define the mean MCDW potential temperature as the potential temperature vertically averaged between the depth of the 0°C isotherm and the bottom. We use a nonlinear regression model to reproduce the observations:

$$\chi(t) = \alpha D(t) + \beta \cos(\omega t) + \gamma \sin(\omega t) \qquad (6.1)$$

where χ represents observations (i.e. MCDW thickness and mean potential temperature), t is time, D is the bottom depth, ω is a frequency and α, β and γ are coefficients. This regression model aims to isolate the seasonality of the MCDW properties from the effect of varying topography that influence the observations, especially the thickness of the layer. The first linear term on the right end side of equation (1) characterizes the effect of topography. The last two terms are used to quantify the seasonal signal and for this purpose we use a frequency ω equal to one cycle per year.

The regression model well reproduces the observations (Figures 6.4A and 6.4B). The misfit between observations and the model is relatively large compared to the seasonality (misfit ~ 40% of the range between minimum and maximum values in Figures 6.4C and 6.4D). The misfit is mostly due to the unresolved high frequency variability described before. The MCDW layer is up to ~75 m thicker and ~0.11°C warmer in autumn and early winter compared to spring and summer (Figures 6.4C and 6.4D). Our regression model confirms that MCDW is warmer (and thicker) in the coolest months of the year. Surface cooling in autumn and winter therefore cannot explain the MCDW seasonality. Moreover, the seasonal variability is observed deep in the water column (> 500 m depth). Injection of glacial meltwater from nearby ice shelves occurs at shallower depths and therefore cannot affect the observed MCDW properties (Silvano et al., 2018). Changes in the properties of the MCDW intruding onto the continental shelf is thus a likely candidate to explain the observed seasonality.

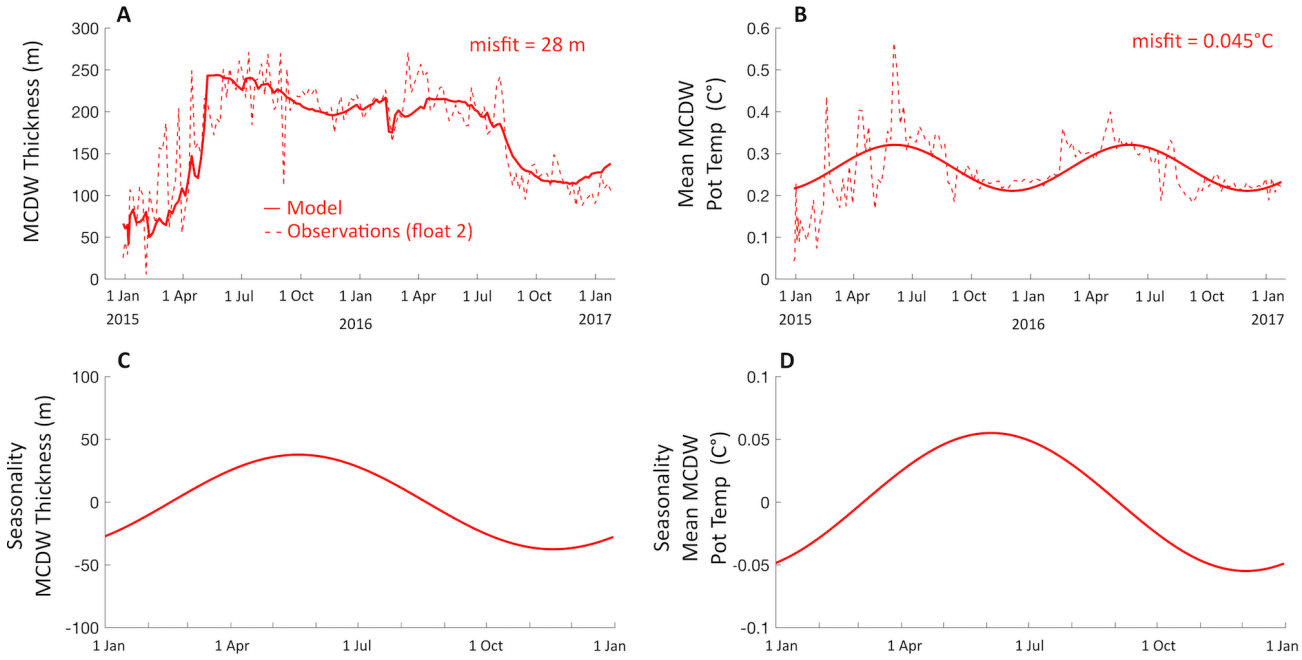

Figure 6.4. MCDW seasonality. Time series of (A) thickness and (B) mean potential temperature (°C) of the MCDW layer from float 2. The dashed lines are the observations while the solid lines are modelled values. Also shown is the mean error (or misfit) between observed and modelled values. Seasonality of the (C) thickness and (D) potential temperature of the MCDW layer.

6.4.1.4. MCDW on the upper continental slope

We now compare the MCDW properties in the depression with the MCDW observed on the upper slope by CTD-instrumented elephant seals (see Methods). We use data from all floats collected between March 2015 and February 2016 in order to include an entire year of observations of MCDW in the depression, avoiding data collected after February 2016 when the properties of the intrusions have been presumably modified by mixing (see previous section). We find that warmer intrusions (> 0.4°C) observed in autumn and early winter (March to June) share similar properties with MCDW found on the upper slope to the east of the depression (Figures 6.5A). The similarity is apparent at depths on the upper slope (500-700 m) slightly deeper than the shelf break depth of the depression (~500 m), consistent with MCDW upwelling on the upper slope. Cooler intrusions in other months resemble MCDW found on the slope to the west of the depression (Figures 6.5B), which is cooler compared to the MCDW found to the east of the depression. The overlap is most apparent with MCDW found at 500 to 700 m depth on the "western" slope, again consistent with upwelling. The opposite comparison shows that warmer intrusions do not overlap with MCDW found to the west of the depression (Figure 6.5C), while cooler intrusions only overlap with MCDW found to the east at ~1000 m depth (Figure 6.5D), too deep to access the depression (Bindoff et al., 2000; Nitsche et al., 2017). Finally, float data revealed a thicker layer of MCDW on the shelf in autumn and early winter (Figure 6.4C), in agreement with the shallower MCDW core

observed on the upper slope to the east of the depression (Figure 6.6A) compared to the west (Figure 6.6B).

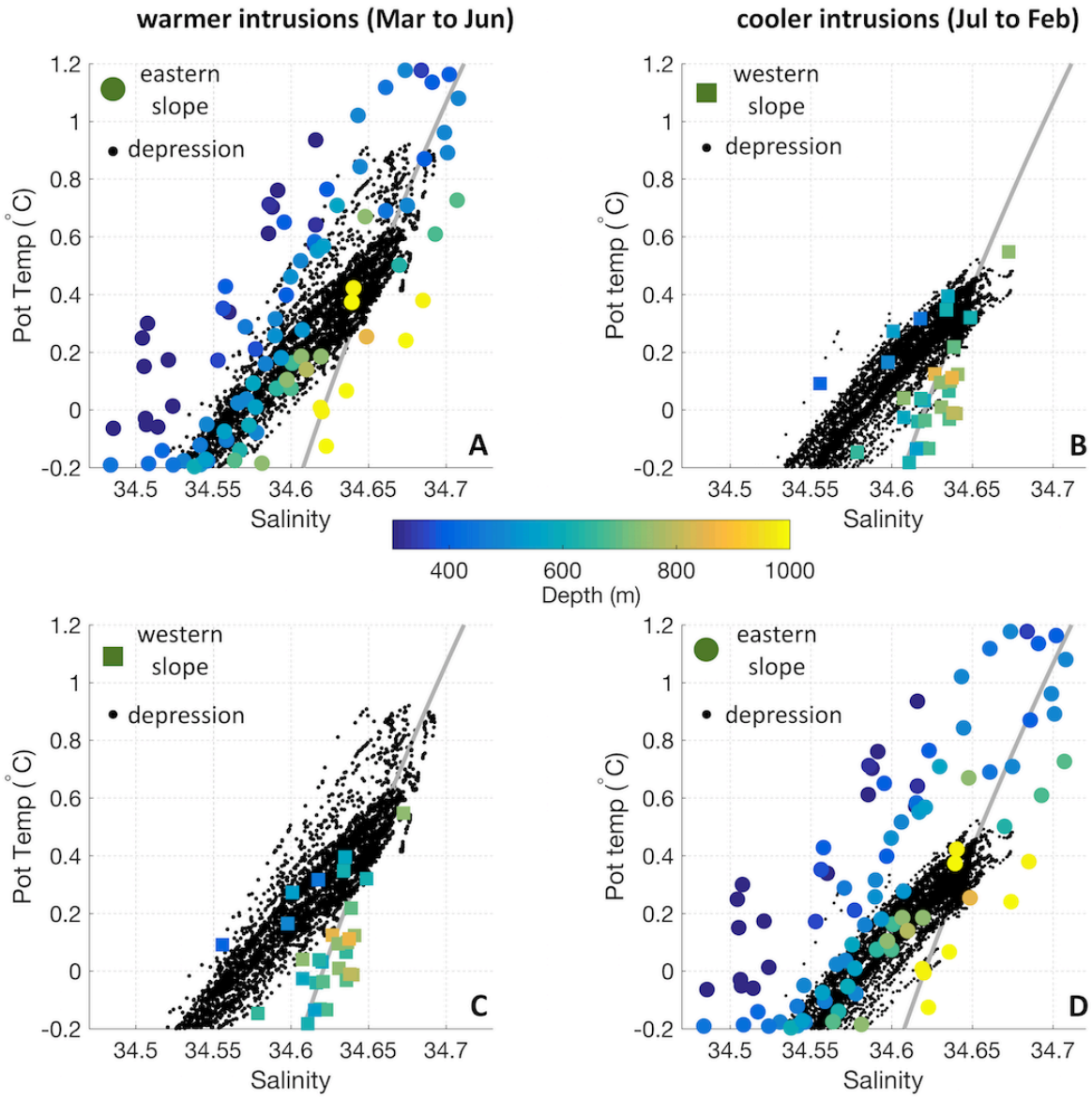

Figure 6.5. Sources of MCDW intrusions. Black dots are data of salinity versus potential temperature (°C) collected by all floats between March 2015 and February 2016 in the depression. Float data are separated in two periods: March to June (A, C) when intrusions are warmer and July to February (B, D) when intrusions are cooler. The 27.8 kg m^{-3} surface-referenced potential density contour is included in grey for reference. Seal data collected on the upper slope to the east of the depression ("eastern slope", green circles in Figure 6.1), color-coded according to depth, are superimposed in (A) and (D). Seal data collected on the upper slope to the west of the depression ("western slope", green squares in Figure 6.1) are shown in (B) and (C).

The data collected by the seals are biased toward autumn and winter. However, the difference in MCDW temperature (~ 0.5°C) between east and west of the depression observed by the seals is also observed in summer (Figure 10B in Wakatsuchi et al., 1994). This suggests that the seal observations provide a representative indication of the MCDW that can access the depression. The combination of on-shelf measurements collected by the floats and off-shelf measurements collected

by the seals suggests that warmer MCDW enters the depression from the east in autumn and early winter, and cooler MCDW enters from the west during the rest of the year. We now use a numerical model to test if this mechanism is plausible.

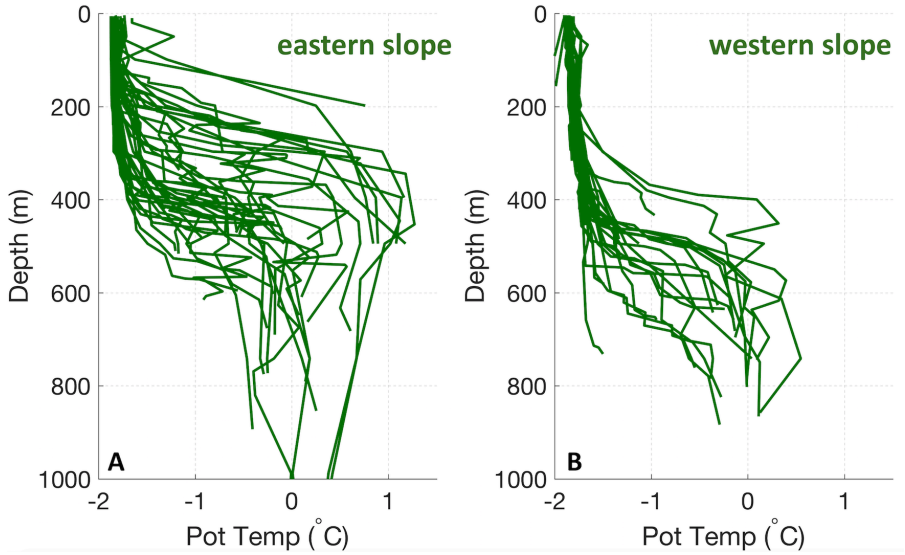

Figure 6.6. MCDW on the upper slope. (A) Vertical profiles of potential temperature (°C) collected by CTD-instrumented seals on the upper slope to the east of the depression (eastern slope, green circles in Figure 6.1). (B) Vertical profiles collected on the upper slope to the west of the depression (western slope, green squares in Figure 6.1).

6.4.2. Modelling MCDW intrusions

In Figure 6.7 we show maps of the monthly model output between March 2015 and February 2016, to compare the modelling results with the float observations shown in the previous section. We show potential temperature and velocity vectors at 450 m depth to capture the modelled intrusions of MCDW onto the depression. In good agreement with our inference from observations, the warmer intrusions in autumn and early winter originate to the east of the depression. The warmest peaks observed by the floats are in March and June (Figure 6.3), consistent with the stronger modelled inflow of MCDW from the east of the depression in the same months. In April and May the model shows also some intrusions from the west of the depression and that might reflect the cooling observed by all floats between late April and early May 2015 (Figure 6.3). During other months (July to February), MCDW accesses the depression only from the west.

As seen in the seal observations, off-shelf MCDW is warmer to the east of the depression, where the "warm core" is closer to the shelf break. However, in contrast to observations, within the depression there is minimal seasonal variability in the MCDW properties. This might be due to the resolution of the model, which is not adequate to represent the temporal variability of the properties

of the intruding MCDW near the seafloor (see Supporting information). Moreover, the model bathymetry is presumably unrealistic at the western entrance of the depression, since it is based on the interpolation of few measurements (Nitsche et al., 2017; see for example the unrealistic bathymetric "bump" centered at ~117°E, 65°S in Figure 6.1). Therefore the flow once the MCDW enters the depression from the west cannot be well reproduced by the model.

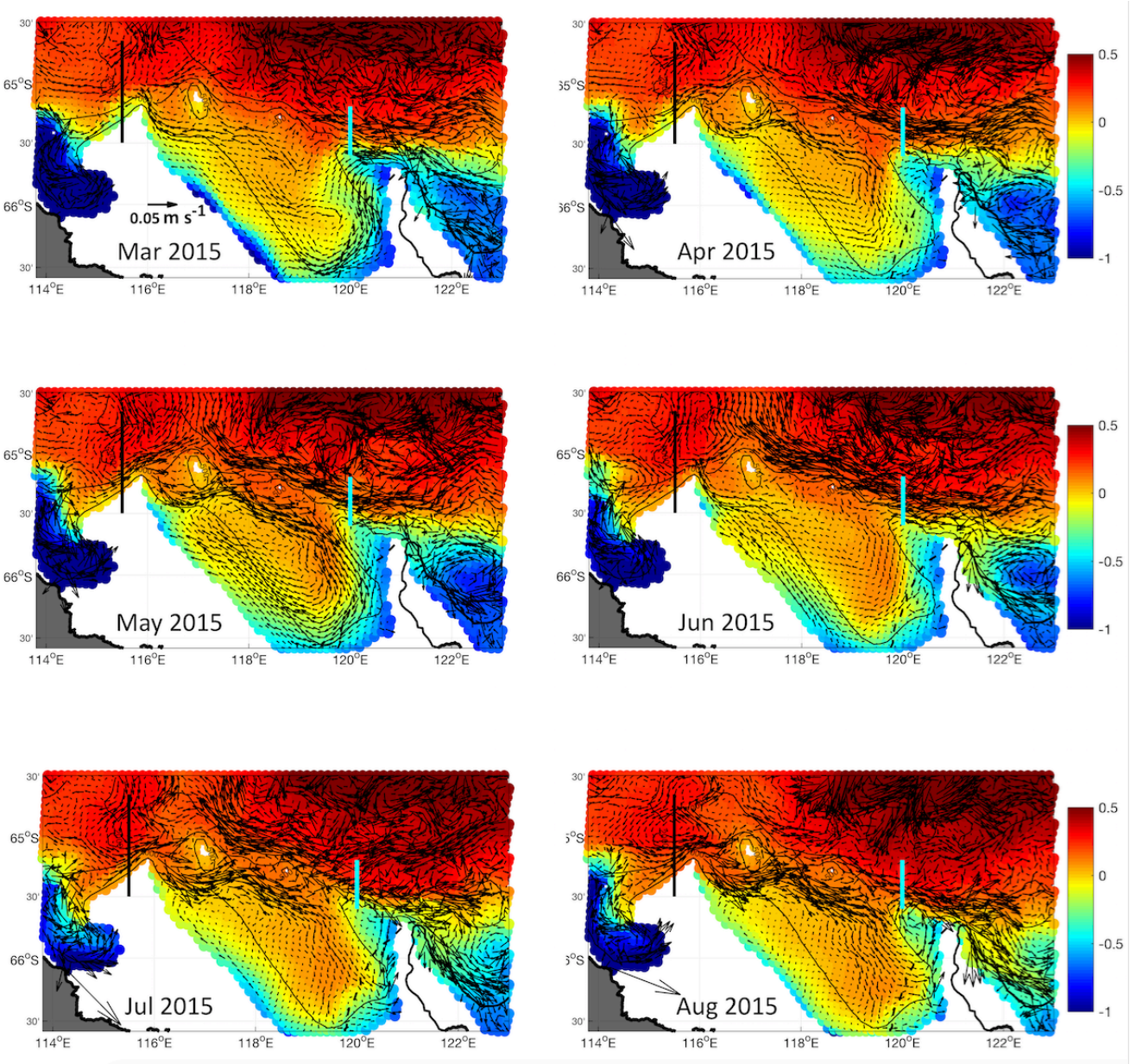

Figure 6.7. Modelled MCDW intrusions. Potential temperature (°C, color) and velocity (vectors) at 450 m depth between March 2015 and February 2016 from the monthly model output. The solid cyan (black line) in the panels indicates the location of transect shown in Figure 6.8 (Figure 6.9).

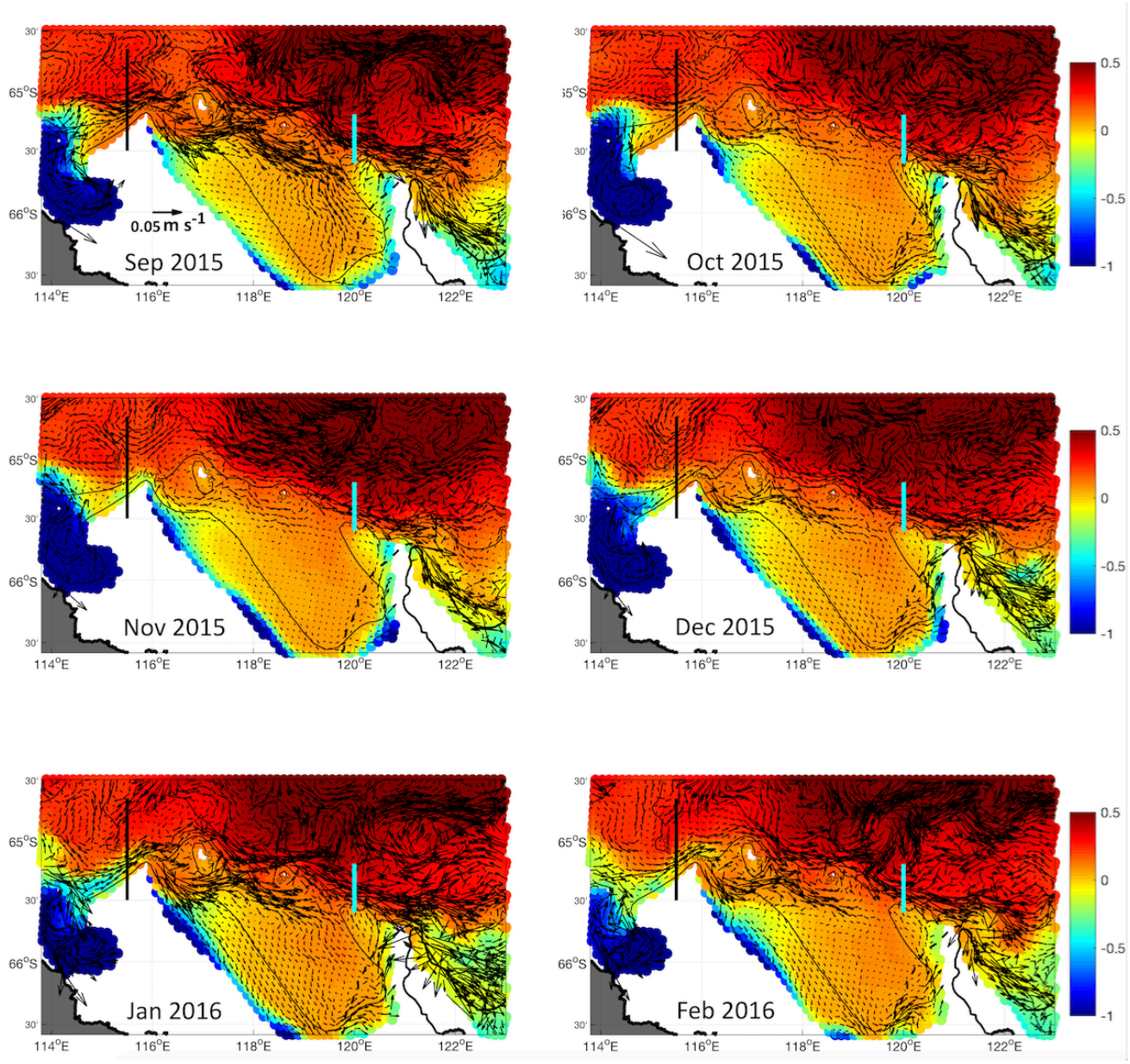

Figure 6.7. Continued.

We now show the modelled currents on the upper slope and shelf break at ~120°E, just east of the depression (Figure 6.8; see Figure 6.11 for comparison with observations at this transect). Between March and June there is a strong westward flow, the Antarctic Slope Current. During this period the westward flow extends from the surface to the bottom, except in April when a weak eastward flow near the sea floor is modelled at the shelf break. MCDW is transported in the bottom layer by the Antarctic Slope Current and is diverted onto the depression at its eastern entrance (Figure 6.7). Between July and February the westward flow weakens and an eastward current develops on the upper slope and at the shelf break. The eastward current is faster near the seafloor, resembling the Antarctic Slope Undercurrent observed in other locations around Antarctica (e.g. Chavanne et al., 2010; Walker et al., 2013). During these months, the eastward flow at the shelf-break depth (~ 500

m) near the western entrance of the depression (see ocean currents at 115°E in Figure 6.9) allows MCDW to enter the depression from the west (Figure 6.7).

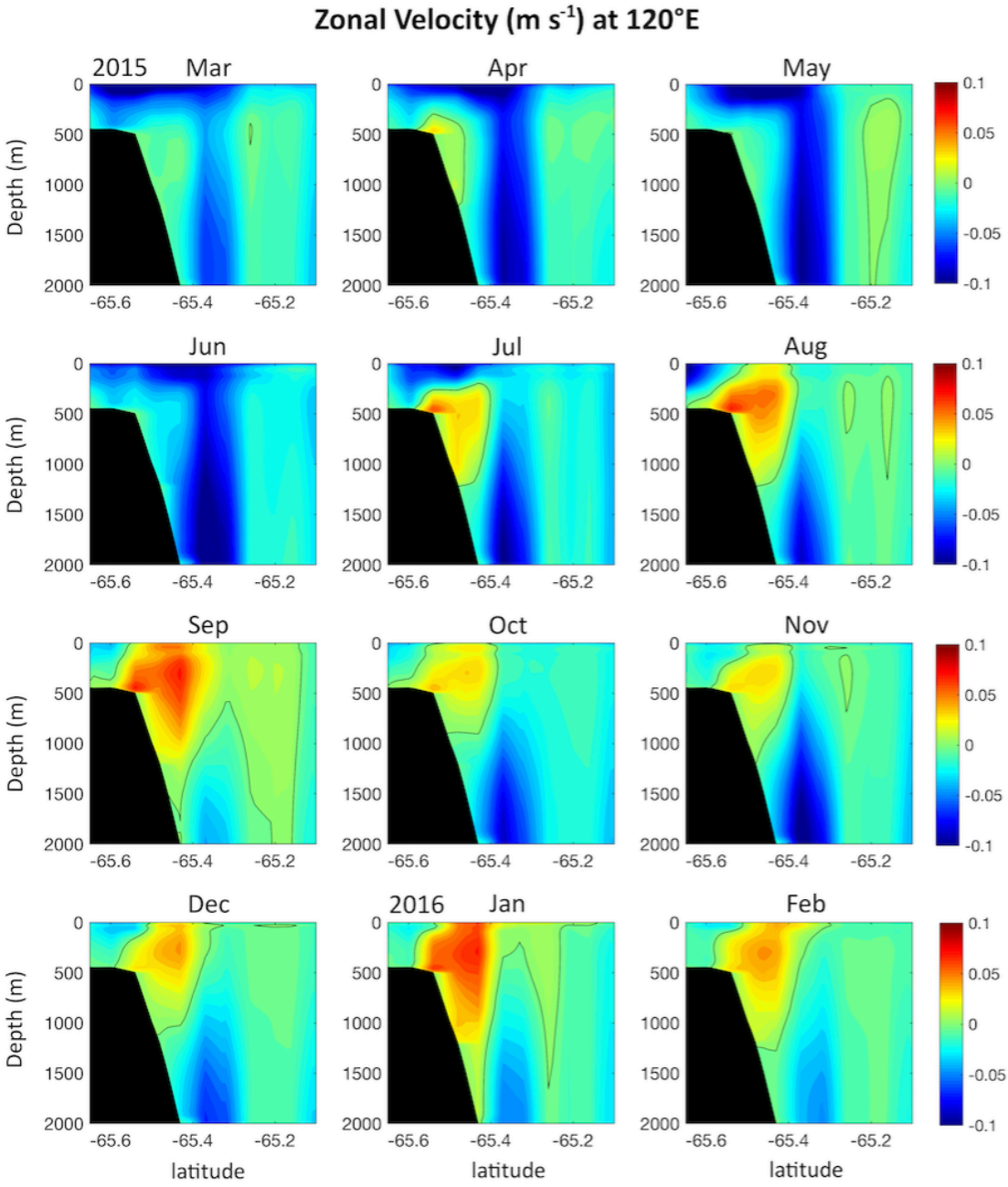

Figure 6.8. Modelled flow on the slope at 120°E. Zonal velocity (m s^{-1}, color) between March 2015 and February 2016 from the monthly model output at ~120°E (see cyan line in Figure 6.7 for location). Positive is eastward. The black line is the contour of 0 m s^{-1}.

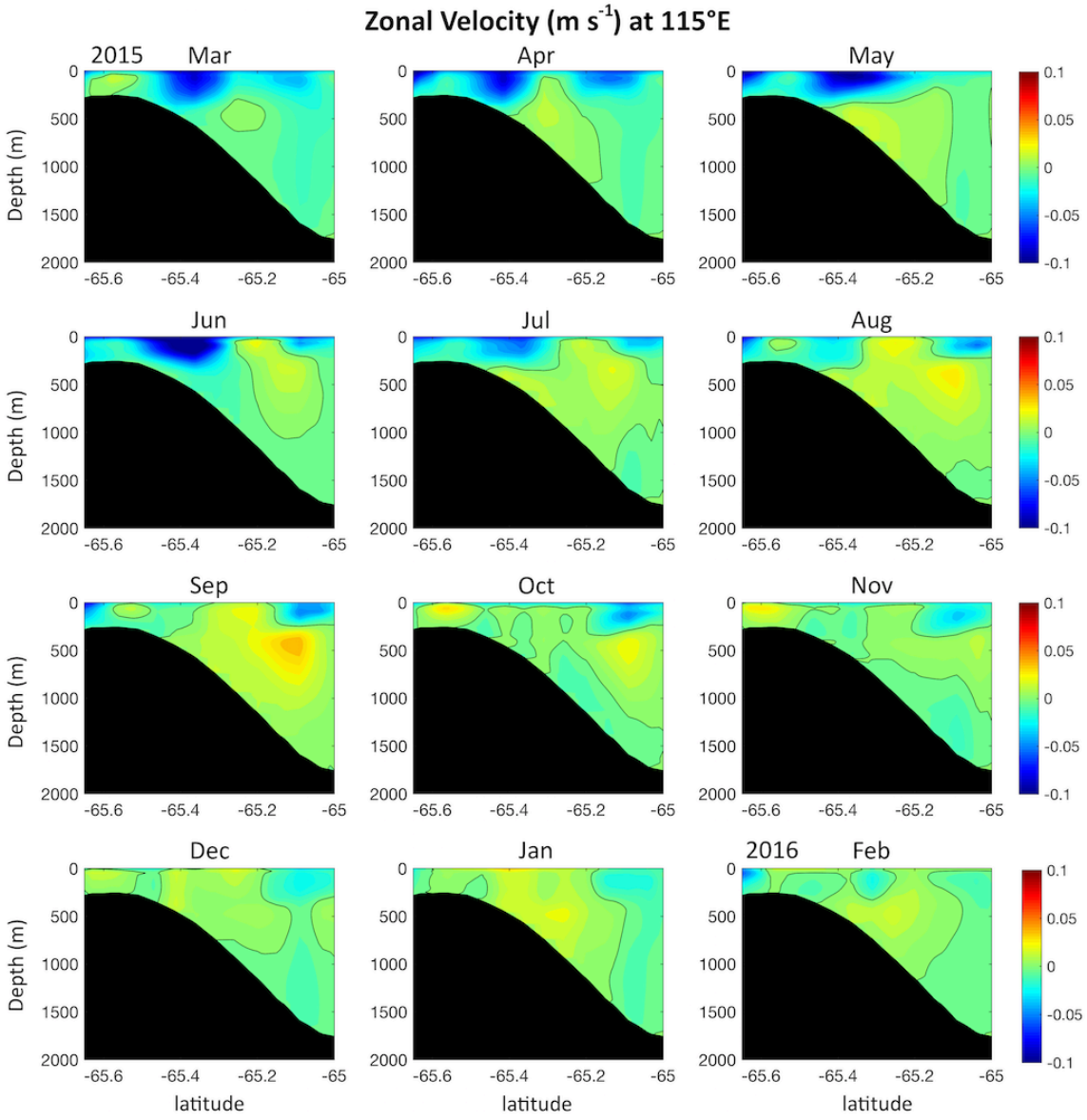

Figure 6.9. Modelled flow on the slope at 115°E. Zonal velocity (m s^{-1}, color) between March 2015 and February 2016 from the monthly model output at 115°E (see black line in Figure 6.7 for location). Positive is eastward. The black line is the contour of 0 m s^{-1}.

6.5. Discussion

Our study shows the unique bathymetric and year-round hydrographic measurements collected in deep (up to 900 m), sea-ice covered areas of the depression located on the continental shelf of the Sabrina Coast. The observations have been collected by ice-capable profiling floats, confirming their ability to collect essential measurements in the sea ice zone for multiple years not only offshore of the shelf break (e.g. Wong et al., 2011; Williams et al., 2011), but also well within the continental shelf. These floats are therefore an important tool to better understand the ocean influence on melting of the Antarctic Ice Sheet.

6.5.1. Impact of bathymetry on MCDW delivery to ice shelves

The depression is ~ 500 m deep and >100 km wide at the shelf break (Nitsche et al., 2017). The depression is most likely the result of glacial erosion as it gets deeper (up to 900 m) poleward of the shelf break (Nitsche et al., 2017). It might be even deeper in areas unsampled by our survey. Previous bathymetric and oceanographic data collected at the front of Totten Ice Shelf revealed that two narrow (< 5 km) and deep (900 and 1100 m) troughs are the main pathway for MCDW into the ice-shelf cavity (Rintoul et al., 2016, see Figure 6.2A). However, the measured MCDW was about -0.4°C at the Totten front, much cooler than the MCDW observed in the depression (> 0°C, see Figure 6.2B). Similar narrow troughs are present in front of the Moscow University Ice Shelf (Gulick et al., 2017; Fernandez et al., 2018) with even cooler (-1.3°C) water (Silvano et al., 2017). These troughs were presumably scoured by basal channels flowing beneath the Antarcic Ice Sheet during past colder climates (Gulick et al., 2017; Fernandez et al., 2018).

Results from our study and those from previous work imply that bathymetric barriers, like sills or steep slopes near the coast, prevent the warmest MCDW found on the continental shelf from reaching the Totten and Moscow University ice shelves (Silvano et al. 2017; Nitsche et al., 2017). Moreover, the presence of multiple narrow troughs at the front of the ice shelves suggest that the depression is not a continuous feature linking the shelf break and the ice-shelf cavities, but rather that the depression has a southern edge just north of the ice shelves, as also suggested by Fernandez et al. (2018) based on bathymetric and seismic data collected on the eastern flank of the depression. The MCDW follows a cyclonic circulation in the depression. Once at the southern edge of the depression, MCDW and water from the thermocline above the depth of the bathymetric barriers can reach the ice-shelf cavities through the narrow troughs, while the deeper and warmer MCDW turns offshore along the western flank of the depression.

The bathymetry on the Sabrina Coast is rather different compared to the Amundsen and Bellingshsausen seas, where deep troughs provide a direct pathway for MCDW between the shelf break and the cavities beneath several ice shelves (Jacobs et al. 2012; Jenkins and Jacobs 2008). Therefore the water reaching the ice shelves in these regions is warmer than on the Sabrina Coast. The presence of a sill beneath an ice shelf can reduce the temperature of the water reaching the deepest areas of the cavity, as seen at Pine Island Glacier in the Amundsen Sea where the "reduction" is of the order of few decimals of a degree (Jenkins et al., 2010; Dutrieux et al., 2014). The reduction observed on the Sabrina Coast (> 0.7°C) is much greater than that beneath Pine Island Glacier due to bathymetric obstacles on the open continental shelf.

6.5.2. Seasonal variability of MCDW intrusions

The measurements collected by the floats show that the MCDW layer in the depression in autumn and early winter is ~0.11°C warmer and ~75 m thicker than in spring and summer. In terms of maximum temperature, the MCDW reaches peaks of 0.9°C during autumn and early winter, while it remains below 0.4°C in other months. The observed seasonality in the depression can then affect the seasonality of the basal melt at the Totten and Moscow University ice shelves. Ocean heat delivery to the ice shelves depends not only on the properties of the MCDW accessing the continental shelf, but also on temporal variability of thermocline depth near the ice shelves. Ekman pumping (Dutrieux et al., 2014; Kim et al. 2017) and buoyancy forcing (Khazendar et al., 2013; Gwyther et al., 2014; St-Laurent et al., 2015) influence the thermocline depth both on seasonal and interannual time scales. Unfortunately, the lack of year-round measurements at the front of ice shelves and the mostly unknown bathymetry on the Sabrina Coast prevent us to assess the interplay between these processes using either observations or models.

The seasonal changes in the depression reflect different origin of MCDW reaching the continental shelf. Warmer and thicker intrusions of MCDW originate on the upper slope to the east of the depression, while cooler and thinner intrusions originate to the west. The seasonality of the flow on the upper slope explains how two different MCDW sources can enter the depression at different times. In autumn and early winter a strong, top-to-bottom westward current (the Antarctic Slope Current) transports the warmer and thicker layer of MCDW from the east into the depression following isobaths. During other months, an eastward current develops near the sea floor (the Antarctic Slope Undercurrent), allowing intrusions of the cooler and thinner layer of MCDW from the west of the depression.

The MCDW is cooler on the slope to the west of the depression due to the presence of a ridge centered at ~115°E (see Figure 6.1). The ridge causes cyclonic recirculation and mixing of cooler water found on the slope with offshore warm water, allowing the formation of a cooler version of MCDW at ~115°E compared to further east at the eastern entrance of the depression (~120°E; Wakatsuchi et al., 1994). Moreover, the cold surface layer is deeper at 115°E than at 120°E (Wakatsuchi et al., 1994; see also Figure 6.6), possibly due the cyclonic circulation which depresses isopycnals near the shelf break. The deeper surface layer means that a thinner layer of MCDW has to access the depression in the west. Thus, the cyclonic circulation in the presence of a ridge helps explain the cooler and thinner layer of MCDW entering the depression from the west.

Observations of seasonal variability of the flow on the Antarctic slope are scarce due to the logistical issues that complicate the deployment and recovery of moorings in this region. Furthermore, the deployment of fixed instruments in the top 500 m of the water column is high risk due to the presence of drifting icebergs. Recently, estimates of the barotropic component of the flow on the Antarctic slope have been obtained through the use of satellite altimeters (Armitage et al., 2018; Dotto et al., 2018) and a few moored arrays (e.g. Núñez-Riboni and Fahrbach, 2009; Peña-Molino et al., 2016). Those estimates are consistent with the results of our model: the westward flow associated with the Antarctic Slope Current is stronger in autumn and winter while it is weaker in spring and summer. The seasonal variability of the Antarctic Slope Current is mostly driven by seasonality of the Easterlies, which are stronger in autumn and winter and weaker in spring and summer (Núñez-Riboni and Fahrbach, 2009; Mathiot et al., 2011; Armitage et al., 2018).

Ship-based observations have been used to obtain a snapshot of the vertical structure of the flow on the upper slope and at the shelf break. Núñez-Riboni and Fahrbach (2009) provide a snapshot in all seasons in the eastern Weddell Sea. Their results are in agreement with our modelling results: top-to-bottom westward flow in autumn and winter (the Antarctic Slope Current) and the presence of an eastward current near the bottom (the Antarctic Slope Undercurrent) in spring and summer. The Antarctic Slope Undercurrent has also been observed in other summer surveys in the eastern Weddell Sea (Heywood et al., 1998; Chavanne et al., 2010) and in the Amundsen Sea (Walker et al., 2013). The mechanisms of formation of the Antarctic Slope Undercurrent are largely unknown. Some studies suggest that waves on the continental slope allow the undercurrent to form (e.g. Chavanne et al., 2010). Other studies associate the undercurrent with Ekman downwelling on the upper continental slope driven by the Easterlies (e.g. Jenkins et al., 2016). The downwelling causes southward deepening of the isopycnals and the formation of the Antarctic Slope Front. The vertical shear associated with the Antarctic Slope Front then allows the undercurrent to form in the bottom layer beneath the westward Antarctic Slope Current. Further investigation is required to understand the mechanisms that allow the development of the Antarctic Slope Undercurrent as well as to understand whether the undercurrent is a permanent feature and whether it is seen only in certain regions.

The mechanism we propose to explain the seasonality of the MCDW intrusions into the depression of the Sabrina Coast is consistent with the results of other studies of the flow on the Antarctic slope. We highlight that in situ and year-round measurements on the slope and at the shelf break are required to corroborate our proposed mechanism. Other mechanisms can also be important on

seasonal time scales, including changes in the bottom Ekman boundary layer (Wåhlin et al., 2012) and deepening/shoaling of isopycnals (Årthun et al., 2012; Mallett et al. 2018) on the slope. Moreover, small scale features on the Antarctic slope are not well resolved by our model. Therefore processes like eddies (Stewart and Thompson, 2015), waves (St-Laurent et al., 2013), tidal fluctuations (Stewart et al., 2018) and the dynamics of jets forming on the slope (Thompson and Heywood, 2008; Peña-Molino et al., 2016) are not well captured in our study and they can influence cross-shelf exchange. Neverthless, the consistency between observations and modelling results in our study suggests that seasonal variability of the flow on the Antarctic slope regulates the seasonality of the MCDW intrusions onto the Sabrina Coast continental shelf.

6.6. Conclusions

Ice-capable profiling floats allowed collection of two years of unprecedented oceanographic and bathymetric measurements on the Sabrina Coast continental shelf. They reveal that the depression found on the shelf is up to 900 m deep and provides a pathway for warm MCDW between the open ocean and the inner continental shelf. The depression is not directly connected with cavities beneath the Totten and Moscow University ice shelves and it has most likely a southern edge to the north of the ice shelves. This implies that the warmest core of the MCDW intrusions cannot reach the ice-shelf cavities at present (Rintoul et al., 2016), in contrast to the Amundsen and Bellingshsausen seas.

Intrusions of MCDW into the depression are warmer and thicker in autumn and early winter than in spring and summer. Using an ocean model, we propose that seasonality of the flow on the upper slope and shelf break explains the seasonality of the MCDW intrusions. In autumn and early winter a strong westward current (the Antarctic Slope Current) promotes warm intrusions from east of the depression. In spring and summer an eastward current develops near the bottom (the Antarctic Slope Undercurrent) that allows intrusions from the west where off-shelf MCDW is cooled by a permanent cyclonic eddy.

Our study shows how changes in the flow on the Antarctic continental slope influence the temperature and thickness of the MCDW layer that can access the continental shelf. As a consequence, future changes of the flow on the slope driven by changes of winds (Spence et al., 2014) or sea ice (Hellmer et al., 2012) can affect the ocean heat delivery to the continental shelf and, ultimately, to the Antarctic Ice Sheet

6.7. Supporting information

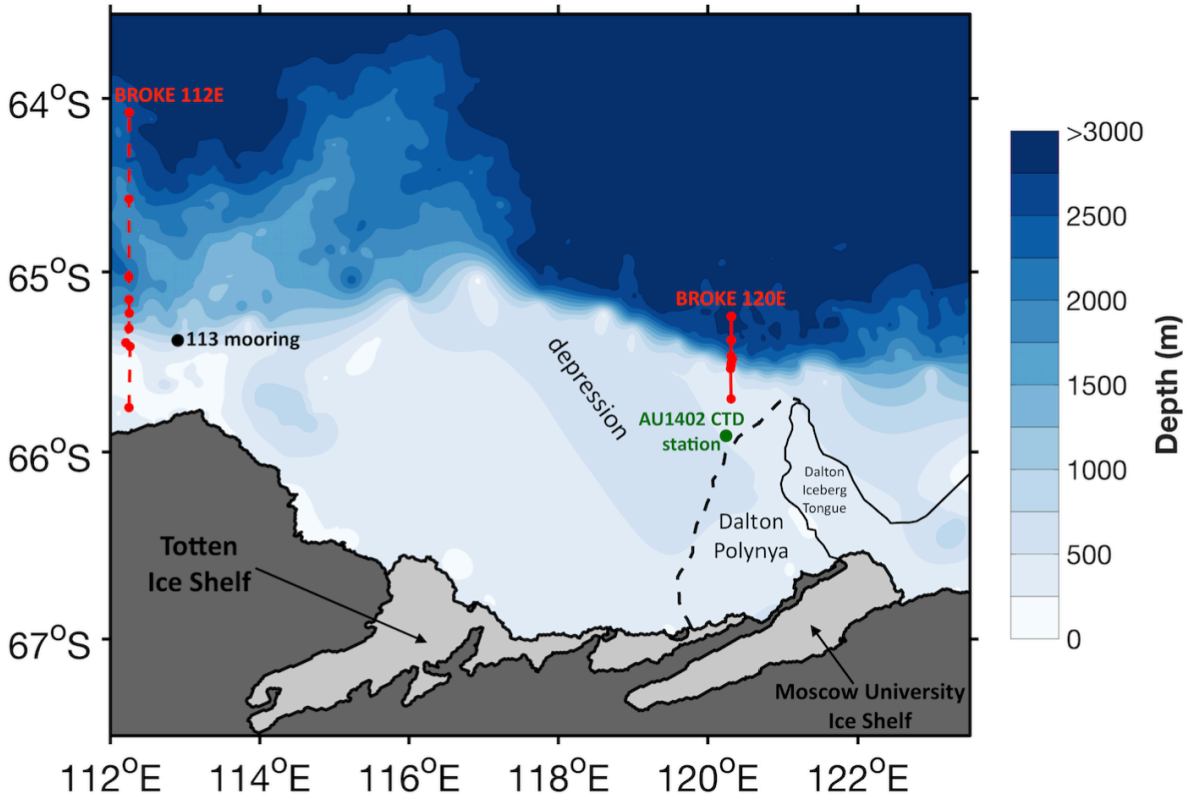

Figure 6.10. Sabrina Coast. Map of the survey area with overlaid bathymetry and coastline (IBCSO, Arndt et al., 2013). In red are the CTD transects completed during the BROKE survey in February 1996 at ~120°E (solid line) and ~112°E (dashed line). The red dots are the CTD stations. The location of the mooring deployed in 2010 on the upper slope at 113°E is in black. The green circle shows the location of a CTD station completed during the AU1402 survey in January 2015.

Here we validate the model using observations collected on the upper slope/shelf break during past oceanographic campaigns on the Sabrina Coast (Figure 6.10). In this way we can test if the model is able to reproduce water masses, stratification, fronts and currents on the upper slope/shelf break, where the modelling focus of our study is. We also show a comparison with data collected on the Sabrina Coast continental shelf to show whether the model can reproduce the ocean stratification there, which can affect ocean properties on the slope (Stewart and Thompson, 2016). To be clear, we do not expect circulation and water masses to be perfectly reproduced on the continental shelf. This is due to the irrealistic bathymetry poleward of the shelf break as well as to the relatively low resolution of the model (both horizontal and vertical) that tends to smooth ocean variability (both spatially and temporally), especially near the seafloor.

In Figure 6.11 we first compare the model output with measurements collected during the Baseline Research on Oceanography Krill and the Environment (BROKE, Bindoff et al., 2000). A meridional transect at ~120°E was conducted across the slope between between February 27 and

28, 1996 (see the solid red line in Figure 6.10 for location). We show potential temperature, neutral density and geostrophic velocity referenced to shipboard Acoustic Doppler Current Profiler (Bindoff et al., 2000). The model captures the main oceanographic features on the upper slope: southward deepening of the isopycnals associated with the Antarctic Slope Front, water from the thermocline and above accessing the continental shelf, and the offshore MCDW layer (> 0°C) centered at ~500m depth and ~500 m thick (Figures 6.11A and 6.11B). The offshore surface layer in the model is thinner and the MCDW is cooler than observed. The velocity structure is well captured, with a westward core on the outer shelf and an eastward current further offshore (Figures 6.11C and 6.11D). Observations reveal a deep and narrow westward flow on the lower slope that is not reproduced by the model.

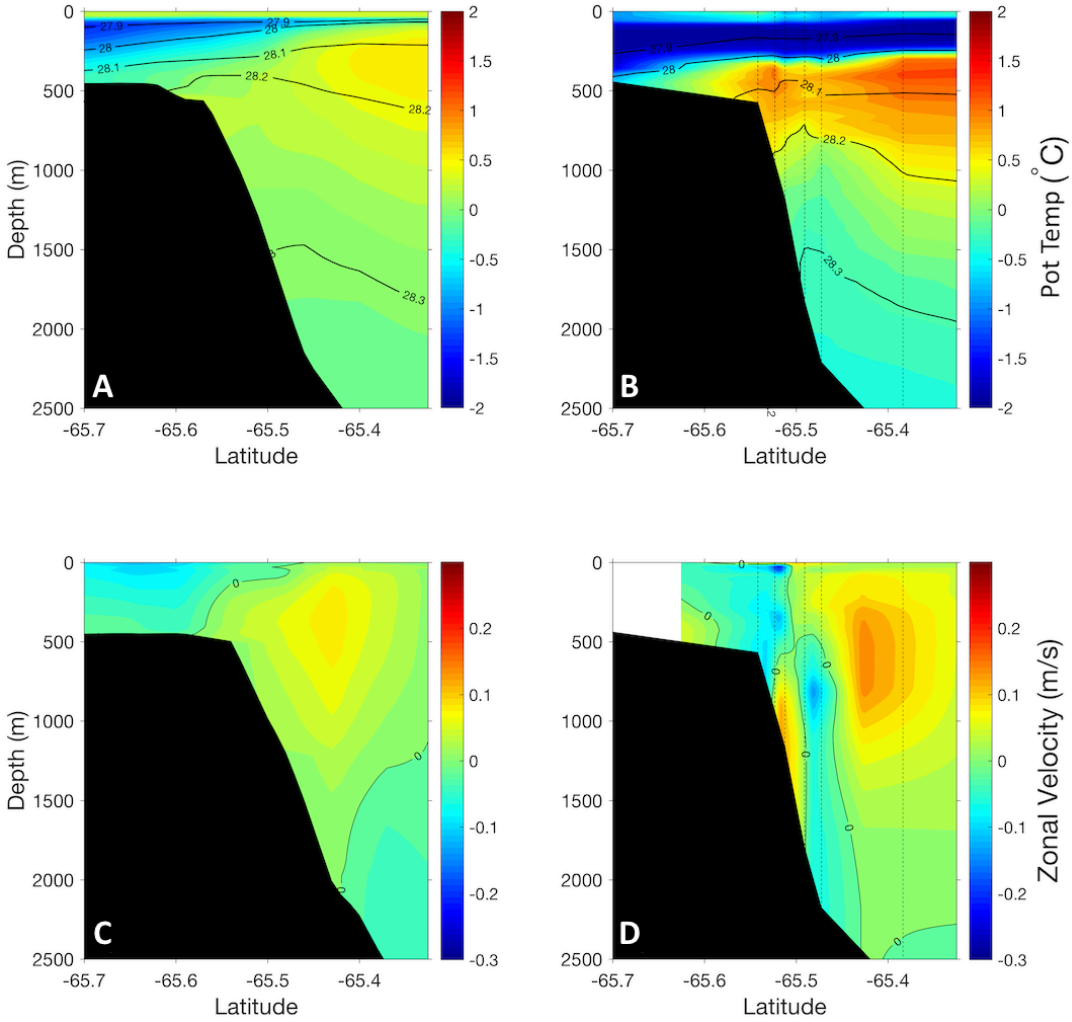

Figure 6.11. Comparison between model and BROKE observations at 120°E. Vertical section of potential temperature (°C) from (A) the model and (B) BROKE observations along a meridional transect at 120°E. The location of the transect is highlighted by the red solid line in Figure 6.10. Contours of neutral density (kg m^{-3}) are overlaid in black. (C) Modelled zonal velocity (m s^{-1}) and (D) observed zonal geostrophic velocity (m s^{-1}). BROKE data were collected in late February 1996 and the output model is a monthly average from the same month. Black dashed vertical lines in (B) and (D) indicate the location of the CTD stations.

We then compare the model output with observations collected during a BROKE transect at ~112°E between February 22 and 24, 1996 (see dashed red line in Figure 6.10 for location). The oceanographic features are reproduced less well here (Figure 6.12) compared to 120°E (Figure 6.11). Nevertheless, the observed differences between the two locations are captured by the model. The Antarctic Slope Front is deeper and steeper at 112°E than at 120°E, only cold surface water reaches the continental shelf, and cooler MCDW approaches the shelf break (Figures 6.12A and 6.12B). As at 120°E, the surface layer is thinner and the MCDW layer is cooler than what observations show (Figures 6.12A and 6.12B). In terms of velocity, the model captures the westward surface flow on the upper slope and the underlying eastward flow near the bottom (Figures 6.12C and 6.12D). However, model velocities are weaker than those observed.

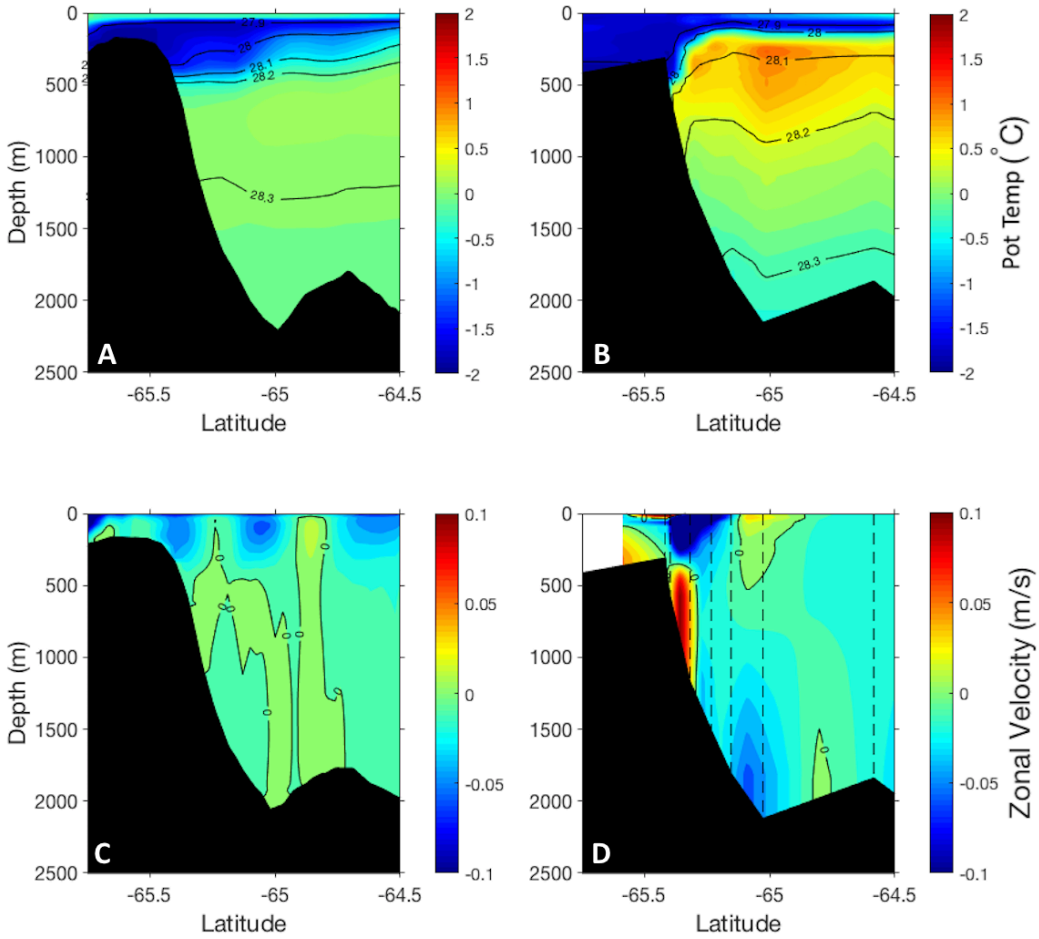

Figure 6.12. Comparison between model and BROKE observations at 112°E. Vertical section of potential temperature (°C) from (A) model and (B) BROKE observations along a meridional transect at 112°E. The location of the transect is highlighted by the red dashed line in Figure 6.10. Contours of neutral density (kg m^{-3}) are overlaid in black. (C) Modelled zonal velocity (m s^{-1}) and (D) observed zonal geostrophic velocity (m s^{-1}). BROKE data were collected in late February 1996 and the output model is a monthly average from the same month. Black dashed vertical lines in (B) and (D) indicate the location of the CTD stations.

We also compare the model with mooring data collected in 2010 on the upper slope (~1000 m isobath) at 113°E (see black dot in Figure 6.10 for location; Peña-Molino et al., 2016). The model reproduces the temporal variability of ocean currents observed at 500 m depth, showing similar seasonality: strong westward current in autumn, weaker current in other seasons with a general eastward flow in summer (Figure 6.13). In terms of signal amplitude, the model better reproduces the 500 m observations at 400 m depth rather than at 500 m. However, the seasonality of the flow doesn't change with depth.

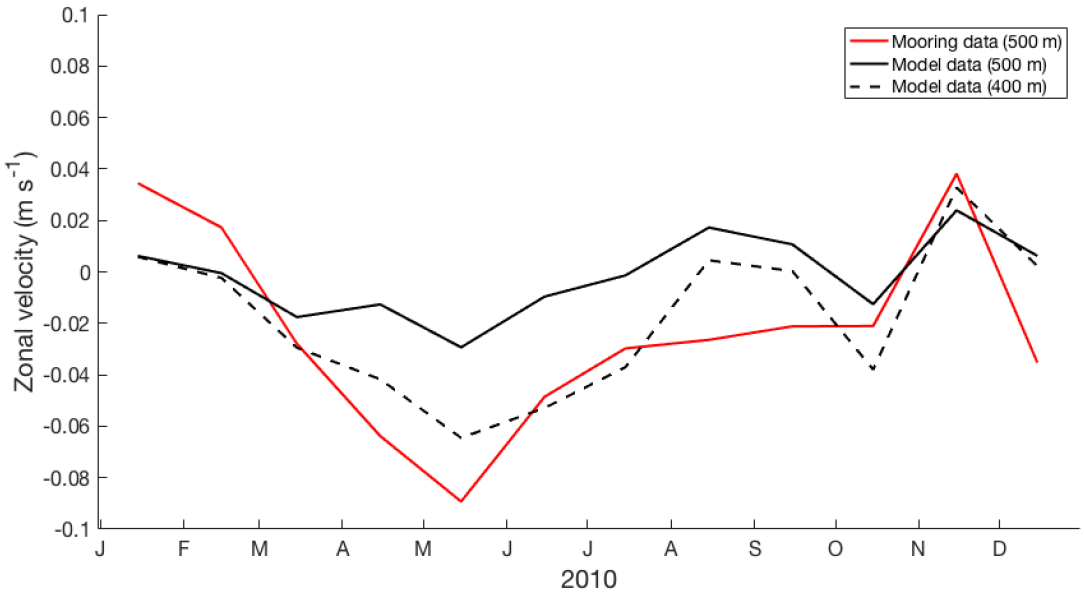

Figure 6.13. Comparison of the zonal velocity (m s^{-1}) between model output (black lines) and mooring observations (red line) on the upper slope at 113°E. Location of the mooring is shown by the black dot in Figure 6.10. Observations were collected throughout 2010 at 500 m depth and monthly means are shown for a better comparison with the model output. Model data are shown at 400 m (dashed black line) and 500 m (solid black line) depth.

The final comparison is done with CTD data collected on the continental shelf of the Sabrina Coast during the Aurora Australis voyage in 2015 (cruise AU1402). We consider a CTD station collected on the outer shelf, where the model seafloor depth is consistent with observed bathymetry (see green dot in Figure 6.10 for location). Most of the other CTD stations during that voyage shows a substantially different (100 to 500 m) bathymetry compared to that used in the model. The model captures the ocean stratification on the shelf: warm and salty MCDW overlaid by fresh and cold Winter Water (Figure 6.14). The modelled surface layer is warmer and saltier than observed. We note that the surface layer on the Antarctic shelf is highly variable in time because of rapid changes in sea-ice melt and atmospheric heating. As a consequence, it is expected that a monthly model output cannot resemble a single snapshot of the observed surface layer.

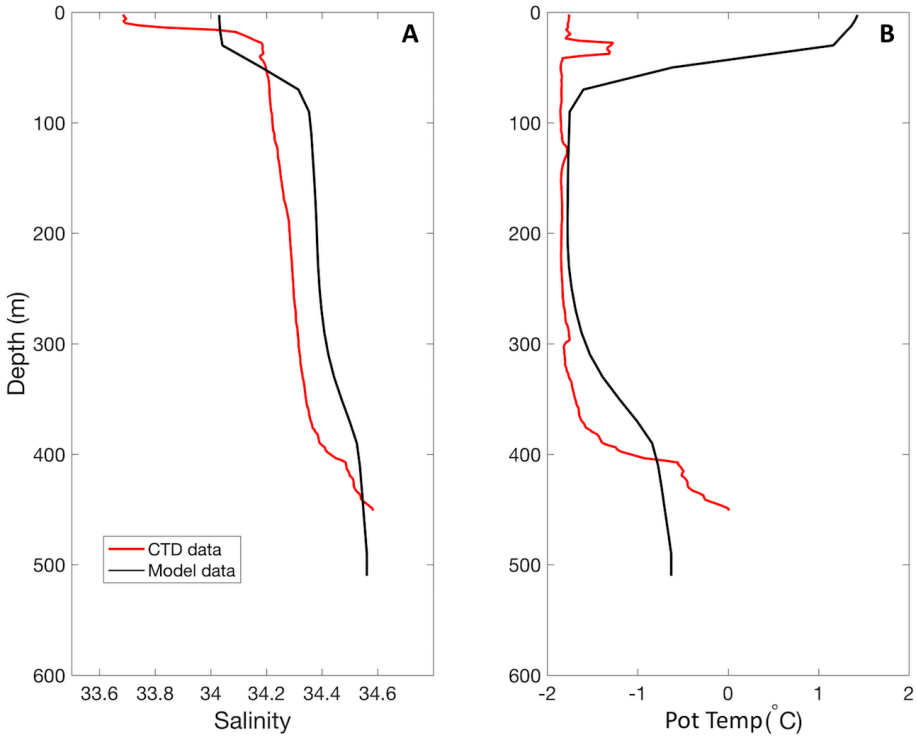

Figure 6.14. Comparison of salinity (A) and potential temperature (°C) (B) between model output (black line) and 2015 CTD observations (red line) on the Sabrina Coast continental shelf. Location of the CTD station is shown by the green dot in Figure 6.10.

Some differences are observed between model and observations. These discrepances can be partly due to the fact that most of the included observations represents a snapshot while the model output is a monthly average. Furthermore, the model resolution prevents perfect reproduction of small-scale ocean features typical of the Antarctic slope. For example, small observed cells of warm MCDW on the slope are not found in the model (e.g. Figure 6.11). Neverthless, the model is able to reproduce the main features that we are interested in: the velocity structure of the flow on the upper slope/shelf break along with its seasonal variability, and the vertical structure of the water masses and thus the ocean stratification.

Chapter 7
Conclusions

7.1. Main results

The Totten Glacier contributed at least 2 meters to global sea level during past warming cycles and modelling studies suggest it might do the same in coming centuries if global warming continues at current rates. However, the processes that drive the present melting of the Totten Glacier, and in particular the role of the ocean, remain poorly understood. Future projections of sea level rise require a better knowledge of the present drivers of mass loss from the Totten Glacier. This thesis, representing the most comprehensive observational study of the oceanic processes happening near the Totten Glacier to date, significantly advances this research. The observations are integrated with models to investigate key processes that measurements alone cannot address. The main results of the thesis are summarized below.

- **Warm water from the Southern Ocean drives rapid basal melt of the Totten Ice Shelf.** A deep trough provides the pathway for warm (-0.4°C) Modified Circumpolar Deep Water (MCDW) to the cavity beneath the Totten Ice Shelf. The warm water is then able to drive rapid basal melt, presumably triggering the observed mass loss of the Totten Glacier. This result highlights that the East Antarctic Ice Sheet is more susceptible to ocean-driven mass loss than previously thought, and its contribution needs to be accounted for in simulations of future sea level rise.

- **On the continental shelf of the Sabrina Coast, warm MCDW is widespread in the bottom layer and glacial meltwater is widespread at shallower depths. Dense Shelf Water, typical of coastal polynya regions, is absent**. These features are atypical of cold East Antarctic seas, resembling more closely the warm Amundsen and Bellingshausen seas. Relatively warm (-1.3°C) water is also able to reach the cavity beneath the Moscow University Ice Shelf through a narrow trough to drive basal melt. The water reaching both the Totten and Moscow University ice shelves is cooler than the MCDW observed elsewhere on the continental shelf (> 0°C). These observations indicate the presence of bathymetric barriers that, at present, prevent the warmest MCDW found on the continental shelf from reaching the ice shelves.

- **Glacial meltwater stops Antarctic Bottom Water formation on the Sabrina Coast.** Glacial meltwater released by basal melt of the Moscow University Ice Shelf inhibits the formation of cold Dense Shelf Water in the Dalton Polynya. The absence of this cold and dense water allows warm MCDW to flood the Sabrina Coast continental shelf and reach the Totten Ice Shelf to drive rapid basal melt. Thus, glacial meltwater injection into the ocean sustains rapid ice-shelf melting, inducing a positive feedback. The same process happens in the Amundsen Sea, where the freshening impact of glacial meltwater is even stronger than on the Sabrina Coast. This positive feedback, currently observed on the Sabrina Coast and in the Amundsen Sea, is thought to have contributed to abrupt sea level rise as well as changes in the global overturning circulation during past warming cycles.

- **MCDW reaches the inner continental shelf of the Sabrina Coast through a deep (up to 900 m) depression. MCDW intrusions are warmer and thicker in Austral autumn and early winter.** Seasonality of the flow on the Antarctic continental slope explains the seasonality of the intrusions. In autumn and early winter a strong, top-to-bottom westward current (Antarctic Slope Current) allows warmer and thicker MCDW intrusions from the upper slope to enter the depression from the east. An eastward current near the seafloor (Antarctic Slope Undercurrent) develops during the rest of the year, allowing cooler and thinner intrusions to enter the depression from the west, where a permanent cyclonic eddy cools waters on the slope. This result suggests that future changes of the currents on the Antarctic slope can influence the ocean heat delivery to the ice shelves.

This thesis improves our understanding of the ocean forcing on the Antarctic Ice Sheet, specifically at the Totten Glacier. Moreover, the thesis shows that not only is the impact of the ocean on the ice sheet important, but the opposite is also true: melting of Antarctic glaciers drives freshening and warming of the surrounding ocean, influencing the global overturning circulation and therefore the capacity of the ocean to store anthropogenic heat and carbon dioxide. As a consequence, the Southern Ocean and the Antarctic Ice Sheet cannot be studied separately because their interaction represents one of the key processes that influences the present and future global climate. While the importance of this interaction was already well documented in West Antarctica and Greenland, this thesis provides strong evidence that ice-ocean interaction in East Antarctica has global implications.

7.2 Future investigations

The global importance of the Totten Glacier is now established. However, the processes that drive temporal changes of this glacier remain largely unknown. Moreover, the impact of glacial meltwater released by melting of the Totten Glacier (and other Antarctic glaciers) on the Southern Ocean has not been fully assessed. Both observations and modelling are required to fill these gaps. Below are some ideas of what can be done in the future, using either measurements already collected or in dedicated future oceanographic campaigns and model runs.

Available observations

- Ocean velocities were recorded by moored instruments and provided year-long measurements that can be used to investigate seasonal changes of the circulation in the Dalton Polynya. These data along with temperature and salinity time series collected at the same mooring locations (Chapter 5) can help assess similarities and differences in circulation and hydrography between the polynya and the depression to the west (sampled by the floats, Chapter 6). In particular, such comparison would allow a better understanding of the interplay between Ekman pumping, cross-shelf exchange and surface buoyancy forcing in determining the ocean heat content at depth (i.e. MCDW thickness and properties) on the Sabrina Coast, both in terms of spatial and temporal variability.
- We used different techniques to estimate the meltwater content and sources on the continental shelf of the Sabrina Coast. In Chapter 3 we used salinity and oxygen measurements to estimate the glacial meltwater content, while in Chapter 5 we used oxygen isotopes to differentiate the contribution of meteoric water (glacial meltwater and precipitation) and sea ice melt to the freshwater budget. The two methods provide consistent results, showing similar meteoric and glacial meltwater content (see Figure 3.6C and Figure 5.2E) and thus confirming a small contribution from precipitation to the freshwater budget of the Sabrina Coast. An improvement in the methodology can be achieved by combining all these measurements into a single budget calculation that includes more tracers, providing thus further constraint on the calculation and helping to better disentangle the contribution from glacial meltwater and precipitation. An oceanographic-based estimate of the contribution of precipitation to the freshwater budget would be helpful, since re-analysis (as used in this thesis) and available atmospheric circumpolar models do not well resolve coastal processes influenced by steep and fine-scale orography, as found on the Sabrina Coast.

Future observations

- Long-term measurements are required near the front of the Totten Ice Shelf to better understand how ocean variability influences temporal changes of basal melt. More specifically, the deployment of moorings in the deep trough found at the ice front is required.
- The western sector of the Totten ice front could not be sampled in 2015 because of thick sea ice. Thus we presumably missed the core of the outflow from the cavity. A complete coverage of the Totten front would allow an improvement on the quantification of basal melt and ventilation of the cavity through a better constraint on mass and salt budgets. Future campaigns to the Totten Ice Shelf will need to cover this gap. The advent in coming years of ice breakers capable of breaking thick sea ice might be helpful for this purpose.
- Sustained observations on the continental slope and at the shelf break on the Sabrina Coast are required to further investigate the processes driving cross-shelf exchange. Among these processes, eddies and waves can be investigated by using gliders, while the deployment of mooring arrays across the continental slope can help examine the interaction between the flow on the slope and the depression at the shelf break.
- In-situ bathymetric data are required in the sea-ice covered areas of the Sabrina Coast, where the pathway(s) for warm water to the Totten Glacier is located. Bathymetric data can be collected by either ships or underwater vehicles.

The final goal is to develop observing systems capable of measuring on-shelf and off-shelf ocean properties simultaneously to determine how local and remote forcing affect the ocean heat delivery to the Totten Glacier. Such observing systems would also help assess how glacial meltwater impacts the global overturning circulation.

Future modelling

- High resolution ocean models are required to resolve small scale oceanic processes (e.g. dynamical instabilities and eddies) that influence circulation and melting beneath the ice shelves, exchange between open ocean and ice-shelf cavities, convection in polynyas and cross-shelf exchange. For example, in Chapter 5 we used a simple mixed layer model to assess the impact of meteoric water on mixed layer deepening and water-mass transformation. While the model can capture the vertical evolution of the mixed layer being not much sensitive to variability of the background ocean (this includes the effect of both changes in MCDW thickness and the depth of the meteoric water injection), it cannot

capture the horizontal spreading of meteoric water on the Sabrina Coast. To capture the horizontal spreading of meteoric water, 3-D models at very high resolution (meter-scale) are required to resolve submesoscale instabilities that govern the lateral mixing (e.g. Naveira Garabato et al., 2017). Similarly, in chapter 6 we used a numerical model at 7-km horizontal resolution to study the intrusions of MCDW onto the Sabrina Coast continental shelf. While the model well describes the intrusions due to interaction between currents on the continental slope and a bathymetric depression at the shelf break, eddies cannot be fully resolved at this resolution and therefore the "eddy component" of cross-self exchange still needs to be assessed.

- Numerical models must not only resolve small scale features, they also need to capture the large scale forcing (e.g. El-Nino-Southern Oscillation, ENSO, and the Southern Annular Mode, SAM) that is known to influence variability of the ocean heat flux to the ice shelves on interannual to decadal time scales.

Computer capabilities are continuously improving so that idealized and regional models can now be run to investigate the interplay between the processes mentioned above. The next step will be to assess such interplay at a circumpolar scale.

Bibliography

Aitken, A. R. A., J. L. Roberts, T. D. van Ommen, D. A. Young, N. R. Golledge, J. S. Greenbaum, D. D. Blankenship, and M. J. Siegert (2016), Repeated large-scale retreat and advance of Totten Glacier indicated by inland bed erosion, *Nature, 533*(7603), 385–389, doi:10.1038/nature17447.

Allen, S., and X. Durrieu de Madron (2009), A review of the role of submarine canyons in deep-ocean exchange with the shelf, *Ocean Sci.*, *5*, 607–620.

Allison, I. (1979), The mass budget of the Lambert Glacier drainage basin, Antarctica, *J. Glaciol.*, *22*(87), 223–235.

Armitage, T. W. K., R. Kwok, A. F. Thompson, and G. Cunningham (2018), Dynamic topography and sea level anomalies of the Southern Ocean: Variability and teleconnections, *J. Geophys. Res. Oceans*, *123*, 613–630, doi:10.1002/2017JC013534.

Arndt, J. E., et al. (2013), The International Bathymetric Chart of the Southern Ocean (IBCSO) Version 1.0: A new bathymetric compilation covering circum-Antarctic waters, *Geophys. Res. Lett.*, *40*, 3111–3117, doi:10.1002/grl.50413.

Årthun, M., K. W. Nicholls, K. Makinson, M. A. Fedak, and L. Boehme (2012), Seasonal inflow of warm water onto the southern Weddell Sea continental shelf, Antarctica, *Geophys. Res. Lett.*, *39*, L17601, doi:10.1029/2012GL052856.

Arzeno, I. B., R. C. Beardsley, R. Limeburner, B. Owens, L. Padman, S. R. Springer, C. L. Stewart, and M. J. M. Williams (2014), Ocean variability contributing to basal melt rate near the ice front of Ross Ice Shelf, Antarctica, *J. Geophys. Res. Oceans*, *119*, 4214– 4233, doi:10.1002/2014JC009792.

Assmann, K. M., A. Jenkins, D. R. Shoosmith, D. P. Walker, S. S. Jacobs, and K. W. Nicholls (2013), Variability of Circumpolar Deep Water transport onto the Amundsen Sea continental shelf through a shelf break trough, *J. Geophys. Res. Oceans*, *118*, 6603–6620, doi:10.1002/2013JC008871.

Biddle, L. C., K. J. Heywood, J. Kaiser, and A. Jenkins (2017), Glacial meltwater identification in the Amundsen Sea, *J. Phys. Oceanogr.*, *47*, 933–954, doi:10.1175/JPO-D-16-0221.1.

Bindoff, N. L., M. A. Rosenberg, and M. J. Warner (2000), On the circulation and water masses over the Antarctic continental slope and rise between 80 and 150°E, *Deep Sea Res. Part II*, *47*(12–13), 2299–2326, doi:10.1016/S0967-0645(00)00038-2.

Bindoff, N. L., G. D. Williams, and I. Allison (2001), Sea-ice growth and water-mass modification

in the Mertz Glacier polynya, East Antarctica, during winter, *Ann. Glaciol.*, *33*, 399–406.

Bohlander, J., and T. Scambos (2007), Antarctic Coastlines and Grounding Line Derived from MODIS Mosaic of Antarctica (MOA) (National Snow and Ice Data Center, 2007), http://nsidc.org/data/atlas/news/antarctic_coastlines.html.

Cavalieri, D. J., and S. Martin (1994), The contribution of Alaskan, Siberian, and Canadian coastal polynyas to the cold halocline layer of the Arctic Ocean, *J. Geophys. Res.*, *99*, 18343–18362.

Chavanne, C. P., K. J. Heywood, K. W. Nicholls, and I. Fer (2010), Observations of the Antarctic Slope Undercurrent in the southeastern Weddell Sea, *Geophys. Res. Lett.*, *37*, L13601, doi:10.1029/2010GL043603.

Christianson, K., et al. (2016), Sensitivity of pine island glacier to observed ocean forcing, *Geophys. Res. Lett.*, *43*, doi:10.1002/2016GL070500.

Church, J. A., et al. (2013), Sea level change, in Climate Change 2013: The Physical Science Basis. Contribution of Working Group I to the Fifth Assessment Report of the Intergovernmental Panel on Climate Change, edited by T. F. Stocker et al., pp. 1137–1216, Cambridge Univ. Press, Cambridge, U. K.

Cook, C. P., et al. (2013), Dynamic behaviour of the East Antarctic ice sheet during Pliocene warmth, *Nat. Geosci, 6*(9), 765–769, doi:10.1038/ngeo1889.

Cook, A. J., P. R. Holland, M. P. Meredith, T. Murray, A. Luckman, D. G. Vaughan (2016), Ocean forcing of glacier retreat in the western Antarctic Peninsula, *Science, 353*, 283–286, doi:10.1126/science.aae0017.

Cougnon, E. A., B. K. Galton-Fenzi, A. J. S. Meijers, and B. Legrésy (2013), Modeling interannual dense shelf water export in the region of the Mertz Glacier Tongue (1992–2007), *J. Geophys. Res. Oceans*, *118*, 5858–5872, doi:10.1002/2013JC008790.

Couldrey, M. P., L. Jullion, A. C. Naveira Garabato, C. Rye, L. Herraiz-Borreguero, P. J. Brown, M. P. Meredith, and K. L. Speer (2013), Remotely induced warming of Antarctic Bottom Water in the eastern Weddell gyre, *Geophys. Res. Lett.*, *40*, 2755–2760, doi:10.1002/grl.50526.

Craven, M., I. Allison, H. A. Fricker, and R. Warner (2009), Properties of a marine ice layer under the Amery Ice Shelf, East Antarctica. *J. Glaciol.*, *55*(192), 717–728, doi:10.3189/002214309789470941.

Cuffey, K. M., and S. J. Marshall (2000), Substantial contribution to sea-level rise during the last interglacial from the Greenland ice sheet, *Nature*, *404*, 591–594.

Darelius, E., I. Fer, and K. W. Nicholls (2016), Observed vulnerability of Filchner-Ronne Ice Shelf

to wind-driven inflow of warm deep water, *Nat. Commun.*, *7*, 12300, doi:10.1038/ncomms12300.

DeConto, R. M., and D. Pollard (2016), Contribution of Antarctica to past and future sea-level rise, *Nature*, *531*(7596), 591–597, doi:10.1038/nature17145.

Dee, D. P., et al. (2011), The ERA-Interim reanalysis: Configuration and performance of the data assimilation system, *Quart. J. Roy. Meteor. Soc.*, *137*, 553–597, doi:10.1002/qj.828.

Depoorter, M. A., J. L. Bamber, J. A. Griggs, J. T. M. Lenaerts, S. R. M. Ligtenberg, M. R. van den Broeke, and G. Moholdt (2013), Calving fluxes and basal melt rates of Antarctic ice shelves, *Nature*, *502*(7469), 89–92, doi:10.1038/nature12567.

Dinniman, M. S., J. M. Klinck, and W. O. Smith Jr. (2003), Cross-shelf exchange in a model of the Ross Sea circulation and biogeochemistry, *Deep Sea Res. Part II*, *50*, 3103–3120.

Dinniman, M. S., J. M. Klinck, E. E. Hofmann, and W. O. Smith Jr (2018), Effects of projected changes in wind, atmospheric temperature, and freshwater inflow on the Ross Sea, *J. Clim.*, *31*(4), 1619–1635, doi:10.1175/JCLI-D-17- 0351.s1.

Dotto, T. S., A. Naveira Garabato, S. Bacon, M. Tsamados, P. R. Holland, J. Hooley, E. Frajka-Williams, A. Ridout and M. P. Meredith (2018), Variability of the Ross Gyre, Southern Ocean: Drivers and responses revealed by satellite altimetry, *Geophys. Res. Lett.*, *45*, 6195–6204, doi:10.1029/2018GL078607.

Dowdeswell, J. A. (2006), The Greenland ice sheet and global sea-level rise, *Science*, *311*, 963–964, doi:10.1126/science.1124190.

Dupont, T. K., and R. B. Alley (2005), Assessment of the importance of ice-shelf buttressing to ice-sheet flows, *Geophys. Res. Lett.*, *32*, L04503, doi:10.1029/2004GL022024.

Dutrieux, P., J. De Rydt, A. Jenkins, P. R. Holland, H. K. Ha, S. H. Lee, E. J. Steig, Q. Ding, E. P. Abrahamsen, and M. Schroder (2014), Strong Sensitivity of Pine Island Ice-Shelf Melting to Climatic Variability, *Science*, *343*(6167), 174–178, doi:10.1126/science.1244341.

Dutton, A., A. E. Carlson, A. J. Long, G. A. Milne, P. U. Clark, R. DeConto, B. P. Horton, S. Rahmstorf, and M. E. Raymo (2015), Sea-level rise due to polar ice-sheet mass loss during past warm periods, *Science, 349*(6244), doi:10.1126/science.aaa4019.

Favier, L., G. Durand, S. L. Cornford, G. H. Gudmundsson, O. Gagliardini, F. Gillet- Chaulet, T. Zwinger, A. J. Payne, and A. M. Le Brocq (2014), Retreat of Pine Island Glacier controlled by marine ice-sheet instability, *Nat. Clim. Change, 4*(2), 117–121, doi:10.1038/nclimate2094.

Fernandez, R., S. Gulick, E. Domack, S. Montelli, A. Leventer, A. Shevenell, and B. Frederick (2018), Past ice stream and ice sheet changes on the continental shelf off the Sabrina Coast,

East Antarctica, *Geomorphology, 317*, 10–22, doi:10.1016/j.geomorph.2018.05.020.

Ferraccioli, F., E. Armadillo, T. Jordan, E. Bozzo, and H. Corr (2009), Aeromagnetic exploration over the East Antarctic Ice Sheet: A new view of the Wilkes Subglacial Basin, *Tectonophysics*, *478*(1–2),62–77, doi:10.1016/j.tecto.2009.03.013.

Flament, T., and F. Remy (2012) Dynamic thinning of Antarctic glaciers from along-track repeat radar altimetry, *J. Glaciol, 58*(211), 830–840, doi:10.3189/2012JoG11J118.

Fogwill, C. J., S. J. Phipps, C. S. M. Turney, and N. R. Golledge (2015), Sensitivity of the Southern Ocean to enhanced regional Antarctic ice sheet meltwater input, *Earth's Future*, *3*, 317–329, doi:10.1002/2015EF000306.

Foldvik, A., and T. Kvinge (1974), Conditional instability of sea-water at freezing-point, *Deep Sea Res. Oceanogr. Abstr.*, *21*(3), 169–174.

Foster, T. D. (1995), Abyssal water mass formation o the eastern Wilkes Land coast of Antarctica. *Deep Sea Res. Part I, 42*(4), 501–522, doi:10.1016/0967-0637(95)00002-N.

Fretwell, P., et al. (2013), Bedmap2: Improved ice bed, surface and thickness datasets for Antarctica, *Cryosphere*, *7*, 375–393, doi:10.5194/tc-7-375-2013.

Fricker, H. A., R. C. Warner, and I. Allison (2000), Mass balance of the Lambert Glacier-Amery Ice Shelf system, East Antarctica: A comparison of computed balance fluxes and measured fluxes, *J.Glaciol.*, *46*(155), 561–570, doi:10.3189/172756500781832765.

Fricker, H. A., S. Popov, I. Allison, and N. Young (2001), Distribution of marine ice beneaththe Amery Ice Shelf, *Geophys. Res. Lett.*, *28*(11), 2241–2244, doi:10.1029/2000GL012461.

Fyke, J. G., L. Carter, A. Mackintosh, A. J. Weaver, and K. J. Meissner (2010), Surface melting over ice shelves and ice sheets as assessed from modeled surface air temperatures, *J. Clim.*, *23*(7), 1929–1936, doi:10.1175/2009JCLI3122.1.

Gade, H. G. (1979), Melting of ice in sea water: A primitive model with application to the Antarctic ice shelf and icebergs, *J. Phys. Oceanogr.*, *9*, 189–198.

Gill, A. E. (1973), Circulation and bottom water production in the Weddell Sea, *Deep Sea Res. Oceanogr. Abstr.*, *20*(2), 111–140.

Gille, S. T., D. C. McKee, and D. G. Martinson (2016), Temporal changes in the Antarctic Circumpolar Current: Implications for the Antarctic continental shelves, *Oceanography, 29*(4), 96–105, doi:10.5670/oceanog.2016.102.

Golledge, N. R., L. Menviel, L. Carter, C. J. Fogwill, M. H. England, G. Cortese, and R. H. Levy (2014), Antarctic contribution to meltwater pulse 1A from reduced Southern Ocean overturning, *Nat. Commun.*, *5*, 5107.

Golledge, N. R., D. E. Kowalewski, T. R. Naish, R. H. Levy, C. J. Fogwill, and E. G. W. Gasson

(2015), The multi-millennial Antarctic commitment to future sea-level rise, *Nature*, *526*(7573), 421–425, doi:10.1038/nature15706.

Gordon, A. L., and P. L. Tchernia (1972), Waters of the continental margin off Adelie coast, Antarctica. Pp. 59–69 in *Antarctic Oceanolgy II: The Australian-New Zealand Sector*. *Antarctic Research Series*, vol. 19, D.E. Hayes, ed., American Geophysical Union, Washington, D.C.

Greenbaum, J. S., et al. (2015), Ocean access to a cavity beneath Totten Glacier in East Antarctica, *Nat. Geosci.*, *8*(4), 294–298, doi:10.1038/ngeo2388.

Greene, C. A., D. D. Blankenship, D. E. Gwyther, A. Silvano, and E. van Wijk (2017), Wind causes Totten Ice Shelf melt and acceleration, *Sci. Adv.*, *3*, e1701681, doi:10.1126/sciadv.1701681.

Gulick, S. P. S., et al. (2017), Initiation and long-term instability of the East Antarctic Ice Sheet, *Nature*, *552*, 225–229, doi:10.1038/nature25026.

Gwyther, D. E., B. K. Galton-Fenzi, J. R. Hunter, and J. L. Roberts (2014), Simulated melt rates for the Totten and Dalton ice shelves, *Ocean Sci.*, *10*, 267–279, doi:10.5194/os10-267-2014.

Harig, C., and F. J. Simons (2015), Accelerated West Antarctic ice mass loss continues to outpace East Antarctic gains, *Earth Planet. Sci. Lett.*, *415*, 134–141, doi:10.1016/j.epsl.2015.01.029.

Hattermann, T., O. A. Nøst, J. M. Lilly, and L. H. Smedsrud (2012), Two years of oceanic observations below the Fimbul Ice Shelf, Antarctica, *Geophys. Res. Lett.*, *39*, L12605, doi:10.1029/2012GL051012.

Hellmer, H. H., S. S. Jacobs, and A. Jenkins (1998), Oceanic erosion of a floating Antarctic glacier in the Amundsen Sea, in *Ocean, Ice, and Atmosphere: Interactions at the Antarctic Continental Margin, Antarct. Res. Ser.*, vol. 75, edited by S. S. Jacobs and R. F. Weiss, pp. 83–99, AGU, Washington, D. C.

Hellmer, H. H. (2004), Impact of Antarctic ice shelf basal melting on sea ice and deep ocean properties, *Geophys. Res. Lett.*, *31*, L10307.

Hellmer, H. H., F. Kauker, R. Timmermann, J. Determann, and J. Rae (2012), Twenty-first-century warming of a large Antarctic ice-shelf cavity by a redirected coastal current, *Nature*, *485*, 225–228, doi:10.1038/nature11064.

Helm, V., A. Humbert, and H. Miller (2014), Elevation and elevation change of Greenland and Antarctica derived from CryoSat-2, *Cryosphere*, *8*(4), 1539–1559, doi:10.5194/tc-8-1539-2014.

Herraiz-Borreguero, L., I. Allison, M. Craven, K. W. Nicholls, and M. A. Rosenberg (2013), Ice shelf/ocean interactions under the Amery Ice Shelf: Seasonal variability and its effect on marine ice formation, *J. Geophys. Res. Oceans*, *118*, 7117–7131,

doi:10.1002/2013JC009158.

Herraiz-Borreguero, L., R. Coleman, I. Allison, S. R. Rintoul, M. Craven, and G. D. Williams (2015), Circulation of modified Circumpolar Deep Water and basal melt beneath the Amery Ice Shelf, East Antarctica, *J. Geophys. Res. Oceans*, *120*, 3098–3112, doi:10.1002/2015JC010697.

Herraiz-Borreguero, L., J. A. Church, I. Allison, B. Peña-Molino, R. Coleman, M. Tomczak, and M. Craven (2016a), Basal melt, seasonal water mass transformation, ocean current variability, and deep convection processes along the Amery Ice Shelf calving front, East Antarctica, *J. Geophys. Res. Oceans*, *121*, 4946–4965, doi:10.1002/2016JC011858.

Herraiz-Borreguero, L., D. Lannuzel, P. van der Merwe, A. Treverrow, and J. B. Pedro (2016b), Large flux of iron from the Amery Ice Shelf marine ice to Prydz Bay, East Antarctica, *J. Geophys. Res. Oceans*, *121*, 6009–6020, doi:10.1002/2016JC011687.

Heywood, K. J., R. A. Locarnini, R. D. Frew, P. F. Dennis, and B. A. King (1998), Transport and water masses of the Antarctic Slope Front system in the eastern Weddell Sea, in *Ocean, Ice and Atmosphere: Interactions at the Antarctic Continental Margin, Antarctic Res. Ser.*, vol. 75, edited by S. S. Jacobs and R. F. Weiss, pp. 203–214, AGU, Washington, D. C, doi:10.1029/AR075p0203.

Hinkel, D. Lincke, A. T. Vafeidis, M. Perrette, R. J. Nicholls, R. S. Tol, B. Marzeion, X. Fettweis, C. Ionescu, and A. Levermann (2014), Coastal flood damage and adaptation costs under 21st century sea-level rise, *Proc. Natl. Acad. Sci. U.S.A.*, *111*(9), 3292–3297, doi:10.1073/pnas.1222469111.

Jacobs, S. S., A. F. Amos, and P. M. Bruchhausen (1970), Ross Sea oceanography and Antarctic bottom water formation, *Deep Sea Res. Oceanogr. Abstr.*, 17(6), 935–962.

Jacobs, S. S., H. H. Hellmer, C. S. M. Doake, A. Jenkins, and R. M. Frolich (1992), Melting of ice shelves and the mass balance of Antarctica, *J. Glaciol.*, *38*(130), 375–387.

Jacobs, S. S., and C. F. Giulivi (2010), Large multidecadal salinity trends near the Pacific-Antarctic continental margin, *J. Clim.*, *23*, 4508–4524, doi:10.1175/2010JCLI3284.1.

Jacobs, S. S., A. Jenkins, C. F. Giulivi, and P. Dutrieux (2011), Stronger ocean circulation and increased melting under Pine Island Glacier ice shelf, *Nat. Geosci.*, *4*(8), 519–523, doi:10.1038/ngeo1188.

Jacobs, S., A. Jenkins, H. Hellmer, C. Giulivi, F. Nitsche, B. Huber, and R. Guerrero (2012), The Amundsen Sea and the Antarctic ice sheet, *Oceanography*, *25*(3), 154–163, doi:10.5670/oceanog.2012.90.

Jacobs, S., C. Giulivi, P. Dutrieux, E. Rignot, F. Nitsche, and J. Mouginot (2013), Getz Ice Shelf

melting response to changes in ocean forcing, *J. Geophys. Res. Oceans*, *118*, 4152–4168, doi:10.1002/jgrc.20298.

Jamieson, S. S. R., N. Ross, J. S. Greenbaum, D. A. Young, A. R. A. Aitken, J. L. Roberts, D. D. Blankenship, S. Bo, and M. J. Siegert (2016), An extensive subglacial lake and canyon system in Princess Elizabeth Land, East Antarctica, *Geology*, *44*(2), 87–90, doi:10.1130/G37220.1.

Jenkins, A. (1999), The impact of melting ice on ocean waters, *J. Phys. Oceanogr.*, *29*, 2370–2381.

Jenkins, A., and S. S. Jacobs (2008), Circulation and melting beneath George VI ice shelf, Antarctica, *J. Geophys. Res.*, *113*, C04013, doi:10.1029/2007JC004449.

Jenkins, A., P. Dutrieux, S. S. Jacobs, S. D. McPhail, J. R. Perrett, A. T. Webb, and D. White (2010), Observations beneath Pine Island Glacier in West Antarctica and implications for its retreat, *Nat. Geosci.*, *3*(7), 468–472, doi:10.1038/ngeo890.

Jenkins, A., P. Dutrieux, S. Jacobs, E. J. Steig, G. H. Gudmundsson, J. Smith, and K. J. Heywood (2016), Decadal ocean forcing and Antarctic ice sheet response: Lessons from the Amundsen Sea, *Oceanography, 29*(4), 106–117, doi:10.5670/oceanog.2016.103.

Johnson, G. C. (2008), Quantifying Antarctic Bottom Water and North Atlantic Deep Water volumes, *J. Geophys. Res.*, *113*, C05027, doi:10.1029/2007JC004477.

Joughin, I., and L. Padman (2003), Melting and freezing beneath Filchner-Ronne Ice Shelf, Antarctica, *Geophys. Res. Lett.*, *30*, 1477, doi:10.1029/2003GL016941.

Joughin, I., and R. B. Alley (2011) Stability of the West Antarctic ice sheet in a warming world, *Nat. Geosci., 4*(8), 506–513, doi:10.1038/ngeo1194.

Joughin, I., B. E. Smith, and B. Medley (2014), Marine ice sheet collapse potentially underway for the Thwaites Glacier Basin, West Antarctica, *Science, 344*(6185), 735–738, doi:10.1126/science.1249055.

Jullion, L., A. C. Naveira Garabato, M. P. Meredith, P. R. Holland, P. Courtois, and B. A. King (2013), Decadal freshening of the Antarctic Bottom Water exported from the Weddell Sea, *J. Clim.*, *26*, 8111–8125, doi:10.1175/JCLI-D-12-00765.1

Khazendar, A., E. Rignot, and E. Larour (2009), Roles of marine ice, rheology, and fracture in the flow and stability of the Brunt/Stancomb-Wills Ice Shelf, *J. Geophys. Res.*, 114, F04007, doi:10.1029/2008JF001124.

Khazendar, A., M. P. Schodlok, I. Fenty, S. R. M. Ligtenberg, E. Rignot, and M. R. van den Broeke (2013), Observed thinning of Totten Glacier is linked to coastal polynya variability, *Nat. Commun.*, *4*, 2857, doi:10.1038/ncomms3857.

Khazendar, A., E. Rignot, D. M. Schroeder, H. Seroussi, M. P. Schodlok, B. Scheuchl, J. Mouginot,

T. C. Sutterley, and I. Velicogna (2016), Rapid submarine ice melting in the grounding zones of ice shelves in West Antarctica, *Nat. Commun.*, *7*, 13243, doi:10.1038/ncomms13243.

Kim, J.-W. (1976), A generalized bulk model of the oceanic mixed layer, *J. Phys. Oceanogr.*, *6*, 686–695.

Kim, I., D. Hahm, T. S. Rhee, T. W. Kim, C. -S. Kim, and S. H. Lee (2016), The distribution of glacial meltwater in the Amundsen Sea, Antarctica, revealed by dissolved helium and neon, *J. Geophys. Res. Oceans*, *121*, 1654–1666, doi:10.1002/2015JC011211.

Kim, T. W., H. K. Ha, A. K. Wåhlin, S. H. Lee, C. S. Kim, J. H. Lee, and Y. K. Cho (2017), Is Ekman pumping responsible for the seasonal variation of warm circumpolar deep water in the Amundsen Sea?, *Cont. Shelf Res.*, *132*, 38–48, doi:10.1016/j.csr.2016.09.005.

Kitade, Y., K. Shimada, T. Tamura, G. D. Williams, S. Aoki, Y. Fukamachi, F. Roquet, M. Hindell, S. Ushio, and K. I. Ohshima (2014), Antarctic Bottom Water production from the Vincennes Bay Polynya, East Antarctica, *Geophys. Res. Lett.*, 41, 3528–3534, doi:10.1002/2014GL059971.

Klinck, J. M. (1996), Circulation near submarine canyons: A modeling study, *J. Geophys. Res.*, *101*(C1), 1211–1223.

Kohut, J., E. Hunter, and B. Huber (2013), Small-scale variability of the cross-shelf flow over the outer shelf of the Ross Sea, *J. Geophys. Res. Oceans*, *118*, 1863–1876, doi:10.1002/jgrc.20090.

Kraus, E. B. and J. S Turner (1967), A one-dimensional model of the seasonal thermocline II. The general theory and its consequences, *Tellus*, *19*, 98–106.

Kulessa, B., D. Jansen, A. J. Luckman, E. C. King, and P. R. Sammonds (2014), Marine ice regulates the future stability of a large Antarctic ice shelf, *Nat. Commun.*, *5*, 3707, doi:10.1038/ncomms4707.

Kusahara, K., H. Hasumi, and T. Tamura (2010), Modeling sea ice production and dense shelf water formation in coastal polynyas around East Antarctica, *J. Geophys. Res.*, *115*, C10006.

Kusahara, K., and H. Hasumi (2013), Modeling Antarctic ice shelf responses to future climate changes and impacts on the ocean, *J. Geophys. Res. Oceans*, *118*(5), 2454–2475, doi:10.1002/jgrc.20166.

Kusahara, K., and H. Hasumi (2014), Pathways of basal meltwater from Antarctic ice shelves: A model study, *J. Geophys. Res. Oceans*, *119*(9), 5690–5704, doi:10.1002/2014JC009915.

Kusahara, K., H. Hasumi, A. D. Fraser, S. Aoki, K. Shimada, G. D. Williams, R. Massom, and T. Tamura (2017), Modeling ocean-cryosphere interactions off Adélie and George V Land,

East Antarctica, *J. Clim.*, *30*, 163–188, doi:10.1175/JCLI-D-15-0808.1.

Lacarra, M., M. N. Houssais, E. Sultan, S. R. Rintoul, and C. Herbaut (2011), Summer hydrography on the shelf off Terre Adelie/George V Land based on the ALBION and CEAMARC observations during the IPY. *Polar Sci.*, *5*, 88–103, doi:10.1016/j.polar.2011.04.008.

Li, X., E. Rignot, M. Morlighem, J. Mouginot, and B. Scheuchl (2015), Grounding line retreat of Totten Glacier, East Antarctica, 1996 to 2013, *Geophys. Res. Lett.*, *42*, 8049–8056, doi:10.1002/2015GL065701.

Li, X., E. Rignot, J. Mouginot, and B. Scheuchl (2016), Ice flow dynamics and mass loss of Totten Glacier, East Antarctica from 1989 to 2015, *Geophys. Res. Lett.*, *43*, 6366–6373, doi:10.1002/2016GL069173.

Liu, Y., J. C. Moore, X. Cheng, R. M. Gladstone, J. N. Bassis, H. Liu, J. Wen, and F. Hui (2015), Ocean-driven thinning enhances iceberg calving and retreat of Antarctic ice shelves, *Proc. Natl. Acad. Sci. U.S.A.*, *112*(11), 3263–3268, doi:10.1073/pnas.1415137112.

Makinson, K., and K. W. Nicholls (1999), Modeling tidal currents beneath Filchner-Ronne Ice Shelf andon the adjacent continental shelf: Their e ecton mixing and transport, *J. Geophys. Res.*, *104*(C6), 13449–13465, doi:10.1029/1999JC900008.

Mallett, H. K. W., L. Boehme, M. Fedak, K. J. Heywood, D. P. Stevens, and F. Roquet (2018), Variation in the distribution and properties of circumpolar deep water in the eastern Amundsen Sea, on seasonal timescales, using seal-borne tags, *Geophys. Res. Lett.*, *45*, 4982–4990, doi:10.1029/2018GL077430.

Marshall, and F. Schott (1999), Open-ocean convection: Observations, theory, and models, *Rev. Geophys.*, *37*, 1–64.

Marshall, J., and K. Speer (2012), Closure of the meridional overturning circulation through Southern Ocean upwelling, *Nat. Geosci.*, *5*(3), 171–180, doi:10.1038/ngeo1391.

Martin, S., and P. Kauffman (1981), A field and laboratory study of wave damping by grease ice, *J. Glaciol.*, *27*, 283–314.

Martinerie, P., D. Raynaud, D. M. Etheridge, J. -M. Barnola, and D. Mazaudier (1992), Physical and climatic parameters which influence the air content in polar ice, *Earth Planet. Sci. Lett., 112*(1–4), 1–13, doi:10.1016/0012-821X(92)90002-D.

Martinson, D. G. (1990), Evolution of the Southern Ocean winter mixed layer and sea ice: Open ocean deepwater formation and ventilation, *J. Geophys. Res.*, *95*, 11641–11654.

Masson-Delmotte, V., et al. (2008), A review of Antarctic surface snow isotopic composition: Observations, atmospheric circulation, and isotopic modeling, *J. Clim.*, *21*, 3359–3387, doi:10.1175/2007JCLI2139.1.

Mathiot, P., H. Goosse, T. Fichefet, B. Barnier, and H. Gallée (2011), Modelling the seasonal variability of the Antarctic Slope Current, *Ocean Sci.*, *7*(4), 445–532, doi:10.5194/os-7-455-2011.

Mazloff, M. R., P. Heimbach, and C. Wunsch (2010), An eddy-permitting Southern Ocean State Estimate, *J. Phys. Oceanogr.*, *40*, 880–899, doi:10.1175/2009JPO4236.1.

McDougall, T. J., and P. M. Barker (2011), *Getting Started with TEOS-10 and the Gibbs Seawater (GSW) Oceanographic Toolbox* (SCOR/IAPSO WG127, ISBN 978-0-646-55621-5, 2011), 28 pp.

Meier, M. F. (1983), Snow and ice in a changing hydrological world, *Hydrol. Sci. J.*, 28(1), 3–22.

Mengel, M., and A. Levermann (2014), Ice plug prevents irreversible discharge from East Antarctica, *Nat. Clim. Change*, *4*, 451–455, doi:10.1038/nclimate2226.

Menviel, L., A. Timmermann, O. E. Timm, and A. Mouchet (2010), Climate and biogeochemical response to a rapid melting of the West Antarctic Ice Sheet during interglacials and implications for future climate, *Paleoceanography*, *25*, PA4231, doi:10.1029/2009PA001892.

Meredith, M. P., M. A. Brandon, M. I. Wallace, A. Clarke, M. J. Leng, I. A. Renfrew, N. P. M. van Lipzig, and J. C. King (2008), Variability in the freshwater balance of northern Marguerite Bay, Antarctic Peninsula: Results from $\delta^{18}O$, *Deep Sea Res. Part II*, *55*, 309–322.

Meredith, M. P., H. J. Venables, A. Clarke, H. W. Ducklow, M. Erickson, M. J. Leng, J. T. M. Lenaerts, and M. R. van den Broeke (2013), The freshwater system west of the Antarctic Peninsula: Spatial and temporal changes, *J. Climate*, *26*, 1669–1684.

Merino, N., J. Le Sommer, G. Durand, N. C. Jourdain, G. Madec, P. Mathiot, and J. Tournadre (2016), Antarctic icebergs melt over the Southern Ocean: Climatology and impact on sea-ice, *Ocean Model.*, 104, 99–110.

Miles, T., S. H. Lee, A. Wåhlin, H. K. Ha, T. W. Kim, K. M. Assmann, and O. Schofield (2016), Glider observations of the Dotson Ice Shelf outflow, *Deep Sea Res. Part II*, 123, 16–29, doi:10.1016/j.dsr2.2015.08.008.

Miller, K. G., et al. (2012), High tide of the warm Pliocene: Implications of global sea level for Antarctic deglaciation, *Geology*, *40*, 407–410.

Moffat, C., B. Owens, and R. C. Beardsley (2009), On the characteristics of Circumpolar Deep Water intrusions to the west Antarctic Peninsula Continental Shelf, *J. Geophys. Res.*, *114*, C05017, doi:10.1029/2008JC004955.

Mohajerani, Y., I. Velicogna, and E. Rignot (2018), Mass loss of Totten and Moscow University glaciers, East Antarctica, using regionally optimized GRACE mascons, *Geophys. Res. Lett.*,

45, doi:10.1029/2018GL078173.

Morales Maqueda, M. A., A. J. Willmott, and N. R. T. Biggs (2004), Polynya dynamics: A review of observations and modeling, *Rev. Geophys.*, *42*, RG1004, doi:10.1029/2002RG000116.

Mouginot, J., E. Rignot, and B. Scheuchl (2014), Sustained increase in ice discharge from the Amundsen Sea Embayment, West Antarctica, from 1973 to 2013, *Geophys. Res. Lett.*, *41*, 1576–1584, doi:10.1002/2013GL059069.

Naish, T., et al. (2009), Obliquity-paced Pliocene West Antarctic ice sheet oscillations, *Nature, 458*, 322–328, doi:10.1038/nature07867.

Naveira Garabato, A. C., A. Forryan, P. Dutrieux, L. Brannigan, L. C. Biddle, K. J. Heywood, A. Jenkins, Y. L. Firing, and S. Kimura (2017), Vigorous lateral export of the meltwater outflow from beneath an Antarctic ice shelf, *Nature*, *542*, 219–222.

Nicholls, K. W. (1997), Predicted reduction in basal melt rates of an Antarctic ice shelf in a warmer climate, *Nature*, *388*, 460–462.

Nicholls, K. W., S. Østerhus, K. Makinson, T. Gammelsrød, and E. Fahrbach (2009), Ice-ocean processes over the continental shelf of the Southern Weddell Sea, Antarctica: A review, *Rev. Geophys.*, *47*(3), 1–23, doi:10.1029/2007RG000250.

Nihashi, S., and K. I. Ohshima (2015), Circumpolar Mapping of Antarctic coastal polynyas and landfast sea ice: Linkages and variability, *J. Clim.*, *28*, 3650–3670, doi:10.1175/JCLI-D-14-00369.1.

Niiler, P., and E. B. Kraus (1977), One-dimensional models of the upper ocean, in *Modeling and Prediction of the Upper Layers of the Ocean*, E. B. Kraus, Ed. (Pergamon Press, 1977), pp. 143–172.

Nitsche, F. O., S. S. Jacobs, R. D. Larter, and K. Gohl (2007), Bathymetry of the Amundsen Sea continental shelf: Implications for geology, oceanography, and glaciology, *Geochem. Geophys. Geosyst.*, *8*, Q10009.

Nitsche, F. O., D. Porter, G. Williams, E. A. Cougnon, A. D. Fraser, R. Correia, and R. Guerrero (2017), Bathymetric control of warm ocean water access along the East Antarctic Margin, *Geophys. Res. Lett.*, *44*, doi:10.1002/2017GL074433.

Nøst, O. A., M. Biuw, V. Tverberg, C. Lydersen, T. Hattermann, Q. Zhou, L. H. Smedsrud, and K. M. Kovacs (2011), Eddy overturning of the Antarctic Slope Front controls glacial melting in the Eastern Weddell Sea, *J. Geophys. Res.*, *116*, C11014, doi:10.1029/2011JC006965.

Núñez-Riboni, I., and E. Fahrbach (2009), Seasonal variability of the Antarctic Coastal Current and its driving mechanisms in the Weddell Sea, *Deep Sea Res. Part I*, *56*, 1927–1941, doi:10.1016/j.dsr.2009.06.005.

Ohshima, K. I., T. Takizawa, S. Ushio, and T. Kawamura (1996), Seasonal variations of the Antarctic coastal ocean in the vicinity of Lützow-Holm Bay, *J. Geophys. Res.*, *101*, 20617–20628.

Ohshima, K. I., et al. (2013), Antarctic Bottom Water production by intense sea-ice formation in the Cape Darnley Polynya, *Nat. Geosci.*, *6*(3), 235–240, doi:10.1038/ngeo1738.

Orsi, A. H., T. Whitworth III, and W. D. Nowlin Jr. (1995), On the meridional extent and fronts of the Antarctic Circumpolar Current, *Deep Sea Res. Part I*, *42*, 641–673.

Orsi, A. H., G. C. Johnson, and J. L. Bullister (1999), Circulation, mixing, and production of Antarctic Bottom Water, *Prog. Oceanogr.*, 43, 55–109.

Orsi, A. H., and C. L. Wiederwohl (2009), A recount of Ross Sea waters, *Deep Sea Res. Part II*, *56*(13–14), 778–795, doi:10.1016/j.dsr2.2008.10.033.

Padman, L., H. A. Fricker, R. Coleman, S. Howard, and L. Erofeeva (2002), A new tide model for the Antarctic ice shelves and seas, *Ann. Glaciol.*, *34*, 247–254.

Padman, L., et al. (2012), Oceanic controls on the mass balance of Wilkins Ice Shelf, Antarctica, *J. Geophys. Res.*, *117*, C01010, doi:10.1029/2011JC007301.

Paolo, F. S., H. A. Fricker, and L. Padman (2015), Volume loss from Antarctic ice shelves is accelerating, *Science*, *348*(6232), 327–331, doi:10.1126/science.aaa0940.

Passchier, S. (2011), Linkages between East Antarctic Ice Sheet extent and Southern Ocean temperatures based on a Pliocene high-resolution record of ice-rafted debris off Prydz Bay, East Antarctica, *Paleoceanography*, *26*, PA4204, doi:10.1029/2010PA002061.

Patterson, M. O., et al. (2014), Orbital forcing of the East Antarctic ice sheet duringthe Pliocene and Early Pleistocene, *Nat. Geosci., 7*(11), 841–847, doi:10.1038/ngeo2273.

Peña-Molino, B., M. S. McCartney, and S. R. Rintoul (2016), Direct observations of the Antarctic Slope Current transport at 113°E, *J. Geophys. Res. Oceans*, *121*, doi:10.1002/2015JC011594.

Petty, A. A., D. L. Feltham, and P. R. Holland (2013), Impact of atmospheric forcing on Antarctic continental shelf water masses, *J. Phys. Oceanogr.*, *43*(5), 920–940, doi:10.1175/JPO-D-12-0172.1.

Petty, A. A., P. R. Holland, and D. L. Feltham (2014), Sea ice and the ocean mixed layer over the Antarctic shelf seas, *Cryosphere*, *8*, 761–783, doi:10.5194/tc-8-761-2014.

Picard, G., and M. Fily (2006), Surface melting observations in Antarctica by microwave radiometers: Correcting 26-year time series from changes in acquisition hours, *Remote Sens. Environ., 104*(3), 325–336, doi:10.1016/j.rse.2006.05.010.

Pollard, D., and R. M. DeConto (2009), Modelling West Antarctica ice sheet growth and collapse

through the past five million years, *Nature, 458*, 329–332, doi:10.1038/nature07809.

Pollard, D., R. M. DeConto, and R. B. Alley (2015), Potential Antarctic ice sheet retreat driven by hydrofracturing and ice cli failure. *Earth Planet. Sci. Lett.*, *412*, 112–121, doi:10.1016/j.epsl.2014.12.035.

Pritchard, H. D., R. J. Arthern, D. G. Vaughan, and L. A. Edwards (2009), Extensive dynamic thinning on the margins of the Greenland and Antarctic ice sheets, *Nature, 461*(7266), 971–975, doi:10.1038/nature08471.

Pritchard, H. D., S. R. M. Ligtenberg, H. A. Fricker, D. G. Vaughan, M. R. van den Broeke, and L. Padman (2012), Antarctic ice–sheet loss driven by basal melting of ice shelves, *Nature*, *484*(7395), 502–505, doi:10.1038/nature10968.

Rackow, T., C. Wesche, R. Timmermann, H. H. Hellmer, S. Juricke, and T. Jung (2017), A simulation of small to giant Antarctic iceberg evolution: Differential impact on climatology estimates, *J. Geophys. Res. Oceans*, *122*, 3170–3190, doi:10.1002/ 2016JC012513.

Randall-Goodwin, E., et al. (2015), Freshwater distributions and water mass structure in the Amundsen Sea Polynya region, Antarctica, *Elem. Sci. Anthropocene*, *3*(1), 000065, doi:10.12952/journal.elementa.000065.

Rignot, E. (2002), Mass balance of East Antarctic glaciers and ice shelves from satellite data. *Ann. Glaciol., 34*(1), 217–227, doi:10.3189/172756402781817419.

Rignot, E., and S. S. Jacobs (2002), Rapid bottom melting widespread near Antarctic ice sheet grounding lines, *Science, 296*(5575), 2020–2023, doi:10.1126/science.1070942.

Rignot, E. (2006), Changes in ice dynamics and mass balance of the Antarctic ice sheet, *Philos. Trans. R. Soc. London, Ser. A*, *364*, 1637–1655.

Rignot, E., J. L. Bamber, M. R. van den Broeke, C. Davis, Y. Li, W. J. van de Berg, and E. van Meijgaard (2008), Recent Antarctic ice mass loss from radar interferometry and regional climate modelling, *Nat. Geosci.*, *1*, 106–110, doi:10.1038/ngeo102.

Rignot, E., I. Velicogna, M. R. van den Broeke, A. Monaghan, and J. T. M. Lenaerts (2011a), Acceleration of the contribution of the Greenland and Antarctic ice sheets to sea level rise, *Geophys. Res. Lett.*, 38, L05503, doi:10.1029/2011GL046583.

Rignot, E., J. Mouginot, and B. Scheuchl (2011b), Antarctic grounding line mapping from differential satellite radar interferometry, *Geophys. Res. Lett.*, *38*, L10504.

Rignot, E., S. Jacobs, J. Mouginot, and B. Scheuchl (2013), Ice-shelf melting around Antarctica, *Science*, *341*(6143), 266–270, doi:10.1126/science.1235798.

Rignot, E., J. Mouginot, M. Morlighem, H. Seroussi, and B. Scheuchl (2014), Widespread, rapid grounding line retreat of Pine Island, Thwaites, Smith, and Kohler glaciers, West Antarctica,

from 1992 to 2011, *Geophys. Res. Lett., 41*, 3502–3509, doi:10.1002/2014GL060140.

Rintoul, S. R. (1998), On the origin and influence of Adélie Land Bottom Water, in *Ocean, Ice, Atmosphere: Interactions at the Antarctic Continental Margin, Antarct. Res. Ser.*, vol. 75, edited by S. S. Jacobs and R. F. Weiss, pp. 151–171, AGU, Washington, D. C.

Rintoul, S. R., and A. C. Naveira Garabato (2013), Dynamics of the Southern Ocean circulation, in *Ocean Circulation and Climate: A 21st Century Perspective, International Geophysics Ser.*, vol. 103, edited by J. G. G. Siedler et al., pp. 471–492, Elsevier, N. Y.

Rintoul, S. R., A. Silvano, B. Peña-Molino, E. van Wijk, M. A. Rosenberg, J. S. Greenbaum, and D. D. Blankenship (2016), Ocean heat drives rapid basal melt of Totten Ice Shelf, *Sci. Adv.*, *2*, e1601610, doi:10.1126/sciadv.1601610.

Rintoul, S. R. (2018), The global influence of localized dynamics in the Southern Ocean, *Nature*, 558, 209-218, doi:10.1038/s41586-018-0182-3.

Roberts, J. L., et al. (2011), Refined broad-scale sub-glacial morphology of Aurora Subglacial Basin, East Antarctica derived by an ice-dynamics-based interpolation scheme, *Cryosphere*, *5*, 551–560, doi:10.5194/tc-5-551-2011.

Roquet, F., J.-B. Charrassin, S. Marchand, L. Boehme, M. Fedak, G. Reverdin, and C. Guinet (2011), Delayed-mode calibration of hydrographic data obtained from animal-borne Satellite Relay Data Loggers, *J. Atmos. Oceanic Technol.*, *28*, 787–801, doi:10.1175/2010JTECHO801.1.

Roquet, F., et al. (2013), Estimates of the Southern Ocean general circulation improved by animal-borne instruments, *Geophys. Res. Lett.*, *40*, 6176–6180.

Roquet, F., et al. (2014), A Southern Indian Ocean database of hydrographic profiles obtained with instrumented elephant seals, *Sci. Data1*, 140028.

Rosenberg, M., and S. R. Rintoul (2016), Aurora Australis marine science cruise AU1402, Totten and Mertz CTDs and moorings – oceanographic field measurements and analysis. ACE Cooperative Research Centre, May 2016, unpublished report, 69 pp.

Scambos, T., J. Bohlander, and B. Raup (1996), *Images of Antarctic Ice Shelves [2002-present]*, Boulder, Colorado USA: National Snow and Ice Data Center, doi:10.7265/N5NC5Z4N.

Scambos, T., B. Raup, and J. Bohlander (2001), *Images of Antarctic Ice Shelves, Version 1* (National Snow and Ice Data Center, 2001), doi:10.7265/N5NC5Z4N.

Scambos, T. A., J. A. Bohlander, C. A. Shuman, and P. Skvarca (2004), Glacier acceleration and thinning after ice shelf collapse in the Larsen B embayment, Antarctica, *Geophys. Res. Lett.*, *31*, L18402, doi:10.1029/2004GL020670.

Scherer, R. P. (1991), Quaternary and Tertiary micro-fossils from beneath Ice Stream B: Evidence

for a dynamic West Antarctic ice sheet history, *Global and Planet. Change*, *4*(4), 395–412.

Schmidtko, S., K. J. Heywood, A. F .Thompson, and S. Aoki (2014), Multidecadal warming of Antarctic waters, *Science*, *346*, 1227–1231.

Schoof, C. (2007), Ice sheet grounding line dynamics: Steady states, stability and hysteresis, *J. Geophys. Res., 112*, F03S28, doi:10.1029/2006JF000664.

Shadwick, E. H., S. R. Rintoul, B. Tilbrook, G. D. Williams, N. Young, A. D. Fraser, H. Marchant, J. Smith, and T. Tamura (2013), Glacier tongue calving reduced dense water formation and enhanced carbon uptake, *Geophys. Res. Lett., 40*, 904–909, doi:10.1002/grl.50178.

Shepherd, A., D. Wingham, and E. Rignot (2004), Warm ocean is eroding West Antarctic Ice Sheet, *Geophys. Res. Lett.*, *31*, L23402, doi:10.1029/2004GL021106.

Shepherd, A., et al. (2018), Mass balance of the Antarctic Ice Sheet from 1992 to 2017, *Nature*, *558*(7709), 219–222, doi:10.1038/s41586-018-0179-y.

Silvano, A., S. R. Rintoul, and L. Herraiz-Borreguero (2016), Ocean-ice shelf interaction in East Antarctica, *Oceanography*, *29*(4), 130–143, doi:10.5670/oceanog.2016.105.

Silvano, A., S. R. Rintoul, B. Peña-Molino, and G. D. Williams (2017), Distribution of water masses and meltwater on the continental shelf near the Totten and Moscow University ice shelves, *J. Geophys. Res. Oceans*, *122*, doi:10.1002/2016JC012115.

Silvano, A., S. R. Rintoul, B. Peña-Molino, W. R. Hobbs, E. van Wijk, S. Aoki, T. Tamura, and G. D. Williams (2018), Freshening by glacial meltwater enhances melting of ice shelves and reduces formation of Antarctic Bottom Water, *Sci. Adv.*, *4*, eaap9467, doi:10.1126/sciadv.aap9467.

Smith, W. H. F., and D. T. Sandwell (1997), Global seafloor topography from satellite altimetry and ship depth soundings, *Science*, *277*, 1956–1962.

Smith, D. A., and J. M. Klinck (2002), Water properties on the west Antarctic Peninsula continental shelf: A model study of effects of surface fluxes and sea ice, *Deep Sea Res. Part II*, *49*, 4863–4886.

Snow, K., B. M. Sloyan, S. R. Rintoul, A. McC. Hogg, and S. M. Downes (2016), Controls on circulation, cross-shelf exchange, and dense water formation in an Antarctic polynya, *Geophys. Res. Lett.*, *43*, 7089–7096, doi:10.1002/2016GL069479.

Spence, P., S. M. Griffies, M. H. England, A. M. C. Hogg, O. A. Saenko, and N. C. Jourdain (2014), Rapid subsurface warming and circulation changes of Antarctic coastal waters by poleward shifting winds, *Geophys. Res. Lett., 41*, 4601–4610, doi:10.1002/2014GL060613.

Spreen, G., L. Kaleschke, and G. Heygster (2008), Sea ice remote sensing using AMSR-E 89-GHz channels, *J. Geophys. Res.*, *113*, C02S03.

Stern, A. A., M. S. Dinniman, V. Zagorodnov, S. W. Tyler, and D. M. Holland (2013), Intrusion of warm surface water beneath the McMurdo Ice Shelf, Antarctica. *J. Geophys. Res. Oceans*, *118*, 7036–7048, doi:10.1002/2013JC008842.

Stewart, A. L., and A. F. Thompson (2015), Eddy-mediated transport of warm Circumpolar Deep Water across the Antarctic Shelf Break, *Geophys. Res. Lett.*, *42*, 432–440, doi:10.1002/2014GL062281.

Stewart, A. L., and A. F. Thompson (2016), Eddy generation and jet formation via dense water outflows across the Antarctic continental slope, *J. Phys. Oceanogr*, *46*(12), 3729–3750, doi:10.1175/JPO-D-16-0145.1.

Stewart, A. L., A. Klocker, and D. Menemenlis (2018), Circum-Antarctic shoreward heat transport derived from an eddy- and tide-resolving simulation, *Geophys. Res. Lett.*, *45*, doi:10.1002/2017GL075677.

St-Laurent, P., J. M. Klinck, and M. S. Dinniman (2013), On the role of coastal troughs in the circulation of warm circumpolar deep water on Antarctic shelves, *J. Phys. Oceanogr.*, *43*(1), 51–64., doi: 10.1175/JPO-D-11-0237.1.

St-Laurent, P., J. M. Klinck, and M. S. Dinniman (2015), Impact of local winter cooling on the melt of Pine Island Glacier, Antarctica, *J. Geophys. Res. Oceans*, *120*, 6718–6732, doi:10.1002/2015JC010709.

Sun, S., S. L. Cornford, D. E. Gwyther, R. M. Gladstone, B. K. Galton-Fenzi, L. Zhao, and J. C. Moore (2016), Impact of ocean forcing on the Aurora Basin in the 21st and 22nd centuries, *Ann. Glaciol.*, 1–8, doi:10.1017/aog.2016.27.

Sutterley, T. C., I. Velicogna, E. Rignot, J. Mouginot, T. Flament, M. R. van den Broeke, J. M. van Wessem, and C. H. Reijmer (2014), Mass loss of the Amundsen Sea embayment of West Antarctica from four independent techniques, *Geophys. Res. Lett.*, *41*, 8421–8428.

Tamura, T., K. I. Ohshima, and S. Nihashi (2008), Mapping of sea ice production for Antarctic coastal polynyas, *Geophys. Res. Lett.*, *35*, L07606.

Tamura, T., K. I. Ohshima, A. D. Fraser, and G. D. Williams (2016), Sea ice production variability in Antarctic coastal polynyas, *J. Geophys. Res. Oceans*, *121*, 2967–2979, doi:10.1002/2015JC011537.

Tang, C. L. (1991), A two-dimensional thermodynamic model for sea ice advance and retreat in the Newfoundland marginal ice zone, *J. Geophys. Res.*, *96* (C3), 4723–4737.

Takahashi, T., et al. (2009), Climatological mean and decadal change in surface ocean pCO_2, and net sea–air CO_2 flux over the global oceans, *Deep Sea Res. Part II*, *56*, 554–577, doi:10.1016/j.dsr2.2008.12.009.

Thoma, M., A. Jenkins, D. Holland, and S. Jacobs (2008), Modelling Circumpolar Deep Water intrusions on the Amundsen Sea continental shelf, Antarctica, *Geophys. Res. Lett.*, *35*, L18602, doi:10.1029/2008GL034939.

Thompson, A. F., and K. J. Heywood (2008), Frontal structure and transport in the northwestern Weddell Sea, *Deep Sea Res. Part I*, *55*(10), 1229–1251.

Thurnherr, A. M. (2010), A practical assessment of uncertainties in full-depth velocity profiles obtained with Teledyne/RDI Workhorse acoustic Doppler current profilers, *J. Atmos. Oceanic Tech.*, *27*, 1215–1227.

Thurnherr, A. M. (2014), How to Process LADCP Data with the LDEO Software, Versions IX.7–IX.10, (Lamont Doherty Earth Observatory, 2014).

Velicogna, I., and J. Wahr (2013), Time-variable gravity observations of ice sheet mass balance: Precision and limitations of the GRACE satellite data, *Geophys. Res. Lett.*, *40*, 3055–3063, doi:10.1002/grl.50527.

Velicogna, I., T. C. Sutterley, and M. R. van den Broeke (2014), Regional acceleration in ice mass loss from Greenland and Antarctica using GRACE time-variable gravity data, *Geophys. Res. Lett.*, *41*, 8130–8137, doi:10.1002/2014GL061052.

Venables, H. J., M .P. Meredith, and J. A. Brearley (2017), Modification of deep waters in Marguerite Bay, western Antarctic Peninsula, caused by topographic overflows, *Deep Sea Res. Part II*, *139*, 9–17, doi:10.1016/j.dsr2.2016.09.005.

Visbeck, M. (2002), Deep velocity profiling using lowered acoustic Doppler current profilers: Bottom track and inverse solutions, *J. Atmos. Oceanic Tech., 19*, 794–807.

Wåhlin, A. K., X. Yuan, G. Bjork, and C. Nohr (2010), Inflow of warm circumpolar deep water in the central Amundsen Shelf, *J. Phys. Oceanogr.*, *40*(6), 1427–1434, doi:10.1175/2010JPO4431.1.

Wåhlin, A. K. , R. D. Muench, L. Arneborg, G. Björk, H. Ha, S. H. Lee, and H. Alsén (2012), Some implications of Ekman layer dynamics for cross-shelf exchange in the Amundsen Sea, *J. Phys. Oceanogr.*, *42*(9), 1461–1474, doi:10.1175/JPO-D-11-041.1.

Wåhlin, A. K., O. Kalen, and K. M. Assmann (2016), Subinertial oscillations on the Amundsen Sea Shelf, Antarctica, *J. Phys. Oceanogr.*, *46*, 2573–2582, doi: 10.1175/JPO-D-14-0257.1.

Wakatsuchi, M., K. I. Ohshima, M. Hishida, and M. Naganobu (1994), Observations of a street of cyclonic eddies in the Indian Ocean sector of the Antarctic Divergence, *J. Geophys. Res.*, *99*(C10), 20417–20426.

Walker, D. P., A. Jenkins, K. M. Assmann, D. R. Shoosmith, and M. A. Brandon (2013), Oceanographic observations at the shelf break of the Amundsen Sea, Antarctica, *J. Geophys.*

Res. Oceans, *118*, 2906–2918, doi:10.1002/jgrc.20212.

Weber, M. E., et al. (2014), Millennial-scale variability in Antarctic ice-sheet discharge during the last deglaciation, *Nature*, *510*, 134–138, doi:10.1038/nature13397.

Weertman, J. (1974), Stability of the junction of an ice sheet and an ice shelf. *J. Glac., 13*(67), 3–11.

Wen, J., Y. Wang, W. Wang, K. C. Jezek, H. Liu, and I. Allison (2010), Basal melting and freezing under the Amery Ice Shelf, East Antarctica, *J. Glaciol., 56*(195), 81–90.

Williams, T., T. van de Flierdt, S. R. Hemming, E. Chung, M. Roy, and S. L. Goldstein (2010a), Evidence for iceberg armadas from East Antarctica in the Southern Ocean during the late Miocene and early Pliocene, *Earth Planet. Sci. Lett.*, *290*(3–4), 351–361, doi:10.1016/j.epsl.2009.12.031.

Williams, G. D., N. L. Bindoff, S. J. Marsland, and S. R. Rintoul (2008), Formation and export of dense shelf water from the Ade´lie Depression, East Antarctica, *J. Geophys. Res.*, *113*, C04039, doi:10.1029/2007JC004346.

Williams, G. D., S. Aoki, S. S. Jacobs, S. R. Rintoul,T. Tamura, and N. L. Bindoff (2010b), Antarctic Bottom Water from the Adélie and George V Land coast, East Antarctica (140–149°E), *J. Geophys. Res.*, *115*, C04027, doi:10.1029/2009JC005812.

Williams, G. D., A. J. S. Meijers, A. Poole, P. Mathiot, T. Tamura, and A. Klocker (2011), Late winter oceanography off the Sabrina and BANZARE coast (117–128 E), East Antarctica, *Deep Sea Res. Part II*, *58*(9-10), 1194–1210, doi:10.1016/j.dsr2.2010.10.035.

Williams, G. D., et al. (2016), The suppression of Antarctic bottom water formation by melting ice shelves in Prydz Bay. *Nat. Commun.*, *7*, 12577, doi:10.1038/ncomms12577.

Wilson, N. J., and F. Straneo (2015), Water exchange between the continental shelf and the cavity beneath Nioghalvfjerdsbræ (79 North Glacier), *Geophys. Res. Lett.*, *42*, 7648–7654.

Wong, A. P. S., and S. C. Riser (2011), Profiling float observations of the upper ocean under sea ice off the Wilkes Land coast of Antarctica, *J. Phys. Oceanogr.*, *41*, 1102–1115.

Worby, A. P., A. Steer, J. L. Lieser, P. Heil, D. Yi, T. Markus, I. Allison, R. A. Massom, N. Galin, and J. Zwally (2011), Regional-scale sea ice and snow thickness distributions from in situ and satellite measurements over East Antarctica during the Sea Ice Physics and Ecosystem eXperiment (SIPEX), *Deep Sea Res. Part II*, 58, 1125–1136.

Worthington, L. V. (1981), The water masses of the world ocean: Some results of a fine-scale census. Pp. 42–69 in *Evolution of Physical Oceanography*. B. A. Warren and C. Wunsch, eds, MIT Press, Cambridge, MA.

Wouters, B., A. Martin-Español, V. Helm, T. Flament, J. M. van Wessem, S. R. M. Ligtenberg, M.

R. van den Broeke, and J. L. Bamber (2015), Dynamic thinning of glaciers on the Southern Antarctic Peninsula, *Science*, *348*(6237), 899–903, doi:10.1126/science.aaa5727.

Young, D. A., et al. (2011), A dynamic early East Antarctic Ice Sheet suggested by ice-covered fjord landscapes, *Nature, 474*(7349), 72–75, doi:10.1038/nature10114.

Zhang, X., A. F. Thompson, M. M. Flexas, F. Roquet, and H. Bornemann (2016), Circulation and meltwater distribution in the Bellingshausen Sea: From shelf break to coast, *Geophys. Res. Lett.*, *43*, 6402–6409, doi:10.1002/2016GL068998.